Durham E-Theses

Structure and dynamics in framework materials

Matthew Richard Hampson

How to cite:

Use policy

Abstract

"Structure and Dynamics in Framework Materials from Solid-State NMR and Powder Diffraction"

PhD Thesis   Matthew Richard Hampson   February 2007

This thesis details a study of framework materials of the AM_2O_8 and AM_2O_7 families, which are of interest due to their unusual thermal expansion properties, phase transitions and often complex structures. The combination of results from NMR and diffraction techniques has enabled several new insights into the structure and dynamics to be made.

Chapter 1 reviews the literature on negative thermal expansion materials that are of relevance to this project.

Chapter 2 outlines the background to the key experimental techniques employed in this work.

Chapter 3 outlines ^{17}O isotopic enrichment techniques and qualitative results for several AM_2O_8 phases. ^{17}O NMR results for cubic ZrW_2O_8 including variable temperature spectra and 2D Exchange Spectroscopy (EXSY) are presented. The $a / ß$ phase transition and low temperature oxygen mobility in ZrW_2O_8 are investigated. NMR results enabled the determination of a mechanism of oxygen exchange different to the previously suggested mechanism, which is disproved. The results of *in situ* diffraction experiments to investigate phase transitions in $ZrMo_2O_8$ are also presented. ^{17}O enriched samples of cubic-, trigonal- and LT- $ZrMo_2O_8$ samples were prepared, and their ^{17}O NMR spectra recorded.

Chapter 4 describes quantitative ^{17}O NMR studies used to characterise oxygen dynamics in ZrW_2O_8. The results of a range of NMR experiments, including a combination of 1D EXSY and saturation recovery experiments, are interpreted to give a measure of the rate and the activation energy for oxygen exchange. The experiments and derivation of the required theoretical background are detailed.

Chapter 5 outlines a range of structural studies on AM_2O_7 materials. The room temperature superstructure of HfP_2O_7 is determined using a combination of X-Ray and neutron diffraction. ^{31}P NMR is reported for the high temperature phases of HfP_2O_7 and ZrP_2O_7 for the first time. The symmetry of the high temperature phase of HfP_2O_7 is investigated by Rietveld refinement of neutron diffraction data. Unusual effects in the ^{51}V NMR spectra of HfV_2O_7 and ZrV_2O_7 are also reported.

Chapter 6 outlines preliminary work on computational methods to investigate the structural dependence of the ^{31}P NMR chemical shift of pyrophosphate materials. DFT calculations of NMR parameters were carried out, and a methodology developed for the derivation of suitable theoretical model structures.

Structure and Dynamics in Framework Materials from Solid-State NMR and Powder Diffraction

Matthew Richard Hampson MSci (Dunelm)

University Of Durham

A thesis submitted in partial fulfilment of the requirements

for the degree of Doctor of Philosophy

Supervisors: Dr Paul Hodgkinson & Dr John S. O. Evans

Department of Chemistry, University of Durham

2007

Acknowledgements

I have had my brain in training, my secret state of mind is better

Since the day that I discovered, how to get it wrong and carry on

How to get it wrong and carry on

Tokyo Adventures, 2004

Declaration and Statement of Copyright

The work described in this thesis is entirely my own, except where I have acknowledged help from a named person *or* given a reference to a published source or a thesis.

The research presented was performed in the Department of Chemistry, University of Durham between October 2002 and October 2005, the results of which have not been submitted for a degree in this or any other university. This thesis conforms to the word limit set out in the Degree Regulations of the university.

Glossary of Symbols and Abbreviations

B_{EQ}	atomic displacement parameter
CSA	chemical shift anisotropy
DFT	density functional theory
DLS	distance least-squares
DSC	differential scanning calorimetry
EXSY	exchange spectroscopy
e.s.d.	estimated standard deviation
FID	free induction decay
FWHM	full width at half maximum
FT	Fourier Transform
I	Spin quantum number
ICSD	Inorganic Crystal Structure Database
INADEQUATE	Incredible Natural Abundance DoublE QUAntum Transfer Experiment
J-Coupling	scalar inter-nuclear coupling
MAS	magic angle spinning
NMR	nuclear magnetic resonance
NOESY	nuclear Overhauser effect spectroscopy
ppm	parts per million
PTFE	polytetrafluoroethylene
q-RUM	quasi-rigid unit mode
R_{Bragg}	residual index for Bragg reflections (in powder diffraction)
REDOR	rotational echo double resonance (NMR experiment)
RF	radio frequency

RMC	reverse Monte Carlo
RUM	rigid unit mode
R_{WP}	weighted profile residual index (in powder diffraction)
SCFH	standard cubic feet per hour
s.f.	significant figures
s/n	signal to noise ratio
S_N2	bimolecular nucleophilic substitution (reaction mechanism type)
TCHZ	Thompson-Cox-Hastings pseudo-Voigt (peak shape) function
TGA	Thermo-Gravimetric Analysis
T_1	Spin-lattice relaxation time
t.o.f.	time of flight
VT	variable temperature
XAFS	X-ray absorption fine structure
XANES	X-ray absorption near-edge structure
XRD	X-ray diffraction
$?$	Wavelength
Z	Formula units per unit cell

Contents

Chapter 1 - Literature Review

1.1 Introduction

Most materials show a positive coefficient of thermal expansion, which may be explained by the increase in average bond lengths with increasing thermal energy. There is, however, a number of phenomena which give an opposing effect and contribute to contraction on heating. In some cases, these effects outweigh the general increase in bond lengths, and lead to a net negative thermal expansion (NTE). NTE is relatively unusual and has lead to great interest in such materials both from an academic and industrial perspective. A range of materials have been shown to demonstrate NTE under certain conditions, but much of the recent interest in NTE has been based on the AM_2O_8 and AM_2O_7 families of materials.[1] The two families are closely related, and the materials demonstrate complex and interesting structural chemistry, which is investigated in this thesis.

In this chapter, the origin of negative thermal expansion is outlined, and the literature on a range of NTE compounds is reviewed. This review focuses particularly on the AM_2O_8 and AM_2O_7 compounds and their structural chemistry, in order to put the experimental work of this thesis into context.

1.2 Origin of the NTE phenomenon

Thermal expansion, for an isotropic material, is usually expressed in terms of the temperature dependence of the cell parameter and given by a value of $\boldsymbol{a}_l$ as defined in Equation 1-1, where a_0 and a_T are the values of the cell parameter at a reference temperature T_0 and temperature T respectively.

$$\boldsymbol{a}_l = \frac{\left((a_T - a_0)/a_0\right)}{T - T_0}$$

[1-1]

In the case of anisotropic materials it is more common to quote a length coefficient as $\boldsymbol{a}_V / 3$, where $\boldsymbol{a}_V$ is the mean volume coefficient of expansion, defined analogously to Equation 1-1.

There are various processes that can cause NTE, some of which are reviewed by Evans.[1] One cause is the excitation of transverse vibrational modes. For example, consider the case of M-O-M linkages in a structure as shown in Figure 1-1. In the longitudinal vibrational mode the average bond length increases with increasing thermal vibration. However, if the M-O bond lengths remain relatively constant whilst a transverse vibrational mode is excited, then there will be an overall decrease in M-M distance. This can lead to a net bulk volume contraction for the material, although usually only at low temperatures since at higher temperatures longitudinal vibrational modes will also be excited, outweighing any decrease in non-bonded lengths.
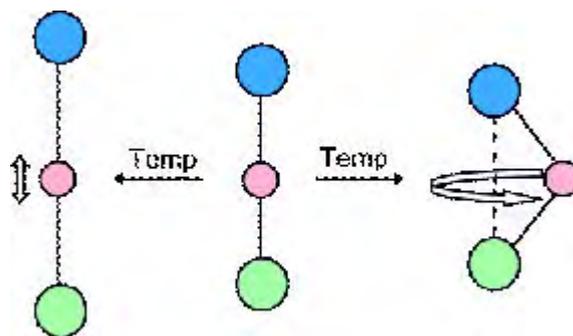
Figure 1-1 A schematic representation of longitudinal and transverse vibrational modes in an M-O-M group.

A more thorough explanation for the specific case of extended framework material involves the concept of Rigid Unit Modes (RUMs) and Quasi-Rigid Unit Modes (qRUMs). RUMs are vibrational modes involving coupled rotation of rigid groups within a structure. This occurs for a number of framework materials where rigid polyhedra are connected by relatively flexible linkages such as two-coordinate bridging oxygen atoms. Excitation of a RUM can lead to an overall volume contraction, which is analogous to that for the simple case of transverse M-O-M bonds described above. This is shown in two dimensions in Figure 1-2.
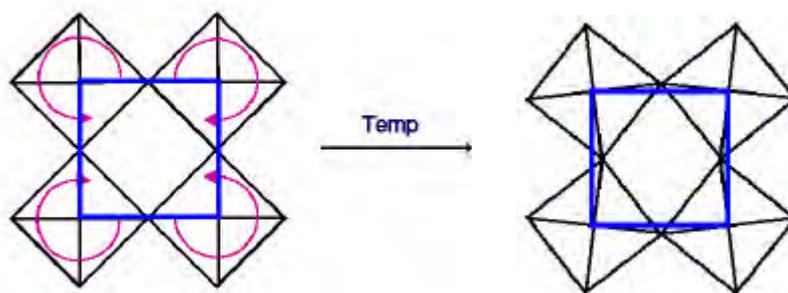
Figure 1-2 Contraction of a lattice in two dimensions due to coupled rotation of corner sharing polyhedra.

RUMs may exist in a structure if the number of degrees of freedom is greater than the number of constraints on the polyhedra. Quasi-rigid unit modes (qRUMs) are conceptually similar but in these cases a small degree of flexibility in the polyhedra is required which allows their distortion during rotation.

Phase transitions can also result in a volume contraction with increasing temperature, albeit over a small temperature range, the most commonly known example being the melting of ice to the more dense liquid water. In the solid state, NTE may be shown when a phase transition results in a regularisation of polyhedra. An example of this is $PbTiO_3$ which undergoes a contraction in volume up to its phase transition at 490 °C. The TiO_6 octahedra are highly distorted at room temperature but regularise and shrink on warming.[2]

Magnetic properties can also cause NTE, or low positive thermal expansion, in the temperature region of a magnetic phase transition. Alloys such as Invar, $Fe_{0.65}Ni_{0.35}$ show extremely low thermal expansion over limited temperature ranges. [3]

NTE over small temperature ranges has also been seen to arise due to electronic effects. There have been reports of negative or zero thermal expansion in materials of the YbGaGe system, caused by an electronic valence transition.[4, 5] Samarium fulleride, $Sm2_{.75}C_{60}$, also shows NTE between 4.2 and 32 K, as a result of an electronic valence change.[6, 7]

1.2.1 Framework NTE Materials

The majority of oxide NTE materials are those consisting of polyhedra linked by M-O-M linkages. There are two main classes of NTE materials that have been the subject of the majority of research into the topic: the AM_2O_7 (where A = Ti, Zr, Hf, Mo, W, Re, Si, Ge, Pb, Sb, Ce, Th, Np, Pu, *etc.*; M = V, P) and AM_2O_8 (where A = Zr, Hf; M = W, Mo) families. NTE is also seen in a number of other framework materials, including zeolites, $A_2(MO_4)_3$ materials and some framework cyanides, which are mentioned in Section 1.5. [8, 9] The research work presented in this thesis is based on cubic vanadates, phosphates, molybdates and tungstates, and these are the main focus of the literature review in this chapter.

1.3 ZrW$_2$O$_8$ family

1.3.1 Cubic ZrW$_2$O$_8$

Graham *et al.* first discovered ZrW$_2$O$_8$ in 1959, they reported that impure samples of ZrW$_2$O$_8$ could be prepared by heating the oxides ZrO$_2$ and WO$_3$ to temperatures above 1423 K and quenching in water or air.[10] They observed that slow cooling lead to decomposition back to the binary oxides. The phase relationships in the ZrO$_2$ - WO$_2$ - WO$_3$ system were investigated in more detail by Chang *et al.* in 1967.[11] They carried out reactions in sealed platinum tubes which were quench-cooled after heating and found that ZrW$_2$O$_8$ was the only thermodynamically stable ternary phase in the system.

Negative thermal expansion in ZrW$_2$O$_8$ was first observed by Martinek and Hummel who used dilatometry to study the expansion between room temperature and 973 K.[12] However the fact that this NTE is isotropic went unnoticed until the crystal structure was solved in the mid-1990s.[13] The structure was solved from powder X-ray and neutron diffraction by Mary *et al.*[13], and independently by Auray *et al.*.[14] As well as solving the room temperature structure Mary *et al.* also carried out variable temperature studies by both diffraction and dilatometry methods to probe the NTE, which were in close agreement.

(a)   (b)
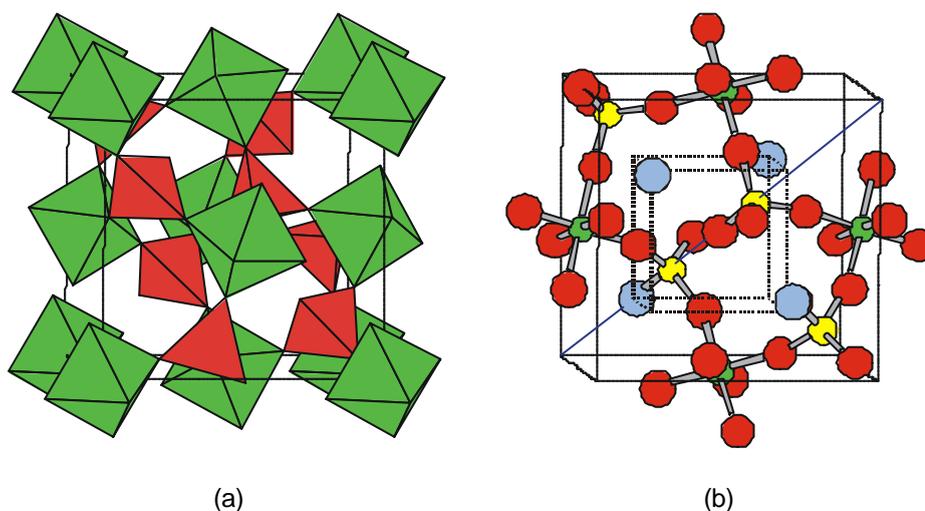
Figure 1-3 The structure of cubic ZrW$_2$O$_8$: (a) Polyhedral representation with ZrO$_6$ octahedra shown in green and WO$_4$ tetrahedra in red (b) Ball and stick representation showing zirconium (green), tungsten (yellow) and oxygen (red) atoms. The one-coordinate O4 site is highlighted in blue.

The room temperature structure was solved and refined in space group *P2$_1$3*. The structure (shown in Figure 1-3) may be described as fundamentally similar to NaCl, with Zr^{4+} cations and W$_2$O$_8^{4-}$ anions on a cubic lattice. The asymmetric unit contains four inequivalent oxygen sites (O1-O4), two tungsten sites (W1, W2) and one zirconium site. The W$_2$O$_8^{4-}$ group consists of two crystallographically distinct WO$_4^{2-}$ tetrahedra and lies along the threefold access of the body diagonal of the unit cell. In each WO$_4$ tetrahedron, three oxygen atoms (O1 and O2 for the tetrahedra containing W1 and W2 respectively) are two-coordinate, shared with ZrO$_6$ octahedra.

The fourth oxygen atom (O4 and O3) of each WO_4 tetrahedron is, unusually for solid state oxides, mono-coordinate which contributes to the flexibility inherent to the structure There is a weak interaction between O3 and W1 ($d = 2.39$ Å), with a much longer inter-atomic distance than the actual W-O bond lengths to other O atoms ($\sim$1.8 Å). The O4 atom is strictly one-coordinate, with a distance of $\sim$3.6 Å to the next nearest metal atom. At room temperature, the oxygen atoms are found to be fully ordered, with the W_2O_8 group aligned in one direction along the unit cell diagonal.

Cubic zirconium tungstate has been shown to undergo negative thermal expansion over the entire temperature range for its existence (2 - 1050 K), as shown in Figure 1-4.[13] The thermal expansion coefficient, $a_l = $ -9.1 $\times$ 10^{-6} K^{-1} (in the range $0 - 350$ K)[15], is of a comparable absolute magnitude to the positive expansion of conventional materials such as alumina ($a_l = $ +7.8 $\times$ 10^{-6} K^{-1})[16] and silicon ($a_l = $ +2.5 $\times$ 10^{-6} K^{-1})[17]. This is a quite extraordinary property and furthermore, due to its cubic symmetry the contraction with increasing temperature is isotropic. This makes ZrW_2O_8 a highly promising compound for use in composite materials, as discussed later (Section 1.6).
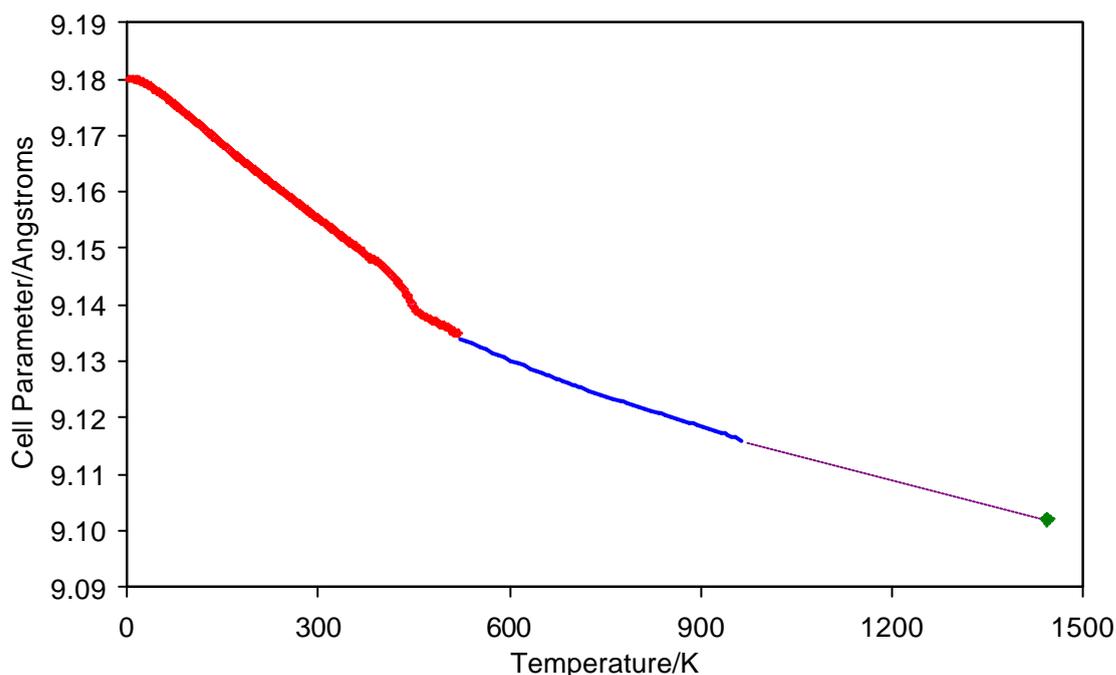
Figure 1-4 Thermal expansion of cubic ZrW_2O_8 determined by neutron diffraction (red), dilatometry (blue), and high temperature neutron diffraction (green). The dashed line indicates the temperature range over which ZrW_2O_8 is thermodynamically unstable. Figure reproduced from reference 13.

Indications of a 2nd order phase transition at $\sim$450 K, are seen by both variable temperature X-ray diffraction experiments and dilatometry.[13] An increase in symmetry is observed by the disappearance of certain reflections (*h0l, h? 2n*) in the X-ray powder pattern with increasing temperature The structure of the high temperature form, *ß*-ZrW_2O_8, is essentially identical to *a*? ZrW_2O_8, but with disordered directions of the $W_2O_8^{4-}$ groups. This corresponds to the addition

of an inversion centre to the symmetry, changing the space group from $P2_13$ to $Pa\bar{3}$. The two different orientations of $W_2O_8{}^{4-}$ groups are illustrated in Figure 1-5.

(a)

(b)

(c)

(d)
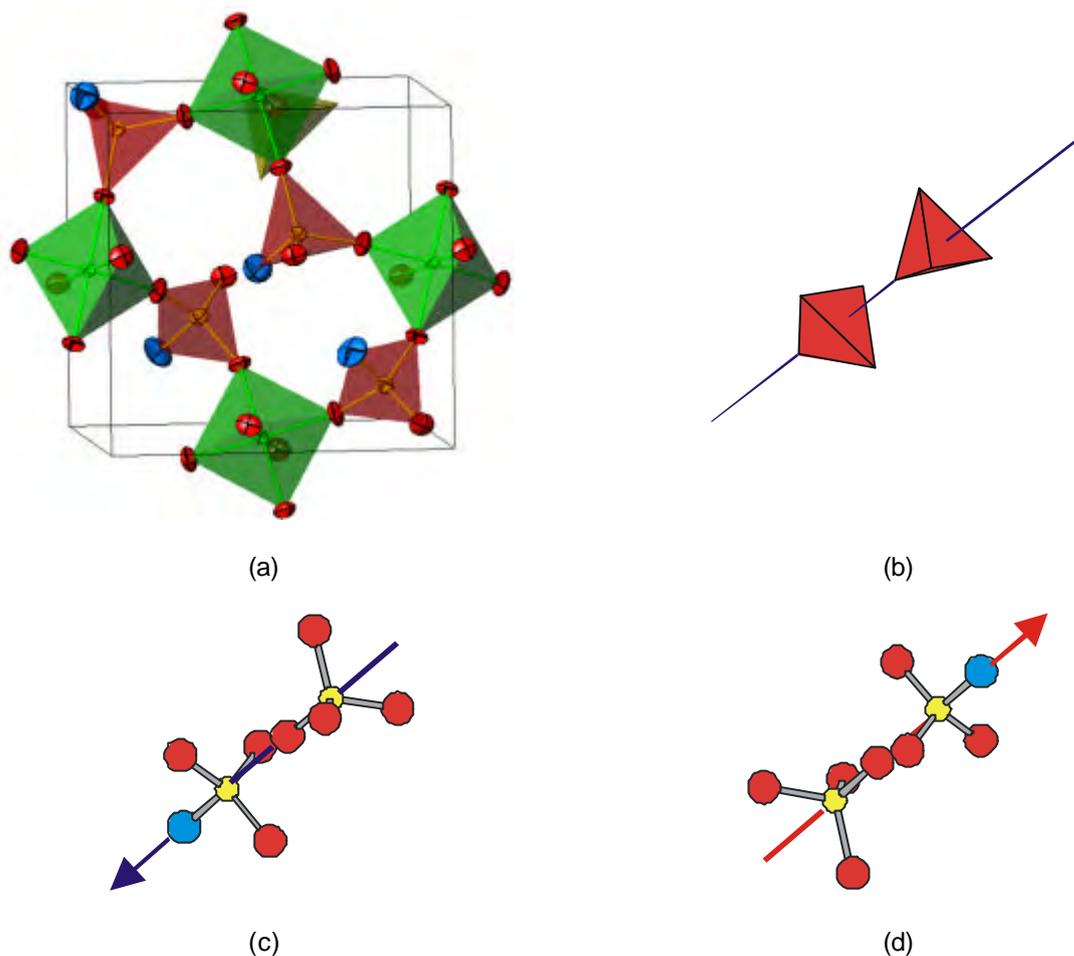
Figure 1-5 Tungstate group orientations in ZrW$_2$O$_8$. (a) the unit cell of ZrW$_2$O$_8$; (b) polyhedral representation of the W$_2$O$_8{}^{4-}$ group consisting of two tetrahedra aligned with the body diagonal of the unit cell; (c) and (d) the two possible W$_2$O$_8{}^{4-}$ orientations, which are related by a centre of inversion.

Variable temperature neutron powder diffraction results may be fitted by Rietveld refinement using a structural model in $P2_13$ with both W_2O_8 orientations allowed. A fractional occupancy parameter (*frac*) is used to account for the relative proportions of each orientation. When *frac* = 0, or *frac* = 1 the structure is in the fully ordered α phase, and in the fully disordered ß phase, *frac* = 0.5.
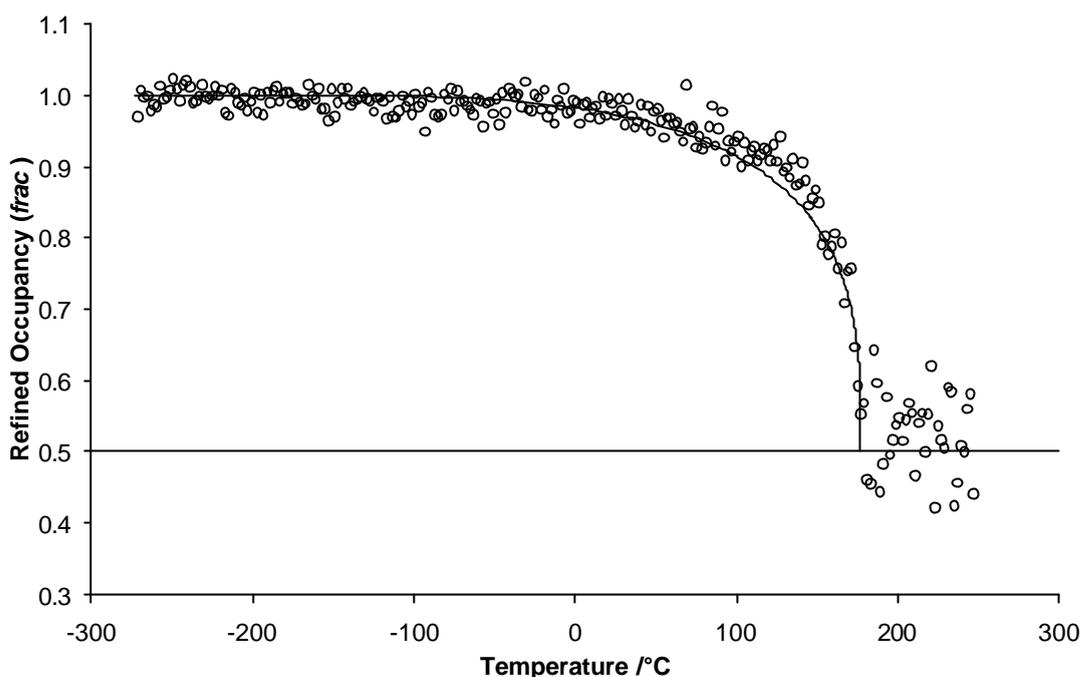
Figure 1-6 Fractional site occupancy of the major W_2O_8 orientation as a function of temperature. The solid line is a fit to a three-dimensional cubic Ising model. Figure adapted from Reference 15.

The variation of the occupancy parameter is shown in Figure 1-6, showing a smooth decrease in ordering from temperature as low as 0°C. This suggests that oxygen mobility occurs at unusually low temperatures; in fact it occurs at significantly lower temperatures than most oxygen ion conductors.[18] A number of models have been proposed to explain the oxygen motion observed, but despite being the subject of much research, the specific mechanism of oxygen migration is currently unknown. One explanation for the disorder is shown schematically in Figure 1-7.
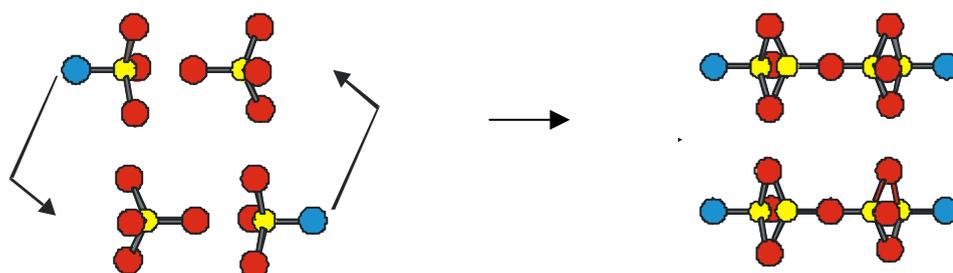
Figure 1-7 A proposed mechanism of oxygen motion associated with the onset of disorder at the *a* / *ß* phase transition in ZrW_2O_8 (the S_N2 like mechanism). The right hand side shows the disordered *ß* structure with superimposed $W_2O_8^{4-}$ groups in both possible orientations.

In this model an "S_N2 like" substitution process occurs, in which oxygen atoms are exchanged between a pair of adjacent W_2O_8 groups. The exchange involves a terminal O4 atom moving from one crystallographic site (for example that at ~(3/4,3/4,1/4)) on one W_2O_8 group to a vacant site ~(3/4,3/4,3/4) on an adjacent W_2O_8 group, in a ~4.6 Å hop, together with a ~0.15Å movement of the O3 site.[19] A small movement of the tungsten atoms would maintain the

geometry of the WO_4 tetrahedra, with the $Zr-O_{bridging}-W$ linkages remaining intact throughout the motion. The net effect of the exchange is a change in orientation of both W_2O_8 units. Although this process would seem plausible, no firm evidence could be presented for this mechanism rather than another from diffraction data. An alternative mechanism, for example, would involve the rotation of intact WO_4 tetrahedra. The nature of the oxygen motion is investigated using ^{17}O NMR in Chapters 3 & 4 of this thesis.

Mary *et al.* originally suggested that the flexible Zr-O-W linkages were the source of negative thermal expansion. This was confirmed by Evans *et al.* who showed that the NTE is related to transverse vibrations of the Zr-O-W bridging oxygen atoms.[15] The polyhedral ZrO_6 and WO_4 units are involved in coupled rotations whilst remaining relatively rigid, leading to a volume contraction as shown schematically in Figure 1-2. The Zr-O and W-O bonds do not increase in length significantly on heating, which would of course lead to positive thermal expansion, and therefore the contracting effect of the transverse vibrations is dominant. Evans *et al.* have also carried out further structural investigation using high resolution powder diffraction.[15]

Pryde *et al.* have also carried out RUM calculations to probe the origins of NTE in ZrW_2O_8, and confirmed that low energy vibrations do exist.[20-22] The RUM model accounts for the fact that there is only a minor change in expansion at the *a* / *ß* phase transition. It was noted that the formation of W_2O_7 and W_2O_9 complexes (involved in a possible W_2O_8 inversion mechanism suggested by Mary *et al.*[13]) would introduce cross-bracing into the structure, and no RUMs would be allowed, as is the case for ZrV_2O_7.[21] Ernst *et al.* measured the phonon density of states by neutron scattering experiments.[23] It was shown that phonon modes with large negative Grunesien parameters, were relevant to the NTE behaviour. A number of other inelastic neutron scattering experiments have subsequently been undertaken, with high pressure results indicating an unusual change in the phonon spectrum at ~0.17 GPa. It was shown that the unusual phonon behaviour could be the cause of NTE.[24] Lattice dynamical calculations also support the model of low energy phonons causing NTE.[25]

Cao *et al.* presented X-ray absorption fine structure (XFAS) results which were interpreted as showing that the motion responsible for NTE was somewhat different to that previously supposed.[26, 27] They suggested that instead of a transverse vibration of the Zr-O-W linkage, NTE was caused by a correlated movement of WO_4 tetrahedron and surrounding ZrO_6 octahedra, with the Zr-O-W linkage remaining rigid throughout the motion. A quantitative analysis of the movement of polyhedra was performed by Tucker *et al.*, who used reverse Monte Carlo modelling of neutron total scattering data.[28, 29] The results were consistent with the predictions made on the basis of rigid unit mode theory. These results are not compatible with *Cao et al.*'s interpretation of the XAFS data, and suggest that the Zr-O-W linkage is indeed flexible.

Specific heat capacity measurements have also provided additional evidence: a low energy phonon (~5 meV or 40 cm^{-1}) exists below 200 K.[30] A low energy vibrational mode with approximately this frequency (40 cm^{-1}) was observed directly by Raman spectroscopy.[19] A number of other Raman spectroscopy studies have been carried out,[31] and a number of other anharmonic modes identified.[32]

David *et al.* carried out an analysis of temperature dependence of lattice parameter from high resolution powder neutron diffraction and showed that this confirmed the presence of low frequency phonon modes, with energies in the range 3-8 meV.[33]

Cubic ZrW_2O_8 is also observed to undergo a further volume contraction upon hydration to $ZrW_2O_8 \cdot xH_2O$, presumably due to hydrogen bonding between water molecules in the structure[34]. It is worth noting that Duan *et al.* were only able to synthesise the hydrate with values of x between 0.5 and 1, suggesting there is some structural significance in the value of $x = 0.5$. Intriguingly, the experiments described in Chapter 3 of this thesis always gave hydrates with values of x of *less than* 0.5.

1.3.2 Other ZrW_2O_8 phases

Zirconium tungstate also exists in several other phases such as the 'low temperature' and trigonal forms. Allen conducted extensive research into the different polymorphs of ZrW_2O_8.[35] All phases are thermodynamically unstable with respect to the binary oxides at room temperature and synthesis requires rapid quenching to temperatures where they are kinetically stable. There are also various phases formed at high pressure, including an amorphous form similar to U_3O_8, in which the Zr and W atoms are disordered.[36]

The effect of moderate pressure on ZrW_2O_8 was first investigated by Evans *et al*[37] who recorded neutron diffraction data as a function of pressure in order to study the structural flexibility responsible for NTE. However it was found that under an applied pressure of 0.21 GPa the material undergoes a phase transition to a hitherto unknown orthorhombic phase, named $?$-ZrW_2O_8. This phase may be quenched to ambient pressure, and its structure was determined from powder diffraction data; thermal expansion properties were also recorded.

The network of ZrO_6 octahedra is essentially unchanged from that in a-ZrW_2O_8; however there are considerable changes in the $W_2O_8^{4-}$ groups. There are 3 crystallographically distinct W_2O_8 groups in $?$-ZrW_2O_8, two of which have distinctly shorter W-W distances than in a-ZrW_2O_8. It is this which accounts for the 5 % reduction in volume at the phase transition. The WO_4 tetrahedra in each $W_2O_8^{4-}$ group are also tilted, whereas in a-ZrW_2O_8 the tungsten and terminal oxygen atoms are co-linear along a 3-fold axis. In $?$-ZrW_2O_8 there is no 3-fold axis and the tilting of the tetrahedra away from linearity allows the terminal oxygen atoms of each $W_2O_8^{4-}$ group, which are formally one-coordinate in a-ZrW_2O_8, to become closer to the tungsten atom of an adjacent $W_2O_8^{4-}$ group.

One of the $W_2O_8{}^{4-}$ groups (W3-W4) is found to have reversed direction relative to the other two, which leads to the terminal oxygen on W4 being only 2.32 Å from W5, making W5 pseudo-octahedral. The increased interactions between WO_4 tetrahedra may be thought of as adding 'cross bracing' between the polyhedral units, which explains the fact that the coefficient of expansion, whilst still negative, is smaller in magnitude than in the cubic phase.

Further compressing ?-ZrW_2O_8 results in pressure-induced amorphization at pressures between 2.4 and 7.6 GPa. Varga *et al.* studied this process by *in situ* and *ex situ* synchrotron XRD and X-ray absorption spectroscopy (XAS).[38] The XAS results suggested that the amorphization process involves a change in tungsten coordination, rather than simply a loss in positional order. The W-O bond distance is seen to increase on compression, and the X-ray absorption near-edge structure (XANES) of the compressed amorphous sample resembles that of ammonium paratungstate, which contains heavily distorted WO_6 octahedra.

1.3.3 Substitution on A site

The effect of substituting a variety of other metal ions (Hf, Sn, Sc, In, Y) on the Zr^{4+} site of ZrW_2O_8 has been investigated. The main aim of these studies has been to investigate changes in the phase transition induced by substitution. This will give an improved understanding of the mechanism behind the ordering transition, and could eventually lead to the development of materials based on ZrW_2O_8 but with a phase transition depressed below room temperature. Such materials would be highly desirable for certain applications where the change in thermal expansion at the phase transition temperature causes difficulties.

HfW_2O_8 is iso-structural with ZrW_2O_8 and may be synthesized by analogous methods to ZrW_2O_8, and shows the same thermal expansion behaviour, with the *a*? *ß* order-disorder phase transition also observed by X-ray diffraction. [13, 19] The initial studies by Evans *et al.* reported that the phase transition occurs at 430 K, a similar temperature to ZrW_2O_8.[19] X-ray diffraction and calorimetry measurements by Yamamuri *et al.* subsequently showed that in fact the phase transition temperature is notably higher in HfW_2O_8 than ZrW_2O_8, this difference being ascribed to the fact that Hf-O chemical bonds are stronger than Zr-O.[39] Yamamuri *et al.* reported the *a*? *ß* phase transition temperatures from adiabatic scanning calorimetry to be 437±1 and 463±2 K for ZrW_2O_8 and HfW_2O_8 respectively, with X-ray diffraction giving values of 444±2 and 468±2 K. Solid solutions of $Zr_xHf_xW_2O_8$ with x = 0-1 were later prepared by the same group, and it was shown that the phase transition temperature increases with increasing Hf substitution. [40, 41] The entropy associated with the phase transition in $Zr_xHf_xW_2O_8$ was measured by calorimetry, and determined to be equal for HfW_2O_8 and ZrW_2O_8, indicating that the same order-disorder mechanism was involved in the transition.[41]

The pressure induced phase transition occurs at significantly higher pressures in HfW_2O_8 than ZrW_2O_8,[42] which potentially makes HfW_2O_8 more suitable for use in composite materials, since

materials processing and thermal mismatch stress in ZrW_2O_8 composites can generate internal pressures sufficient to induce conversion to the γ phase, as discussed in Section 1.6.

De Meyer *et al.* investigated the effect of Sn^{4+} substitution, using conventional solid state reaction between ZrO_2, SnO_2 and WO_3 to prepare materials with formula $Zr_{(1-x)}Sn_xW_2O_8$.[43] The synthesized materials were always found to contain amounts of the un-reacted binary oxides with the percentage of the $Zr_{(1-x)}Sn_xW_2O_8$ phases decreasing with increasing values of the degree of substitution, *x*. X-ray and neutron diffraction showed that the $Zr_{(1-x)}Sn_xW_2O_8$ materials structure had the same framework and symmetry as ZrW_2O_8 in both the α and β phases, with Sn^{4+} substituted on the Zr^{4+} sites. The cell parameter was found to decrease on addition of the Sn^{4+} ions, as would be expected from the ionic radii (Sn^{4+} 0.69 Å, Zr^{4+} 0.72 Å).[44] Variable temperature X-ray diffraction and dilatometry showed that the materials demonstrated NTE over the measured temperature range of 300 to 900 K. The α?β order-disorder phase transition was also observed in the variable temperature results, in the variation of the cubic cell parameter and the tungstate group orientations. The phase transition occurred at 400 K, significantly lower temperature than ZrW_2O_8 itself (448 K), which was attributed to the lower bond dissociation energy for Sn-O (532 ± 12 kJ·mol^{-1}) than Zr-O (776 ± 13 kJ·mol^{-1}).[44] Weaker A-O bonds would provide less inhibition to the ratcheting tungstate motion understood to occur during disordering[45] (see Chapter 3). The maximum shifts of the phase transition temperature and cell parameter were obtained for values of $z = 0.2$-0.3 in the molar ratio of starting reagents of $SnO_2/ZrO_2/WO_3 = z:(1-z):2$, suggesting that $x = \sim 0.3$ is the maximum achievable level of substitution for $Zr_{(1-x)}Sn_xW_2O_8$.

Morito *et al.* showed that doping ZrW_2O_8 with a small amount of Y^{3+} to produce $Zr_{1-x}Y_xW_2O_8$ ($x = 0.00$-0.02) enabled higher density samples to be produced by a press-free process, without affecting the NTE behaviour,[46] although the thermal conductivity was lower than pure ZrW_2O_8.[47] Yamamura *et al.* conducted experiments into substituting a range of M^{3+} ions onto the Zr^{4+} site of ZrW_2O_8, producing solid solutions with formula $Zr_{1-x}M_xW_2O_{8-y}$ which contain oxygen defects.[48, 49] Compounds with M = Sc, In and Y were synthesized, with $x = 0$-0.04, and characterised by powder XRD. It was found that the compounds formed showed the same structure as ZrW_2O_8 and that the lattice parameters decreased linearly with increasing M content, despite the ionic radii of the substituents (Sc^{3+} 0.885 Å, In^{3+} 0.940 Å, Y^{3+} 1.040 Å) all being larger than that of Zr^{4+}. This was explained by the presence of increasing amounts of oxygen defects to conserve electrical neutrality on replacing Zr^{4+} with trivalent ions. The cell parameters amongst the different substituted compounds increased in the same order as the ionic radii as the substituents. The variation of lattice parameter from powder XRD showed that all of the substituted compounds showed negative thermal expansion throughout the measured temperature range of 90 to 560 K, but the phase transition temperatures were markedly lower than in the un-substituted compound - despite the low amount of substitution ($x = 0$-0.04), the phase transition temperatures were decreased by as much as 80 K relative to that of ZrW_2O_8.

The M^{3+}-O bond dissociation energies for these compounds (Sc-O 681.6 ±11.3 kJ·mol^{-1}, Y-O 719.6 ±11.3 kJ·mol^{-1}, In-O< 320.1 ±41.8 kJ·mol^{-1} [44]) are all weaker than those of Hf-O and Zr-O, and this may contribute to lower phase transitions, as in the Sn^{4+} substituted compounds. However, the main contributing factor to the lower phase transition temperatures is presumed to be a more drastic change in ordering caused by the presence of 3+ ions. Yamamura *et al.* carried out synchrotron powder diffraction experiments, particularly investigating the effect of metal substitution on the peaks associated with ordering.[49] They showed that adding substituent metal ions decreased the order shown at low temperature (below the phase transition temperature), and therefore reasoned that a certain amount of disorder was 'frozen in' due to the presence of 3+ ions. The FWHM of ordering peaks was seen to increase with increasing substitution, although the width of fundamental peaks remained constant, suggesting that ordering in certain planes (those associated with WO_4 orientation) is decreased, whilst the majority of the structure is unaffected, with substituent atoms distributed homogeneously throughout the sample. A model, consistent with their diffraction data, was proposed, in which local regions around the substituted atoms were disordered, and estimated that one Sc ion, 'forbids' ten WO_4 tetrahedra from taking orientational order. Two possible reasons were offered to explain such a disturbance in the ordering: the 3+ ions (larger than the Zr^{4+} ions they substitute) could enlarge the AO_6 octahedra, and thus restrict WO_4 movement by forcing the tungsten atoms closer together; alternatively the oxygen vacancies in the lattice could create a distortion which confines motion.

1.3.4 Substitution on M site

A range of $ZrW_{(2-x)}Mo_xO_8$ compounds has been prepared, over the entire composition range (0=*x*=2) including $ZrMo_2O_8$ which is discussed separately (Section 1.3.5).[50-52] At room temperature, $ZrWMoO_8$ has the disordered structure seen in *ß*-ZrW_2O_8. Variable temperature powder neutron diffraction shows strong NTE behaviour ($\boldsymbol{a_l}$ = -8.7 × 10^{-6} K^{-1} on cooling between 200 and 2 K).[18] Comparison of data recorded on slow-cooling and that recorded during warming of a quench-cooled sample revealed hysteresis in the cell parameter, suggesting that a phase transition occurs, with the formation of an ordered structure (as in *a*-ZrW_2O_8) occurring at around 280 K. Rietveld refinement showed that the variation in oxygen site occupancy confirms this theory, although unlike ZrW_2O_8, $ZrWMoO_8$ never reaches a fully ordered structure, even at 2 K the major oxygen site occupancy is only 0.8. Further experiments into the kinetics of the oxygen mobility associated with the phase transition were undertaken by Allen and Evans, who used a variety of time- and temperature- dependent X-ray diffraction experiments.[53] Rietveld refinement of data sets recorded as a function of time as a quench cooled sample equilibrated at a number of temperatures was used to determine the activation energy for reorientation of the ordered tetrahedra, which was estimated as 34(5) kJ·mol^{-1} from both cell parameter and fractional occupancy.
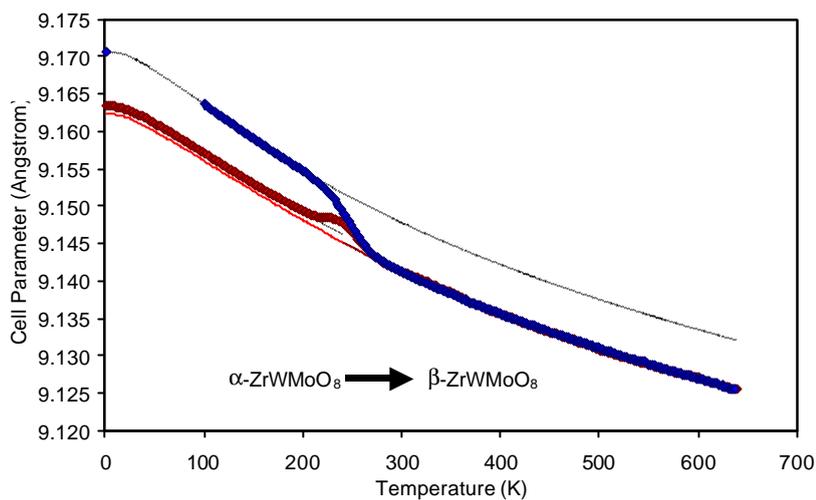
Figure 1-8 Variation of cell parameter of cubic ZrWMoO$_8$ with temperature on warming (red) and cooling (blue). Figure reproduced from reference 53.

As a quenched-cooled sample of ZrWMoO$_8$ is warmed at a fixed rate, a hump in cell parameter is observed at around 200 K (as shown in Figure 1-8).[53] This shows that the thermal energy at this point is sufficient to convert the disordered oxygen array (which has been 'frozen in' by quench cooling) to the thermodynamically preferable ordered configuration, but due to the fixed rate of heating, the sample is never allowed to fully order. The 'excess' oxygen occupancy in the humped region over that observed in slow cooling was studied as the sample was warmed, and analysed in terms of Arrhenius behaviour, enabling an additional independent measure of the activation energy, which was estimated by this approach to be 39 kJ·mol^{-1}.

1.3.5 ZrMo$_2$O$_8$

There are several zirconium molybdate phases, and the phase diagram is considerably more complex than that of ZrW$_2$O$_8$, as illustrated by Figure 1-9. It should be noted that the nomenclature of ZrMo$_2$O$_8$ phases is entirely separate to that of ZrW$_2$O$_8$. A monoclinic phase, β-ZrMo$_2$O$_8$, is formed on heating the binary oxides ZrO$_2$ and MoO$_3$ to ~873 K.[54] Heating the monoclinic phase to around 900 K results in a phase transition to a trigonal phase a-ZrMo$_2$O$_8$, which is stable at higher temperatures.

A cubic form analogous to a-ZrMo$_2$O$_8$ does exist, but it is significantly more difficult to prepare than in the tungstate case. This cubic polymorph, $?$-ZrMo$_2$O$_8$, can not be synthesised directly from the binary oxides, as it is at no point thermodynamically stable. Annealing at high temperatures is therefore not a viable route to cubic ZrMo$_2$O$_8$ as it is not stable and also this would result in the loss of MoO$_3$ ($T_{sublime}$ ~ 1068 K), which is considerably more volatile than WO$_3$ ($T_{sublime}$ ~ 1746 K). In fact cubic ZrMo$_2$O$_8$ was not reported until 1998 when Lind *et al.* discovered a fundamentally different approach to its synthesis, by dehydrating a precursor material ZrMo$_2$O$_7$(OH)$_2$.2H$_2$O.[55] As can be seen from Figure 1-9, prolonged heating of the precursor will result in the formation of trigonal ZrMo$_2$O$_8$, and stopping the dehydration of the precursor at the correct point is difficult. A further investigation by Lind into the required

synthetic conditions showed that the source of the precursor material is critical in determining the purity of cubic $ZrMo_2O_8$ obtained.[56] It was found that using $ZrO(ClO_4)_2$ as the Zr source (the "perchlorate route") produced purer samples than a "chloride route" using $ZrOCl_2$. It was also found that an excess of Zr over Mo is essential in producing pure precursor material, to prevent precipitation of molybdenum oxide. An intermediate phase (LT-$ZrMo_2O_8$) in the formation of pure cubic $ZrMo_2O_8$ from the precursor was observed by Lind,[56] and its structure and key role in the synthesis of cubic $ZrMo_2O_8$ later determined by Allen. [35, 57]
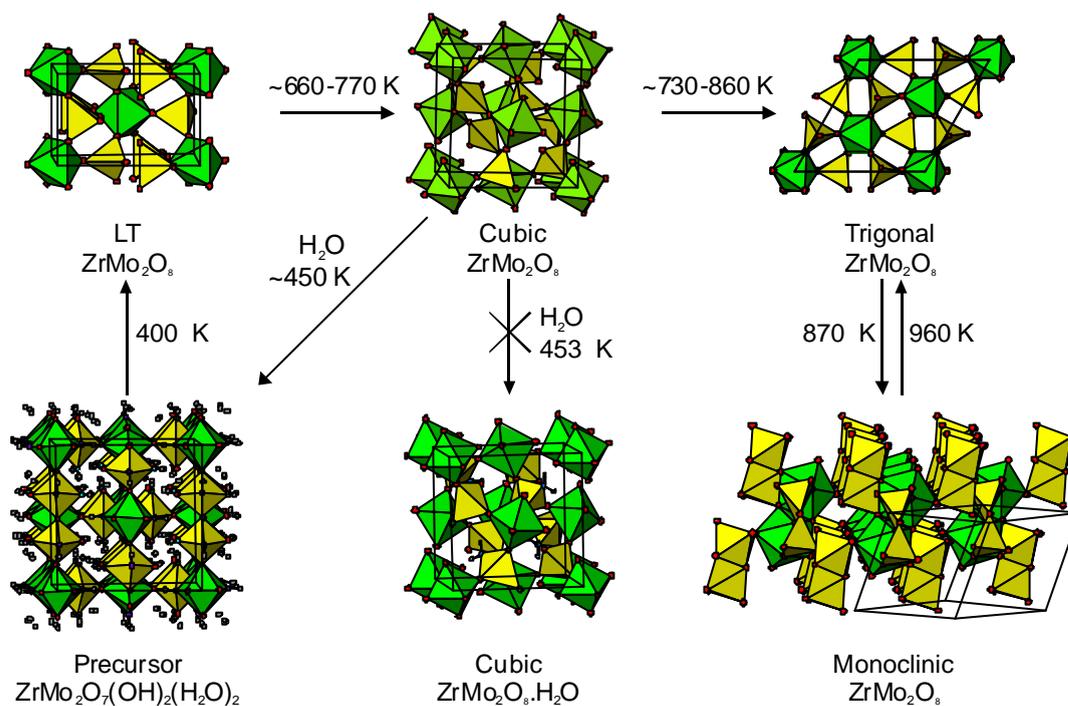
Figure 1-9 Ambient pressure phases of $ZrMo_2O_8$.

The cubic form of $ZrMo_2O_8$ is iso-structural with β-ZrW_2O_8 at room temperature and also exhibits NTE,[58] with an average expansion coefficient of -6.9×10^{-6} K^{-1} between 2 and 200 K and -5.0×10^{-6} K^{-1} between 250 and 502 K. Initial thermal expansion studies by Lind[59] suggested there was no phase transition associated with oxygen disorder, and a subsequent more thorough VT neutron diffraction investigation by Evans[18] showed that while there was no dramatic change in thermal expansion coefficient as at the a / β phase transition in ZrW_2O_8, a significant hysteresis effect in thermal expansion is seen on warming and cooling a sample, as with $ZrWMoO_8$.[18]

The hysteresis and the fact that thermal history is important in determining the cell parameter indicate that oxygen disorder plays an important role in the structural chemistry of cubic $ZrMo_2O_8$. X-ray diffraction experiments suggest that a transition at around 200 K involves oxygen motion. It has been proposed that this is a transition from a statically disordered to a dynamically disordered state, as ordered oxygens have not been observed at any temperature.[58, 59] Allen and Evans remarked that this may be explained by the higher covalency

of Mo-O bonds over W-O bonds.[53] As molybdenum is introduced, electrostatic interactions are reduced, therefore lowering the ordering temperature. This is consistent with the observation of intermediate behaviour in $ZrWMoO_8$, where some, although not full, ordering is observed, in slow cooled samples.

A pressure-induced phase transition occurs at pressures of 0.7-2.0 GPa, compared to 0.21 GPa for the similar transition in ZrW_2O_8. This higher pressure is potentially advantageous for the development of composite materials, since the pressure induced transition can cause problems with material processing, for example in ZrW_2O_8/Cu composites.[60, 61] $ZrMo_2O_8$ also has the potential advantage that the pressure-induced transition is reversible at room temperature, unlike that for ZrW_2O_8.

The structure[62, 63] of trigonal a-$ZrMo_2O_8$ consists of layers made up of linked ZrO_6 octahedra and MoO_4 tetrahedra which are isolated rather than in Mo_2O_8 pairs. The octahedra share all of their corners with the tetrahedra, whilst only three of the oxygens of each tetrahedra are shared, leaving a one-coordinate oxygen atom (O4) pointing into the van der Waals bonded inter-lamellar space. At 487 K trigonal $ZrMo_2O_8$ undergoes a displacive phase transition to a higher symmetry structure, a'-$ZrMo_2O_8$ with space group *P3m1*. In the high temperature phase the MoO_4 tetrahedra are orientated such that the M-$O_{terminal}$ vectors are aligned with the *c* axis, whilst the 3 basal oxygens are in the *ab* plane. In the low temperature trigonal form the tetrahedra are twisted away from the *ab* plane.

Variable temperature powder diffraction studies by Allen *et al.* showed that thermal expansion in trigonal $ZrMo_2O_8$ is highly anisotropic as would be expected from its layered structure.[63] In fact there is a positive coefficient of expansion in the *c* direction (perpendicular to the layers), with NTE in the *ab* plane. This is clearly related to the weak Van der Waals interactions between the layers. In addition to the ambient pressure phases, $ZrMo_2O_8$ also undergoes a number of pressure induced phase transitions.[64]

Krogh-Anderson and Carlson carried out *in situ* synchrotron X-ray powder diffraction studies on trigonal a-$ZrMo_2O_8$.[64] They solved the structure of the high pressure form d-$ZrMo_2O_8$ and observed the packing of the anions. The precursor material has Zr atoms in a pentagonal bi-pyramidal geometry. The molybdenum atom is in 5-coordinate square pyramidal environment, with the oxygen atom of the water molecules making a 6th bond to complete a distorted octahedron.

1.4 AM$_2$O$_7$ materials

The AM$_2$O$_7$ (M = P, V) family of metal pyrovanadates and pyrophosphates also show interesting thermal expansion properties. The AM$_2$O$_7$ materials are related to the AM$_2$O$_8$ materials described above. In simple terms they may be considered as having one fewer oxygen atom in their structure, so that an M$_2$O$_7$ unit with a bridging M-O-M oxygen is present in place of two MO$_4$ tetrahedra. Hence, in contrast to AM$_2$O$_8$ materials, all oxygen atoms in AM$_2$O$_7$ materials are fully two-coordinate.

At high temperature these materials tend to form simple (Formula units per unit cell, Z = 4) structures, analogous to the cubic AM$_2$O$_8$ phases, as shown in Figure 1-10. The structure may be considered as being based on a face centred cubic NaCl structure, with A atoms on the Na sites, and the bridging O atoms of the M$_2$O$_7$ units at the Cl sites. The most symmetric arrangement possible has M$_2$O$_7$ units with D$_{3d}$ symmetry, with the bridging O site on a centre of inversion and a three fold axis along the linear M-O-M axis. This highly symmetric arrangement gives the unit cell *Pa3* space group symmetry.
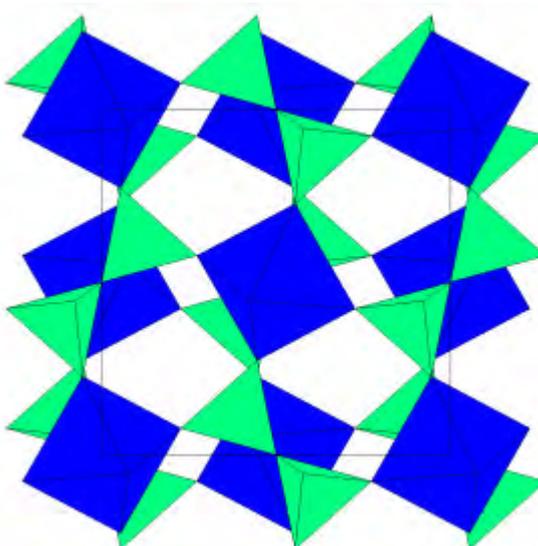
Figure 1-10 An example of the simplest possible cubic structure of AM$_2$O$_7$ materials – the high temperature phase of ZrP$_2$O$_7$.[65] ZrO$_6$ octahedra are shown in blue, and PO$_4$ tetrahedra in green.

A number of phases have been shown to adopt this simple structure at high temperature. However at low temperatures AM$_2$O$_7$ materials often show significantly more complex structures. Any distortion away from the ideal M$_2$O$_7$ geometry as described above results in a lowering of symmetry. Since linear M-O-M bond angles are unfavourable, it is presumably in order to satisfy the requirement of these bonds to adopt a more stable configuration that the complex structures occur. Several of these materials have been shown to have a 3×3×3 (Z = 108) superstructure at room temperature.[66] There is a large variety of structures seen for this class of materials, due to the range of metal (M) ions possible. The state of research for a number of these materials is described in this literature review, with particular emphasis on

compounds of Group 4 metals as these were the subject of the majority of the research in Chapter 5.

1.4.1 Group 4

1.4.1.1 TiP$_2$O$_7$

TiP$_2$O$_7$ has been subject to a great deal of research. Soria *et al.* synthesised TiP$_2$O$_7$ from Ti(HPO$_4$)$_2$·2H$_2$O and presented a 1D ^{31}P NMR spectrum showing nine peaks.[67] Sanz *et al.* identified the space group of the 3×3×3 superstructure as *Pa3* by a combination of Rietveld refinement of XRD data and MAS NMR, with an NMR spectrum apparently showing nine peaks, which they deduced were due to 11 phosphorus sites (with 2 peaks obscured by overlap) by analysis of their relative intensities.[68] Rietveld refinement was performed using a starting model determined using the distance least squares (DLS) method. The refined structure showed anomalously high thermal parameters for two of the bridging oxygen sites (O5 and O6) which could be explained either by disorder of the sites around the 3-fold axes or high thermal mobility. They noted that the width and shape of all NMR components was similar in MAS spectra recorded at a range of temperatures (-15, -50 and -75 °C). The chemical shift anisotropies of all phosphorus sites were noted to be similar, suggesting that all tetrahedra have similar mobility. On the basis of these observations it was concluded that thermal motion was not significantly greater for O5 and O6 in comparison to the other oxygen sites and that static disorder of the oxygen sites O5 and O6 was the most likely explanation for the high thermal parameters.

In 2000, Helluy *et al.* were able to use 2D NMR to carry out a complete spectral assignment of the solid state ^{31}P NMR.[69] Although their initial spectra were consistent with those previously published, they were still unable to resolve 11 individual peaks, and acknowledged that overlap of the peaks meant that the space group assignment from the 1D MAS spectrum alone is ambiguous, and a lower symmetry space group, with a greater number of phosphorus sties in the asymmetric unit could be possible. The "TOtal through-Bond correlation SpectroscopY" (TOBSY) pulse sequence, which probes homonuclear through-bond *J* coupling interactions whilst suppressing homonuclear dipolar and anisotropic chemical shielding effects, was used. The *J* coupling was used to identify intra-P$_2$O$_7^{4-}$ connectivities only, and thus count the number of unique pyrophosphate groups in the structure. Four P-O-P connectivities were immediately identified by off-diagonal peaks in the 2D TOBSY spectrum, one more was indicated by a broadening of another peak around the diagonal. One of the diagonal peaks showed no off-diagonal intensity, showing that it was not *J*-coupled, which could only be explained by it corresponding to a P$_2$O$_7$ unit where the P sites were related by a centre of inversion and hence magnetically equivalent. They were also able to use the 2D spectrum to assign the 1D MAS spectrum, and thus unambiguously determine the space group to be *Pa*3, which has 11 P sites, in P$_2$O$_7^{4-}$ units.
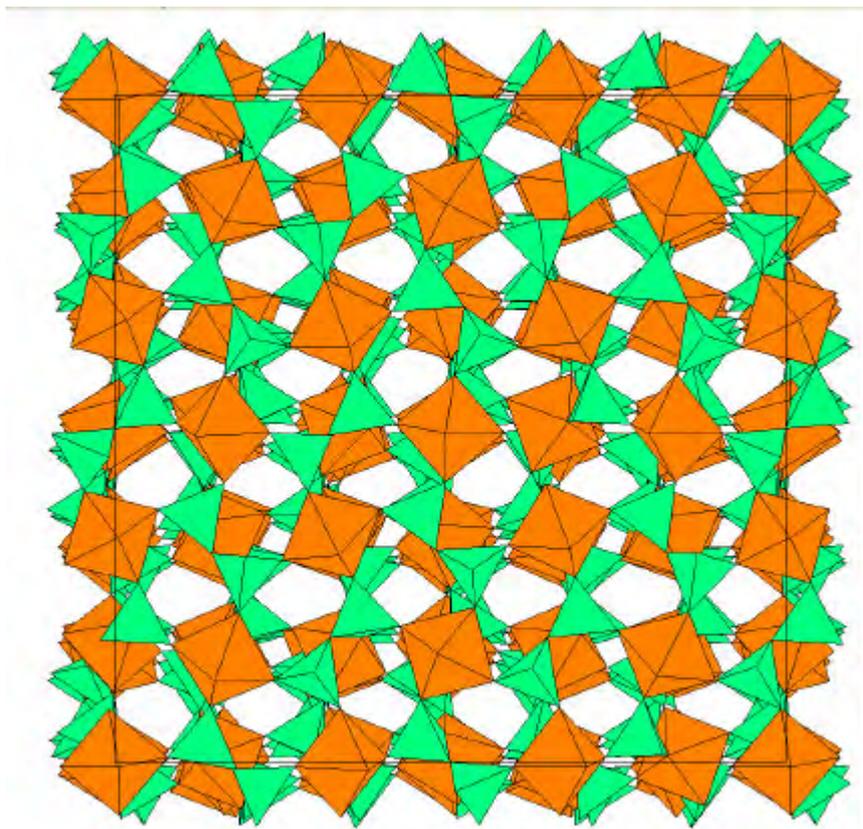
Figure 1-11 TiP$_2$O$_7$ superstructure in *Pa$\bar{3}$*, as determined by Norberg *et al.*.[70] TiO$_6$ octahedra are shown in orange, and PO$_4$ tetrahedra in green.

The full superstructure (Figure 1-11) was determined from single crystal synchrotron X-ray data by Norberg *et al.*, who were able to use the high quality data to carry out a full anisotropic structural refinement. [70] The most intense super lattice reflection had approximately 30 % of the intensity of the strongest substructure reflection. This is significantly higher than the 1 % observed by Evans *et al.*[66] for ZrV$_2$O$_7$ which suggests that the superstructure is considerably more distorted relative to the subcell structure than for ZrV$_2$O$_7$. Norberg *et al.*'s structure was in agreement with that determined by Sanz,[68] and again enlarged thermal parameters were seen for O5 and O6, suggesting that these sites are disordered as Sanz *et al.* had suggested. The shape of the thermal ellipsoid for O5 suggested that the P9-O5-P11 group has an infinite number of possible orientations, whereas that for O6 appears to show disorder between two configurations. Carlson *et al.* carried out studies of TiP$_2$O$_7$ at elevated pressures upto 40.3 GPa and found that the cell parameter decreased smoothly with increasing applied pressure, with no evidence of pressure-induced phase transitions.[71]

1.4.1.2 ZrP$_2$O$_7$ and HfP$_2$O$_7$

A structural model for *a*-ZrP$_2$O$_7$ was first reported by Levi and Peyronel in 1935, who used a *Pa$\bar{3}$* structure.[72] In 1963, developments in experimental equipment allowed Vollenke *et al.* to observe additional peaks, which could be explained by the presence of a supercell, with *Pa$\bar{3}$* symmetry and the unit cell length tripled. [73]

The first hint that the true supercell symmetry may be lower than *Pa3* was the ^{31}P NMR results published in 1995 by Korthuis *et al.* in which 12 overlapping peaks were observed.[74] The *Pa3* superstructure model has only 11 unique phosphorus sites, although the extra peak (at ~45 ppm) was explained as being due to an impurity phase, despite the lack of impurities observed in X-ray and neutron diffraction. A complete superstructure was refined in *Pa3* by Khosrovani *et al.* but this structure contained chemically implausible bond angles, suggesting that the symmetry was incorrect.[65]

King *et al.* demonstrated the advantages of a multi-technique approach with an extremely elegant and intelligent combination of powder XRD and two-dimensional NMR experiments used to give an unambiguous space group determination for the room temperature superstructure of ZrP_2O_7.[75] A number of overlapping peaks, including that originally ascribed to an impurity by Korthuis *et al.* were observed in the 1D spectrum. A range of two-dimensional NMR experiments were used to show correlations between P sites, both by dipolar and indirect *J* couplings. This showed that all observed peaks belonged to the same phase, and that there were 14 P_2O_7 units, containing 27 unique phosphorus sites – a self correlation was seen for one of the sites, indicating that it was related by symmetry to the other phosphorus in the same P_2O_7 unit. *Pbca* is the only space group compatible with the number of phosphorus sites and pyrophosphate groups, and this model contains one P_2O_7 unit in which the phosphorus atoms are related by an inversion centre. Electron diffraction studies by Withers *et al.* showed a glide extinction condition compatible with both *Pa3* and *Pbca* symmetry.[76]

In 2005, the full room temperature *Pbca* superstructure was solved from powder diffraction data by Stinton *et al.*,[77, 78] and independently by Birkedal *et al.* using single crystal diffraction data.[79] The crystal structure determination confirmed that the P_2O_7 group (P14-O14-P14) which appears to have a 180 ° P-O-P bond angle is actually disordered, with the bridging oxygen angle occupying one of two sites (each of which has a 142.0 ° P-O-P angle). The average P-O-P bond angle in the structure is 146 °. The cell parameters were derived from Synchrotron X-ray powder diffraction of a crushed single crystal as $a = 24.7390(2)$ Å, $b = 24.7184(2)$ Å, $c = 24.74312(2)$ Å. These values are very close to metrically cubic (with differences from their average value of -0.022/0.061/-0.039 %), and so it is unsurprising that previous powder diffraction studies were unable to distinguish the cell symmetry as lower than cubic.

Stinton *et al*'s structure[78] was derived by simultaneous Rietveld refinement of synchrotron X-ray and neutron diffraction data. Although they did not observe any peak splitting, the fitting of peak intensities was noticeably improved by using the *Pbca* rather than the *Pa3* structure. The structure determined was in excellent agreement with Birkedal *et al.*'s single crystal structure- the average shift of atomic positions (excluding the disordered oxygen atom) between the two structures was 0.056 Å. This distance is comparable in magnitude to the error in position of an oxygen atom in the powder-derived structure (0.035 Å).

Birkedal *et al.* also used DFT calculations to calculate the optimum geometry of an isolated pyrophosphate ($P_2O_7^{4-}$) anion, which gave a P-O-P angle of 154.342 °, slightly higher than the observed average in ZrP_2O_7 and the barrier to P-O-P inversion of 3.6 kJ·mol^{-1}. The authors of this study also attempted to use the derived inversion barrier to estimate the phase transition temperature, based on the rather simplistic assumption that the phase transition apparently involves the inversion of the P-O-P linkages to give the time averaged *Pa*3 structure, which obeys a simple Boltzmann relationship (k_BT). In fact the factors affecting the phase transition temperature are likely to be considerably more complex, and it is unrealistic to interpret these DFT calculations for isolated $P_2O_7^{4-}$ anions in this way. This is shown by the fact that the true observed phase transition temperature (563 K) would give a value of 4.7 kJ·mol^{-1} for the "effective inversion barrier", higher than that obtained by DFT, which does not take account of Zr coordination. This approach would also not predict the different phase transitions observed for different members of the AP_2O_7 family.

Like many other members of the AM_2O_7 family, ZrP_2O_7 undergoes a superstructure-subcell phase transition; this was shown to occur at around 290 °C by an abrupt change in the lattice parameter in a variable temperature diffraction study by Korthuis *et al.*.[74] The material showed normal positive thermal expansion below the phase transition temperature, and much lower, although still positive, expansion above the phase transition (with coefficient of expansion of ~3.5 × 10^{-6} K^{-1} between 290 and 610 °C).[65]

A study by Withers *et al.* using electron diffraction showed the presence of an intermediate incommensurate phase which exists over a narrow temperature window around the phase transition temperature. Although accurate temperature determination is not possible for electron diffraction, it was estimated that the incommensurate phase exists over a 5-10 °C range around 294 °C. Withers *et al.* also used neutron powder diffraction to determine the variation of the unit cell parameters from -53 to 463 °C, as shown Figure 1-12.
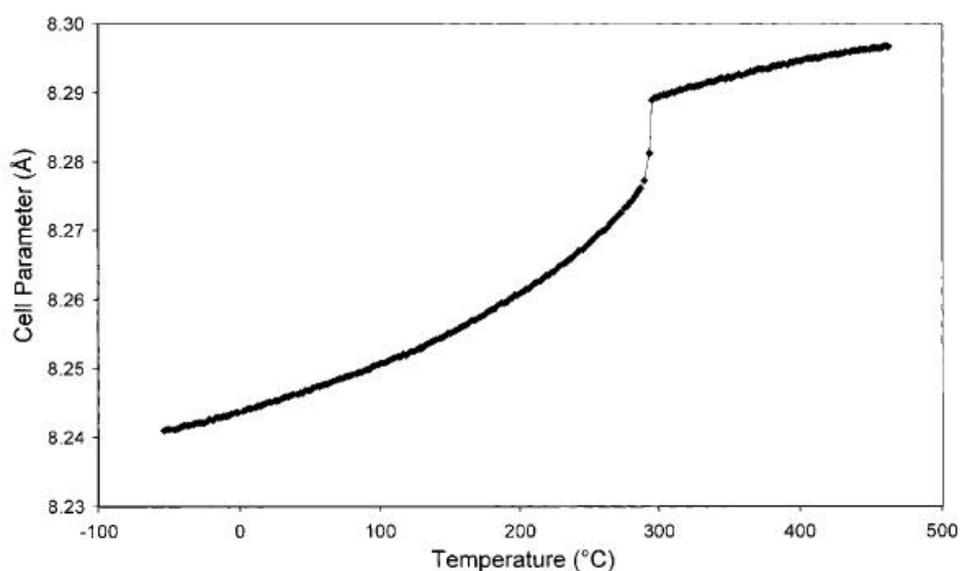
Figure 1-12 Variation of sub-cell cell parameter for ZrP$_2$O$_7$ as a function of temperature, as determined by Withers *et al.*[76].

The high temperature form of ZrP$_2$O$_7$ is currently believed to have the simple cubic Pa3 symmetry with only one phosphorus site in the asymmetric unit and a P-O-P bond angle that is linear by symmetry, at least on average.[65, 75]

Carlson *et al.* carried out synchrotron X-ray powder diffraction studies of ZrP$_2$O$_7$ at pressures up to 20.5 GPa.[71] The material was found to compress smoothly with increasing pressure, as TiP$_2$O$_7$ does, with no pressure-induced phase transitions. The authors suggested that this may be related to the thermal expansion properties, since ZrV$_2$O$_7$ (which does exhibit NTE) shows pressure induced amorphization at around 4 GPa, indicating a more flexible structure more likely to support contraction-causing vibrational modes. Although pressure induced transitions and NTE are both likely to be affected by the degree of structural flexibility, the authors offered no clear explanation of a correlation between the two phenomena.

ZrP$_2$O$_7$ also exists in another polymorphic state, with orthorhombic symmetry, as discovered by Anderson and Norby.[80] This phase forms at 688 K when Zr(HPO$_4$)$_2$ is heated, and is transformed to the alpha phase at temperatures above 973 K The structure of this phase was solved by *ab initio* methods and refined by Rietveld refinement.

There is very little literature published on HfP$_2$O$_7$, which is understood to be iso-structural with ZrP$_2$O$_7$; as might be expected given the extremely similar radii of the Zr(IV) and Hf(IV) ions in a six-coordinate environment (86 pm and 85 pm respectively). Tait showed that the room temperature structure has a superstructure with *a* = 24.64 Å, and that between 455 °C and 705 °C low thermal expansion is exhibited. [81] Variable temperature X-ray diffraction experiments show positive thermal expansion from 100 K to 670 K.[82] Supercell reflections were observed throughout this temperature range, with no evidence of any phase transitions. Later work by Tait involved using neutron diffraction to characterise the thermal expansion between 4 K and

305 K, but the analysis of the weak supercell peaks has still not been carried out, due to doubts about the precise purity of the sample.[81]

1.4.1.3 ZrV_2O_7

The first structural report on ZrV_2O_7 was published in 1942 by Peyronel, who described a sub cell structure (*Pa3*) with linear V-O-V bonds.[83] The 3×3×3 superstructure, which is expected by analogy to other AM_2O_7 materials, was first reported by Korthuis *et al.,*[74] who recorded X-ray diffraction data as well as ^{51}V NMR spectra, which showed several overlapping peaks. It was not possible to determine the exact number of vanadium sites due to the high degree of peak overlap, but this confirmed that a superstructure was present, as the simple cubic subcell structure would have only one vanadium peak.

A variety of space groups (*P2$_1$3*, *R3 and R3*) have been used to fit neutron powder diffraction data for the low temperature phase, but none gave an improved fit over the simple *Pa3* superstructure.[84] Unusually for these materials, it has been possible to obtain a single crystal, and the room temperature super-structure was solved using single crystal synchrotron X-ray data by Evans *et al.*[66] The structure was solved in space group *Pa3*, in which there are six unique V_2O_7 units, two of which are constrained by symmetry to have 180 ° bond angles. Electron diffraction results supported the choice of space group *Pa3*, as an *a*-glide plane was observed for the superstructure.[66, 85]

.
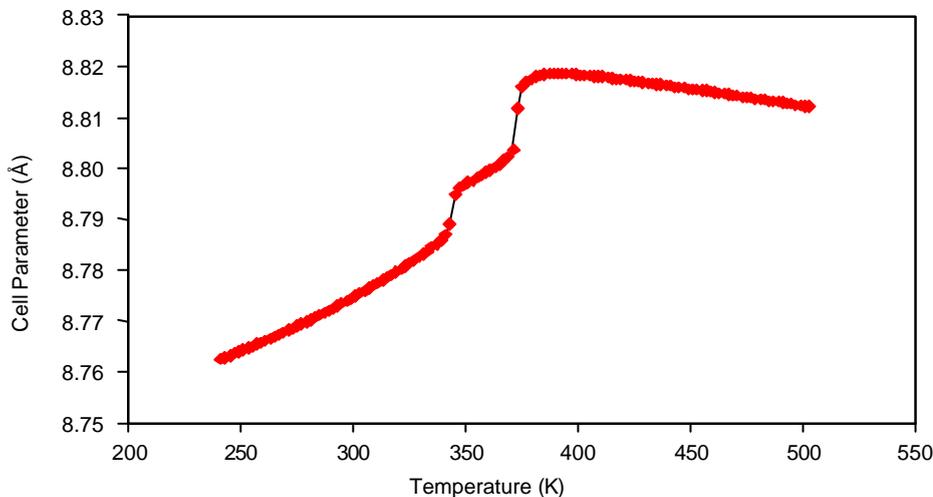
Figure 1-13 Variation of sub-cell cell parameter for ZrV_2O_7 as a function of temperature, as determined by Withers *et al.*[85] from neutron powder diffraction.

ZrV_2O_7 has been shown by variable temperature X-ray diffraction to undergo two phase transitions (at 77 and 102 °C) on warming.[74, 84, 85] The thermal expansion is illustrated by Figure 1-13. The high temperature phase shows negative thermal expansion from its formation at 102 °C up to temperatures of ~800 °C, although the room temperature and intermediate phase both show conventional positive thermal expansion.

The intermediate phase has been shown by electron diffraction to be incommensurately modulated, as in the case of ZrP_2O_7, although it is not iso-morphous with the intermediate ZrP_2O_7 phase and the temperature window for its formation is much wider, enabling studies of the intermediate phase alone.[85]

An NMR spectrum above the 102 °C phase transition was published by Korthuis *et al.,*[74] this appeared to show two peaks, although this was explained as being due to one site with a quadrupolar coupling effect producing an unusual lineshape. However, no evidence was offered for this explanation and the effect of changing magnetic field strength was not investigated. Further investigations are required since the high temperature NMR may indicate a symmetry lower than *Pa3* for the high temperature phase.

The origin of the NTE in the high temperature phase was investigated by Pryde *et al.,*[21] who concluded that the reasons for NTE are different than in the case of ZrW_2O_8, since cross-linking in the structure (due to the VO_4 tetrahedra being linked in V_2O_7 units) reduces the inherent flexibility, for example in comparison to ZrW_2O_8. The ZrV_2O_7 structure does not allow rotations of rigid polyhedra, and the structure has no RUMs. However, polyhedra may rotate if coupled with distortions in their shape; these modes are known as quasi-RUMs. Unlike the case of pure rigid unit modes, the presence of quasi-RUMs is strongly dependent on the polyhedra having some flexibility. Khosrovani *et al.* noted that the tendency for NTE amongst AM_2O_7 materials increases with the size of unit cell, since oxygen-oxygen repulsion decreases with large polyhedra, allowing greater flexibility of the polyhedra themselves.[84] This theory explains why ZrV_2O_7 shows more strongly negative expansion in its high temperature phase than other AM_2O_7 materials.

Carlson *et al.* studied the properties of ZrV_2O_7 at high pressure, and discovered an irreversible transition at pressures of 4 GPa.[71] The pressure-induced transition involves the formation of a new phase, labelled $ß$-ZrV_2O_7, followed by amorphization. This property is not seen in TiP_2O_7 or ZrP_2O_7, leading Carlson *et al.* to suggest that the amorphization process may be due to the more open frameworks, a condition also linked to NTE.

1.4.1.4 HfV_2O_7

HfV_2O_7 is understood to have a similar structure to ZrV_2O_7. The presence of a room temperature superstructure (with cell parameter $a = 26.3$ Å) was first noted by Baran in 1976.[86] As with ZrV_2O_7, HfV_2O_7 shows two phase transitions (at 67 °C and 96 °C), with only the high temperature phase showing NTE.[87] The temperature induced phase transitions have been observed by DSC and X-ray and neutron diffraction.[87] Although the structure of the intermediate phase has not yet been solved, it is suspected to be incommensurate by analogy with ZrV_2O_7.

The effect of pressure on the room temperature structure was investigated by both synchrotron XRD and Raman spectroscopy.[88] At pressures below 3.7 GPa, the cell parameter decreases

smoothly as the sample is compressed, enabling the determination of a bulk modulus of $K = 12.8 \pm 0.4$ GPa to be determined. At 3.7 ± 0.3 GPa, diffraction peaks due to the normal ambient-pressure phase of HfV_2O_7 disappear, followed by the emergence of a new diffraction pattern. The structure of this phase, not iso-structural with high temperature subcell structure, was not determined. Further compression of the sample resulted in a gradual reduction of intensity of all Bragg peaks, suggesting pressure-induced amorphization, but this was not complete even at the maximum recorded pressure of 41.7 GPa. Raman studies showed that several peaks undergo discontinuous shifts in position at ~1.5-1.9 GPa, which may be indicative of subtle changes in the ordering of HfV_2O_7 which are undetectable by powder XRD.

1.4.1.5 $ZrV_xP_{2-x}O_7$ solid solutions

Korthuis *et al.* prepared solid solutions of ZrV_2O_7 and ZrP_2O_7 with formula $ZrV_xP_{2-x}O_7$ and measured their thermal expansion.[74] No evidence of a room temperature superstructure was observed in the composition range (0.4-1.6), although the end members of the series, ZrP_2O_7 and ZrV_2O_7, both show phase transitions, as previously discussed. The structures of these solid solutions may contain a mixture of P-O-P, P-O-V and V-O-V dimers, introducing disorder into the system. The local structure of these dimers were investigated by Hudalla *et al.* using ^{31}P and ^{51}V NMR experiments.[89] The results showed a preference for the formation of mixed P-O-V dimers. Although it should be stated that Hudalla *et al.* assumed a fictitious spin ½ formalism for ^{51}V ($I = {}^{7}/_{2}$) in the absence of a precise theoretical description of REDOR involving quadrupolar nuclei, they were able to determine an estimate of O⋯V inter-nuclear distance in P-O-V dimers. The estimated distance of 3.42 Å is consistent with linear geometry, as would be required by symmetry if the structure really does belong to the *Pa3* space group.

1.4.2 Group 14

1.4.2.1 SiP_2O_7

SiP_2O_7 exists in several polymorphic phases. The cubic form has been studied most extensively, and is of most relevance to the other AM_2O_7 compounds studied in detail in this thesis. Unusually, silicon is in a 6-coordinate (octahedral) environment rather than the much more common tetrahedral geometry. The existence of weak supercell peaks was first observed by Vollenke.[73]

The structure is iso-structural with TiP_2O_7 and ZrV_2O_7, the space group has been proved to be *Pa*3 by both diffraction and NMR studies, which showed 11 unique phosphorus sites. The symmetry of the structure is such that two of the P_2O_7 groups in the structure have linear P-O-P bond angles. It is extremely unlikely that the P-O-P groups are entirely linear, their preferred bond angle being 150 - 170 °. The structure was thought to contain bridging oxygen atoms in bent P-O-P groups which are subject to either dynamic or static disorder, so that the average

position gives rise to the observed linear position. A ^{31}P NMR by Iuliucci *et al.* later excluded the possibility of static disorder. [90]

1.4.2.2 GeP$_2$O$_7$

Losilla *et al.* reported three germanium pyrophosphate compounds, which were formed on heating Ge(HPO$_4$)$_2$.[91] The structure of the *a*-phase remains unknown, as it has low crystallinity, but it may be related to the *I* form of SiP$_2$O$_7$. The *ß*-phase, formed by heating the *a*-phase to 930 °C, was a previously known triclinic structure.[92] The *?*-phase, formed at 1020 °C, is similar to the other pseudo-cubic phases discussed in this Chapter. A pure sample of *?*-GeP$_2$O$_7$ was prepared by heating *a*- GeP$_2$O$_7$ to 1000 °C at 20 kbar of applied pressure.

?-GeP$_2$O$_7$ was initially believed to have a cubic (*a*~22.86 Å) 3×3×3 supercell as with SiP$_2$O$_7$ and many of the other AP$_2$O$_7$ structures. Losilla *et al.* showed that the diffraction pattern did not fit to a cubic unit cell, since peak splittings consistent with either monoclinic or triclinic symmetry were present. The data were fitted by Le Bail's method to a *P2$_1$/c* structure, with a 3 × 3 × 3 monoclinic cell (*a* = 22.8647(4) Å, *b* = 22.8783(4) Å, *c* = 22.9429(4) Å, *ß* = 90.328(1) °), although the full structure was not solved.[93]

The ^{31}P NMR spectrum, of *?*-GeP$_2$O$_7$ also reported by Losilla *et al.*, shows at least 35 resonances, although it was not possible to determine precisely the number of sites due to peak overlap. Losilla *et al.* concluded that although they were unable to unambiguously determine the space group from their experiments, it is *P2$_1$/c* or possibly *P2$_1$* or *Pc*. The thermal expansion derived from the variation of the monoclinic unit cell volume was seen to be approximately linear and positive ($\textbf{\textit{a}}_V$ = 33 × 10^{-6} K^{-1}) from room temperature to 750 °C, with no evidence of any phase transitions. The thermal expansion data are subject to a number of errors, due to factors such as correlations between overlapped peaks in the LeBail fits and variation in sample height, and once the structure has been solved, a full analysis of thermal expansion may yet reveal the existence of phase transitions.

1.4.2.3 SnP$_2$O$_7$

The superstructure is shown by additional peaks in the diffraction powder patterns.[94] Electron diffraction showed that there is no *a*-glide plane, as would be expected for the cubic space group *Pa*3, and indicated space group symmetry of *P2$_1$3* or lower. An extensive range of ^{31}P NMR experiments on the room temperature phase have been used by Fayon *et al.* to show the presence of at least 49 unique P$_2$O$_7$$^{4-}$ units in the asymmetric unit, suggesting the symmetry is monoclinic with space group *Pc* or *P2$_1$*.[95] In as yet unpublished results, Stinton has recently compared Rietveld refinements of synchrotron X-ray and neutron diffraction in both *Pc* and *P2$_1$* and found that the *P2$_1$* superstructure gives a considerably better fit to the data. *P2$_1$* is also consistent with electron diffraction data, and is believed to be the true structure.[96]

The variation of the cell parameter over the temperature range 100 to 1243 K was studied by powder neutron and X-ray diffraction by Gover *et al.*, who observed two reversible phase transitions at ~560 K and 830 K.[97] Although the cell determined was approximately metrically cubic ($a \sim b \sim c$; a ~ ß ~ ? ~ 90 °), the positions of the subcell peaks were not all well fitted by a cubic cell, and so a triclinic cell was used to fit the data at all temperatures.[97] The variation of the unit cell with temperature clearly showed discontinuities indicating two phase transitions. Differential scanning calorimetry (DSC) showed no heat gain or loss at the phase transition temperatures, and thus that the transitions are second order or higher. It was suggested that the intermediate phase (observed between ~560 K and 830 K) could be incommensurately modulated.

Unlike other members of the AM_2O_7 family, the structure does not form a simple cubic sub cell at high temperatures, and the superstructure remains at all temperatures, right up to the decomposition temperature. Above the second phase transition temperature (830 K), supercell reflections are still present, with a peak splitting pattern consistent with a rhombohedral symmetry.

1.4.2.4 PbP_2O_7

PbP_2O_7 was first synthesised in 1939 by heating PbO_2 and H_3PO_4 to 300 °C, and identified as having $Pa3$ symmetry with $a = 8.01$ Å.[98] A cubic superstructure has been reported for PbP_2O_7, with $a = 24.10$ Å. More recently electron diffraction studies have been carried out, which show that the superstructure is, unusually amongst AM_2O_7 structures, incommensurate at room temperature.[82] King carried out NMR studies which show a single broad peak in the NMR spectrum.[99] This is in agreement with the structure being incommensurate, since a continuum of chemical shifts would be present. Two-dimensional ^{31}P NMR experiments showed no resolved cross peaks to indicate resolved sites linked by dipolar coupling, as in the case of ZrP_2O_7.

1.5 Other NTE materials

NTE also occurs for a number of other compounds, beyond the scope of this project. Another large class of materials known to show NTE is the $A_2(MO_4)_3$ family (where A = Sc, Zr, Fe *etc.*; M = W, Mo) [100-102] Quartz and a number of zeolites also show NTE over certain temperature ranges,[8, 9] and it is also worth noting that NTE is not a property only possessed by exotic materials, in fact ice shows NTE in its hexagonal and cubic phases at very low temperatures (below -200 °C).[103]

Recently a number of cyanide-bridged framework materials have been shown to exhibit NTE. The NTE in these materials is due to RUMs, many more of which can be supported than for oxide frameworks due to the more flexible nature of M-CN-M rather than M-O-M linkages.[104] Goodwin and Kepert showed that cyanide-bridged materials can support many more RUMs than single atom bridged analogues.[104]

Several materials of the YbGaGe[4, 5] system also show NTE over limited temperature ranges. Negative thermal expansion has also been observed in some metal intercalation compounds of C_{60}, such as samarium fulleride, $Sm2_{.75}C_{60}$, which shows NTE between 4.2 and 32 K.[6, 7]

$Fe[Co(CN)_6]$, the structure of which may be considered as the perovskite (ReO_3) structure, with the singe atom bridges replaced by diatomic CN linkages, is seen to under go NTE.[105] In fact in this material has an exceptionally small, though negative, coefficient of expansion (a_a = -1.47(1) × 10^{-6} K^{-1} over the temperature range 4.2 – 300 K).

$Zn(CN)_2$ has been shown to exhibit the strongest isotropic negative thermal expansion behaviour yet reported (a_a = -18 × 10^{-6} K^{-1}).[104, 106] Its structure consists of two identical interpenetrating networks, each being made up of interlinking $Zr(CN)_4$ tetrahedra. Each of the networks is a cyanide-containing analogue of ß-cristobalite (SiO_2), with a disordered orientation of the CN units. Transverse vibrational modes have been shown to be responsible for NTE in $Zn(CN)_2$ by pair distribution function (PDF) analysis of X-ray scattering data, which showed that the transverse displacement of cyanide bridges increases with increasing temperature, supporting a mechanism of contraction similar to that shown in Figure 1-1.[107]

Oxyfluorides such as TaO_2F showing NTE have also been reported[108], and the cuprite structure of Cu_2O and Ag_2O also shows NTE, due to flexibility of O-M-O linkages, rather than M-O-M. Some of these more recent discoveries are reviewed by Barrera *et al.*.[109]

1.6 Composite materials and applications

There are numerous technological applications of NTE materials. Most of these centre on the concept of producing materials with a mixture of NTE and conventional positive thermal expansion materials in controlled proportions to tune the thermal expansion properties of the resulting composite. Such materials would have many potential uses in engineering where at present allowances must be made for thermal expansion. It is possible to envisage the use of NTE materials in tooth fillings, since a material could be produced with the same thermal expansion behaviour as enamel. As well as simply avoiding problems due to positive thermal expansion, it is also possible that uses for NTE materials will be found in sensor technology. In high precision optical systems, such as optoelectronic devices and fibre Bragg gratings, NTE may be desirable to compensate for increases in refractive index with temperature.[110]

ZrW_2O_8 is an attractive NTE material for production of composite materials owing to the isotropic nature of thermal contraction, and the magnitude of its thermal contraction (comparable to conventional ceramics' expansion). Anisotropic thermal expansion is undesirable in composite materials as it causes strain, which can lead to cracking in the bulk sample.

Much of the structural characterisation of ZrW_2O_8 materials has used powdered samples, synthesised either by standard high temperature solid state methods,[111] or more recently by hydrothermal techniques.[112] Several investigations have also been carried out into the production of ZrW_2O_8 in a more industrially useful form: both by sintering to produce dense materials,[113] and the production of composite materials, such as metal matrix composites (MMCs).[60, 114]

ZrW_2O_8 has successfully been combined with cement to produce a composite concrete, with results suggesting that 60 % addition of ZrW_2O_8 would give a zero thermal expansion material.[115] This seems to be largely of academic interest, as the cost of using such a high concentration of ZrW_2O_8 in large-scale structural engineering would clearly be prohibitive.

The microelectronics industry is a more likely area for applications, for example composites for components such as heat sinks on printed circuit boards could be made with coefficients of thermal expansion matched to silica or alumina. Copper is a desirable matrix for such applications as it has high thermal conductivity, is relatively easily processed at temperatures at which *a*-ZrW_2O_8 is metastable, and is already used extensively in microelectronic applications.[60] Early attempts at producing a Cu / ZrW_2O_8 composite material by hot isostatic pressing were plagued by reactions between the components forming complex oxides and oxidation of the copper producing Cu_2O precipitates.[60] Holier and Dunard and solved these problems by carrying out a systematic investigation into the conditions under which reaction occurs, and identified a time-temperature window which allowed densification of Cu / ZrW_2O_8 composites without reaction between the components.[61] They also discovered that the thermal expansion of the composite materials is higher than predicted, which was attributed to the unwanted formation of *?*-ZrW_2O_8 during processing and thermal cycling. The thermal expansion mismatch between Cu and *a*-ZrW_2O_8 produces sufficient stress in the ZrW_2O_8 particles that the pressures generated are high enough to induce phase transformation to *?*-ZrW_2O_8. This was believed to be the first observation of a phase transformation in a composite material being induced by thermal mismatch stress, and several subsequent investigations have focused on understanding and preventing this process.[116] Wilma carried out variable temperature synchrotron X-ray diffraction on Holier and Dunand's sample of 60 volume % ZrW_2O_8 / Cu composite, and determined the copper lattice strain from the Cu diffraction rings.[61] It was found that the hydrostatic pressure stress in the copper matrix at room temperature was 448 ± 90 MPa at room temperature, corresponding to 299 ± 90 MPa in the ceramic, higher than the minimum stress (200 MPa) required to induce the *a*? *?* phase transformation.[117]

ZrO_2-ZrW_2O_8 composites may be prepared, either by using pre-prepared ZrW_2O_8 and ZrO_2, or, in an *in situ* method developed by deBuysser *et al.*, [118, 119] using a non-stoichiometric mixture of ZrO_2 and WO_3. Samples were prepared with a variety of compositions, and the coefficient of expansion was found to decrease as the amount of ZrW_2O_8 was increased. A 33 % mass ZrO_2

sample was reported to have zero thermal expansion,[120] although *in situ* measurement from 0 to ~300 C showed that there was an onset of slight positive expansion at 450 K.[119] This may be explained quite simply, since this is the temperature of the a / ß phase transition in ZrW_2O_8, at which there is a decrease in the negative thermal expansion coefficient. This variation in thermal expansion is not perfectly compensated for by ZrO_2, which has constant thermal expansion coefficient of $+9.6 \times 10^{-6}$ K^{-1}.

Polymer-based composites containing ZrW_2O_8 have also been investigated. For example, ZrW_2O_8-containing polyimide composite films have been prepared, and have also been shown to exhibit reduced thermal expansion over the pure polyimide.[121] Polyimide thin films have uses in a range of applications including coatings in electronic components, and so controlling their expansion is potentially important.

1.7 References

1   J. S. O. Evans, *J. Chem. Soc. Dalton*, 1999, 3317-3326.
2   G. A. Rossetti, J. P. Cline, and A. Navrotsky, *J. Mater. Res.*, 1998, **13**, 3197-3206.
3   R. J. Weiss, *Proc. Royal Soc. London.*, 1963, **A82**, 281-288.
4   J. R. Salvador, F. Gu, T. Hogan, and M. G. Kanatzidis, *Nature*, 2003, **425**, 702-705.
5   S. Margadonna, K. Prassides, M. Chondroudi, J. R. Salvador, and M. G. Kanatzidis, *Chem. Commun.*, 2005, 5754-5756.
6   J. Arvanitidis, K. Papagelis, S. Margadonna, K. Prassides, and A. N. Fitch, *Nature*, 2003, **425**, 599-602.
7   J. Arvanitidis, K. Papagelis, S. Margadonna, and K. Prassides, *J. Chem. Soc. Dalton*, 2004, 3144-3146.
8   P. Lightfoot, D. A. Woodcock, M. J. Maple, L. A. Villaescusa, and P. A. Wright, *J. Mater. Chem.*, 2001, **11**, 212-216.
9   M. P. Attfield and A. W. Sleight, *Chem. Commun.*, 1998, 601-602.
10   J. Graham, A. D. Wadsley, J. H. Weymouth, and L. S. Williams, *J. Am. Chem. Soc.*, 1959, **42**, 570.
11   L. L. Y. Chang, M. G. Scroger, and B. Phillips, *J. Am. Ceram. Soc.*, 1967, 211-215.
12   C. Martinek and F. A. Hummel, *J. Am. Ceram. Soc.*, 1968, **51**, 227-228.
13   T. A. Mary, J. S. O. Evans, T. Vogt, and A. W. Sleight, *Science*, 1996, **272**, 90-92.
14   M. Auray, M. Quarton, and M. Leblanc, *Acta Cryst. C*, 1995, **51**, 2210-2213.
15   J. S. O. Evans, W. I. F. David, and A. W. Sleight, *Acta Crystallogr. B*, 1999, **55**, 333-340.
16   Multilab-Ltd., 'Expansion coefficient for Alsint® 99.7% alumina', Newcastle-Upon-Tyne, 1999.
17   Y. Okada and Y. Tokumaru, *J. Appl. Phys.*, 1984, **56**, 314-320.
18   J. S. O. Evans, P. A. Hanson, R. M. Ibberson, U. Kameswari, N. Duan, and A. W. Sleight, *J. Am. Chem. Soc.*, 2000, **122**, 8694-8699.
19   J. S. O. Evans, T. A. Mary, T. Vogt, M. A. Subramanian, and A. W. Sleight, *Chem. Mater.*, 1996, **8**, 2809-2823.
20   A. K. A. Pryde, M. T. Dove, and V. Heine, *J. Phys. C.*, 1998, **10**, 8417-8428.
21   A. K. A. Pryde, K. D. Hammonds, M. T. Dove, V. Heine, J. D. Gale, and M. C. Warren, *J. Phys.-Condes. Matter*, 1996, **8**, 10973-10982.
22   A. K. A. Pryde, K. D. Hammonds, M. T. Dove, V. Heine, J. D. Gale, and M. C. Warren, *Phase Transitions*, 1997, **61**, 141-153.
23   G. Ernst, C. Broholm, G. R. Kowach, and A. P. Ramirez, *Nature*, 1998, **396**, 147-149.
24   R. Mittal, S. L. Chaplot, H. Schober, and T. A. Mary, *Phys. Rev. Lett.*, 2001, **86**, 4692-4695.
25   R. Mittal and S. L. Chaplot, *Phys. Rev. B*, 1999, **60**, 7234-7237.
26   D. Cao, F. Bridges, G. R. Kowach, and A. P. Ramirez, *Phys. Rev. Lett.*, 2002, **89**, art. no. 215902.

27   D. Cao, F. Bridges, G. R. Kowach, and A. P. Ramirez, *Phys. Rev. B.*, 2003, **68**, Art. No. 014303.

28   M. G. Tucker and J. S. O. Evans, *unpublished results*, 2006.

29   M. G. Tucker, A. L. Goodwin, M. T. Dove, D. A. Keen, S. A. Wells, and J. S. O. Evans, *Phys. Rev. Lett.*, 2005, **95**, Art. No. 255501.

30   A. P. Ramirez and G. R. Kowach, *Phys. Rev. Lett.*, 1998, **80**, 4903-4906.

31   T. R. Ravindran, A. K. Arora, and T. A. Mary, *Phys. Rev. Lett.*, 2001, **84**, 3879-3882.

32   T. Ravindran, A. Arora, and T. Mary, *Phys. Rev. B.*, 2003, **67**, Art. No. 064301.

33   W. I. F. David, J. S. O. Evans, and A. W. Sleight, *Europhys. Lett.*, 1999, **46**, 661-669.

34   N. Duan, U. Kameswari, and A. W. Sleight, *J. Am. Chem. Soc.*, 1999, **121**, 10432-10433.

35   S. Allen, 'Thermoresponsive Behaviour of AM_2O_8 Materials', PhD Thesis, University Of Durham, 2003.

36   A. Grzechnik, W. A. Crichton, K. Syassen, P. Adler, and M. Mezouar, *Chem. Mater.*, 2001, **13**, 4255-4259.

37   J. S. O. Evans, Z. Hu, J. D. Jorgensen, D. N. Argyriou, S. Short, and A. W. Sleight, *Science*, 1997, **275**, 61-65.

38   T. Varga, A. Wilkinson, A. Jupe, C. Lind, W. Bassett, and C. Zha, *Phys. Rev. B.*, 2005, **72**, Art. No. 024117.

39   Y. Yamamura, N. Nakajima, and T. Tsuji, *Phys. Rev. B*, 2001, **64**, 184109.

40   T. Tsuji, Y. Yamamura, and N. Nakajima, *Thermochim. Acta*, 2004, **416**, 93-98.

41   N. Nakajima, Y. Yamamura, and T. Tsuji, *J. Thermal Anal. Calorim.*, 2002, **70**, 337-344.

42   J. D. Jorgensen, Z. Hu, S. Short, A. W. Sleight, and J. S. O. Evans, *J. Appl. Phys.*, 2001, **89**, 3184-3188.

43   C. De Meyer, F. Bouree, J. S. O. Evans, K. De Buysser, E. Bruneel, I. Van Driessche, and S. Hoste, *J. Mater. Chem.*, 2004, **14**, 2988-2994.

44   D. R. Lide, 'CRC Handbook of Chemistry and Physics', CRC Press, 2005.

45   M. R. Hampson, P. Hodgkinson, J. S. O. Evans, R. K. Harris, I. J. King, S. Allen, and F. Fayon, *Chem. Commun.*, 2004, 392-393.

46   Y. Morito, K. Takahashi, S. Wang, H. Abe, A. Katoh, and T. Hashimoto, *J. Ceram. Soc. Jpn*, 2002, **110**, 807-812.

47   T. Hashimoto, J. Kuwahara, T. Yoshida, M. Nashimoto, Y. Takahashi, K. Takahashi, and Y. Morito, *Solid State Commun.*, 2004, **131**, 217-221.

48   N. Nakajima, Y. Yamamura, and T. Tsuji, *Solid State Commun.*, 2003, **128**, 193-196.

49   Y. Yamamura, N. Nakajima, T. Tsuji, A. Kojima, Y. Kuroiwa, A. Sawada, S. Aoyagi, and H. Kasatani, *Phys. Rev. B.*, 2004, **70**, Art. No. 104107.

50   U. Kameswari, A. W. Sleight, and J. S. O. Evans, *Int. J. Inorg. Mat.*, 2000, **2**, 333-337.

51   C. Closmann, A. W. Sleight, and J. C. Haygarth, *J. Solid State Chem.*, 1998, **139**, 424-426.

52   A. P. Wilkinson, C. Lind, and S. Pattanaik, *Chem. Mater.*, 1999, **11**, 101-108.

53   S. Allen and J. S. O. Evans, *J. Mater. Chem.*, 2004, **14**, 151-156.

54   M. Auray, M. Quarton, and P. Tarte, *Powder Diff.*, 1987, **2**, 36-38.

55   C. Lind, D. G. VanDerveer, A. P. Wilkinson, J. Chen, M. T. Vaughan, and D. J. Weidner, *Chem. Mater.*, 2001, **13**, 487-490.

56   C. Lind, A. P. Wilkinson, C. J. Rawn, and E. A. Payzant, *J. Mater. Chem.*, 2001, **11**, 3354-3359.

57   S. Allen, N. R. Warmingham, R. K. B. Gover, and J. S. O. Evans, *Chem. Mater.*, 2003, **15**, 3406-3410.

58   S. Allen and J. S. O. Evans, *Phys. Rev. B*, 2003, **68**, art. no. 134101.

59   C. Lind, A. P. Wilkinson, Z. B. Hu, S. Short, and J. D. Jorgensen, *Chem. Mater.*, 1998, **10**, 2335-2337.

60   C. Verdon and D. C. Dunand, *Scripta Materialia*, 1997, **36**, 1075-1080.

61   H. Holzer and D. C. Dunand, *Journal of Materials Research*, 1999, **14**, 780-789.

62   M. Auray, M. Quarton, and P. Tarte, *Acta Crystallogr. C*, 1986, **42**, 257-259.

63   S. Allen, R. J. Ward, M. R. Hampson, R. K. B. Gover, and J. S. O. Evans, *Acta Crystallogr.,Sect.B*, 2004, **60**, 32-40.

64   A. M. Krogh Andersen and S. Carlson, *Acta Cryst.*, 2001, **B57**, 20-26.

65   N. Khosrovani, V. Korthuis, A. W. Sleight, and T. Vogt, *Inorg. Chem.*, 1996, **35**, 485-489.

66   J. S. O. Evans, J. C. Hanson, and A. W. Sleight, *Acta. Cryst.*, 1998, **B54**, 705-713.
67   J. Soria, J. E. Iglesias, and J. Sanz, *J. Chem. Soc. Farad. T.*, 1993, **89**, 2515-2518.
68   J. Sanz, J. E. Iglesias, J. Soria, E. R. Losilla, M. A. G. Aranda, and S. Bruque, *Chem. Mater.*, 1997, **9**, 996-1003.
69   X. Helluy, C. Marichal, and A. Sebald, *J. Phys. Chem. B*, 2000, **104**, 2836-2845.
70   S. T. Norberg, G. Svensson, and J. Albertsson, *Acta Crystallographica Section C-Crystal Structure Communications*, 2001, **57**, 225-227.
71   S. Carlson and A. M. K. Andersen, *J. Appl. Crystallogr*, 2001, **34**, 7-12.
72   G. R. Levi and G. Peyronel, *Z. Kristallogr.*, 1935, **92**, 190-209
73   H. Vollenke, A. Wittmann, and H. Novotny, *Monatsh. Chemie*, 1963, **94**, 956-963.
74   V. Korthuis, N. Khosrovani, A. W. Sleight, N. Roberts, R. Dupree, and W. W. Warren, *Chem. Mater.*, 1995, **7**, 412-417.
75   I. J. King, F. Fayon, D. Massiot, R. K. Harris, and J. S. O. Evans, *Chem. Commun.*, 2001, 1766-1767.
76   R. L. Withers, Y. Tabira, J. S. O. Evans, I. J. King, and A. W. Sleight, *J. Solid State Chem.*, 2001, **157**, 186-192.
77   G. Stinton and J. S. O. Evans, 'PhD thesis (unpublished at time of writing)', University of Durham, 2006.
78   G. W. Stinton, M. R. Hampson, and J. S. O. Evans, *Inorg. Chem.*, 2006, **45**, 4352-4358.
79   H. Birkedal, A. M. Krogh Andersen, A. Arakcheevaa, G. Chapuis, P. Norbyd, and P. Pattisona, *Inorg. Chem.*, 2006, **45**, 4346-4351.
80   A. M. K. Andersen and P. Norby, *Acta Crystallogr. B*, 2000, **56**, 618-625.
81   M. Tait, 'The Structure and Properties of AM_2O_7 Materials', Undergraduate Project, University Of Durham, 2003.
82   J. Brindley, 'NTE and AM_2O_7 materials', Undergraduate Project, University Of Durham, 2003.
83   G. Peyronel, *Gazz. Chim. Ital.*, 1942, **72**, 83-88.
84   N. Khosrovani, A. W. Sleight, and T. Vogt, *J. Solid State Chem.*, 1997, **132**, 355-360.
85   R. L. Withers, J. S. O. Evans, J. Hanson, and A. W. Sleight, *J. Solid State Chem.*, 1998, **137**, 161-167.
86   E. J. Baran, *J. Less-Common Met.*, 1976, **46**, 343-345.
87   C. Turquat, C. Muller, E. Nigrelli, C. Leroux, J. L. Soubeyroux, and G. Nihoul, *Eur. Phys. J.-Appl. Phys.*, 2000, **10**, 15-27.
88   U. Hemamala, F. El-Ghussein, A. Goedken, B. Chen, C. Leroux, and M. Kruger, *Phys. Rev. B.*, 2004, **70**, Art. No. 214114.
89   C. Hudalla, H. Eckert, and R. Dupree, *J. Phys. Chem.*, 1996, **100**, 15986-15991.
90   R. J. Iuliucci and B. H. Meier, *J. Am Chem. Soc.*, 1998, **120**, 9059-9062.
91   E. R. Losilla, A. Cabeza, S. Bruque, M. A. G. Aranda, J. Sanz, J. E. Iglesias, and J. A. Alonso, *Journal of Solid State Chemistry*, 2001, **156**, 213-219.
92   U. Kaiser and R. Glaum, *Z. Anorg. Allg. Chem.*, 1994, **620**, 1755-1759.
93   E. R. Losilla, A. Cabeza, S. Bruque, M. A. G. Aranda, J. Sanz, J. E. Iglesias, and J. A. Alonso, *J. Solid State Chem.* , 2001, **156**, 213-219.
94   C. H. Huang, O. Knop, D. A. Othen, F. W. D. Woodhams, and R. A. Howie, *Can. J. Chem.*, 1975, **53**, 79-91.
95   F. Fayon, I. J. King, R. K. Harris, R. K. B. Gover, J. S. O. Evans, and D. Massiot, *Chem. Mater.*, 2003, **15**, 2234-2239.
96   G. Stinton and J. S. O. Evans, *unpublished results*, 2005.
97   R. K. B. Gover, N. D. Withers, S. Allen, R. L. Withers, and J. S. O. Evans, *J. Solid State Chem.*, 2002, **166**, 42-48.
98   G. Peyronel, *Gazz. Chim Ital.*, 1939, **69**, 254-262.
99   I. J. King, 'Combined Use of Powder Diffraction and Magic-Angle Spinning NMR to Structural Chemistry', Ph.D. Thesis, University of Durham, 2003.
100   J. S. O. Evans and T. A. Mary, *Int. J. Inorg. Mater.*, 2000, **2**, 143-151.
101   J. S. O. Evans, T. A. Mary, and A. W. Sleight, *J. Solid State Chem.*, 1998, **137**, 148-160.
102   S. C. Abrahams, *J. Chem. Phys.*, 1966, **45**, 2745-2752.
103   K. Röttger, A. Endriss, J. Ihringer, S. Doyle, and W. F. Kuhs, *Acta Cryst.*, 1994, **B50**, 644-648.
104   A. L. Goodwin and C. J. Kepert, *Phys. Rev. B*, 2005, **17**, art no 140301.

105   S. Margadonna, K. Prassides, and A. N. Fitch, *J. Am Chem. Soc.*, 2004, **126**, 15390-15391.

106   D. J. Williams, D. E. Partin, F. J. Lincoln, J. Kouvetakis, and M. O'Keeffe, *J. Solid State Chem.*, 1997, **134**, 164-169.

107   K. W. Chapman, P. J. Chupas, and C. J. Kepert, *J. Am Chem. Soc.*, 2005, **127**, 15630-15636.

108   J. Z. Tao and A. W. Sleight, *J. Sol. State. Chem.*, 2003, **173**, 45-48.

109   G. D. Barrera, J. A. O. Bruno, T. H. K. Barron, and N. L. Allan, *J. Phys.: Condens. Mater.*, 2005, **17**, 217-252.

110   H.-L. Wen, J. Lin, and Y.-L. Lo, in 'Process for preparation of zirconium tungstate ceramic body, zirconium tungstate ceramic body prepared thereby, and temperature compensated fiber bragg grating device', United States Patent, 2005.

111   A. Clearfield and R. H. Blessing, *J. Inorg. Nucl. Chem.*, 1974, **36**, 1174-1176.

112   Q. Xing, X. R. Xing, L. Du, Y. R.B., J. Chen, J. X. Deng, and J. Luo, *Acta Metallurgica Sinica*, 2005, **41**, 669-672.

113   C. De Meyer, L. Vandeperre, I. Van Driessche, E. Bruneel, and S. Hoste, *Cryst. Eng*, 2002, **5**, 469-478.

114   A. Matsumoto, K. Kobayashi, T. Nishio, and K. Ozaki, *THERMEC'2003, PTS 1-5 Materials Science Forum*, 2003, **426**, 2279-2283.

115   M. Kofteros, S. Rodriguez, V. Tandon, and L. E. Murr, *Scripta Mater.*, 2001, **45**, 369-374.

116   S. Yilmaz, *Compos. Sci. Technol.*, 2002, **62**, 1835-1839.

117   J. D. Jorgensen, Z. Hu, S. Teslic, D. N. Argyriou, S. Short, J. S. O. Evans, and A. W. Sleight, *Phys. Rev. B*, 1999, **59**, 215-225.

118   P. Lommens, C. De Meyer, E. Bruneel, K. De Buysser, I. Van Driessche, and S. Hoste, *J. Europ. Ceram. Soc.*, 2005, **25**, 3605-3610.

119   K. De Buysser, P. Lommens, C. De Meyer, E. Bruneel, S. Hoste, and I. Van Driessche, *Ceram-Silikaty*, 2004, **48**, 139-144.

120   E. Niwa, S. Wakamiko, T. Ichikawa, S. R. Wang, T. Hashimoto, K. Takahashi, and Y. Morito, *J. Ceram. Soc. Jpn*, 2004, **112**, 271-275.

121   L. M. Sullivan and C. M. Lukehart, *Chem. Mater.*, 2005, **17**, 2136-2141.

Chapter 2 - Characterisation techniques

The work presented in this thesis is mainly concentrated on studies by solid state nuclear magnetic resonance (NMR) and powder diffraction methods. These two techniques give very different, but mutually complementary information so their combined use can give many useful insights into the structure and dynamics of a chemical system. The conceptual basis of the techniques and relevant details of their use in work for this thesis are reviewed in this chapter.

2.1 Solid state NMR

NMR is a probe of the interaction between a nuclear spin and the local magnetic field, which is strongly dependent on the local electronic environment of the nucleus. NMR spectroscopy may therefore be used as a probe of the local structure and dynamics of a system. The NMR of solid state samples is significantly more complex than that of solution or liquid state samples (which is a routine characterisation method in analytical chemistry), and has thus developed more slowly, although much progress has been made in the past twenty years. The principles of NMR and its application to solid state studies are briefly outlined here, the main purpose of this section being to describe the specific techniques used in this work, and to give relevant details of experimental practice.

The most significant difference between NMR in the solution and solid states is that the latter is complicated by a number of anisotropic interactions not (directly) seen in solution-state NMR, where molecular tumbling causes an averaging of these effects

The chemical shift of a nucleus is anisotropic (although averaged to its isotropic value in the solution state by molecular motion). The chemical shift anisotropy generally causes a broadening of NMR lines in the solid state, in the absence of techniques such as magic angle spinning (Section 2.1.3).

Dipolar coupling arises due to pair-wise interaction between nuclear magnetic dipoles. Dipolar coupling occurs between nuclei of the same type (homonuclear coupling) and different types (heteronuclear coupling), and is dependent on the gyro-magnetic ratios of the nuclei and the distance between the nuclei ($D_{IS} \propto r^{-3}$, where D_{IS} is magnitude of dipolar coupling and r is the inter-nuclear distance), and may therefore be used to determine structural information about the conformation and geometry of molecules.

The indirect spin-spin (*J*) coupling is the coupling of nuclear spins via bonding electrons, and can provide information about connectivity within a molecule. The magnitude of this interaction is typically tens of Hz, and so it is not usually observed directly in solid state spectra.

In the case of quadrupolar nuclei (with $I > ½$) quadrupolar coupling adds a further complexity to the systems studied by NMR. This arises due to the interaction of a nuclear quadrupole moment with an electric field gradient at the nucleus. These effects can often be sufficiently large (of the order of several MHz) as to completely dominate spectra.

In a strong magnetic field, the orientational dependence of the above anisotropic interactions is proportional to $\left(1 - 3\cos^2 q\right)$ where q is the angle between the principal axis of the interaction and the applied magnetic field, B_0. If a large enough single crystal is used, then the orientational dependence of these interactions may be studied directly using a goniometer NMR probe head (which allows for physical rotation of the crystal). However, this technique is rarely used as it is not usually possible to obtain sufficiently large single crystals. The anisotropy of the interactions is much more commonly encountered when studying powdered samples, as was the case for all samples in this work.

A powdered solid is made up of many crystallites, each of which is randomly orientated such that the powdered sample as a whole contains nuclei in all possible orientations. As described above, the frequency and intensity of an NMR resonance is dependent on a range of anisotropic effects, and so a distribution of peaks is seen for a powdered solid state sample. The broadening of the peaks may be so extreme as to make the spectra unobservable under the experimental conditions usually used for simple solution state NMR experiments. Whilst these anisotropic effects may present an inconvenience for spectroscopy, they may also be interpreted to give additional information about the structure and dynamics of a solid state material – in this way solid state NMR may be used to provide a great insight into the chemistry of a material - much more than simply reproducing the simple spectra obtained in the solution state.

2.1.1 Spin ½ nuclei

Nuclei with spin quantum number $I=½$ are the simplest to study by NMR, since there is only one transition, between two states $m_I=+½$ and $m_I=-½$. ^{1}H and ^{13}C are both examples of spin ½ nuclei routinely used for the study of organic compounds, and a wide range of advanced techniques have been developed to elucidate information from these nuclei. Neither of these nuclei is present in the compounds studied in this thesis, but there are some spin ½ nuclei which may be used: ^{31}P and ^{183}W.

^{31}P is a very favourable nucleus for NMR, both in the solution and solid state. It has 100% natural abundance and relatively high receptivity ($6.63{\times}10^{-2}$ relative to ^{1}H). A huge range of experiments have been undertaken, including studies of AP_2O_7 (as studied in Chapter 5)[1-4] and $A_2P_2O_7$ (Chapter 6)[5] compounds. The ZrP_2O_7 study by King *et al.* is a particularly good example of the use of ^{31}P NMR in assisting structure determination.[1]

^{183}W (natural abundance 14.3 %) is the only spin active nucleus of tungsten. Unfortunately it is inherently a very insensitive nucleus for NMR due to its low receptivity (1.07×10^{-5} relative to ^{1}H). This is compounded in the solid state by very long T_1 relaxation times (typically 100's of seconds), which necessitate long pulse repetition delays, further increasing experimental time. Perhaps unsurprisingly very few solid state ^{183}W studies have been published. Many of the published results are by Knight *et al.*, who predicted that ^{183}W NMR could become a commonly used, if not entirely straightforward, technique.[6]

Compound	Tungsten coordination number and geometry	Tungsten oxidation state	Chemical shift /ppm	Reference
Li_2WO_4	4, tetrahedral	6+	-40	[6]
Na_2WO_4	4, tetrahedral	6+	-63	[6]
K_2WO_4	4, tetrahedral	6+	-18	[6]
Cs_2WO_4	4, tetrahedral	6+	-36	[6]
$CaWO_4$	4, tetrahedral	6+	29	[6]
$SrWO_4$	4, tetrahedral	6+	-33	[6]
$BaWO_4$	4, tetrahedral	6+	-78	[6]
$H_3[P(W_{12}O_{40}].nH_2O$	5, square pyramidal 6, octahedral	6+	-174	[6]
$(NH_4)_2WO_4$	4, tetrahedral	6+	-38.6, -55.8, -63.6, -80.0, -95.6, -107.4, -115.9	[7]
$(NH_4)_2WS_4$	4, tetrahedral	6+	3639.6	[7]
WO_3	6, octahedral	6+	-414, -438	[6]
H_2WO_4	6, octahedral	6+	-251.1	[7]
$W(CO)_6$	6, octahedral	0	-3470	[6]

Table 2-1 Published solid state ^{183}W NMR chemical shifts in various tungsten compounds

Since there are very few published solid state ^{183}W NMR studies, a summary of the published chemical shifts for tungsten compounds is given in Table 2-1. This is intended to put the ^{183}W experiment in this work (Chapter 3) in context, and to provide some values for comparison of the measured chemical shift. In addition to the direct acquisition of ^{183}W NMR signal, some experiments have been carried out using ^{1}H-^{183}W cross polarisation magic angle spinning (MAS) NMR, in which sensitivity is improved by transferring magnetisation from protons to the

tungsten nuclei.[7] Although this technique is highly effective in increasing sensitivity, it is dependent on the presence of a high receptivity nucleus (such as ^{1}H) for cross polarization, and therefore can not be applied to the compounds studies in this thesis.

2.1.2 Quadrupolar nuclei

The NMR of quadrupolar ($I > ½$) nuclei is considerably more complex than that of spin ½ nuclei for two reasons. Firstly, a nuclear spin may adopt $2I+1$ magnetic states (where I is the spin quantum number) and so quadrupolar nuclei exhibit multiple transitions. In the case of half integer spins, a central transition between $m_I = +½$ and $m_I = -½$ is observed, as in the spin ½ case, and the additional transitions are referred to as satellite transitions. The central transition is unaffected to first order by the quadrupole interaction. The NMR spectra are further complicated by the nuclear quadruple moment, since there is a coupling interaction between the quadrupole electric moment of the nucleus and the electric field gradient.

The work in this thesis has used two quadrupolar nuclei: ^{17}O and ^{51}V. ^{17}O ($I = \frac{5}{2}$) has a natural abundance of 0.038 %. In the solution state, natural abundance spectra may usually be observed without difficulty, enabling the use of tap water as a chemical shift reference. However, in the solid state, the sensitivity is effectively reduced by the considerably increased linewidths (due to anisotropic interactions, usually dominated by quadrupolar coupling), and isotopic enrichment is usually required.

Early solid state ^{17}O NMR studies have mainly focussed on simple oxide materials in which the oxygen environments are highly symmetric.[8] ^{17}O NMR of materials with large quadrupolar interactions, where oxygen is in a highly unsymmetrical environment is particularly difficult due to the extremely large linewidths (often in the order of MHz). However techniques in this an area are advancing rapidly, and recently it has even been possible to carry out some structural studies on proteins by solid-state ^{17}O NMR.[9]

The spin active isotope of vanadium, ^{51}V ($I = \frac{7}{2}$), is another nucleus which has properties favourable for NMR, since it has a high natural abundance (99.76 %) and receptivity. ^{51}V NMR has previously been used to study a large range of inorganic materials, including some of the $A^{4+}(V_2O_7^{4-})$ compounds, such as $ZrV_{2-x}P_xO_7$.[10]

2.1.3 Magic Angle Spinning

Magic angle spinning (MAS) is a routinely used technique in high resolution solid state NMR of powdered samples, which averages the effect of anisotropic interactions. This involves physically rotating the sample, at speeds typically in the range 5 – 30 kHz, about an axis inclined at the so-called magic angle of 54.74 ° to the applied magnetic field B_0.
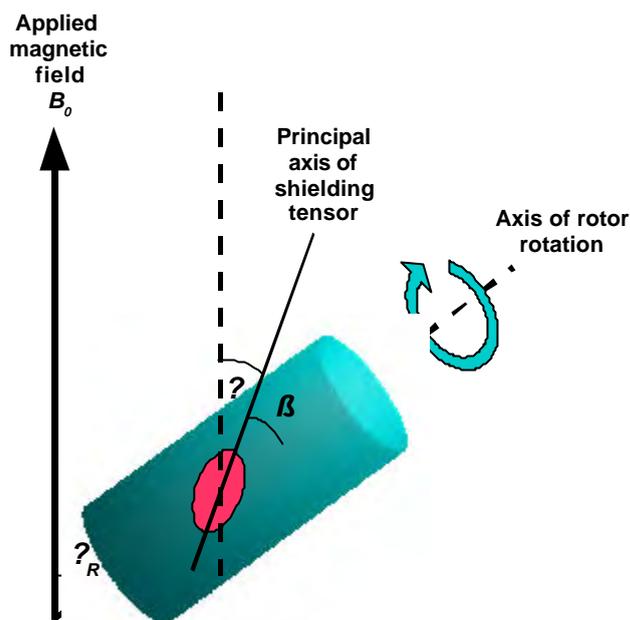
Figure 2-1 Schematic diagram of the magic angle spinning experiment. The blue cylinder represents the spinning sample rotor, with the pink ellipse representing the tensor of a shielding interaction.

The technique makes use of the fact that the orientational dependence of the anisotropic interactions is proportional to $(1-3\cos^2 q)$. It can be shown that the average value of this term, $\langle(1-3\cos^2 q)\rangle$ is given by Equation 2-1, where the angles b and q_R are as defined in Figure 2-1.

$$\langle 3\cos^2 q -1\rangle = \frac{1}{2}(3\cos^2 q_R -1)(3\cos^2 b -1) \qquad \text{[2-1]}$$

The angle q_R may be adjusted experimentally, such that $(3\cos^2 q_R -1)=0$ at a value of 54.74 °. Under these conditions, the average orientation dependence of nuclear spin interactions is also zero, and provided the rate of spinning is rapid compared to the magnitude of the anisotropy in frequency units, the interaction is simply equal to its isotropic value. The rate of MAS rotation should usually be significantly larger than the anisotropy, in order to completely average the effect. Incomplete averaging occurs when the spinning speed is insufficiently fast; in this intermediate situation, a centre-band peak is seen at the isotropic shift, with a series of 'spinning sidebands' seen at intervals of the spinning rate (in frequency units). The pattern of sidebands is dependent on the anisotropic interaction, and so fitting using a calculated pattern can be used to give values of the spin interactions.

The sample rotation in the MAS technique is practically achieved by directing a flow of gas (usually air or N_2) around a rotor, providing both a rotational driving force and a gas bearing to hold the rotor in the constant orientation during rotation. The sample is packed into a rotor

(usually made of zirconia, ZrO_2), which is fitted with a fluted drive tip. The angle of rotation may be adjusted whilst setting up the NMR probe for each experiment. Accurate setting of this angle is essential for the MAS technique, and is achieved by observing the ^{79}Br NMR signal of a standard sample of KBr. The orientation of the sample spinning module is manually adjusted so that the extent of rotational echo train in the free induction decay (FID) is maximised (typically to ~10 ms), indicating that the sample spinning axis is at the magic angle to the applied field.

The centre band can be identified by varying the spinning speed – since its frequency will remain constant while the position of the spinning sidebands will change. The spinning speed is usually selected to provide optimum averaging of anisotropic effects, whilst avoiding overlap between sidebands and centre band peaks.

As described later (Section 2.1.11) spinning the sample can cause sample heating due to friction between the gas and the rotor, and so accurate temperature calibration must take account of spin speed.

2.1.4 Relaxation

Relaxation in NMR is the process of a spin system returning to thermal equilibrium following a perturbation. The time taken for the system to return to equilibrium provides information about the processes which cause the transitions. There are a number of different relaxation time constants in NMR, but in this thesis only T_1 is studied.

T_1 relaxation is driven by fluctuations in the local magnetic field, which allows transitions between Zeeman energy levels. Such fluctuations are often caused by a variety of motional processes. Relaxation times in solids tend to be significantly longer than in the liquid state due to reduced mobility. Although this causes some difficulties for the experimentalist - longer recycle delays must be used, reducing the signal to noise which can be acquired in a given experiment time – interpretation of the relaxation times and particularly their temperature dependence can yield useful information about the dynamics of a system.

In the case of solids, there is likely to be a number of motions contributing to relaxation. Where a single motional process is dominant, it may be possible to interpret relaxation times to determine the rate of motion or the activation energy. When relaxation is driven by motion, an Arrhenius type expression may be used to relate the relaxation time to the correlation time for the motion. For example T_1 may be expressed as in Equation 2-2.

$$\ln\left(T_1\right)=\ln\left(t_c\right)-\frac{E_a}{kT} \qquad\qquad [2\text{-}2]$$

where t_C is the correlation time and E_a is the activation energy for the motion, k is the Boltzmann constant and T is the temperature. A plot of $\ln(T_1)$ against inverse temperature will allow the determination of the activation energy from the gradients at high and low temperature.

Relaxation in quadrupolar systems is considerably more complex than in the spin ½ case, since there are more than two spin states, and relaxation will involve all allowed transitions. The theory of quadrupolar relaxation was first studied by Andrew and Tunstall in 1961, who considered the cases of quadrupolar relaxation (caused by fluctuations of the electric field gradient at the quadrupolar nucleus) and magnetic relaxation (caused by magnetic fluctuations due to the movement of surrounding spin-active nuclei).[11, 12] The mechanism of quadrupolar relaxation is discussed further in Chapter 3, in relation to the study of ZrW_2O_8.

2.1.5 FT NMR and Pulse sequences

Almost all modern NMR spectrometers work on the principle of Fourier Transform (FT)-NMR in which the sample is held in a static magnetic field (B_0) and short pulses (typically with duration 1-100 µs) of radiofrequency radiation are used to excite a range of frequencies. The magnetisation returns to its equilibrium state following the pulse in a free induction decay (FID), which may then be Fourier transformed to give a frequency spectrum. This concept forms the basis of a wide range of techniques in which sequences of pulses are used.

The simplest possible FT-NMR experiment is a single pulse excitation, as illustrated in Figure 2-2. This straightforward and reliable sequence was used for the 1D spectra reported in this thesis. Others which are relevant to the work in this thesis are outlined in this section.
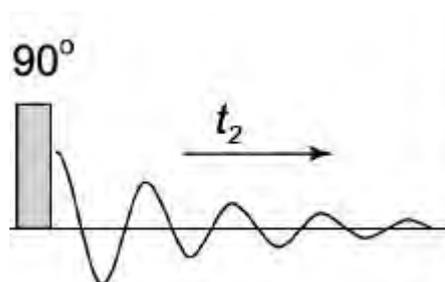
Figure 2-2 Pulse sequence for single pulse NMR experiment

2.1.5.1 Inversion Recovery

As described in section 2.1.4, NMR relaxation times can give information about motion in a material, and there are a number of NMR experiments which may be used for their measurement. A common method is inversion recovery, in which a 180 ° pulse is applied (inverting the signal), and then a read pulse acquired after a delay in which the signal recovers.

This method is well suited to systems in which the 90 ° pulse is well defined, but works less well for quadrupolar systems, in which excitation is more complex and so a well defined signal inversion may be impossible to achieve.

$$M_Z(t) = M_0 \left(1 - 2e^{-t/T_1} \right)$$ [2-3]

Equation 2-3 gives the recovery of magnetization, M_Z, as a function of delay time, t, where M_0 is the equilibrium magnetisation.

2.1.5.2 Saturation-Recovery

An alternative to the inversion recovery experiment is the saturation recovery method. This involves first 'saturating' the magnetisation, (i.e. ensuring that there is zero M_Z,), waiting for a period, t, of the order of T_1 to allow recovery towards the equilibrium magnetisation, M_0, and then acquiring a spectrum by applying a 90° 'read' pulse. The signal intensity is then proportional to $M_Z(t)$ which is given by an exponential recovery expression, as given in Equation 2-4.

$$M_Z(t) = M_0 \left(1 - e^{(t/T_1)} \right)$$ [2-4]

Saturation of the magnetisation is achieved by the application of a 'comb' of several 90 ° pulses, each separated by an interval much shorter than T_1. The pulse sequence for such an experiment is shown in Figure 2-3. $M_Z(t)$ is measured as a function of t so that T_1 may be determined. Short repetition times, considerably shorter than T_1, may be used as full recovery of M_Z is not required, since the first stage of the experiment is to saturate the magnetisation. This makes the saturation recovery experiment particularly suitable for compounds with long T_1 values. This is not the case with other techniques for measuring T_1, for example the inversion recovery method, which requires the magnetisation to have relaxed back to equilibrium before repeating the pulse sequence. This technique was used for the studies of relaxation times in Chapter 4.

Figure 2-3 Pulse sequence for the saturation recovery experiment.

2.1.6 Two-dimensional NMR

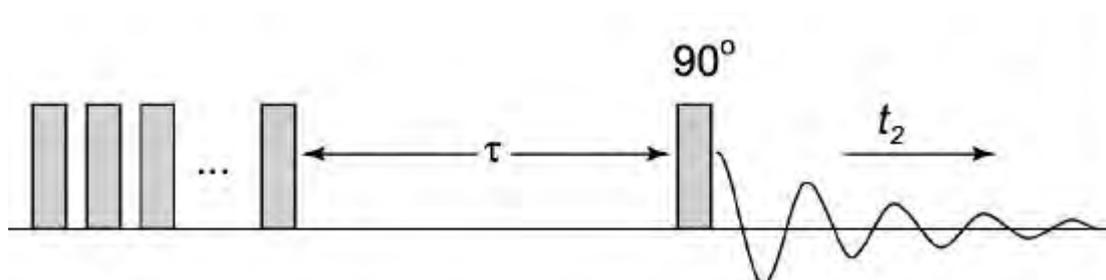There is a range of experimental techniques based on the principle of "two dimensional" NMR, which have been developed since the 1970s.[13] In a two dimensional experiment, an additional time period is introduced, during which the magnetisation evolves. A series of FIDs are recorded with different lengths of the evolution period. The data are processed in the normal way and then additionally Fourier-transformed with respect to the varied time parameter to give a second frequency dimension, and can be plotted as a contour plot, with the two frequency dimensions along perpendicular axes.

The 2D spectra will give additional information according to the nature of the processes occurring during the evolution period, and many experiments have been devised to give both structural and dynamic information. It is common to use 2D–NMR techniques to elucidate structure and atomic connectivity by various methods which allow correlation of nuclei through interactions such as *J*-coupling and dipolar coupling across a range of length scales.

A variety of experiments has been also developed to assist in structural characterisation by determining the distances, and connectivity, between atoms. The INADEQUATE (Incredible Natural Abundance DoublE QUAntum Transfer Experiment) was initially developed to study carbon connectivity in organic molecules through *J*-coupling of nuclei.[14] It has subsequently been used for a variety of nuclei, including ^{31}P. The two dimensional version of this experiment shows atoms coupled by direct, through-space *J* interactions. This can be applied, for example, to $^2J_{^{31}P^{31}P}$ couplings in pyrophosphate materials, in order to determine which phosphorus sites belong to the same P_2O_7 unit. This technique allowed King *et al.* to determine the number and local site symmetry of phosphorus sites in the superstructure of ZrP_2O_7, providing information about the symmetry which could not be determined by powder diffraction alone (See Chapter 1).[1, 15]

2.1.6.1 EXSY

The EXSY (Exchange Spectroscopy)[16] experiment is one of many 2D NMR techniques originally devised for solution state NMR which has successfully been applied to solids. It enables spin exchange, either by physical exchange or spin diffusion, between sites to be seen via cross peaks in the two dimensional spectrum. The pulse sequence (shown in Figure 2-4) consists of three pulses. An excitation pulse is first used to rotate the magnetisation from its equilibrium position to the transverse (*xy*) plane; the signals are allowed to evolve during a time period t_1, in which time they precess around B_0 and become frequency labelled. The second pulse then rotates the magnetisation about the *x* axis, so that a component is parallel to the *z* axis; the *z*-magnetisation is then allowed to undergo relaxation and exchange during the mixing period, before being detected during t_2 after the third (read) pulse.

Signals are recorded for a range of values of the evolution time t_1, and then the array of FIDs is Fourier transformed with respect to both t_1 (the indirect dimension) and t_2 (the standard time dimension as used for a simple 1D spectrum).

A given nucleus at a site A will contribute a component with frequency $?_A$ to the final NMR signal recorded $s(t_1,t_2)$. If exchange of this nucleus to a second site, B, occurs during the mixing period, then it will also have a contribution with frequency $?_B$. Thus Fourier transform in the two dimensions will give a signal intensity at the position $?_A$ in the t_1 dimension, and $?_B$ in the t_2 dimension, i.e. a 'cross peak' will be observed. Experimentally, it is important to choose a sufficiently long mixing time to allow exchange to occur.
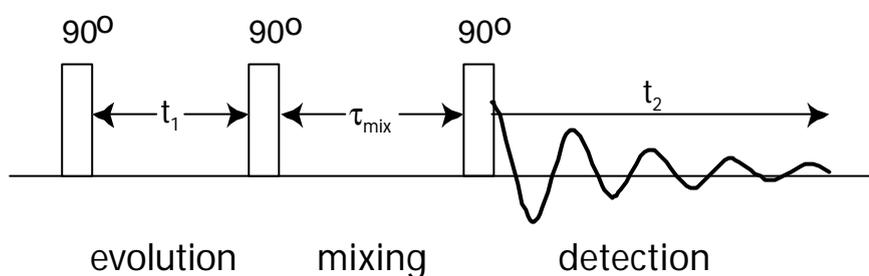
Figure 2-4 Schematic diagram of the EXSY pulse sequence.

The 2D spectrum may be interpreted as consisting of the one dimensional spectrum along the diagonal of the 2D plot, with off diagonal cross peaks showing chemical exchange. Qualitative information about dynamics may be relatively simply inferred from the presence or absence of cross peaks, which show which sites are in exchange with each other.

However, the EXSY experiment is not limited to qualitative observation, and a number of approaches may be used to extract quantitative results. The intensity of cross peaks in a spectrum will be dependent on the fraction of nuclei undergoing exchange during the mixing time. As well as the 2D-EXSY technique, a useful variant is the 1D-EXSY experiment, in which the change in intensity with mixing time can be studied to give kinetic information. The same information could be extracted from an array of 2D-EXSY spectra recorded with a range of mixing times, but this is usually prohibitively time consuming. The 1D-EXSY method involves recording spectra using the standard EXSY pulse sequence – however instead of varying t_1, spectra are recorded with a range of values of t_{mix}. A fixed, non-zero value is used for t_1 in order to create a non-equilibrium state at the start of the mixing period. The resulting plots of the signal intensity against t_{mix} may be fitted to models of the site exchange/ motion and magnetisation relaxation.

The 1D-EXSY technique has been used for a variety of systems, including a study of the dynamics of the inverse spinel structure of Li_2MgCl_4 in which the activation energy for exchange between the two Li sites was determined by ^6Li (I=1) experiments.[17] The 1D-EXSY experiment is not known to have been applied to half integer quadrupolar nuclei in the solid state. The technique for fitting the data is relatively simple for spin ½ nuclei, but is considerably more complex for multi-site exchange in a quadrupolar system. The development of the experiments and theoretical background for the case of chemical exchange in ZrW_2O_8 are described in Chapter 4.

2.1.7 Spectrometers used for this work

A range of spectrometers were used for work presented in this thesis, as listed in Table 2-2.

Manufacturer and model	Magnetic field /Tesla	Location	Software
Chemagnetics CMX 200	4.7	Department of Chemistry, University of Durham	Spinsight [18]
Varian Infinity Plus 500	11.7	Department of Chemistry, University of Durham	Spinsight [18]
Varian Inova Plus 300	7.05	Solid-State NMR Research Service, University of Durham	VNMR [19]
Varian Infinity 600	14.0	Department of Physics, University Of Warwick	Spinsight [18]

Table 2-2 NMR spectrometers used for work in this thesis.

The choice of probe for each series of experiments was based mainly on the rotor diameter, since all experiments in this work used single channel excitation only.

^{31}P NMR experiments were carried out with a 3.2 mm rotor diameter probe, since the sensitivity of ^{31}P is not a problem, and the small diameter rotors allow high MAS speeds to be used.

^{51}V NMR experiments were carried out with a 3.2 mm rotor diameter probe on the Varian 500 and a 4.0 mm probe on the Varian 300.

The 7.5 mm rotor diameter probe was used for the ^{183}W experiments since the sensitivity of ^{183}W is very low, and so it was necessary to use the largest possible sample volume.

^{17}O NMR experiments were carried out with a 4.0mm rotor diameter HFX probe. This rotor diameter was chosen based on the synthetic technique for the preparation of ^{17}O samples. The sensitivity of ^{17}O can be problematic, and so it was desirable to use a relatively large sample

volume, which precluded the use of the 3.2 mm probe. Using a larger volume of sample (and hence larger rotor diameter) would have increased signal intensity further, but this was not considered feasible due to the expense of ^{17}O-enriched water, and furthermore the synthetic technique designed around the preparation of ~0.2 g samples – larger samples would have required a modification of the technique. In practice, preliminary experiments showed that the sensitivity was sufficiently high for the 2D experiments in which signal to noise is particularly critical, and so 4.0 mm rotors were used for all ^{17}O experiments.

High temperature ^{31}P NMR of ZrP_2O_7 and HfP_2O_7 was recorded using the Varian 300 with a specialised Doty high temperature probe and heater unit, specified for use at temperatures up to 500 ºC.

All samples were packed in zirconia (ZrO_2) rotors, with end caps of Teflon or Kel-F. In the case of high-temperature experiments, an inner boron nitride sample container was fitted inside a zirconia rotor.

In all cases, the probe tuning was adjusted to approximately the frequency of a given nucleus by changing fixed capacitors (for low frequencies these were replaced with short circuits), and fine tuned by adjusting the position of tuning rods to alter the capacitance of variable capacitors. The reflected power was minimised by adjusting the tuning, and monitored using either a spectrum analyser, or a pulse program within the spectrometer control software.

2.1.8 Referencing

The frequencies recorded on an NMR spectrometer are absolute frequencies which depend on the precise magnetic field strength. To enable comparisons between spectra recorded on different spectrometers, the spectra (in units of chemical shift, ppm) must be referenced to a standard sample. The referencing of all work in this thesis was set whilst setting up the probe using an external standard, listed in Table 2-3.

Nucleus	Reference Sample	Reference Chemical shift /ppm
^{31}P	$CaHPO_4 \cdot 2H_2O$, Brushite	1.2
^{17}O	H_2O, Tap water	0
^{51}V	$NaVO_3$, sodium metavanadate (aqueous solution)	0
^{183}W	Na_2WO_4, sodium tungstate (saturated aqueous solution)	0

Table 2-3 Reference materials used for NMR experiments.

A secondary reference, a solid state sample of brushite was used for ^{31}P due to its convenience and safety rather than using 85% H_3PO_4 in aqueous solution, the standard primary reference.

2.1.9 Shimming

A highly homogenous applied magnetic field (B_0) is essential for high resolution NMR, since any magnetic field gradient across the sample would result in a distribution of precession frequencies, and a broadening of the observed peaks. In fact in solid state NMR the requirements for precise shimming are less stringent than in the solution state, since other factors usually dominate the peak widths. The homogeneity of the magnetic field is adjusted by the use of shimming coils, which modify the magnetic field in the region of the sample. These are adjusted whilst observing the spectrum of a standard sample (usually the same standard as is used for chemical shift referencing) to give a symmetrical peak with minimum line width. The shimming settings for a given probe are usually approximately constant, and so values may be saved between experiments.

2.1.10 Recycle delay

When setting up an NMR experiment, it is essential to chose an appropriate recycle delay (T_R) between transient acquisitions, to allow the system to return to its equilibrium state. In solution state ^{1}H NMR, where the T_1 relaxation time is usually of the order of a few seconds, this is not usually a significant problem. However, in the case of solids relaxation times are considerably longer, and the choice of recycle delay is often an important consideration. It may be assumed that complete relaxation following a 90 ° pulse occurs in $5 \times T_1$, which is therefore the minimum recycle delay required for the acquisition of data with quantitative signal intensities. In order to maximise the number of transients recorded in a given experiment time (and hence signal to noise), the recycle delay should be as short as possible whilst still allowing relaxation. It is therefore important to approximately determine T_1 whilst setting up an NMR experiment – this is usually done by one of the techniques described previously (Section 2.1.5).

Since T_1 is heavily influenced by molecular motion, it is site- as well as sample- dependent, and it is important to ensure that the recycle delay is chosen to be appropriate for all sites in a sample. T_1 is often particularly long for framework solids such as those studied in this thesis, due to the restricted motion of nuclei. In cases where T_1 is extremely long, or sensitivity is particularly low, it may be desirable to increase the number of transients recorded in a given time at the expense of quantitative signal intensities. This may be achieved by flipping the *z*-magnetisation through an angle smaller than 90 ° angle. On applying repetitive excitation pulses, a steady state of *z*-magnetization recovery is reached, which is dependent on the flip angle, the repetition delay time and T_1. The optimum flip angle to achieve maximum

magnetization recovery along the *z*-axis in such situations is called the "Ernst angle", $\boldsymbol{b}_E$ and may be determined by Equation 2-5, which is valid as long as $T_R < T_1$.[20]

$$\cos \boldsymbol{b}_E = \exp(-T_R / T_1) \qquad\qquad [2\text{-}5]$$

This approach was used for the [183]W experiments described in Chapter 3, in which the sensitivity was very low.

2.1.11 Variable Temperature NMR and Temperature Calibration

With the exception of the high temperature (>300 °C) ^{31}P NMR experiments which utilised a specialised high temperature probe, all variable temperature experiments for this thesis were carried out using the standard MAS probes in conjunction with a heater stack which fitted inside the magnet, on top of the probe. A flow of gas, referred to as the 'VT gas' (which may be compressed air or N_2), is directed through the heater stack into the probe and around the spinning sample rotor. The heater is controlled by the spectrometer software[18, 19] and heats the gas before it enters the probe, with a thermocouple (mounted in the heater stack) providing a measurement of the true gas temperature. In order to carry out low temperature experiments, the N_2 gas is directed through a copper coil inside a dewar filled with liquid N_2 to cool it prior to it reaching the heating stack.

In addition to the VT gas, there are typically three other gas supplies to the NMR probes: the 'drive' flow which drives MAS sample spinning, the 'bearing' flow which provides an air bearing around the spinning sample rotor and the 'purge' gas used to maintain a flow of air around the electronic components and prevent overheating. Compressed air may be used from room temperature up to a set temperature of 120 °C, dry nitrogen gas must be used for temperatures above and below this range, as at low temperatures water condenses (and freezes) from moist air, and at high temperature damage to the probe may result from oxidation of components.

The interactions between the various gas flows are extremely complex and largely unpredictable. There will be an increase in frictional heating on increasing spinning speed, for example, but this may be offset to an extent by the increased flow rate of ambient temperature drive and bearing gases entering the probe. In order to ensure the results of a temperature calibration are valid, consistent gas flow values must be used. The drive and bearing flow rates are set automatically according to the desired spin speed, but the purge and VT gas flow rates must be controlled manually. For ambient temperature experiments (where precise temperature control is not required), the VT gas flow was turned off, and the purge gas set at 30 SCFH (Standard Cubic Feet Per Hour). When carrying out controlled temperature experiments, the purge and VT gas flows were both be set at 90 SCFH. The temperature was always allowed to

stabilise for 15 minutes after changing temperature in VT NMR experiments before collecting data.

A thorough calibration of the sample temperature was carried out for the 4.0 mm rotor diameter HFX probe on the Varian Infinity Plus 500 spectrometer, using the well established method of observing chemical shift variation in the ^{207}Pb spectrum of Pb(NO$_3$)$_2$.[21] This method is used because the chemical shift of the single peak is extremely sensitive to the sample temperature. Spectra were obtained at a range of spinning speeds (2.5-15 kHz) and set temperatures (20-220 °C) to represent the full range of operating conditions for elevated temperature experiments with this probe.

The absolute temperature of a sample under certain conditions was first determined from the chemical shift difference between CH$_3$ and OH proton resonances in the ^{1}H NMR spectrum of methanol. The temperature dependence of this shift has been well-studied, and the conversion to determine sample temperature is well established.[21] In order to determine the temperature under standard conditions for solid state NMR, the spectra of a liquid methanol sample was recorded under identical conditions. A standard zirconia solid state NMR rotor was filled with liquid methanol and spun at an average spinning speed of around 2.5 kHz, with the temperature set to 25 ºC, and the flow rates of both VT and purge gas set to 90 SCFH. Although spinning was unstable, an average spinning speed of around 2.5 kHz was achieved reproducibly, and spectra recorded three times. In each spectrum, the difference between the chemical shift of the CH$_3$ and OH protons was measured. The temperature was calculated using a macro in the Spinsight spectrometer control software ('methanol_pick'), and the results were as listed in Table 2-4.[18]

filename	Peak separation (ppm)	Corrected temperature (°C)
MeOH_1	1.554	26.54
MeOH_4	1.559	26.04
MeOH_5	1.564	25.53

Table 2-4 Corrected sample temperatures derived from MeOH ^{13}C NMR peak separation.

This gives an average temperature of 26.0 ± 0.5 °C for these experimental conditions.

^{207}Pb NMR spectra were then recorded at a range of spin rates and set temperatures, and for each experiment the correct sample temperature was calculated from the formula given by Bielecki, as given in Equation 2-6.[21]

$$T_{actual} = T_{ref} + \frac{d}{0.753\ ppm\ K^{-1}} \qquad [2\text{-}6]$$

where T_{actual} is the calibrated temperature and $\textbf{\textit{d}}$ is the chemical shift relative to that of the lead nitrate signal in the standard conditions (T_{ref}). All the [207]Pb NMR spectra were referenced to the peak for lead nitrate recorded in equivalent conditions to the methanol spectra (2.5 kHz MAS, 90 SCFH VT flow, 90 SCFH purge flow) *i.e.* T_{ref} was 26.0 ℃.

2.1.11.1 Ambient temperature work

A calibration of the sample temperature in 'ambient temperature' configuration was carried out. In this experimental set up, the temperature is not usually accurately controlled, but it is important to understand how large an effect sample spinning has on sample temperature.

The variation of sample temperature with increasing MAS rate was measured. It was noted that the actual temperature was within 1℃ of the reading temperature at 2.5 kHz, However the difference increases with MAS speed and at 14 kHz the sample temperature is 30 ℃ higher than the reading temperature. This variation (shown in Figure 2-5) is due to the frictional heating due to spinning, to which the thermocouple in the heating stack is insensitive.
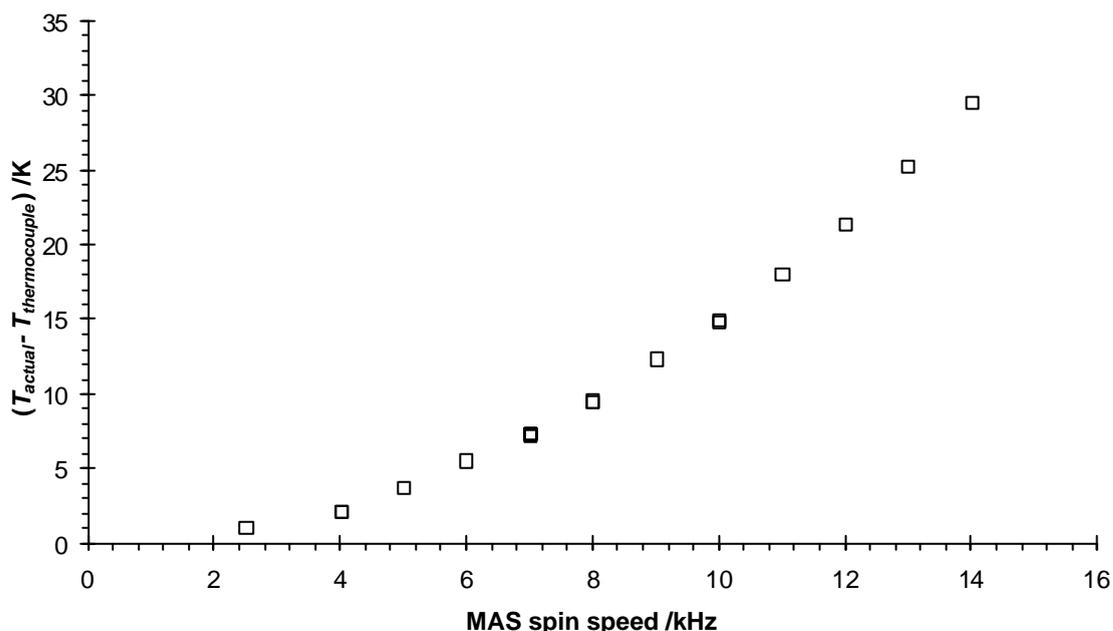
Figure 2-5 Difference between actual sample temperature and recorded (thermocouple) temperature as a function of spinning speed for 4.0 mm probe of Varian Infinity Plus 500 spectrometer.

The variation of sample temperature with spinning speed (v_{spin}) was fitted to a second order polynomial expression using Excel. The fitting gave the expression stated in Equation 2-7.

$$T = 0.22(v_{spin})^2 - 0.29 v_{spin} + 23.6 \qquad \text{[2-7]}$$

where T is the sample temperature (°C) and v_{spin} is the MAS rotation speed (kHz). This calibration has highlighted the importance of applying a correction function to the temperature readings, particularly at high spinning speeds.

2.1.11.2 Variable temperature work

A calibration of the temperature reading under variable temperature conditions was also performed for the same probe (4.0 mm probe of Varian Infinity Plus 500 spectrometer). This involved recording [207]Pb MAS NMR spectra at various values of the set temperature (25-220 °C) and spinning rate (2.5-14 kHz), to cover the full range of conditions used for elevated temperature NMR experiments.

[207]Pb NMR spectra of the lead nitrate sample were recorded with gas flows of 90 SCFH for both the VT gas and the purge gas; these are used as standard settings for future VT work on this probe. An equilibration time of at least 10 minutes was allowed on changing temperature before recording spectra (with a 5 minute equilibration time on changing spin speed). Test experiments confirmed that these equilibration times were sufficient to give consistent results.

The chemical shift was taken as the position of the maximum of the [207]Pb peak. The temperature range across the sample, as estimated by taking the chemical shift range of the peak envelope at half its maximum intensity, was found to range from 0.40 °C to 3.45 °C (mean value 1.78 °C, standard deviation 0.52 °C) over all the conditions used. It should be noted that this method will over estimate the temperature range since the inherent width of the peak is not considered.

In order to determine a single formula to calculate the actual sample temperature from a set of experimental conditions (both spinning speed and set/thermocouple temperature), the data were fitted, to a two-dimensional surface, using the Matlab program.[22] In some cases, data points had been recorded twice to check reproducibility; in these cases the calculated temperature was averaged to give the most accurate result. A matrix of data, with three columns of data, set temperature (T_{set}), spin speed (v_{spin}) and corrected temperature (T_{actual}), was produced and saved as a text file 'normal_data_reg'. A Matlab input file 'fitsurface_normal' (given in the e-appendix) was used to fit the data to an equation of form given in Equation 2-8.

$$T_{actual} = c + c_T T_{set} + c_{T^2}(T_{set})^2 + c_S \mathbf{n}_{spin} + c_{S^2}(\mathbf{n}_{spin})^2 + c_{TS} T_{set}\mathbf{n}_{spin} \quad [2\text{-}8]$$

It would be extremely difficult to physically model the complex interactions of the various gases in the NMR probe. It was expected that the entirely empirical approach used here would reproduce the experimental data sufficiently well.

Initially all 6 parameters of Equation 2-8 were allowed to vary during the fitting; however the error in the c_S parameter was unreasonably large (greater than the parameter value itself), indicating that this parameter is not required and so this was fixed at zero for the final fitting. Having determined a technique to fit the data, this was then applied to all the data, which were fitted to a single surface function, as shown in Figure 2-6. The fitted surface is described by Equation 2-9.

$$T_{actual} = 1.97 + 0.907 T_{set} + 4.25 \times 10^{-4} (T_{set})^2 + 9.96 \times 10^{-2} (n_{spin})^2 - 5.32 \times 10^{-3} T_{set} n_{spin} \quad \text{[2-9]}$$
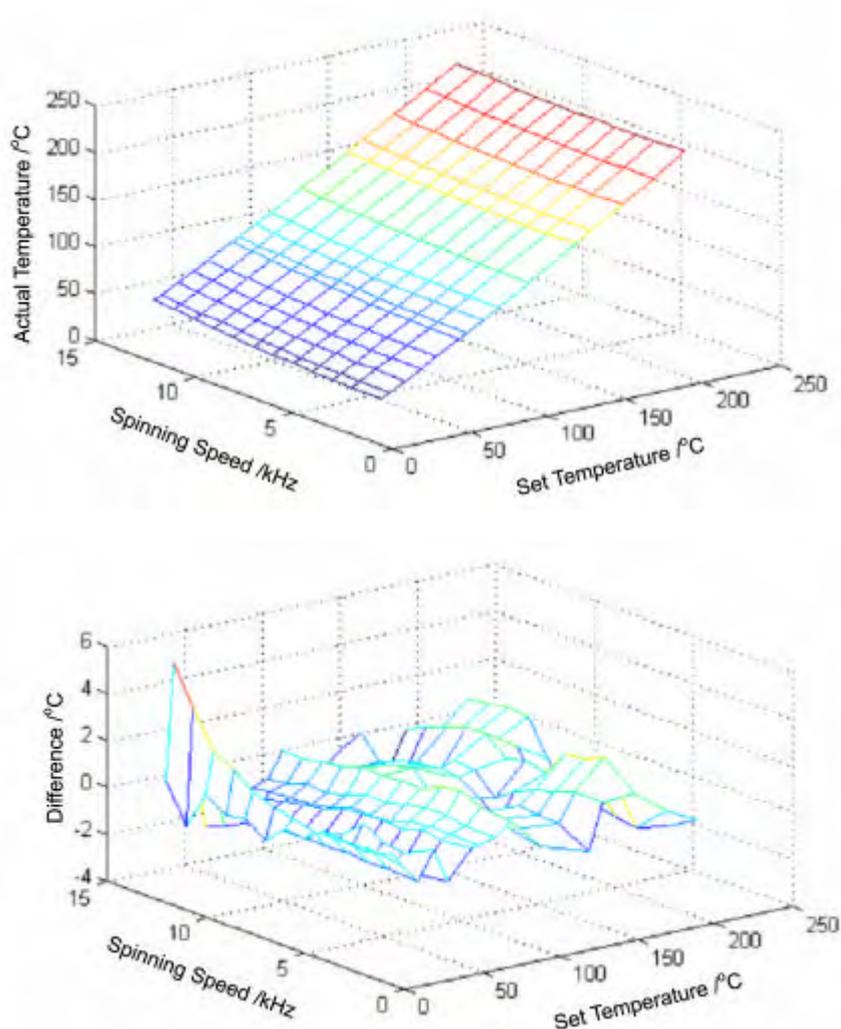
Figure 2-6 Fitting of variable temperature calibration results for 4.0 mm probe of Varian Infinity Plus 500 spectrometer. 2D surface plots of data fitting (top) and difference (observed – calculated data) (bottom).

The maximum difference, also shown in Figure 2-6, between the experimentally observed temperature and that calculated from the fitting function was ~4 °C, approximately equal to the temperature gradient across the sample. The largest difference between calculated and

observed temperatures was at low spinning speed at room temperature, the same conditions which gave the largest temperature gradient across the sample. This indicates that the fitting has been successful, justifying the empirical approach used.

A technique has been developed to accurately calibrate the temperature readings on a MAS solid sate NMR probe for elevated temperature operation. The equation derived from this fitting is applicable to all data recorded using this probe, and was used to calculate the true sample temperatures in Chapters 3 and 4.

2.2 Powder Diffraction (X-ray and neutron)

X-Ray diffraction is a very powerful structural characterisation technique, which can be used to determine the full structure of a material. The basis of this technique is that X-rays have a similar wavelength to inter-atomic spacings, and so undergo diffraction. The technique is dependent on long range order in a material, and so is essentially limited to ordered crystalline materials. X-ray diffraction and solid state NMR are in many ways complementary, and so use of the two techniques in parallel gives a more complete understanding of the structure of a material.

In powder diffraction much of the information of a single crystal experiment is lost as the information is compressed into only one dimension (cones of diffracted intensity are observed, rather than isolated spots as in single crystal cases). However, since powdered samples are often much more easily obtained than crystals large enough for single crystal crystallography, a wide range of materials may be studied. Additionally, powdered samples tend to be physically robust in comparison to single crystals, which can shatter due to changes in temperature for example. This has enabled techniques to be developed to allow powder diffraction to be carried out under a wide range of variable experimental conditions such as temperature, pressure and gas flow. The course of phase transitions and even solid state reactions may be followed by *in situ* powder diffraction experiments.

A powder diffractogram may be thought of as consisting of three principal types of information: the position of peaks (determined by the size and symmetry of the unit cell), the intensity of the peaks (determined by the positioning of atoms) and the width and shape of peaks (determined by a variety of instrument and sample effects, but often dominated by the size and strain of the individual crystallites).

2.2.1 Rietveld Refinement

Although it is often difficult to solve structures using powder X-ray diffraction alone, structure refinement is more straightforward. The Rietveld method is based on least squares refinement, and allows a structural model to be fitted to experimental powder diffraction data. A diffraction pattern is calculated from a model containing experimental factors such as X-ray wavelength and a structural model.

Rietveld refinement is used to simultaneously fit the whole profile of the powder pattern by using a model to describe fully the observed diffraction. The quality of fit between the calculated and experimentally determined patterns is expressed by a residual index (or R-factor); the definitions of commonly used residual indices are given below.

R_{WP} is a weighted profile residual index and is a measure of the fit of the whole diffraction pattern, defined as in Equation 2-10,

$$R_{WP} = \sqrt{\left\{ \frac{\sum_i w_i [y_i(obs) - y_i(calc)]^2}{\sum_i w_i [y_i(obs)]^2} \right\}}$$

[2-10]

where $y_i(obs)$ and $y_i(calc)$ are the intensity of the ith data points in the observed and calculated patterns respectively, and w_i is a weighting factor for the ith data point.

The expected residual index, R_{exp}, is defined as in Equation 2-11.

$$R_{exp} = \sqrt{\left\{ \frac{(n-p)}{\sum_{i=1}^{n} w_i y_i^2} \right\}}$$

[2-11]

where n is the number of observations and p is the number of refined parameters.

The goodness of fit, or c^2, may be used to judge the quality of the a refinement – this is simply the ratio of R_{exp} and R_{WP} (Equation 2-12), which should approach a value of 1 for a high quality refinement.

$$c^2 = \frac{R_{WP}}{R_{exp}}$$

[2-12]

It is important when carrying out Rietveld refinements to take care when considering residual indices, as they may give a misleading impression. For example a low value of R_{WP} can be

achieved despite an incorrect structural model, as it is biased by a good fit to the background intensity.

R_{Bragg} is the residual index factor based only on the intensity of Bragg reflections, defined as in Equation 2-13,

$$R_{Bragg} = \frac{\sum_{hkl} |I_{hkl}(obs) - I_{hkl}(calc)|}{\sum_{hkl} |I_{hkl}(obs)|}$$

[2-13]

where I_{hkl} is the intensity of Bragg reflections with Miller indices hkl.

R_{Bragg} is unaffected by factors such as the quality of fitting of the background, although it should be noted that it is dependent on the correct assignment of the peaks to *hkl* indices, (*i.e.* it is biased by the structural model).

In order to refine a reliable structural model, it is essential that the shape of peaks in the observed pattern is reproduced well in the calculated pattern. This can be done using a range of functions, including empirical methods and those based on a physical model. A simple pseudo-Voigt function, the combination of Gaussian and Lorentzian peak shapes, with up to six refined parameters is often used. Although this is a purely empirical technique, it often enables a good fit to the observed peak shapes.

When considering the physical basis for the width (usually quantified by the full width at half maximum, FWHM) and shape of peaks, the size and strain of the crystallites are usually the dominant effects. The size of crystallites affects the width of observed peaks. At its simplest this may be expressed as a broadening of the form FWHM = (*K* × *?*)/(size × cos *?*), where *K* is a constant known as the Scherrer constant, *?* is the wavelength of the X-rays and *?* is the Bragg diffraction angle. Strain in a crystallite will also contribute to additional broadening of the peaks, and typically shows a tan *?* dependence.
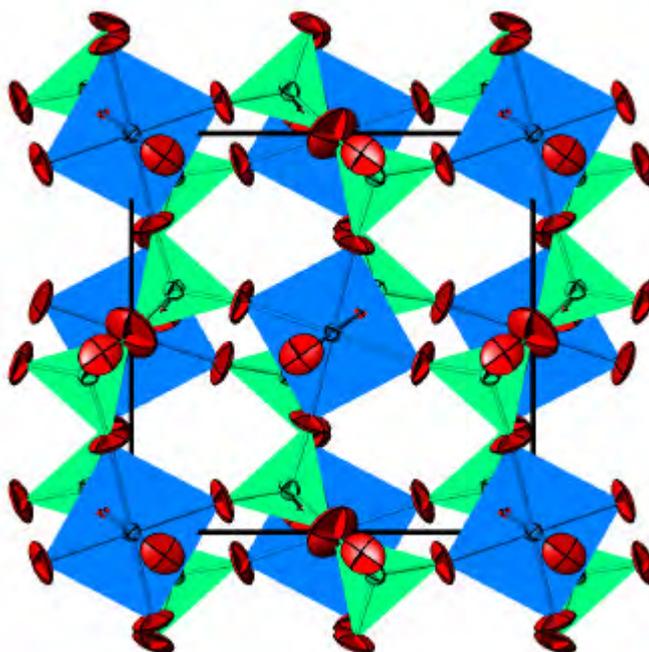
Figure 2-7 An example of a structure showing anisotropic displacement of atoms as thermal ellipsoids (50% probability) – the refined structure of high temperature HfP$_2$O$_7$ in *Pa3* (Chapter 5).

The displacement of atoms from their mean positions causes a smearing of the electron density. This often has an effect on the X-ray diffraction pattern, and a structural model usually incorporates atomic displacement parameter (ADP) terms to model such displacement. These are commonly known as 'temperature factors' since thermal motion is often the dominant cause of such displacement. Atomic motion may be modelled either isotropically (using one parameter) or anisotropically (using up to 6 parameters, depending on the site symmetry). Anisotropic ADPs may be displayed graphically as 'thermal ellipsoids', which show the probability surface of the atomic motion (see Figure 2-7, for example).

In cases where motion is strongly directional, this is often shown by the form of anisotropic ADPs and so careful consideration of ADPs can give valuable information.

Background intensity results from a range of sources, including diffuse diffraction from amorphous materials, such as air and the sample holder. Typically a Chebychev polynomial is used to fit the background intensity curve empirically, that is all the intensity at points in the powder pattern other than those to which Bragg reflections contribute.

The results of a variable temperature diffraction experiment consist of a number of scans recorded at temperature intervals. The analysis of these data were carried out using a DOS batch program which executes command line TOPAS for each individual scan in succession for the whole range of data recorded. [23] A seed refinement was first set up using the first scan in an

experiment. The refinement of each data set uses the results of the preceding refinement as a starting point.

2.2.2 Experimental details

All of the X-ray diffraction data sets presented in this thesis were recorded using laboratory diffractometers, as listed in Table 2-5, which are henceforth referred to by their abbreviated names.

All of these instruments were used in flat-plate reflection geometry. Samples for ambient temperature measurements were prepared either by packing a powder into a bulk sample holder, or, when only small amounts of a sample were available, by sprinkling the powder onto a slide coated with a thin layer of Vaseline to act as an adhesive. Slides were made of either amorphous glass or SiO_2 or a single crystal of silicon cut parallel to the 510 crystal plane so as to give no diffracted intensity in the observable angle range.

Manufacturer and model	X-ray source	Wavelength	Monochromator	Detector	Abbreviated local name
Siemens d5000	Cu K_a	1.5418 Å	Graphite (001)	Scintillation counter	D5
Bruker d8 Advance	Cu K_a	1.540598 Å	Ge (111)	Position Sensitive Detector (PSD)	D8
Bruker d8 Advance	Cu K_a	1.540598 Å	n/a	SOLX	D9

Table 2-5 Details of laboratory X-ray diffractometers used.

A variety of sample environments may be achieved by mounting sample stage attachments on the goniometer. The D8 was equipped with a Anton Parr HTK1200 furnace attachment which was used for variable temperature experiments. This allows the sample temperature to be varied from room temperature (298 K) to 1473 K, under laboratory air, dynamic vacuum or gas flow (e.g. Ar, N_2). This furnace uses flat plate geometry, with the sample sprinkled onto a Vaseline covered amorphous silica plate. Furnace windows made of polyimide foil allow transmission of the X-ray beams.

Bruker Diffrac+ v4.0 (Bruker XRD commander on the d9) software was used to control all of these diffractometers.[24] All laboratory X-ray data sets recorded were given a number of the form yy_xxxxx, where yy is the abbreviated instrument name (as stated in Table 2-5) and xxxxx is a sequential number.

All Rietveld refinement of X-Ray powder diffraction data was carried out using Bruker AXS TOPAS software.[23] TOPAS uses an input file made up of instructions for refinement and the parameters to be refined, in a simple programming language. The input files for all Rietveld refinements are included in the electronic appendix CDR.

2.2.3 Neutron Diffraction

Neutron diffraction experiments make use of the fact that the de Broglie wavelength of a neutron is similar in length to inter-atomic distances in a solid, and hence undergo neutron diffraction in a manner analogous to X-rays. Many of the principles of X-ray diffraction may be transferred to neutron diffraction.

Neutron diffraction experiments were performed at the ISIS neutron source at the Rutherford Appleton Laboratory, UK. Protons are accelerated in a synchrotron ring and directed to a tantalum target, where a process of spallation produces white neutrons. This instrument works on the time-of-flight (TOF) principle, in which the whole pattern is obtained simultaneously, with fixed-position detectors recording intensity as a function of time of flight. Two diffractometers at ISIS were used for work in this thesis: the HRPD (High Resolution Powder Diffractometer) and GEM (General Materials) instruments. The resolution at HRPD, quoted as 4×10^{-4} in $?d/d,$ is achieved by having a very long distance, approximately 95 metres, between the spallation target and the sample.

2.3 Complementary nature of NMR and powder diffraction

The information obtained from solid state NMR may be used to complement that from diffraction techniques in a variety of ways. It is important to note that the time and length scales for the two techniques are very different, and whilst this may prevent a direct comparison between data, it also enables significant insight to be derived from a combination of the two techniques.

NMR is a local probe of the environment of individual nuclei, in contrast to diffraction, and a given NMR experiment effectively probes one type of nucleus – this enables the motion of different sites in a material to be studied separately. The timescale of the signal recorded in NMR is typically of the order of microseconds, but a range of experiments enable motion to be detected on a range of timescales: from nanoseconds (shown by relaxation) to seconds or minutes (using exchange experiments such as EXSY).

The time scale of XRD measurements is usually considered to be the time taken for a whole scan to be recorded (usually minutes or hours), although the actual interaction of X-ray beams with the sample is essentially instantaneous. It is possible to carry out time-resolved XRD experiments using high intensity (Synchrotron) X-ray beams, in order to study molecular motions such as protein folding on a nanosecond timescale, but these techniques are not

relevant to the current work. Typically diffraction techniques 'see' an average view of the material over the timescale of the experiment, and dynamical disorder and other motional effects are difficult to characterise from XRD experiments alone. Since X-ray diffraction is dependent on long range order, it effectively sees an average over whole crystals, rather than individual sites.

The two methods also differ in the range of materials they can be used to study, while NMR may be used on samples in liquid, liquid crystal as well as solid states, conventional diffraction experiments are limited to solid crystalline samples. Amorphous samples may be studied by solid state NMR, although peak broadening occurs due to the range of environments for a given crystallographic site. X-ray diffraction of amorphous samples usually gives extremely broad lines, from which it is difficult to extract structural information, though there has been significant recent progress made in this area.

The relationships between structure and a powder diffraction pattern are well understood, and the structure in terms of atomic positions and cell parameters may often be derived from XRD. If the symmetry of a system (which itself can be derived form the X-ray diffraction) is known, the pattern of diffracted X-rays may be inverted to give a 3 dimensional electron density map. A range of methods, including Rietveld refinement, may therefore be used to correlate the observed diffraction pattern with a model of the structure. Interpretation of solid state NMR results is considerably more complex, and it is not possible to directly obtain the atomic positions for example. The relationships between NMR parameters are generally only known empirically, which enables correlations to be deduced.

One of the difficulties with X-ray diffraction of powders is that assignment of the crystallographic space group is often difficult. A solid state NMR spectrum can often assist in assigning the correct space group to the structure, which may be ambiguous from powder diffraction alone. Counting the number of sites in a well resolved NMR spectrum gives information about the number of sites in the asymmetric unit. This is probably the simplest and most obvious way in which XRD and solid state NMR can be combined, but there are several other ways in which a more complete picture of structure and dynamics can be determined.

The coupling between nuclei, by *J*-coupling or dipolar coupling, means that information about the distance and, in the case of *J*-coupling, bonding connectivity may also be extracted from solid state NMR results.[1, 5] This information about the local environments is complementary to that obtained from X-ray diffraction.

The ability to follow dynamic processes by NMR is extremely important, and allows the determination of both the mechanism and rate of motion, as demonstrated by the work in

Chapters 3 and 4. Such information is complementary to the averaged picture determined by diffraction.

2.4 References

1   I. J. King, F. Fayon, D. Massiot, R. K. Harris, and J. S. O. Evans, *Chem. Commun.*, 2001, 1766-1767.
2   X. Helluy, C. Marichal, and A. Sebald, *J. Phys. Chem. B*, 2000, **104**, 2836-2845.
3   J. Sanz, J. E. Iglesias, J. Soria, E. R. Losilla, M. A. G. Aranda, and S. Bruque, *Chem. Mater.*, 1997, **9**, 996-1003.
4   F. Fayon, I. J. King, R. K. Harris, R. K. B. Gover, J. S. O. Evans, and D. Massiot, *Chem. Mater.*, 2003, **15**, 2234-2239.
5   M. Feike, R. Graf, I. Schnell, C. Jager, and H. W. Spiess, *Journal of the American Chemical Society*, 1996, **118**, 9631-9634.
6   C. T. G. Knight, G. L. Turner, R. J. Kirkpatrick, and E. Oldfield, *J. Am Chem. Soc.*, 1986, **108**, 7426-7427.
7   L. H. Merwin and A. Sebald, *Solid State Nucl. Magn. Reson.*, 1992, **1**, 45.
8   K. J. D. Mackenzie and M. E. Smith, 'Multinuclear solid state NMR of inorganic materials', ed. R. W. Chan, Pergamon, 2002.
9   V. Lemaîrte, M. R. R. de Planque, A. P. Howes, M. E. Smith, R. Dupree, and A. Watts, *J. Am Chem. Soc.*, 2004, **126**, 15320-15321.
10   C. Hudalla, H. Eckert, and R. Dupree, *J. Phys. Chem.*, 1996, **100**, 15986-15991.
11   E. R. Andrew and D. P. Tunstall, *Proc. Phys. Soc.*, 1961, **78**, 1-11.
12   K. Ikushima, S. Tsutsui, Y. Haga, H. Yasuoka, R. E. Walstedt, N. M. Masaki, A. Nakamura, S. Nasu, and Y. Onuki, *Phys. Rev. B.*, 2001, **63**, Art.No. 104404.
13   W. P. Aue, E. Bartholdi, and R. R. Ernest, *J. Chem. Phys.*, 1976, **64**, 2229.
14   A. Bax, R. Freeman, and S. P. Kempsall, *J. Am. Chem. Soc.*, 1980, **102**, 4849-4851.
15   I. J. King, 'Combined Use of Powder Diffraction and Magic-Angle Spinning NMR to Structural Chemistry', Ph.D. Thesis, University of Durham, 2003.
16   N. M. Szeverenyi, M. J. Sullivan, and G. E. Maciel, *1982*, 1982, **47**, 462.
17   R. Nagel, T. W. Groß, H. Günther, and H. D. Lutz, *J. Sol. State. Chem.*, 2002, **165**, 303-311.
18   *Spinsight Spectrometer Control Software*, 1996, Varian/Chemagnetics.
19   *VNMR Spectrometer Control Software*, 1998, **v6.1B**, Varian.
20   R. K. Harris, 'Nuclear Magnetic Resonance Spectroscopy', Longman, 1983.
21   A. Bielecki and D. P. Burum, *J. Magn. Reson.*, 1995, **116**, 215-220.
22   *Matlab (student edition)*, 1997, **Version 5**, The Math Works.
23   A. A. Coelho, *General Profile and Structure Analysis Software for Powder Diffraction Data*, 2000, **TOPAS v2.0**, Bruker AXS, Karlsruhe
24   *Diffrac + Diffractometer Control Software*, 2000, Bruker AXS Ltd.

Chapter 3 - Isotopic enrichment and qualitative NMR studies of ZrM$_2$O$_8$ phases (M = W, Mo)

The AM$_2$O$_8$ family of materials are of great interest due to their properties of negative thermal expansion (NTE)[1] and dynamic oxygen disorder,[2, 3] as previously discussed in Chapter 1. Solid-state NMR is a technique which enables the local environments of nuclei to be probed directly. It was therefore hoped that the study of these materials by this technique would provide information which would be complementary to that obtained from diffraction based techniques, which only give information about the long range structure. A local picture of structure and dynamics, as may be derived from NMR results, is particularly important for studying the oxygen dynamics in these materials.

This chapter describes attempts to determine appropriate techniques for the preparation of pure, highly ^{17}O enriched samples of ZrW$_2$O$_8$ (cubic phase) and ZrMo$_2$O$_8$ (LT, cubic and trigonal phases), and qualitative solid-state NMR experiments (^{17}O and ^{183}W) on these phases. The ^{17}O NMR results for ZrW$_2$O$_8$ are interpreted to give mechanistic information about the nature of oxygen exchange, which could not be obtained by diffraction methods alone.

3.1 Cubic ZrW$_2$O$_8$

As discussed in Chapter 1, zirconium tungstate, ZrW$_2$O$_8$, exists in a variety of phases. The research presented in this chapter focuses on the cubic phase, which exhibits isotropic negative thermal expansion over an extremely wide temperature range (2 - 1050 K), including the phase transition from the *a* to the *ß* form at 448 K (175 ºC).[4, 5]

The aims of the work described in Section 3.1 of this chapter were to obtain ^{183}W NMR data, to devise a method for the preparation of highly ^{17}O-enriched pure samples of cubic ZrW$_2$O$_8$, and then to use ^{17}O NMR to investigate the oxygen mobility. A variety of NMR experiments is described including simple 1D spectra and 2D experiments to qualitatively determine the exchange mechanism.

3.1.1 ZrW$_2$O$_8$ structure

The structure of *a*-ZrW$_2$O$_8$ was previously described in Chapter 1, and is shown in Figure 3-1(a). It contains a network of corner-sharing ZrO$_6$ octahedra and WO$_4$ tetrahedra with a W$_2$O$_8$$^{4-}$ unit, made up of a pair of WO$_4$$^{2-}$ tetrahedra, along the main 3-fold axis of the cubic unit cell. There are four inequivalent oxygen sites: O1 and O2, which bridge between Zr and W, are on *12c* Wyckoff sites, the 'terminal' O3 and O4 are on *4a* sites. O4 is formally one-coordinate, with the next nearest tungsten atom being 3.6 Å away, whereas there is a weak interaction between O3 and W1 (*d* = 2.4 Å). There is only one zirconium site (a *4a* site).

The phase transition, in which the space group symmetry changes from *P2$_1$3* to *Pa*3, is understood to be related to oxygen dynamics in the material.[5] In the high temperature *ß* phase,

high temperature diffraction (neutron and X-ray) shows that the direction in which WO$_4$ tetrahedra point along the 3-fold axis becomes dynamically disordered (Figure 3-1 (b)).[5] The *a* to *ß* phase transition therefore involves a formal inversion of the W$_2$O$_8$ groups. Whilst the phase transition has been studied extensively,[4, 6-11] the specific mechanism of oxygen mobility and tungstate group inversion was unknown prior to this work.
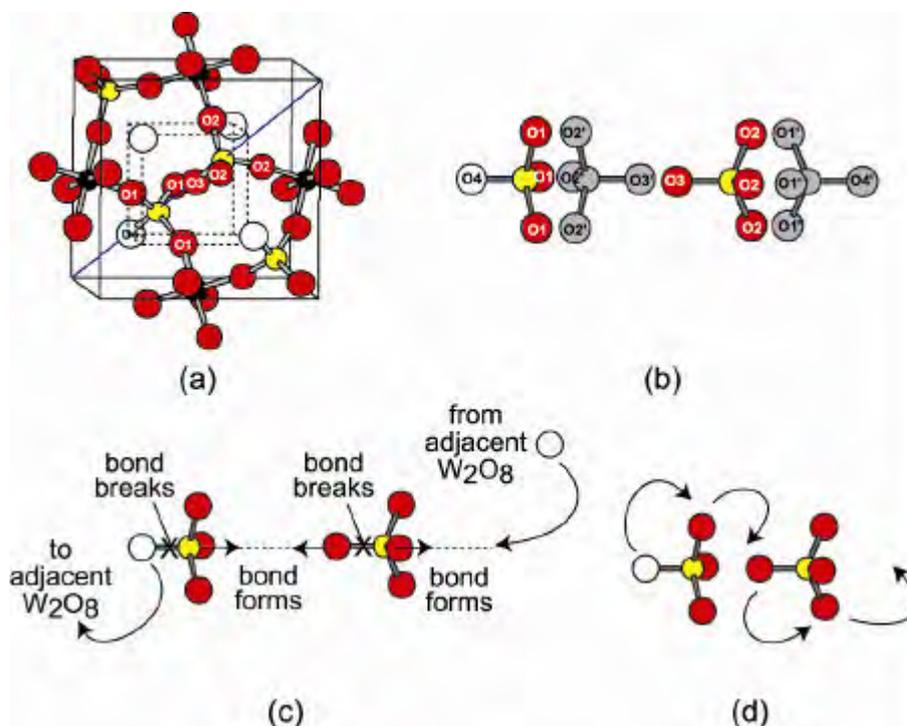

Figure 3-1 (a) Structure of cubic ZrW$_2$O$_8$, showing two-coordinate oxygen sites in red and one-coordinate sites in white. (b) Ball and stick representation of the W$_2$O$_8$ group in the high temperature *ß* form. For clarity tetrahedra have been displaced slightly so that atoms do not overlap. The ratio of the numbers of O1:O2:O3:O4 sites is 3:3:1:1. Coloured atomic sites are fully occupied in the ordered *a* phase; all sites are 50 % occupied in the disordered *ß* phase. (c), (d) Schematic diagrams showing two possible mechanisms of oxygen exchange.

Two feasible mechanisms can be proposed for this inversion, as illustrated in Figure 3-1 c-d. In one extreme view, suggested by Evans *et al.,*[4] one can envisage a "coupled S$_N$2" mechanism in which the formation of a W1-O3 bond leads to cleavage of the W1-O4 bond and a local inversion of tetrahedra (Figure 3-1 c). This process could occur in a cooperative way throughout the crystal or proceed *via* the local process of $4WO_4^{2-} \rightarrow W_2O_9^{6-} + W_2O_7^{2-}$. Alternatively, a mechanism may be proposed in which adjacent tetrahedra could rotate as a whole in a "ratchet" motion, causing mutual exchange between all oxygen sites (Figure 3-1 d). This ratcheting rotation seems plausible, and a similar rotation has been observed by ^{17}O NMR lineshape analysis for PO$_4^{3-}$ ions in low temperature Na$_3$PO$_4$.[12]

It has not been possible to distinguish between the above processes by diffraction methods, which only 'see' average atomic positions. [183]W NMR is potentially useful, since the tungsten environments change during the disordering process. NMR of the zirconium nuclei (^{91}Zr, I=$^5/_2$,

natural abundance 11.2 %) is extremely difficult, due to very broad quadrupolar lineshapes. An additional complication is that the standard rotors used for MAS NMR are made of ZrO$_2$, which would therefore dominate the ^{91}Zr NMR signal. ^{91}Zr NMR was therefore not attempted. ^{17}O NMR is potentially an ideal characterisation technique for studying such motion since it directly probes the local environment of oxygen nuclei.[13-15] However it has the drawback that the natural isotopic abundance of ^{17}O ($I = ^5/_2$), the only spin-active oxygen isotope, is just 0.037 %. Sensitivity is therefore often a problem, and isotopically enriched samples are required for NMR experiments to be performed in a practical length of time. The bulk of this chapter is concerned with ^{17}O NMR.

3.1.2 ^{183}W NMR experiments

^{183}W (spin $I = ½$) is the only NMR-active isotope of tungsten, and has a natural abundance of 14.3 %. Although there are no quadrupolar interactions, and isotopic enrichment is not essential, there is a major problem with sensitivity for ^{183}W NMR – the receptivity of the ^{183}W nucleus is only 1.07 x 10^{-5} relative to ^{1}H = 1. The low sensitivity means that acquiring spectra with good signal-to-noise in a practical length of time is a major problem. Extremely long T_1 times are also a characteristic of ^{183}W in the solid-state, which compounds the sensitivity problem as long delays must be left between repetitions of a NMR pulse sequence.

^{183}W MAS NMR experiments on ZrW$_2$O$_8$ were carried out using a Varian InfinityPlus 500 spectrometer operating at a ^{183}W Larmor frequency of 20.82 MHz, with a Chemagnetics 7.5 mm MAS probe, and an external low frequency tuning box. All spectra were referenced to a saturated aqueous solution of Na$_2$WO$_4$ at 0 ppm. The 90 º pulse duration was calibrated as 11 μs on a solution state sample of Na$_2$WO$_4$. The T_1 relaxation time of the ZrW$_2$O$_8$ sample (JSOE421/mrh077, synthesised by standard solid state methods[16]) was estimated as approximately 500 s by fitting the results of a saturation recovery experiment (with delay times of 15, 30, 60, 120, 240 s). Due to time constraints and the lack of sensitivity it was impossible to determine T_1 more accurately. In the cases of compounds with very long T_1 times, it is often preferable to carry out experiments with a tip angle smaller than 90 º, so that shorter repetition times may be used. The optimum tip angle (Ernst angle, Chapter 2) for the ZrW$_2$O$_8$ data acquisition was calculated as being 29.6 ° for a pulse delay of 70 s, enabling this short pulse delay to be used, despite a T_1 of 500 s.

Sensitivity proved to be a major problem – the spectrum shown in Figure 3-2 required a 65 hour experiment. Several NMR spectra were recorded at room temperature, and attempts were made to obtain spectra at higher temperatures (200-240 °C), but this proved impossible, presumably due to the signals being broadened by motional effects and thus having even lower signal to noise ratios.
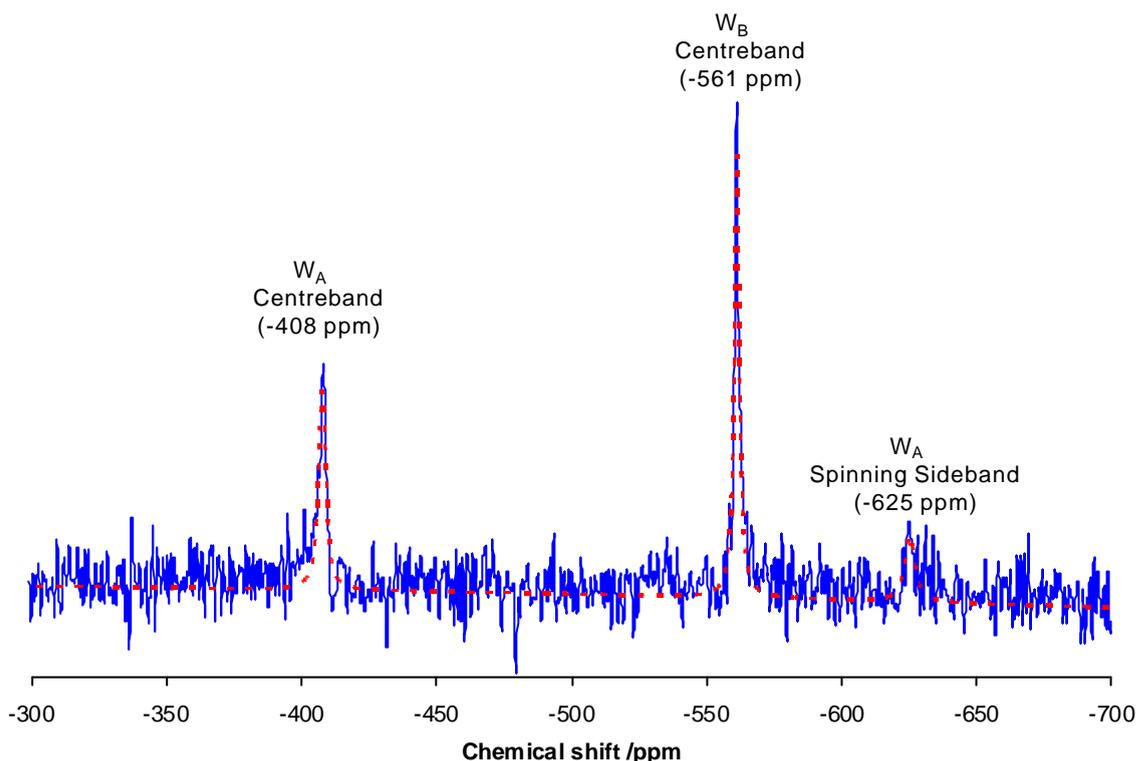
Figure 3-2 ^{183}W spectrum of ZrW$_2$O$_8$ (JSOE421/mrh077) at 25 °C. An excitation pulse duration of 3.6 µs (29.6 °) and pulse delay of 70 s were used. MAS rate was 4.5 kHz. 3360 transients were recorded in a total time of 65.3 hours. The FID was transformed with a 65536 point Fourier transform. A fit to 3 pseudo-Voigt peaks, with parameters given in Table 3-1, is shown by the red dotted line.

The room temperature ^{183}W spectrum (Figure 3-2) shows two centreband peaks at -408 ppm and -561 ppm; the frequency difference between the two sites is 3.2 kHz. One spectrum, recorded with a spinning speed of 4.5 kHz did show a third peak at -625 ppm, presumably a spinning sideband for W$_A$, (frequency difference to -408 ppm peak was 4.5 kHz, equal to MAS rate) although the signal to noise ratio was low and no spinning sidebands were seen in any in other spectra. All three resolved peaks were deconvoluted with a pseudo-Voigt peak shape, as indicated by the dotted red line on the spectrum. Details of the fitted peaks are given in Table 3-1.

	Site W$_A$ Centreband	Site W$_B$ Centreband	Site W$_A$ Spinning Sideband
Chemical Shift /ppm	-407.58 ± 0.07	-561.16 ± 0.03	-625.1 ± 0.2
Area / arbitrary units	12200 ± 500	20200 ± 500	6300 ± 500
FWHM /Hz	66 ± 5	43 ± 3	89 ± 16

Table 3-1 Properties of the three peaks in the ^{183}W NMR spectrum of ZrW$_2$O$_8$ (JSOE421/mrh077) at 25 °C as deconvoluted with pseudo-Voigt functions.

The tungsten NMR spectrum of ZrW_2O_8 would be expected to show two distinct peaks for the low temperature phase. This is indeed the case, and the NMR is therefore consistent with the known structure of the material. The higher frequency peak (W_A) is noticeably broader (and so its height is less) than the other peak. The presence of a spinning sideband for W_A and none for W_B suggests a larger CSA for W_A. The geometry of the W1 site is more distorted than that of W2, and so it is likely that the W_A site corresponds to W1 in the crystal structure. The difference in total peak area (A_n) for the W_A (including sideband) and W_B sites is A_B-A_A=1600 ± 900 (8± 4 % of A_B). The two sites would be expected to give equal total intensities as there are equal numbers of W1 and W2 sites in the structure. It should be noted that, in statistical terms, the discrepancy observed is not significant, and it is also possible that there are additional spinning sidebands which could not be distinguished from the noise. A spectrum with higher signal to noise could confirm this theory, although the time required to record such a spectrum would be prohibitively long.

If the current understanding of the dynamics in ZrW_2O_8 is correct then an exchange of tungsten environments occurs due to movement of oxygen atoms: an atom at a W1 site is transformed into a W2 by the oxygen movement, and *vice versa*. It would therefore be expected that the tungsten exchange would be closely correlated to the oxygen exchange. In the high temperature phase, one would expect to see a coalescence of the signals from the two tungsten sites, analogous to the behaviour of the oxygen sites as seen by ^{17}O NMR, which is described later (Section 3.1.8). It proved impossible to obtain a [183]W NMR spectrum of the high temperature phase. It is likely that this is due to broadening of the NMR signals, which would be consistent with exchange of the sites. It is unfortunate that the signal to noise of the spectra was not sufficiently high to allow a comprehensive variable temperature study as was performed for ^{17}O NMR. However, this is a fundamental limitation of [183]W NMR, and this work was not pursued further.

3.1.3 Preparation of [17]O-labelled *a*-ZrW_2O_8

Preliminary [17]O studies have been carried out on ZrW_2O_8 by King[17] using a sample prepared by Allen[18] *via* the individually labelled oxides $Zr*O_2$ and $W*O_3$. Unfortunately this sample was impure due to several significant problems with this synthetic strategy, both with the formation of the labelled starting materials and with their combination to produce ZrW_2O_8. The first problem occurs when forming $W*O_3$ under anaerobic conditions, which invariably gives partially reduced WO_{3-x} materials. These could not be used to produce ZrW_2O_8, and so had to be oxidised to WO_3 by briefly heating in air, potentially allowing exchange with atmospheric oxygen. A major problem with the synthesis of ZrW_2O_8 is that rapid quenching of the product is required due to its metastability; slow cooling of the product results in decomposition back to the binary oxide starting materials. Synthesis in a sealed tube (required to prevent exchange with atmospheric oxygen) does not allow rapid cooling, and so impurity phases tended to be present. Powder

X-ray diffraction and the ^{17}O NMR spectra showed that the sample studied was contaminated by a ZrO$_2$ impurity.

The technique used here differs fundamentally to that described above in that unlabelled ZrW$_2$O$_8$ was first synthesised in an open crucible, thus enabling rapid quenching and giving a pure product. It was hoped that a highly enriched sample of ZrW$_2$O$_8$ could be produced by proceeding *via* the recently identified ZrW$_2$O$_8$.xH$_2$O phase.[19] The ZrW$_2$O$_8$ was hydrated with [17]O-enriched water and subsequently dehydrated. It was hoped that scrambling of the oxygen atoms occurs during the hydration due to the high mobility of the oxygen atoms at the hydration temperature, so that isotopically enriched oxygen would remain in the dehydrated product.

## 3.1.4 Synthetic method & determination of optimum conditions

The technique involved three stages: preparation of ZrW$_2$O$_8$ by standard solid state methods;[16] hydration under hydrothermal conditions with [17]O enriched water to produce ZrW$_2$O$_8$.xH$_2$O; dehydration under vacuum to produce enriched ZrW$_2$O$_8$. A number of test experiments are outlined here, and the full details of the actual synthesis is given in Section 3.1.5.

In order to determine suitable conditions for hydration and dehydration, a number of practice runs were carried out with un-enriched deionised water. In each experiment, ZrW$_2$O$_8$ was prepared by heating freshly-ground stoichiometric amounts of the oxides ZrO$_2$ and WO$_3$ in a platinum crucible; X-ray diffraction was used to confirm the purity of the samples. The hydration reaction was performed with a freshly ground sample of ZrW$_2$O$_8$ and a ~33 fold molar excess amount of water in a Pyrex glass ampoule (with approximate volume 1 cm^3), which was flame-sealed under dynamic vacuum and placed in a PTFE lined steel autoclave to minimise risks of explosion. Water was added to the PTFE liner to surround the ampoule and equalise the pressure as it was heated to temperatures of around 200 °C in a furnace. After the autoclave had cooled to room temperature, the sample was removed and characterised by thermo-gravimetric analysis (TGA) and powder X-ray diffraction.

Rietveld refinement of the powder X-ray diffraction data for hydrated ZrW$_2$O$_8$ (mrh016) was carried out in Topas 3 (local version 47), with a total of 18 independent parameters refined. The following experimental parameters were refined: the sample height, an axial divergence parameter, twelve coefficients of a Chebychev polynomial to model the background function, a crystallite size for a simple peak shape description and a histogram scale factor. The data were refined against a structural model consisting of the *P2$_1$3* structure of ZrW$_2$O$_8$ with an additional oxygen site for the water oxygen atom situated at the 0.77, 0.77, 0.77 position.[19] Only two structural parameter parameters were refined for the *P2$_1$3* structure: a cubic cell parameter and one isotropic temperature factor (*B$_{iso}$*) for all atoms. The Rietveld fit is shown in Figure 3-3.
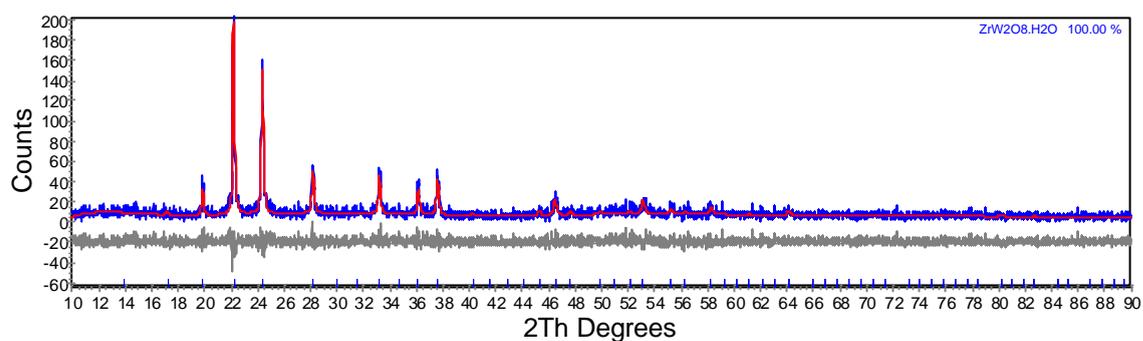
(a)
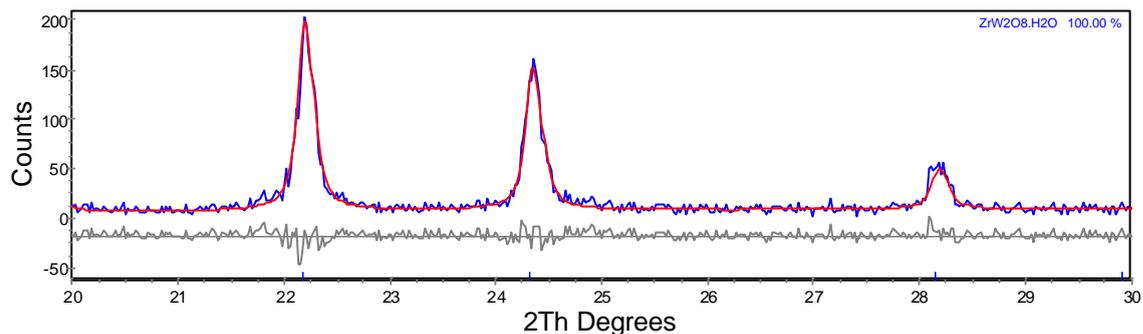
(b)

Figure 3-3 Rietveld refinement plot for (d5_04661) mrh016 ZrW$_2$O$_8$.xH$_2$O: observed powder pattern (blue); calculated diffraction pattern (red); difference plot (grey). Tick marks indicate the positions of Bragg reflections. The whole powder pattern in shown in (a); a zoomed region is shown in (b). 32 independent parameters were refined using data in the 2*?* range 10 – 90 °.

The occupancy of the oxygen sites could not be successfully refined using the powder XRD data, due to the low atomic number, and hence relative scattering factor, of oxygen in relation to tungsten and zirconium. However, the cubic unit cell parameter of the hydrated form, ZrW$_2$O$_8$.xH$_2$O, gives an indication of the degree of hydration. The cell parameters obtained for all test samples were in the range 8.93-9.00 Å (Table 3-2) which, by comparison with the results of Duan *et al*. [19] (Figure 3-4), corresponds to a value of *x* of 0.4 -0.7.

Thermo-gravimetric analysis (TGA) was performed using a Perkin Elmer Pyris 1 instrument with a platinum sample crucible, to provide an independent measure of hydration. TGA is a method of determining mass loss from a sample as a function of temperature. It may be used to observe phase transitions, and the loss of solvents, most commonly water. In each case the sample was heated from room temperature to 300 °C under a flow of nitrogen gas The value of *x* in ZrW$_2$O$_8$.xH$_2$O was calculated from the % mass remaining after heating, assuming that only one phase was present, as is indicated by the XRD data.
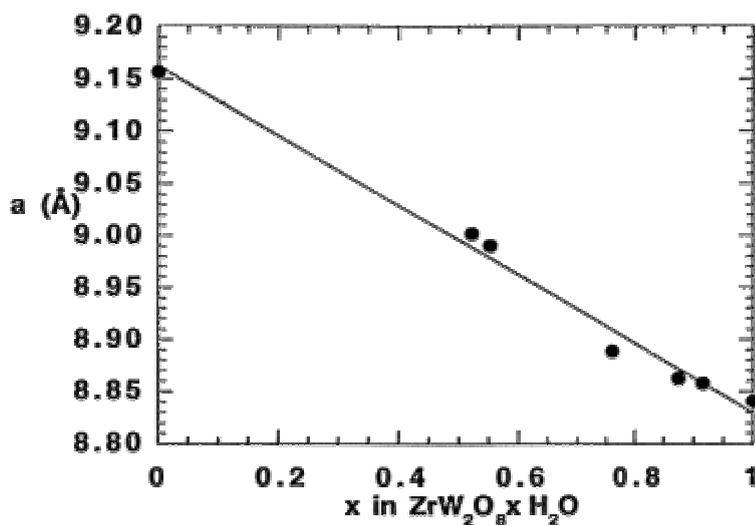
Figure 3-4 The variation of the cell length of ZrW$_2$O$_8$ (at 25 °C) on hydration, figure taken from reference 19.

| Sample ID	Heating conditions		Cell parameter (Å)	Mass remaining after dehydration by TGA	*x* from TGA
	Temperature (ºC)	Time (hours)			
mrh007	230	14	8.984(1)	98.72%	0.42
mrh009	230	48	8.932(3)	98.67%	0.44
mrh015	240	48	8.932(2)	98.66%	0.44
mrh016	240	184	8.954(2)	98.53%	0.49
mrh017	240	100	8.970(1)	96.20%	1.29
mrh019	180	24	9.031(2)	98.71%	0.42

Table 3-2 Results of test experiments on hydration of ZrW$_2$O$_8$: cell parameters and TGA results.

The high value of *x* from TGA for sample mrh017 is presumably because the sample contained an amount of surface water, rather than a genuinely high degree of hydration as this result does not fit in with the other results obtained. The values of *x* derived form the TGA results, with the exception of this one anomalous result, fall in the range 0.42 – 0.49, which is consistent with the measured cell parameters. Intriguingly, TGA data suggest that a degree of hydration of *x* > 0.5 was never achieved, whereas Duan *et al.* did not produce any hydrate with *x* < 0.5. Achieving the highest possible degree of hydration is not critical to the enrichment strategy however, and this was not investigated further. In all test experiments, both XRD and TGA results show that hydration (and, it is hoped, isotopic exchange between the water and ZrW$_2$O$_8$) occurs.

Test dehydration experiments were also performed, this involved first drying the product under dynamic vacuum in a Schlenk tube and then heating it in an alumina boat in an evacuated tube furnace to temperatures of around 200 °C. Powder X-ray diffraction data were used to confirm that dehydration had occurred. It was found by Rietveld refinement that heating at 240 °C for 2 hours gave a fully dehydrated sample.
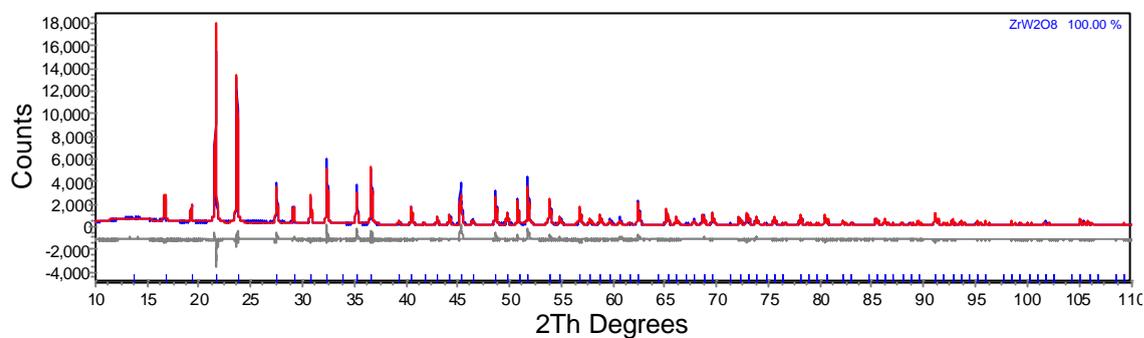
(a)
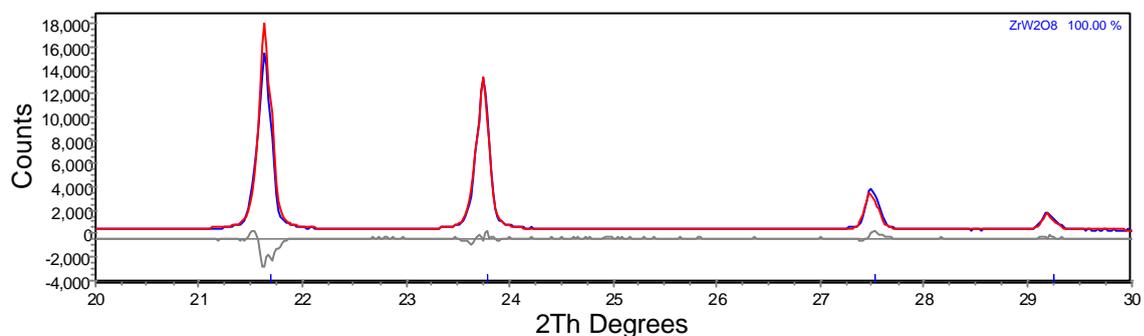
(b)

Figure 3-5 Rietveld refinement of dehydrated ZrW₂O₈ (mrh024): observed powder pattern (d5_04784) (blue); calculated diffraction pattern (red); difference plot (grey). The whole powder pattern in shown in (a); a zoomed region (20 – 30 °) is shown in (b). Refined with 21 independent parameters, using data in the 2? range 10 – 110 °.

A sample of dehydrated ZrW_2O_8 (mrh024) was mounted onto a glass slide using Vaseline. Powder X-ray diffraction data were collected on a Siemens d5000 diffractometer in the 2? range 10 - 110 ° with a measurement time of 12.5 hours. Rietveld refinement of dehydrated ZrW_2O_8 (mrh024) was carried out in Topas 3 (local version 47), with a total of 19 independent parameters refined. The following experimental parameters were refined: the sample height, an axial divergence parameter, twelve coefficients of a Chebychev polynomial to model the background function, a crystallite size for a simple peak shape description and a histogram scale factor. Three structural parameter parameters were refined for the $P2_13$ ZrW_2O_8 structure: a cubic cell parameter, one isotropic temperature factor (B_{iso}) for all atoms and a fractional occupancy parameter to allow for disorder of the directions of $W_2O_8^{4-}$ groups.

The Rietveld fit shown in Figure 3-5 shows that the dehydration method used produced pure ZrW_2O_8. Thus having determined suitable reaction conditions for both hydration and

dehydration, the procedure was carried out using isotopically enriched water - the synthetic procedure is given in detail in Section 3.1.5.

3.1.5 Details for preparation of ^{17}O enriched samples

Unlabelled ZrW$_2$O$_8$ (mrh012) was first prepared by the following method. Stoichiometric amounts of ZrO$_2$, 1.25966 g, (Aldrich, 99 %) and WO$_3$, 4.74034 g, (BDH) were ground in an agate pestle and mortar, the powder was poured into a platinum crucible and placed in a furnace (JSOE3), heated at a rate of 10 2 K·min^{-1} to 1175 ºC, and held at this temperature for 20 hours. The crucible was removed at 1175 °C and allowed to cool in air (quench to room temperature). A three-phase Rietveld refinement with 26 independent parameters refined gave phase fractions as 96 % ZrW$_2$O$_8$, 3 % WO$_3$ and 1 % ZrO$_2$. The product was then re-ground and re-heated in the same manner as the first heating for a further 22 hours, followed by quenching as before. Powder X-ray diffraction confirmed that pure ZrW$_2$O$_8$ (mrh012) had been formed. Rietveld refinement gave phase fractions as 99 % ZrW$_2$O$_8$ and 1 % ZrO$_2$.

0.2017 g of ZrW$_2$O$_8$ (mrh012) was ground using an agate pestle and mortar and transferred to an open-ended Pyrex glass ampoule. A gas-tight syringe was then used to add an excess (0.2107 g) of isotopically enriched water (Isotec, 40.2 % ^{17}O, 7.4 % ^{18}O). The ampoule was then frozen immediately by immersion in liquid nitrogen, before being evacuated and sealed. The sealed ampoule was placed in a 23 ml Anton Parr steel autoclave with PTFE liner. Tap water was poured around the ampoule so that the total volume occupied by ampoule and water was 66 % of the total internal volume, this procedure was intended to help balance the pressure inside and outside the ampoule once it was heated.

The steel autoclave was assembled and placed in a furnace and heated to 200 ºC at a rate of 10 K·min^{-1} and then to 240 ºC at a rate of 2K·min^{-1}, and held at 240 ºC for 21 days. The autoclave was then removed from the furnace and allowed to cool to room temperature. The ampoule was opened by scoring and thermal shocking, water was removed with a pipette and the open ampoule was placed in a Schlenk tube which was then evacuated, and left under dynamic vacuum for 2 hours in order to thoroughly dry the product.

The resulting grey powder (mrh026) was then transferred to an alumina boat, and placed in a tube furnace for dehydration under vacuum. The tube furnace was immediately evacuated and then heated to 225 ºC at a rate of 10 K·min^{-1} and then to 240 ºC at a rate of 1.5 2 K·min^{-1}, and held at 240 ºC for 2 hours. Although it is difficult to determine experimentally the level of isotopic enrichment, a theoretical maximum ^{17}O abundance may be estimated. It was assumed that the water used for hydration, which had been stored in a vial sealed with parafilm, had not lost any ^{17}O by exchange with atmospheric moisture and contained the manufacturer's stated ^{17}O abundance of 40.2 % (giving 4.7×10^{-3} moles ^{17}O), and that the ZrW$_2$O$_8$ had the natural abundance of 0.038 % ^{17}O (1.0×10^{-6} moles ^{17}O). Hence, on the assumption of a statistical

scrambling of oxygen atoms between starting materials (total amount of oxygen from ZrW$_2$O$_8$ and H$_2$O is 1.4 × 10^{-3} moles), an abundance of ~30 % is obtained, which may be considered as an upper limit for the true level of enrichment.

A second sample of enriched ZrW$_2$O$_8$ (mrh146) was prepared so that the effect of a lower concentration of ^{17}O on the observed NMR could be observed. This was prepared by an identical method to that described above, and using the mrh012 ZrW$_2$O$_8$ sample (0.2768 g), but with 0.3048 g of a different source of isotopically enriched water (Euriso-top, 28.0 % ^{17}O, 29.8 % ^{18}O). The estimated maximum ^{17}O abundance for this sample is around 20 %.

3.1.6 ^{17}O NMR studies of ZrW$_2$O$_8$

A range of ^{17}O NMR experiments on a sample of ZrW$_2$O$_8$ (mrh026, unless otherwise stated) was carried out using a Varian InfinityPlus 500 spectrometer operating at a ^{17}O Larmor frequency of 67.78 MHz, with a Chemagnetics 4.0 mm MAS probe. All spectra were referenced to un-enriched H$_2$O at 0ppm – since anisotropic effects are averaged by motion in a liquid sample, the ^{17}O peak for water is sharp and intense, and no enrichment is required.

The most significant initial conclusion from preliminary NMR studies was that the signal to noise that could be obtained was very good. The signal to noise (S/N) ratio was 130 for the highest intensity peak in a spectrum with 8 acquisitions, acquired in just seven minutes. This demonstrates that the enrichment method was indeed successful, and means that NMR experiments are practical in a reasonable amount of time.

The spectra (as shown in Figure 3-6) showed well resolved peaks, indicating that the quadrupolar coupling is relatively small – in many compounds quadrupolar couplings are sufficiently large (several MHz) to prevent efficient excitation by RF pulses leading to sufficient broadening that it is impossible to resolve individual peaks. If the environment at the nucleus is highly symmetrical, the quadrupolar coupling (determined by the electric field gradient at the nucleus) is small. In this case, soft pulses may be used to excite only the central transition ($m_I = + ½ ? \; m_I = - ½$) and the NMR spectra may be treated in the same way as for a spin ½ nucleus effect. In ZrW$_2$O$_8$, the symmetry of the oxygen environments lies between these two extreme cases. Although individual peaks can be resolved, there is also a significant manifold of spinning side bands, as shown in the inset of Figure 3-6. This is because the satellite transitions, as well as the central transition, are excited to a significant extent by the RF pulses. Spectra were initially obtained at a variety of spinning speeds from 10-15 kHz, so that these spinning sidebands could be distinguished from centre-band peaks.
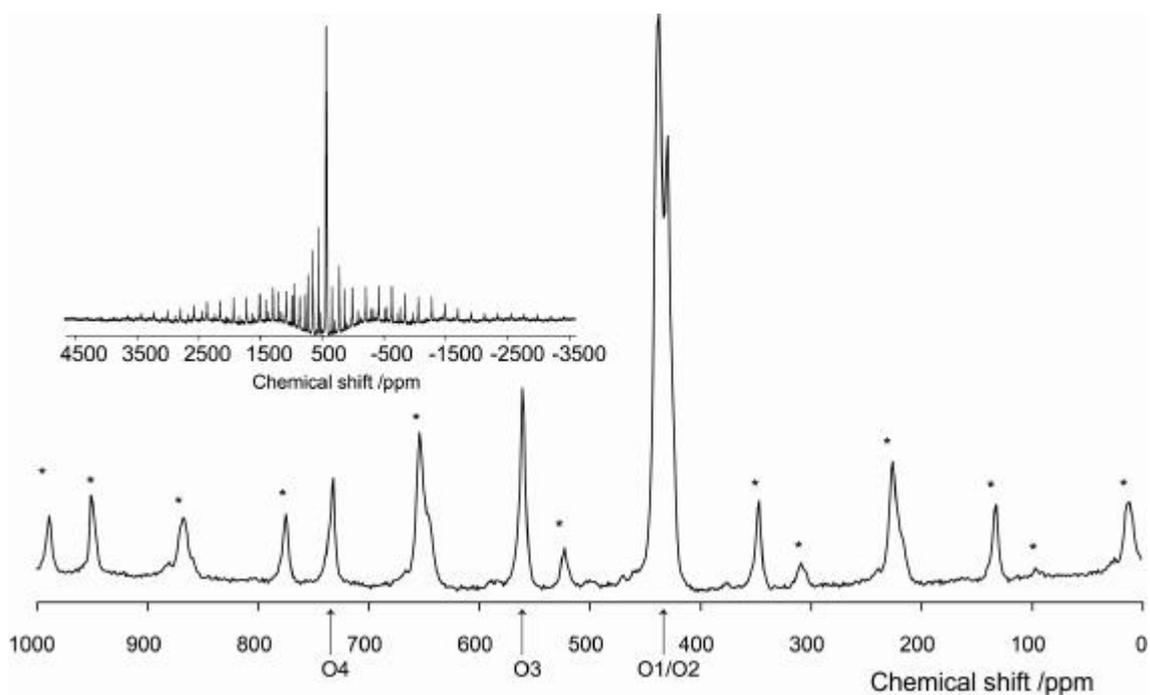
Figure 3-6 ^{17}**O NMR spectrum of ZrW$_2$O$_8$. MAS rate 14.5 kHz, temperature 40 ºC, asterisks denote spinning sidebands. The inset shows the full spectrum, illustrating the extent of the full spinning sideband manifold.**

The four inequivalent sites observed have previously been assigned to sites in ZrW$_2$O$_8$ using shielding arguments.[17] As the O4 site is strictly one-coordinate, one would expect it to be the least shielded oxygen site in the structure, and so its NMR signal would be at the highest frequency; it is thus assigned as the peak at 734 ppm. The peak at 561 ppm is assigned as the O3 site, which is two-coordinate but with one very long bond (W1-O3) and so would be expected to have a chemical shift in between that of O4 and the fully two-coordinate Zr-O-W bridging oxygen atoms O1 and O2. This assignment is consistent with that for the similar oxygen environments in trigonal and LT phases of ZrMo$_2$O$_8$ (see Section 3.2.8). The O3 and O4 peaks are of approximately similar intensities, with the overlapping O1 and O2 peaks (centred at 434 ppm) having a total of approximately 6 times the area. This is consistent with the 3:3:1:1 ratio of O1:O2:O3:O4 sites in the structure. The purity of the sample is confirmed by the absence of additional peaks; for example the ZrO$_2$ peaks at 401 ppm and 323 ppm observed by King[17] are not present.

It is also worth mentioning that the peak intensity ratios (Figure 3-6) are similar to those observed for Allen's sample[17] which was prepared from enriched precursor oxides, where equal enrichment of all sites would be expected. A simple hydration / dehydration mechanism without further site exchange might be expected to preferentially enrich the O4 site. The fact that all sites appear to be equally labelled is indirect support for full exchange between all oxygen sites at the hydration temperature of 240 ºC, which is consistent with observations from high temperature measurements described later in this chapter.

3.1.7 Estimation of quadrupolar coupling constant

The [17]O quadrupole coupling constants (C_Q) in ZrW$_2$O$_8$ are moderately large, as can be seen from the spinning sideband patterns in the spectra. The width of the sideband manifold is dependent mainly on the quadrupole coupling, and so a fitting procedure may be used to determine C_Q.

A high signal to noise spectrum of ZrW$_2$O$_8$ recorded at 57 °C was fitted with the STARS program.[20] The sideband pattern of the O3 site was used since this is well resolved and does not suffer from the overlap which affects the more intense peaks from O1 and O2. The overall width and pattern of intensities in the manifold of sideband peaks fits well to a spectrum calculated using a single site modelled with C_Q of 0.5 MHz, asymmetry of 0.5, and 1000 ppm chemical shift anisotropy (CSA) with asymmetry of 0.9. The comparison of the experimental and calculated sideband patterns is shown in Figure 3-7.
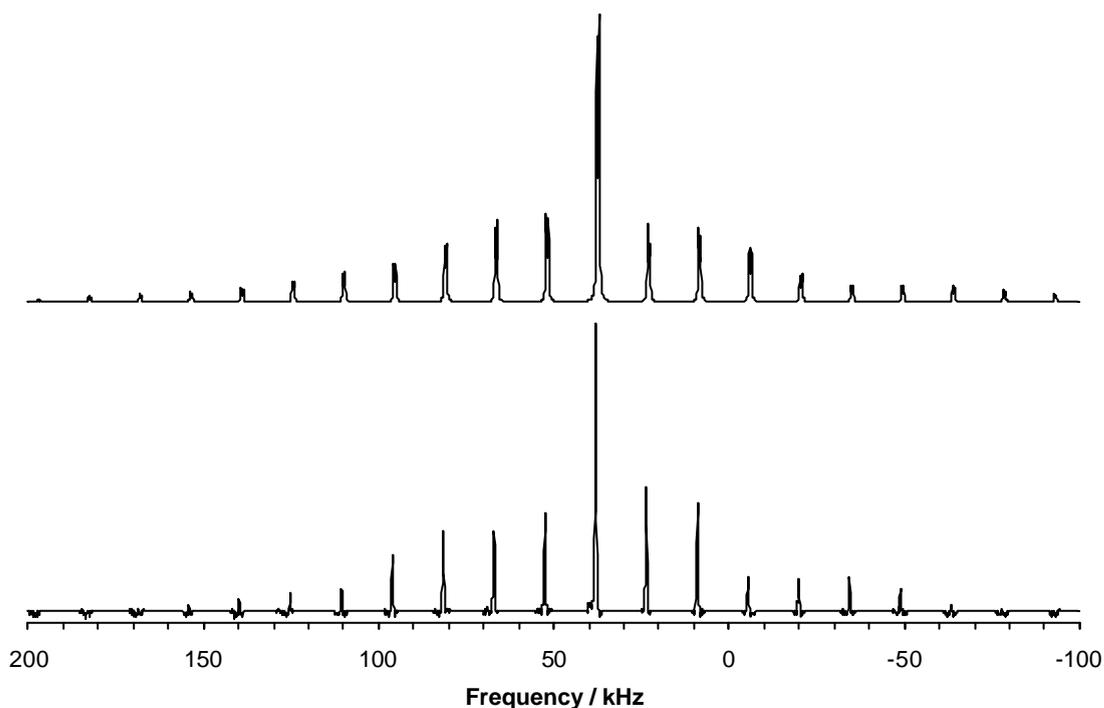

Figure 3-7 Fitting of the sideband pattern to determine C_Q. Experimental spectrum (bottom) is taken from a ^{17}O magic-angle spinning NMR spectrum of ZrW$_2$O$_8$ at 57 °C, MAS rate of 14.5 kHz. An excitation pulse duration of 1.17 µs and a pulse delay of 90 s were used and 256 transients were recorded in a total time of 6.4 hours. The spectrum was processed with a 16384 point Fourier Transform and a baseline correction applied. For clarity, only the peaks for the O3 site (centre band and spinning sidebands) are shown. The calculated spectrum (top) was determined using the STARS software[20], using parameters of 67.78 MHz Larmor frequency, 14.5 kHz MAS speed, 300 Hz Lorentzian line broadening, 560 ppm isotropic shift.

The intensity of the individual sideband peaks will be affected by a number of factors, including the oxygen exchange process. The aim of this calculation was to determine an estimate of the quadrupolar coupling constant only, and detailed modelling of the effect of motion on the

spectra was not undertaken. Although the peak intensities are not fitted exactly, the overall width of the pattern is reproduced reasonably well. This provides some confidence that the C$_Q$ estimate is accurate since the width of the manifold is highly dependent on C_Q. It was not possible to perform a similar fitting for the other oxygen sites. However, the widths of both individual peaks and spinning sideband manifolds are similar for all oxygen sites, indicating that C_Q is approximately similar, and the value derived here may be taken as an order of magnitude estimate of C_Q for all sites.

3.1.8 Variable temperature ^{17}O NMR

A variable temperature study was performed, with spectra acquired at a range of temperatures from room temperature to 229 °C, (the maximum operating temperature of the NMR probe). The spectra are shown in Figure 3-8.
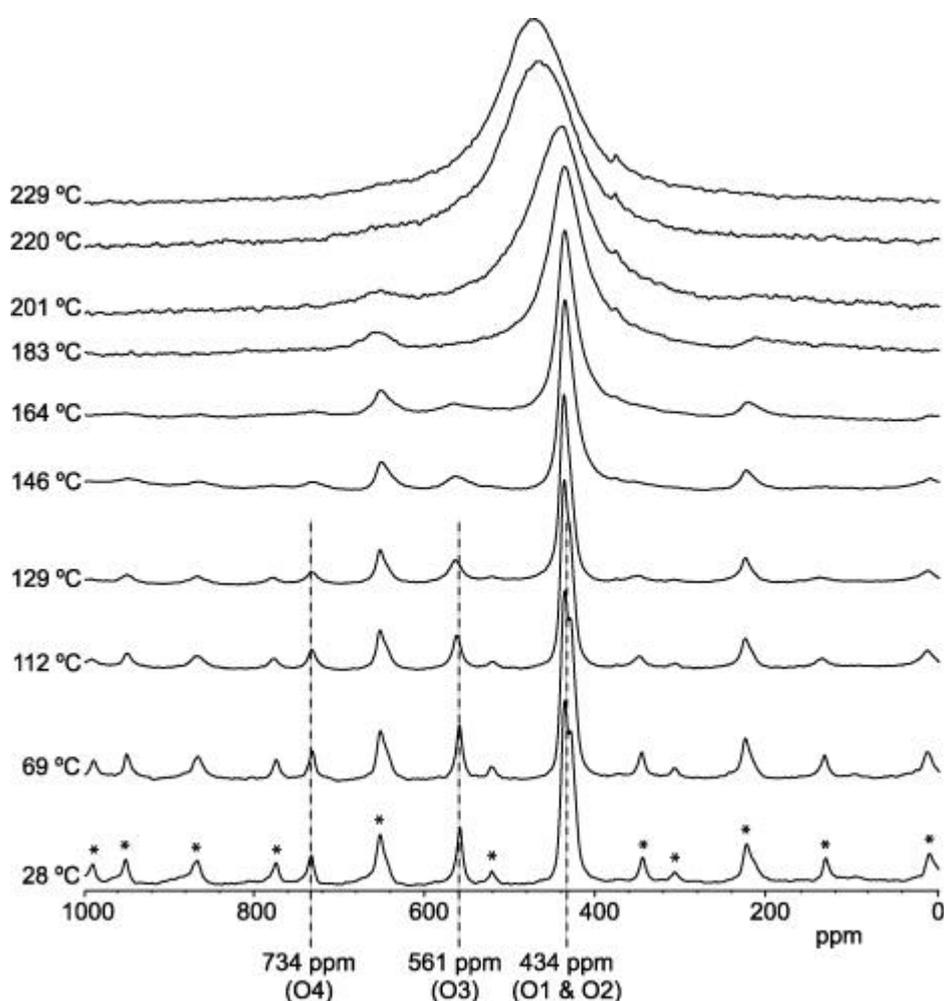

Figure 3-8 Variable temperature ^{17}O MAS spectra of ZrW$_2$O$_8$. A MAS speed of 14.5 kHz was used throughout. Excitation pulse duration 2.0 µs. Pulse repetition times were between 3 s and 120 s depending on T_1. The number of transients per spectrum was varied between 32 and 1024. An exponential apodization of 100 Hz was applied to each spectrum. Asterisks indicate spinning sidebands.

At each temperature, the T_1 relaxation time (studies of which are discussed in detail in Chapter 4) was first approximately evaluated by saturation recovery experiments so that appropriate

pulse repetition delays could be determined. The number of transients recorded for each spectrum was also varied in order to maintain adequate signal to noise. The sample temperatures were calibrated using the variation of the [207]Pb chemical shift in an external Pb(NO$_3$)$_2$ standard (see Chapter 2).[21]

The spectrum at room temperature shows the expected peaks for the four oxygen atoms in the asymmetric unit. All peaks are seen to broaden with increasing temperature, with the peaks for O3 and O4 becoming impossible to distinguish above the baseline at around 164 °C. At temperatures of 183 °C, a single broad peak is seen, which continues to increase in width with increasing temperature.

In order to quantitatively study the variation of the peaks as a function of temperature, they were each deconvoluted as pseudo-Voigt functions. The overlapping peaks for O1 and O2 were treated as two peaks in the temperature range 28 – 146 °C. The chemical shift of all peaks increases slightly with temperature, as shown in Figure 3-9 (a), and from approximately 60 °C, the FWHM of the individual peaks is also seen to increase significantly, as shown in Figure 3-9 (b).
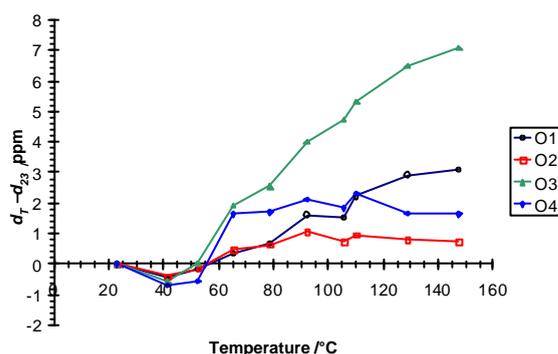
(a)
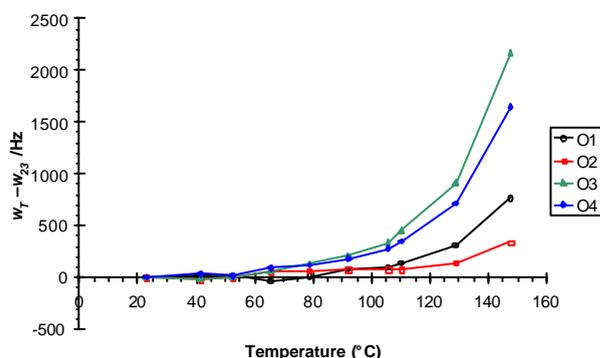
(b)

Figure 3-9 Variation of (a) chemical shift, and (b) line width (FWHM) with temperature for individually deconvoluted centre-band peaks in the ^{17}O MAS NMR spectra of ZrW$_2$O$_8$. Changes in chemical shift and FWHM are expressed as a difference between the values (d_T and W_T) at temperature T and the values at 23 °C, the lowest sample temperature used (d_{23} and W_{23}).

The small increase in chemical shift of the separate peaks observed between room temperature and 140 °C (Figure 3-9) may be due to the effect on the electronic environment caused by the change in cell parameter, which decreases by ~1 % from 9.1556 Å at 23 °C to 9.1452 Å at 140 °C.[22] The change in position of the O3 peak is much more pronounced than that observed for other peaks and suggests that this oxygen undergoes the most significant change in environment. Increased movement of the O3 site is plausible since this site has a long bond to W1 as well as its bond to W2, and may move closer to a central position as the temperature is increased. This observation is consistent with interpretation of recent total scattering experiments.[23]

A low temperature spectrum at an indicated temperature of -100 °C was also recorded for this sample of ZrW_2O_8. This is not included in the plots above since the sample temperature was not calibrated. The chemical shifts of the sites are compared to those at 23 °C in Table 3-3. These results confirm that the behaviour of the O3 site is different to that of the other sites, with the chemical shift decrease being much more pronounced that for O1 and O2, a continuation of the trend seen above room temperature, as in Figure 3-9(a). The change in peak position for O4 between 23 °C and -100 °C is dramatically different to the other sites, the peak shifts to higher chemical shift as the temperature is decreased over this range, in contrast to the other peaks which shift to lower chemical shifts.

| Oxygen site	Peak position at 23 °C, d_{23} / ppm	Peak position at -100 °C d_{-100} / ppm	Change in peak position $d_{-100} - d_{23}$ / ppm
O1	430.1	429.6	-0.5
O2	438.7	437.5	-1.2
O3	560.3	556.6	-3.7
O4	733.6	736.9	+3.2

Table 3-3 [17]O Chemical shifts for oxygen sites in ZrW_2O_8 at room temperature and -100 °C (indicated thermocouple temperature).

At temperatures above ~140 °C, it is only possible to distinguish one broad peak, at around the chemical shift of the O1/O2 overlapped peaks. The position of this peak continues to shift to higher chemical shift, and at the highest observed temperature is at 457 ppm, as shown in Figure 3-10 (a). The width of the broad peak also continues to increase, with the rate of broadening with temperature decreasing at ~220 °C, as shown in Figure 3-10 (b).

The smooth broadening of all peaks with increasing temperature suggests that all oxygen sites are involved in an exchange process. The disappearance of peaks for O3 and O4, leading to a single broad peak is indicative of rapid exchange causing coalescence of all NMR signals.
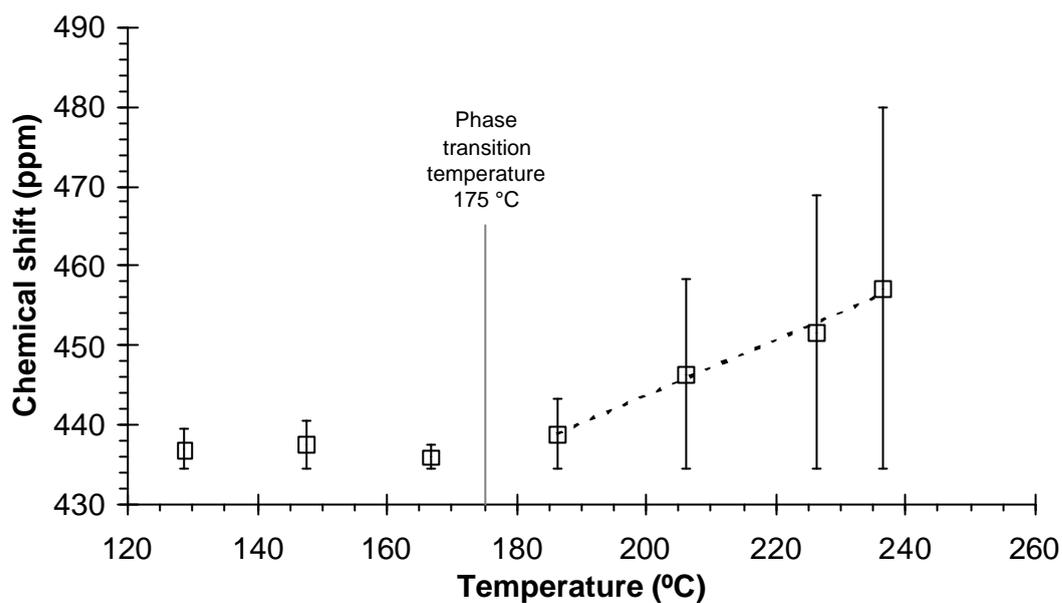
(a)
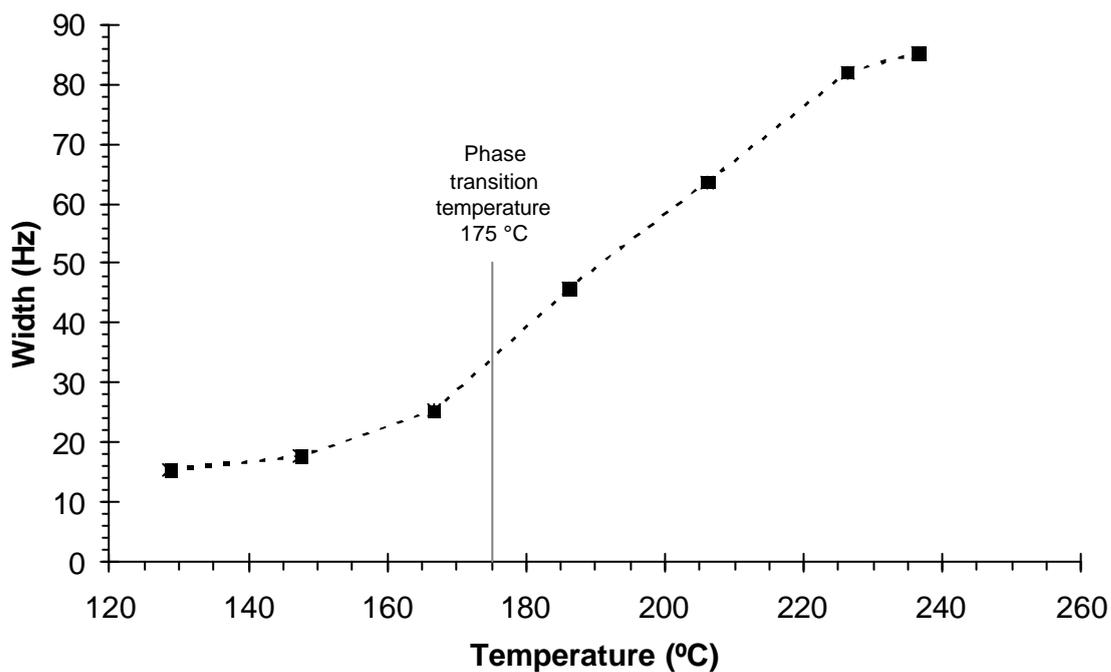
(b)

Figure 3-10 Variation of (a) chemical shift and (b) width (FWHM) with temperature for the coalesced centre-band peak in the ^{17}O MAS NMR spectra of ZrW$_2$O$_8$ above 120 °C. Dotted line on (a) shows fit to a linear fit for chemical shift above phase transition temperature. Dotted line on (b) is a guide to the eye.

If the apparent coalescence of peaks is due to exchange between all sites, then two effects would be seen at high temperature, where the exchange rate(s) are greater than the frequency differences between the NMR resonances:

- The broad coalesced hump would decrease in width leading to a single sharp peak

- The chemical shift of the coalesced line would be equal to the weighted average of the individual resonances corresponding to the exchanging sites.

The width of the peak increases throughout the temperature range studied, with a decrease in the rate of increase at around 220 °C. At higher temperatures a decrease in width may occur. The position of the coalesced peak remains relatively constant from ~130 °C to ~170 °C, and then starts to increase following an approximately linear trend (as shown in by the dotted line in Figure 3-10(a)) - this change in behaviour occurs at around the known phase transition temperature of 180 °C. The weighted average chemical shift of the separate resonances at room temperature is 487 ppm. At 236 °C, the broad peak is centred around 457 ppm; assuming that the linear trend continues, the position of the line would reach 487 ppm at 325 °C. Unfortunately, it was not possible to confirm this since it was not possible to record spectra at higher sample temperatures with the equipment available.

Previous studies by King[17] did appear to show a decrease in width at temperatures between 205 and 245 °C. The ZrW$_2$O$_8$ sample used for King's studies was impure and less highly enriched than that used for these studies, and so the observed signal to noise was significantly worse. King also used a different spectrometer, with different magnetic field, and so a direct comparison of the results is not possible. The effect of exchange on a spectrum is dependent on the ratio of $k/\Delta u$ (where k is the exchange rate and Δu is the frequency difference between sites), and so the spectra recorded at a different magnetic field would be expected to differ. The spectrometer used by King also used a fundamentally different temperature control system. The observation of peak narrowing at >205 °C by King may be considered as being consistent with the width reaching a maximum at ~230 °C here when one allows for small (~15 °C) errors in the temperature calibration of the respective NMR probes.

The spectra recorded are all consistent with the coalescence of the four peaks, and it may be concluded that a chemical exchange process affecting all sites is occurring. However from 1D spectra alone it is not possible to definitively conclude which sites are interchanging.

3.1.9 Two-Dimensional Exchange Spectroscopy (EXSY)

In order to confirm the nature of the exchange process below the phase transition temperature, two-dimensional exchange spectroscopy[24] (^{17}O EXSY) was used. The EXSY pulse sequence is relatively simple and robust. This allows us to neglect quadrupolar effects and, in the case of ZrW$_2$O$_8$ where the quadrupolar couplings are relatively modest, we may treat ^{17}O as a pseudo spin ½ system. A schematic diagram of the pulse sequence is shown in Figure 2-4. The pulse program consists of only 3 pulses, with a set mixing time to allow atomic exchange to transfer magnetisation between sites. FIDs are recorded as a function of the evolution time, t_1, and then the data are Fourier transformed with respect to both the direct time dimension (t_2) and the

indirect t_1 dimension. The EXSY pulse program is discussed further in Chapter 4, in which its use for quantitative kinetic studies is described.
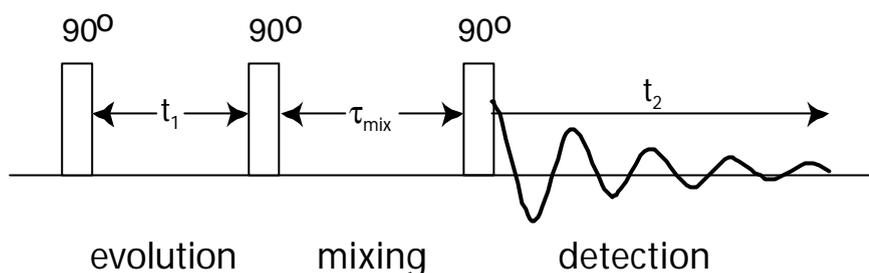

Figure 3-11 Schematic diagram of the EXSY pulse sequence.

The resulting processed 2D EXSY spectrum is quite simple to analyse qualitatively. The usual 1D NMR spectrum is obtained if one takes a "slice" of the contour plot along the diagonal. The separated peaks in the 2D plot are either seen along the diagonal, for nuclei in the same environment at the start and end of the mixing time, or as off diagonal cross peaks for nuclei which undergo a change in environment (implying chemical exchange on the timescale of the mixing time) during the mixing time. These experiments are only to be treated qualitatively, simply looking for the presence or absence of cross peaks, and it is therefore unnecessary to consider the exact excitation conditions in detail.

2D EXSY spectra were acquired at temperatures of 57 °C and 110 °C, with mixing times of 1 ms and 50 ms. Only 24 increments of t_1 were used, since only limited resolution in the indirect dimension is required for a qualitative observation of the presence of cross-correlation peaks. In the processing of the data, linear prediction was used to extend the FID in the indirect (t_1) dimension to 64 points, and 300 Hz exponential apodization was applied in both dimensions to improve visibility of the peaks (300 Hz being the approximate full width at half maximum of the narrowest peaks in the spectrum). A control experiment at 57 °C with a 1 ms mixing time showed no cross peaks. The 57 °C 2D EXSY spectrum with mixing time of 50 ms is shown in Figure 3-12(a).
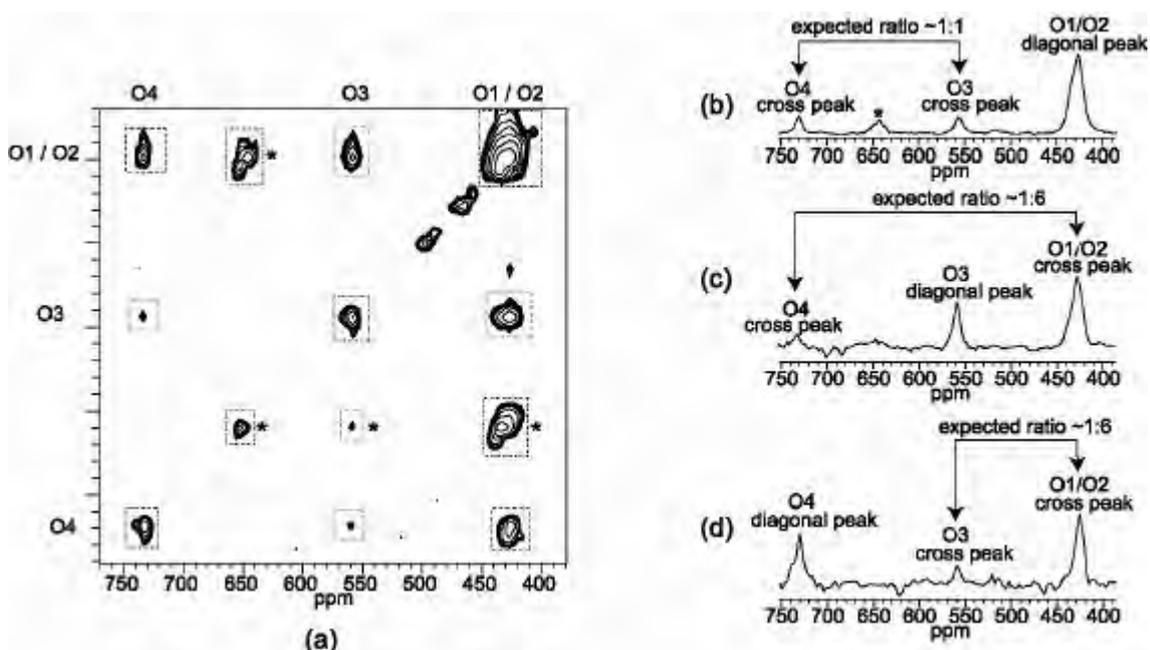
Figure 3-12 ^{17}O EXSY spectrum of ZrW$_2$O$_8$ at 57 ºC: (a) 2D spectrum – dashed rectangles highlight peaks showing exchange (O1/O2? O3 red, O1/O2? O4 blue, O3? O4 green) and dotted rectangles show peaks which would be expected in the absence of exchange. Asterisks denote spinning sidebands; (b-d) Spectral slices in the direct dimension through diagonal peaks for O1 and O2 (b), O3 (c), O4 (d). MAS speed of 14.5 kHz. 32 transients per increment, with 24 increments in t_1. Excitation pulse durations of 2.80 μs were used, with a dwell time in t_2 of 4.31 μs and a recycle delay of 90 s. Connecting arrows indicate integral ratios expected on the basis of equal probability exchange between sites

In order to interpret these qualitative EXSY results, it is necessary to consider the effects of exchange by the proposed mechanisms described in Section 3.1.1. The S$_N$2 mechanism involves the transfer of an O4 atom between W$_2$O$_8^{4-}$ units. Somewhat counter-intuitively, due to inversion of the W$_2$O$_8^{4-}$ unit, the environments of O3 and O4 atoms are in fact unchanged during the exchange. The O1 and O2 sites remain part of the same tetrahedra throughout the motion, but their environments are exchanged by the motion. The ratcheting motion on the other hand would lead to mutual exchange of all oxygen sites. A schematic may be constructed to show the sites which exchange, and the positions of predicted cross peaks in the EXSY spectra, as in Figure 3-13.

	O4	O3	O2	O1
O1	¦	¦	**?**¦	[**?**¦]
O2	¦	¦	[**?**¦]	**?**¦
O3	¦	[¦]	¦	¦
O4	[¦]	¦	¦	¦

Figure 3-13 Pattern of oxygen exchange for different proposed mechanisms. Symbols indicate exchange between sites for the ratcheting (blue squares), and S$_N$2 (red circles) mechanisms. The full table is shown in this layout to correspond to the EXSY spectrum in Figure 3-12.

Considering the 2D EXSY spectrum, separate peaks for the centre band and spinning sideband peaks for O1/O2, O3 and O4 are clearly resolved along the diagonal, as in the 1D spectrum recorded at this temperature (Section 3.1.8). It is not possible to separately resolve the overlapped resonances for O1 and O2, and so exchange between the O1 and O2 sites would be difficult to observe by ^{17}O NMR. It is immediately clear however that there are cross peaks linking all diagonal peaks (sites O1/O2, O3 and O4) with each other. Comparison of the EXSY spectrum in Figure 3-12(a) and the predicted peaks as illustrated in Figure 3-13 shows that the results are consistent with the ratcheting mechanism, and not the S$_N$2 model.

It is also possible to extract some qualitative information from the intensities of the various peaks in the EXSY spectrum. The intensities of the peaks may be seen most clearly by taking spectral "slices" through the plot, as shown in Figure 3-12 (b)-(d). Assuming that complete exchange occurs during the mixing time, the relative intensities of the diagonal and cross peaks are dependent on the relative numbers of sites undergoing exchange. The ratio of the number of sites O1, O2, O3 and O4 in the structure is 3 : 3 : 1 : 1. If every nucleus in the sample were to undergo mutual exchange with all other sites, one would therefore expect to see a 1 : 1 : 6 ratio of intensities for O4 : O3 : O1/O2 in each of the spectral slices.

The ratios of cross peak intensities in the spectral slices are consistent with random scrambling, of the nuclei undergoing exchange during the mixing time. For example, a ^{17}O nucleus originally at the O4 site is ~6 times more likely to move to O1 than O3 at the end of the mixing time – as would be expected on the basis of the relative numbers of sites (Figure 3-12 (d)).

The diagonal peaks are consistently higher in intensity than would be expected if complete scrambling occurs. Two explanations may be offered for this observation. The simplest and most probable explanation is that the mixing time is simply not sufficiently long as to allow

complete exchange of all sites (*i.e.* $t_{mix} \neq >> t_{exchange}$) Alternatively it may be that statistical scrambling of some of the sites does occur during the mixing time, but that a proportion of sites do not undergo any change of environment, although there is no evidence to suggest this is the case. A 2D spectrum recorded at 110 °C also shows cross peaks for all sites, but with increased intensities in the cross peak relative to the diagonal peaks. All EXSY experiments were performed at temperatures below the phase transition, since it is not possible to resolve individual sites in the spectra recorded above the phase transition temperature.

The observation of cross peaks allows a distinction between the two proposed exchange mechanisms (Figure 3-1) to be made. If the "S_N2" mechanism were in operation, then the only sites actually involved in chemical site exchange would be O1 and O2. Although O3 and O4 physically move in this model, they would end the exchange process in the same type of environment as they started in, albeit bonded to different tungsten atoms. On the other hand, the "ratcheting" model, entailing rotation of intact WO_4 tetrahedra, involves mutual exchange of all 4 oxygen sites. The ratcheting model is consistent with the results, whereas the S_N2 mechanisms has been disproved.

Although the ratcheting model is the simplest explanation for the results, other models which involve mutual exchange of all oxygen sites would also be consistent. Other mechanisms, such as a series of uncorrelated hops between the oxygen sites could not be disproved from this data.

The fact that the exchange process involves all oxygen environments supports the variable temperature results discussed in Section 3.1.8. These 2D NMR experiments have allowed the mechanism of oxygen exchange at low temperature to be determined. Information about the kinetics of exchange was subsequently derived from the quantitative experiments described in Chapter 4.

3.2 ZrMo$_2$O$_8$ phases

This section describes experiments to prepare enriched samples of three phases of ZrMo$_2$O$_8$ (LT, cubic and trigonal) and ^{17}O NMR studies, which it was hoped would give an insight into dynamics in these materials. The oxygen dynamics in the cubic phase are of particular interest, since they are similar to those in cubic-ZrW$_2$O$_8$. A sample of enriched cubic-ZrMo$_2$O$_8$ was therefore particularly desirable. However, the ambient pressure phase diagram of ZrMo$_2$O$_8$ (Figure 3-14) is considerably more complex than that for ZrW$_2$O$_8$. A hydrate phase analogous to ZrW$_2$O$_8$.xH$_2$O is not formed for the molybdate, and it is not possible to produce labelled cubic ZrMo$_2$O$_8$ by a simple hydration/ dehydration route as was done for ZrW$_2$O$_8$.
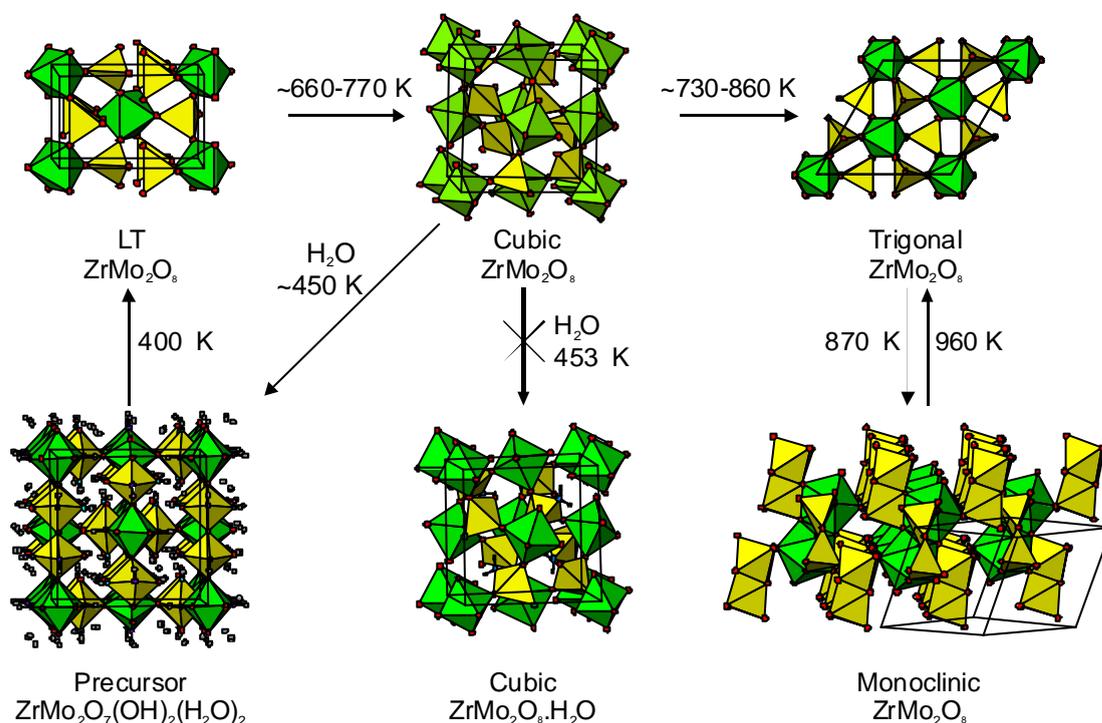

Figure 3-14 Ambient temperature phase diagram for ZrMo$_2$O$_8$.

A different route to enriched cubic-ZrMo$_2$O$_8$ was therefore investigated. From Figure 3-14, it should be possible to take a sample of cubic ZrMo$_2$O$_8$ (itself obtained by dehydration of the precursor ZrMo$_2$O$_7$(OH)$_2$·2H$_2$O), and re-hydrate it with ^{17}O-enriched H$_2$O then carefully dehydrate the resulting precursor compound to give enriched cubic ZrMo$_2$O$_8$. The full proposed route is thus: ZrMo$_2$O$_7$(OH)$_2$·2H$_2$O ? LT-ZrMo$_2$O$_8$? cubic-ZrMo$_2$O$_8$? ZrMo$_2$*O$_7$(*OH)$_2$·2H$_2$*O ? LT-ZrMo$_2$*O$_8$? cubic-ZrMo$_2$*O$_8$. Experiments into the hydration of ZrMo$_2$O$_8$ and the subsequent conversion of the precursor phases were carried out in order to obtain enriched samples of the LT, cubic and trigonal phases of ZrMo$_2$O$_8$.

3.2.1 Preparation of ^{17}O enriched ZrMo$_2$O$_7$(OH)$_2$(H$_2$O)$_2$

A sample of ~0.2 g cubic ZrMo$_2$O$_8$ (SA97B, pale pink powder) was ground in a pestle and mortar and added to ~0.2 g ^{17}O-enriched water, in a Pyrex glass ampoule which was then sealed under dynamic vacuum (~ 1.0 × 10^{-1} mbar). The sealed ampoule was then placed in a steel autoclave with PTFE liner. In order to equalise the pressure of water inside the ampoule, water was put into the liner surrounding the ampoule such that two thirds of the internal volume was filled. The assembled autoclave was then placed in a furnace at room temperature, and programmed to heat to 200 °C in 2 stages (to 160 °C at 10 K·min^{-1} and then to 200 °C at 2 K·min^{-1}) and then remain at this temperature for 16 hours before cooling back to room temperature.
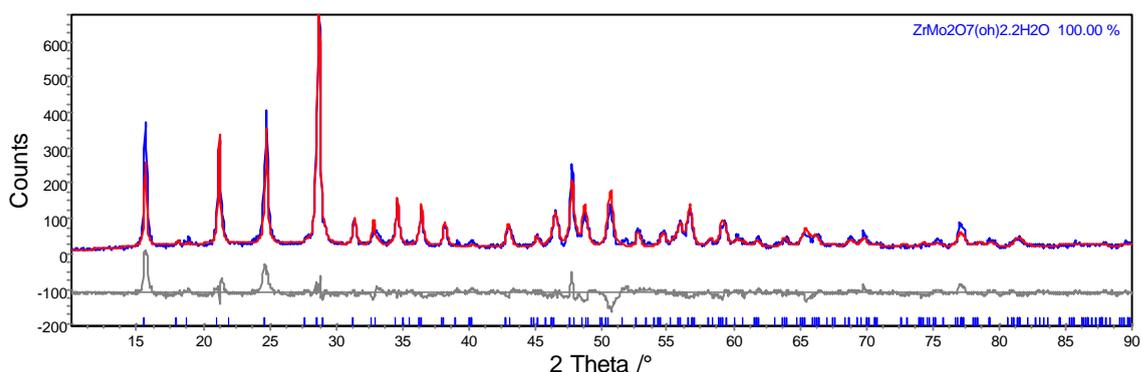

Figure 3-15 Rietveld refinement of powder diffraction data (d5_05878) for ZrMo$_2$O$_7$(OH)$_2$·2H$_2$O (mrh050), data re-binned with step size of 0.05 °.

The resulting wet pale grey sludge was identified as being the precursor material by powder X-Ray diffraction, as shown in Figure 3-15. This suggests that producing an enriched sample of the precursor material presents no experimental difficulties.

3.2.2 Preparation of ^{17}O enriched LT-ZrMo$_2$O$_8$

A sample of ~0.2 g ^{17}O enriched precursor material (mrh159) was placed in a porcelain boat which was then placed in a tube furnace, under dynamic vacuum (~ 1.0 × 10^{-1} mbar). The furnace was programmed to heat to 210 °C in 2 stages (to 160 °C at 10 K·min^{-1} and then to 210 °C at 2 K·min^{-1}) and then remain at this temperature for 2 hours before cooling back to room temperature.

The resulting grey / beige powder (mrh160) was identified as being LT-ZrMo$_2$O$_8$ by powder X-Ray diffraction, as shown in Figure 3-16.
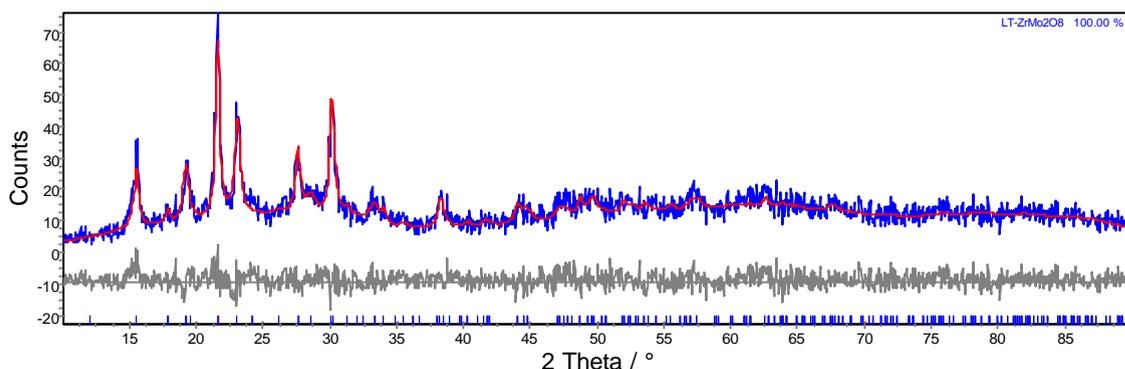
Figure 3-16 Rietveld refinement of lab X-Ray data (d9_00829) for LT-ZrMo2O8 (mrh160). data re-binned with step size of 0.05 °.

The X-ray powder pattern (d9_00829) shown was recorded within 15 minutes of the sample being removed from the evacuated furnace, by which time the sample for NMR had already been packed into a zirconia MAS rotor. Long periods of exposure to air were avoided due to the tendency of the material to partially re-hydrate to the precursor phase over a period of a few hours. A short scan time of 13 minutes was also used to avoid re-hydration during the diffraction measurement. The peaks observed for LT-ZrMo$_2$O$_8$ are always particularly broad, due to strain in the material, a consequence of the low temperature topotactic route by which it is formed. It is considerably less crystalline than the other ZrMo$_2$O$_8$ phases under investigation in this Chapter. The absence of crystalline impurities, such as trigonal or cubic ZrMo$_2$O$_8$ is clear from the diffraction pattern.

3.2.3 Preparation of ^{17}O enriched trigonal ZrMo$_2$O$_8$

A sample of LT-ZrMo$_2$O$_8$, prepared as described in Section 3.2.2, was ground with a pestle and mortar for one minute, pressed into a 13 mm diameter pellet at 15 tons and then sealed in a quartz tube and placed in a furnace at 1000 K for 1 hour. It was hoped that carrying out the conversion in a sealed tube would prevent loss of ^{17}O through exchange with air.
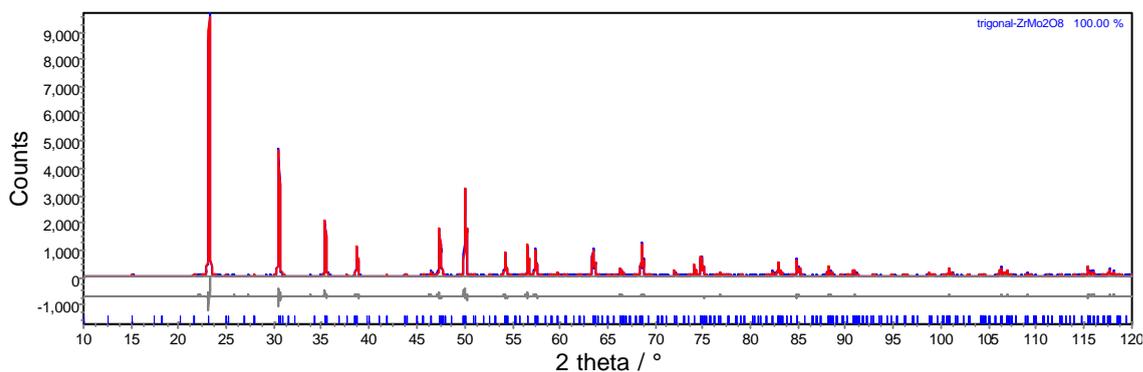

Figure 3-17 Rietveld refinement of lab X-Ray data (d9_0798) for mrh158 trigonal-ZrMo$_2$O$_8$

The product was a white powder (mrh158), which was identified as being trigonal-ZrMo$_2$O$_8$ by powder X-ray diffraction. Rietveld refinement as shown in Figure 3-17 showed it was >99 % pure, with minor impurity peaks seen at: 22.2 °, 25.7 ° and 27.4 ° 2?.

3.2.4 Preparation of ^{17}O enriched cubic ZrMo$_2$O$_8$

Cubic ZrMo$_2$O$_8$ is significantly more difficult to prepare than either trigonal or LT phases. The phase transition temperatures for the LT ? cubic and cubic ? trigonal conversions are very close to each other, and cubic-ZrMo$_2$O$_8$ is metastable. Temperature and heating time are both critical variables in the synthesis of ZrMo$_2$O$_8$, and impure samples containing a mixture of LT, cubic and trigonal are often obtained. In order to determine the optimum synthetic conditions to convert enriched precursor to cubic ZrMo$_2$O$_8$, *in situ* diffraction experiments were carried out.

3.2.4.1 *In situ* diffraction

A range of *in situ* experiments were carried out on the d8 Advance diffractometer with Anton Parr htk1200 furnace. In each experiment, a sample of ZrMo$_2$O$_7$(OH)$_2$·2H$_2$O precursor material was mounted on an amorphous silica disc using Vaseline as an adhesive and inserted into the furnace. The sample was heated in 10 K steps at a rate of 0.2 K·s^{-1} from 41 °C to 711 °C, and diffraction data recorded from 5 to 90 ° 2?.

The percentage of each ZrMo$_2$O$_8$ polymorph for each temperature in the experiment was determined by Rietveld refinement. Except where stated otherwise, a total of 31 independent parameters were refined: 12 background parameters, a sample height correction, a single temperature factor for all atomic sites in each phase, 4 structural parameters for ZrMo$_2$O$_7$(OH)$_2$·2H$_2$O (*I4$_1$cd*) (2 cell parameters, crystallite size and a histogram scale factor); 6 structural parameters for LT-ZrMo$_2$O$_8$ (*Pmn2$_1$*) (3 cell parameters, 2 parameters for the size and strain of crystallites as part of a spherical harmonic peak shape description and a scale factor); 3 structural parameters for cubic-ZrMo$_2$O$_8$ (*P2$_1$3*) (1 cell parameter, crystallite size and a histogram scale factor); 4 structural parameters for trigonal-ZrMo$_2$O$_8$ (*P3$_1$c*) (2 cell parameters, crystallite size and a histogram scale factor).

The first *in situ* experiments were performed using a sample of precursor (mrh059) synthesised by the method described in Section 3.2.1. Experiments were carried out both under dynamic vacuum (~7 × 10^{-1} mbar) and under air at atmospheric pressure. The composition as a function of temperature is shown in Figure 3-18.
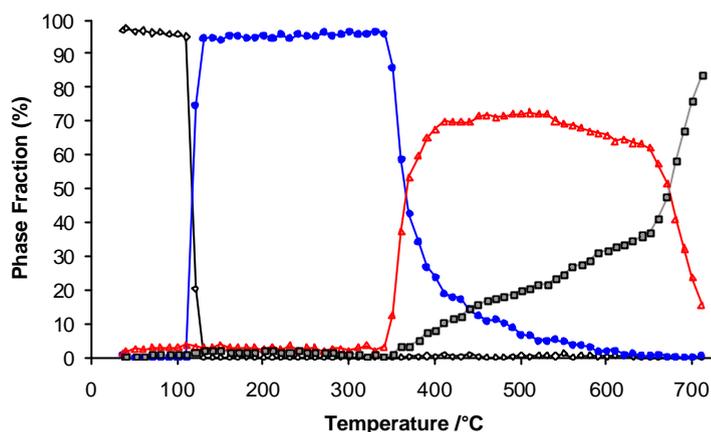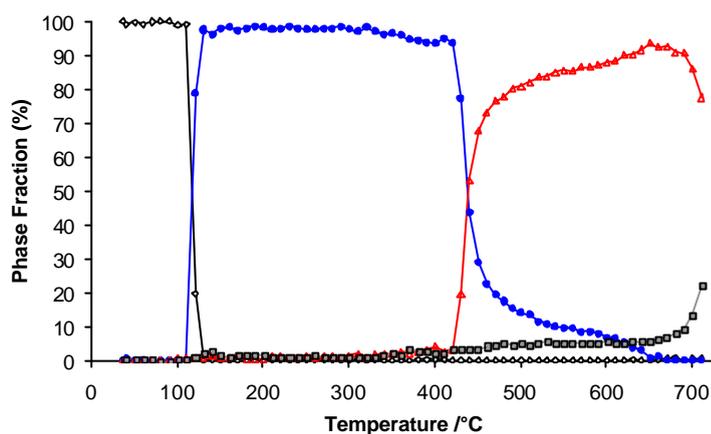
(a)
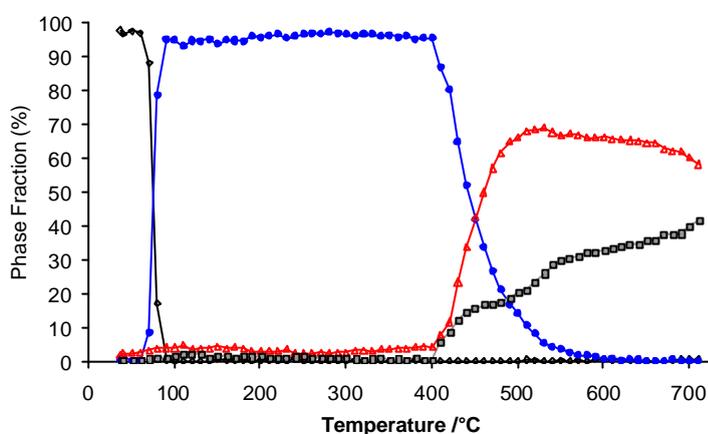
(b)

Figure 3-18 Percentage composition as a function of temperature for variable temperature diffraction experiments on $ZrMo_2O_7(OH)_2 \cdot 2H_2O$ (mrh059). In each case open diamonds represent $ZrMo_2O_7(OH)_2 \cdot 2H_2O$, closed (blue) circles $LT-ZrMo_2O_8$, open (red) triangles cubic-$ZrMo_2O_8$ and closed (grey) squares trigonal-$ZrMo_2O_8$. (a) Heating in air (d8_02700) (b) Heating under dynamic vacuum (d8_02658).

The figures show that the onset of formation of the trigonal phase occurs at approximately the same temperature as the cubic phase, and there is no clear temperature window for formation of a pure sample of the desired cubic phase. The conversion to the cubic phase is considerably lower than on the first cycle of heating, in which high concentrations of the cubic phase (>90 %) were obtained between ~ 450 and 550 °C before significant amounts of the trigonal phase were formed (in experiments performed by Allen[18]). The sample heated under vacuum shows that the production of the cubic and trigonal phases occur at approximately the same temperature, although this temperature (~400 °C) is slightly higher than the analogous experiment in air (~350 °C).

Lind *et al.* have shown the purity of precursor-derived cubic-$ZrMo_2O_8$ to be dependent on the acid used to produce the precursor, with samples prepared with $HClO_4$ giving the highest purity of the acids tested.[25] This suggests that the presence of ClO_4^- ions may favour the formation of

the cubic phase. It was therefore decided to investigate the effect of the presence of HClO$_4$ on the second cycle of dehydration of cubic ZrMo$_2$O$_8$.

A sample of precursor material (mrh085) was prepared from the cubic phase by a similar method to that described in Section 3.2.1, but with HClO$_4$ added. 0.2035 g cubic-ZrMo$_2$O$_8$ (SA97B), 0.2363 g H$_2$O and 0.0981 g HClO$_4$ (70 %, Lancaster) were used. The product was a cream coloured slurry, shown to be pure precursor by powder diffraction. Variable temperature diffraction experiments were carried out on this sample, the results of which are shown in Figure 3-19.

(a)
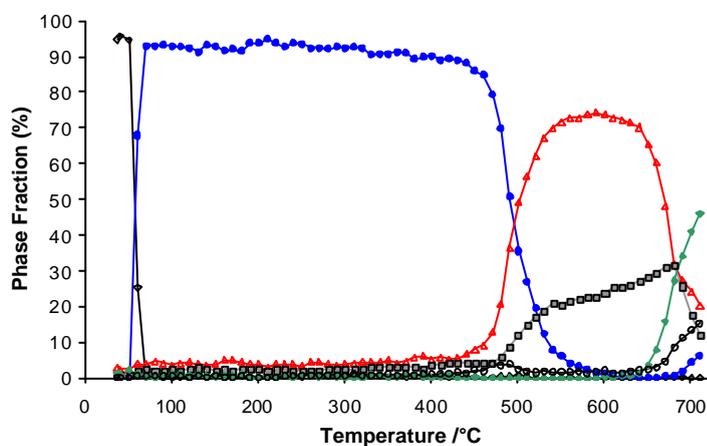
(b)

Figure 3-19 Percentage composition as a function of temperature for variable temperature diffraction experiments on mrh085 ZrMo$_2$O$_7$(OH)$_2$·2H$_2$O (prepared in the presence of 0.1 g HClO$_4$). In each case open diamonds represent ZrMo$_2$O$_7$(OH)$_2$·2H$_2$O, closed (blue) circles LT-ZrMo$_2$O$_8$, open (red) triangles cubic-ZrMo$_2$O$_8$ and closed (grey) squares trigonal-ZrMo$_2$O$_8$. (a) Heating in air (d8_02698) (b) Heating under dynamic vacuum (d8_02694), showing the formation of monoclinic and tetragonal phases of ZrO$_2$, shown by closed (green) diamonds and open circles respectively.

The experiment under ambient pressure shows that adding HClO$_4$ has a significant effect on the sequence of transformations on heating and allows much higher conversion to cubic ZrMo$_2$O$_8$,

with a temperature of 650 – 670 °C giving ~ 93 % cubic material. The experiment carried out under dynamic vacuum (d8_02694) shows the formation of trigonal ZrMo$_2$O$_8$ at lower temperatures than under ambient pressure. It also shows the appearance of a number of additional diffraction peaks at temperatures above 640 °C, which can be explained by the presence of monoclinic and tetragonal ZrO$_2$. The data from this experiment were therefore fitted to a model including monoclinic ZrO$_2$ (P2$_1$/c, 6 refined parameters: 4 cell parameters, crystallite size and histogram scale factor)[26] and tetragonal ZrO$_2$ (P4$_2$/nmcz, 4 refined parameters: 2 cell parameters, crystallite size and histogram scale factor),[27] giving a total of 41 refined parameters.

Another sample of precursor (mrh087) was synthesised using an increased amount of HClO$_4$. 0.1879 g cubic-ZrMo$_2$O$_8$ (SA97B), 0.2056 g H$_2$O and 0.1957 g HClO$_4$ (70 %, Lancaster) were used. It was hoped that this sample might show even higher conversion to cubic ZrMo$_2$O$_8$, but the results were very similar to those obtained with mrh085, and in fact the conversion to cubic was slightly lower, as shown in Figure 3-20, though the cubic phase was stable over a wider temperature window
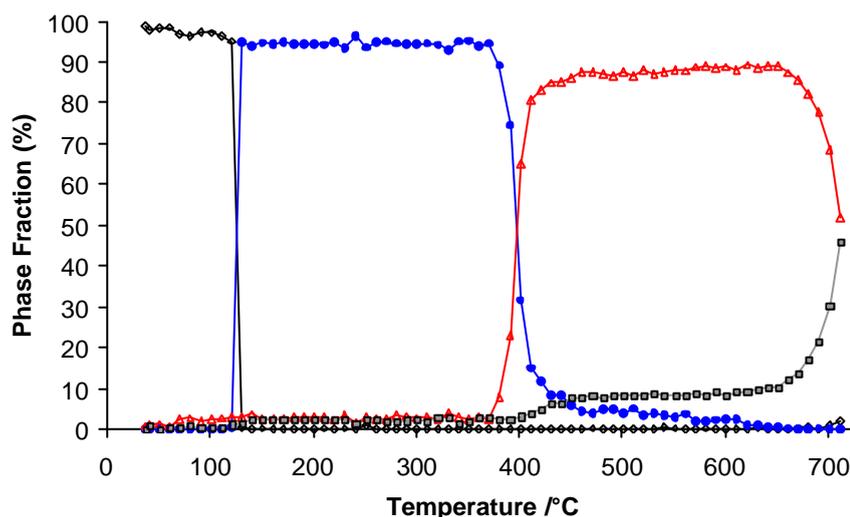

Figure 3-20 Percentage composition as a function of temperature for variable temperature diffraction experiments on mrh087 ZrMo$_2$O$_7$(OH)$_2$·2H$_2$O 2H$_2$O (prepared in the presence of 0.2 g HClO$_4$) heated under air. Open diamonds represent ZrMo$_2$O$_7$(OH)$_2$·2H$_2$O, closed (blue) circles LT-ZrMo$_2$O$_8$, open (red) triangles cubic-ZrMo$_2$O$_8$ and closed (grey) squares trigonal-ZrMo$_2$O$_8$.

The results of the *in situ* experiments therefore suggest that the optimum method for obtaining a high purity sample of enriched cubic ZrMo$_2$O$_8$ is to use a precursor from hydration in the presence of HClO$_4$, and that the conversion back to the cubic phase should be carried out under ambient pressure. Initial *ex situ* tests confirmed the conclusion that 500 °C was an optimal temperature.

A number of further experiments were carried out to determine the conditions to use in a furnace rather than in the diffractometer. In these experiments, a sample of precursor material

prepared as mrh085 (in the presence of HClO$_4$) was dehydrated under vacuum to produce LT-ZrMo$_2$O$_8$, as described in Section 3.2.2 and then heated in an open platinum crucible to temperatures in the range 400 - 670 °C. There are a variety of possible reasons for the discrepancy between the *in situ* and *ex situ* experiments. The gradient of temperatures throughout the volume of the furnace and the rate of cooling are examples of factors which are likely to be very different for the two furnaces. In cases such as this where the outcome of a reaction is highly dependent on temperature, and there are a number of competing reactions, it is can be extremely difficult to transfer the reaction between such different heating equipment.

The highest percentage of cubic ZrMo$_2$O$_8$ in any of the test samples was obtained by mrh123, which was heated to 500 °C, and so the ^{17}O enriched sample was prepared by heating a sample of Lt-ZrMo$_2$O$_8$ (mrh142, prepared as described in Section 3.2.2) to 500 °C for 13 minutes. The product (mrh143) was a pale pink powder. XRD of the sample confirmed that although cubic-ZrMo$_2$O$_8$ was the major phase, impurities of LT-ZrMo$_2$O$_8$ and trig-ZrMo$_2$O$_8$ were also present. Rietveld refinement of XRD data, shown in Figure 3-21. was used to determine the composition as 12 % LT-ZrMo$_2$O$_8$, 68 % cubic-ZrMo$_2$O$_8$, and 20 % trigonal-ZrMo$_2$O$_8$.
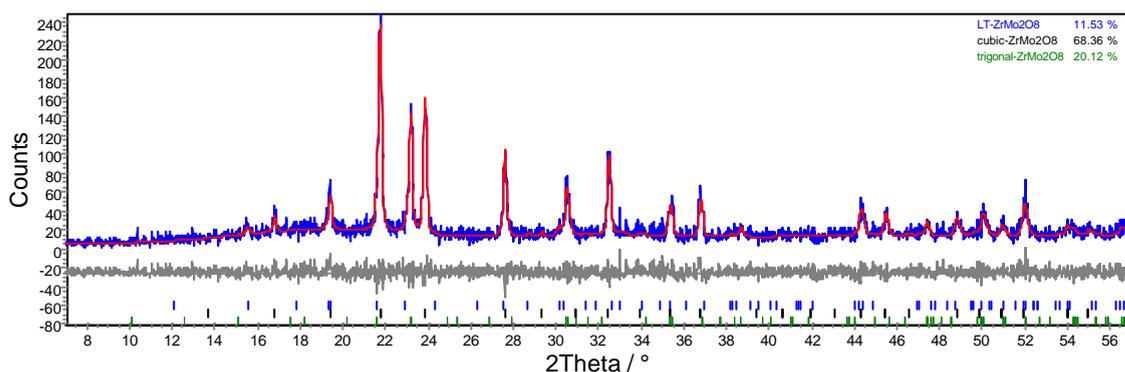

Figure 3-21 Rietveld refinement of XRD data (d9_00412) of ^{17}O enriched cubic ZrMo$_2$O$_8$. (mrh143) Bragg peak positions are shown by tick marks for LT-ZrMo$_2$O$_8$ (blue), cubic-ZrMo$_2$O$_8$ (black) and trigonal-ZrMo$_2$O$_8$ (green)

3.2.5 ^{17}O NMR of Trigonal ZrMo$_2$O$_8$ (mrh158)

^{17}O MAS NMR spectra were acquired at a range of temperatures. The spectrum at 47 °C is shown in Figure 3-22. Two centre band peaks were observed in all spectra, one at 868 ppm, and a broader peak around 518 ppm, which may be due to overlap of several peaks.
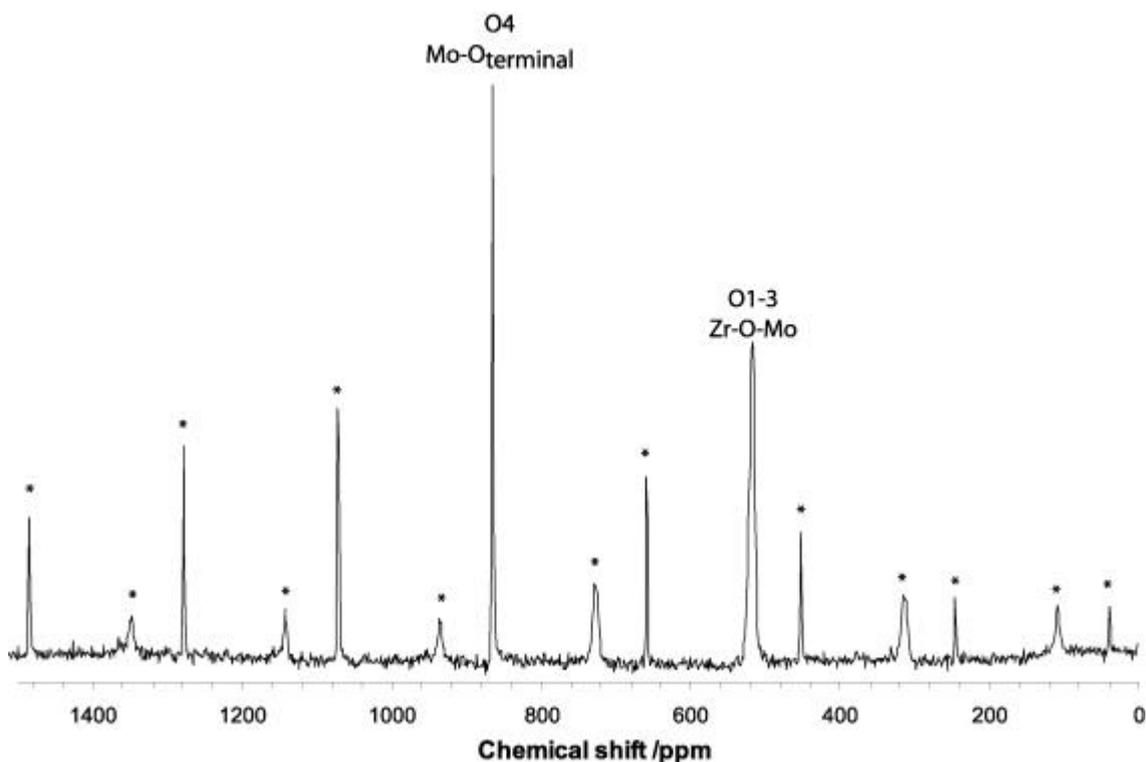

Figure 3-22 ^{17}O MAS NMR spectrum of trigonal ZrMo$_2$O$_8$, 47 °C, 100 transients, pulse repetition delay 400s, excitation pulse duration of 1.1 µs, 14 kHz MAS rate. Spinning sidebands are indicated by asterisks.

The structure of ZrMo$_2$O$_8$, as shown in Figure 3-23, consists of ZrO$_6$ octahedra which share all of their corners with MoO$_4$ tetrahedra. The Zr and Mo polyhedra are arranged in layers, with the mono-coordinate oxygen atoms (O4) pointing into the inter-lamellar space. The sharper peak at ~868 ppm presumably corresponds to the O4 site. The other sites O1-3, which are in very similar environments, have very similar chemical shifts and contribute to the broader peak. This assignment is consistent with shielding arguments since the resonance for the mono-coordinate, less shielded O4 site is at higher frequency. This pattern is similar to that seen in cubic–ZrW$_2$O$_8$ (Section 3.1.6).
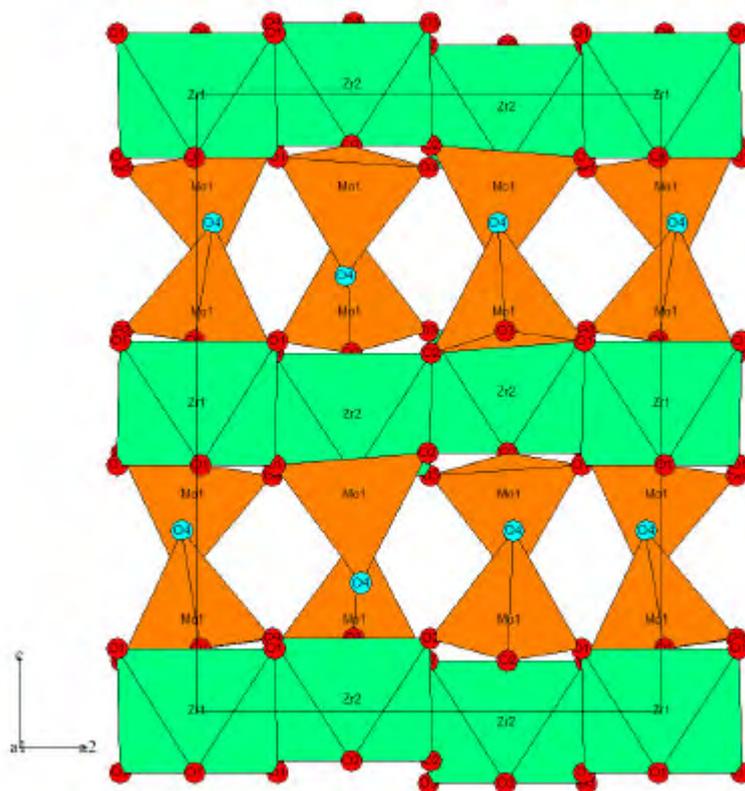
Figure 3-23 Room temperature structure of trigonal ZrMo$_2$O$_8$ according to Auray *et al..*[28]. The ZrO$_6$ octahedra are shown in green, with MoO$_4$ tetrahedra in orange. Oxygen atoms are shown as spheres, with O1-O3 in red and the mono-coordinate O4 in pale blue.

There is a phase transition reported by diffraction methods at 214 °C, which involves a reorientation of the MoO$_4$ tetrahedra such that O1-3 become equivalent. There are no noticeable changes in the spectrum with temperature within the range reachable by the NMR probe. It is not possible to be certain that spectra were recorded above the phase transition, since the maximum operating temperature (230 °C) is very close to the phase transition temperature.
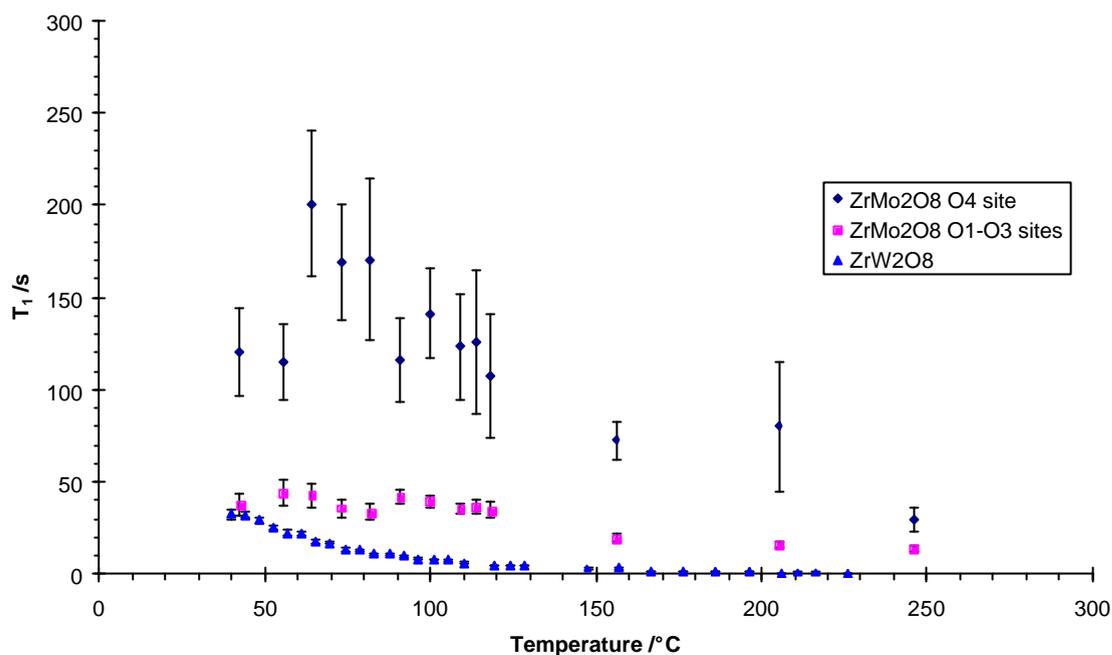
Figure 3-24 T_1 variation for two peaks (pink squares and dark blue diamonds) in trigonal ZrMo$_2$O$_8$ (mrh158) determined by saturation recovery experiments, with ZrW$_2$O$_8$ T_1 (Chapter 4) values shown for comparison (pale blue triangles). Error bars shown are those obtained from the fitting.

The variation of T_1 was investigated by saturation recovery experiments, and the results are shown in Figure 3-24. It is seen that the values of T_1 for the O1-O3 sites are noticeably and consistently smaller than that for O4. There is little variation in T_1 (which is highly dependent on motion) across the temperature range studied, when compared with that seen for ZrW$_2$O$_8$, and no noticeable temperature variation in the ^{17}O spectra themselves. It may therefore be surmised that there is no significant change in the oxygen dynamics across the temperature range accessible by standard solid state NMR methods, and these studies were not pursued further. ZrW$_2$O$_8$, on the other hand, is known to have highly mobile oxygen atoms, and the T_1 variation is studied in detail to gain quantitative information about the dynamics (Chapter 4).

3.2.6 ^{17}O NMR of LT-ZrMo$_2$O$_8$

The sample of LT-ZrMo$_2$O$_8$ (mrh160) was packed into a MAS rotor as soon as it was removed from the furnace following the dehydration reaction. It is known that this phase re-hydrates on a time scale of hours, and so the ^{17}O NMR spectrum was acquired within 30 minutes of the preparation of the sample. XRD of part of the sample was recorded at the same time as the first NMR spectrum, and confirmed that re-hydration had not yet occurred.
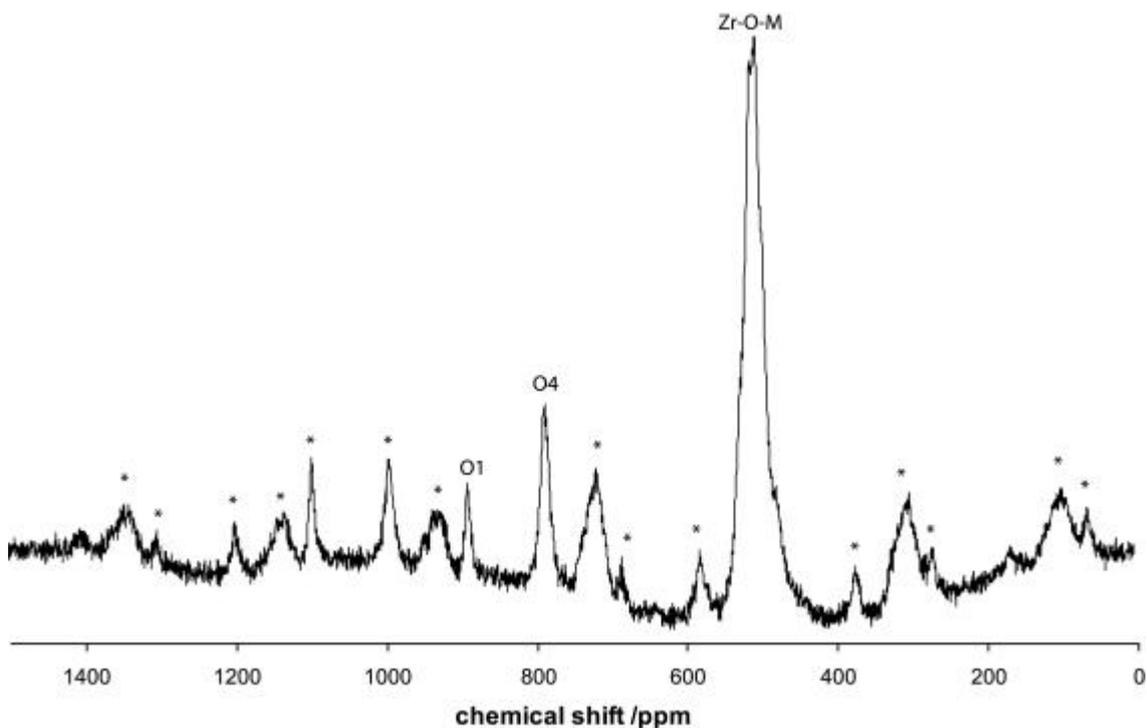

Figure 3-25 ^{17}O MAS NMR spectrum of LT ZrMo$_2$O$_8$ at 43 °C. 1024 transients, pulse repetition delay 50 s, excitation pulse duration of 1.1 µs, 14 kHz MAS rate.

The spectrum shows three broad centre-band peaks at 519 ppm, 796 ppm and 895 ppm. The structure is shown in Figure 3-26.
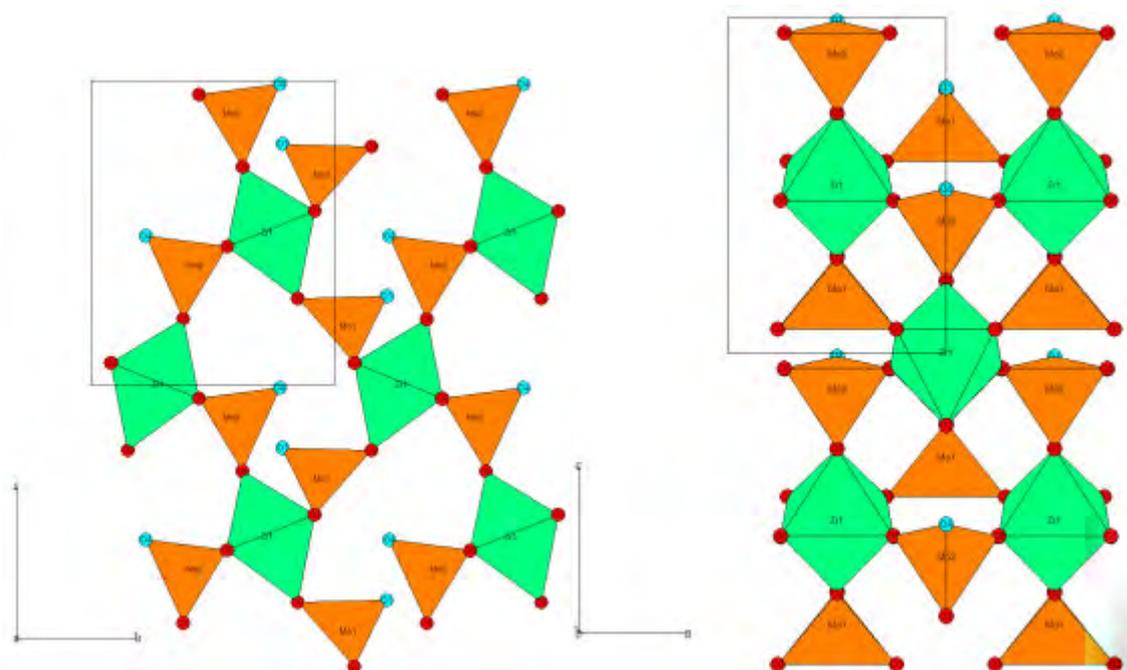
Figure 3-26 Structure of LT-ZrMo$_2$O$_8$ according to Allen *et al..*[29] The ZrO$_6$ octahedra are shown in green, with MoO$_4$ tetrahedra in orange. Oxygen atoms are shown as spheres, with two-coordinate oxygens in red and the mono-coordinate oxygens in pale blue.

There are six inequivalent oxygen atoms in the asymmetric unit of LT-ZrMo$_2$O$_8$, as determined by Allen *et al..*[29] It is straightforward to assign the peak at lowest frequency (519 ppm) to the six two-coordinate, Zr-O-Mo bridging, oxygens. The highest frequency peak (895 ppm) may be assigned to the strictly mono-coordinate O1 site. The peak at 796 ppm may be assigned to O4, which although formally mono-coordinate will also be additionally shielded due to the interaction with Mo1 (d = ~2.74 Å). This pattern is very similar to that seen for cubic-ZrW$_2$O$_8$ (Section 3.1.6).

3.2.7 ^{17}O NMR of cubic ZrMo$_2$O$_8$ (mrh143)

It is the NMR of the cubic phase that is potentially the most interesting, as cubic-ZrMo$_2$O$_8$ undergoes a phase transition similar to that seen for cubic-ZrW$_2$O$_8$, but involving a change from static to dynamic oxygen disorder (rather than from an order-disorder transition as in ZrW$_2$O$_8$). This phase transition has been suggested to occur ~-73 °C by diffraction.[3] The room temperature ^{17}O NMR spectrum of the enriched but impure sample of cubic-ZrMo$_2$O$_8$ (mrh143) was acquired on the InfinityPlus spectrometer, and is shown in Figure 3-27. Three centre band peaks are observed, at 522, 791, 868 (sharp) ppm. These are marked as P1, P2 and P3 respectively in Figure 3-27.
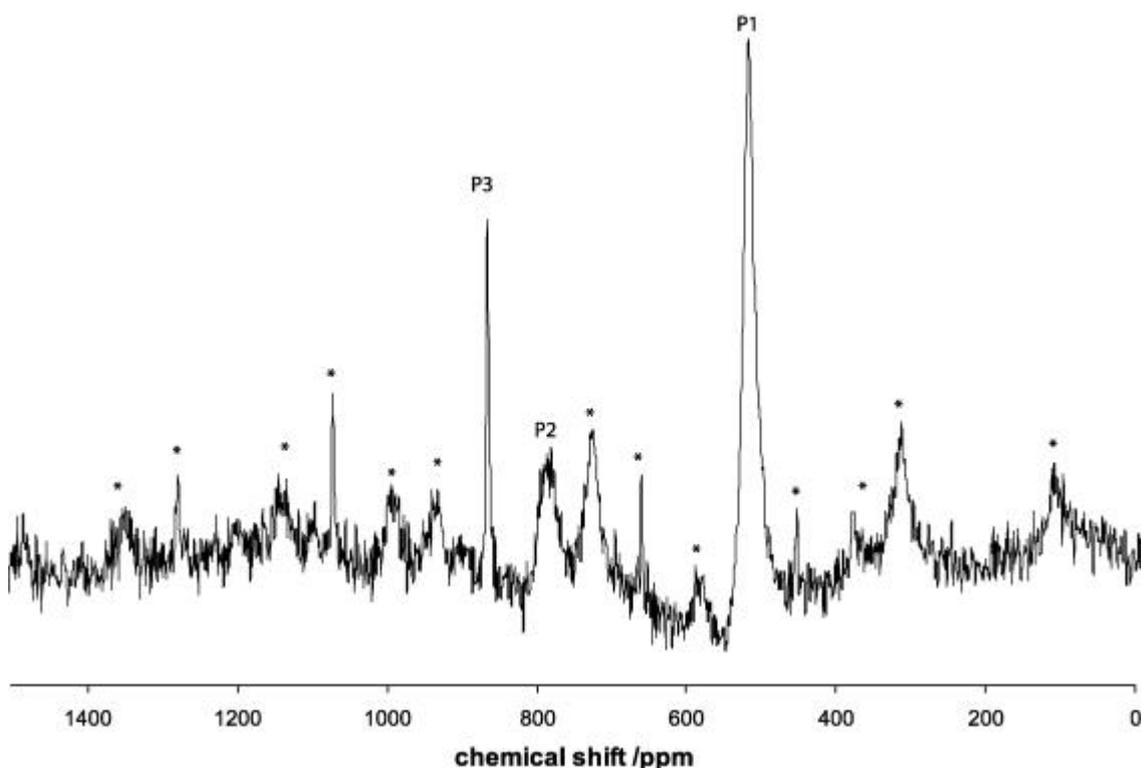
Figure 3-27 ^{17}O NMR spectrum of (impure) cubic ZrMo$_2$O$_8$, 42 °C 64 transients, pulse repetition delay 65 s, excitation pulse duration of 1.8 µs. 14 kHz MAS. Showing the three centre band peaks (P1, P2, P3) with spinning sidebands indicated by asterisks.

Unfortunately there is considerable overlap between the peaks due to the major phase (cubic ZrMo$_2$O$_8$) and those due to the impurity phases, as is illustrated in Figure 3-28. There are no isolated peaks which may be unambiguously assigned to cubic ZrMo$_2$O$_8$ alone, although the peaks seem slightly broader and may well include intensity from the cubic phase.

Figure 3-28 Ambient temperature ^{17}O MAS NMR spectra of: impure cubic ZrMo$_2$O$_8$, mrh143 (black); trigonal ZrMo$_2$O$_8$, mrh158 (red) and LT- ZrMo$_2$O$_8$ (blue). MAS speed of 14.5 kHz was used for all spectra. Top: centreband region, with spinning sidebands marked with asterisks. Bottom: Enlarged view of spectra around position of P1 peak.
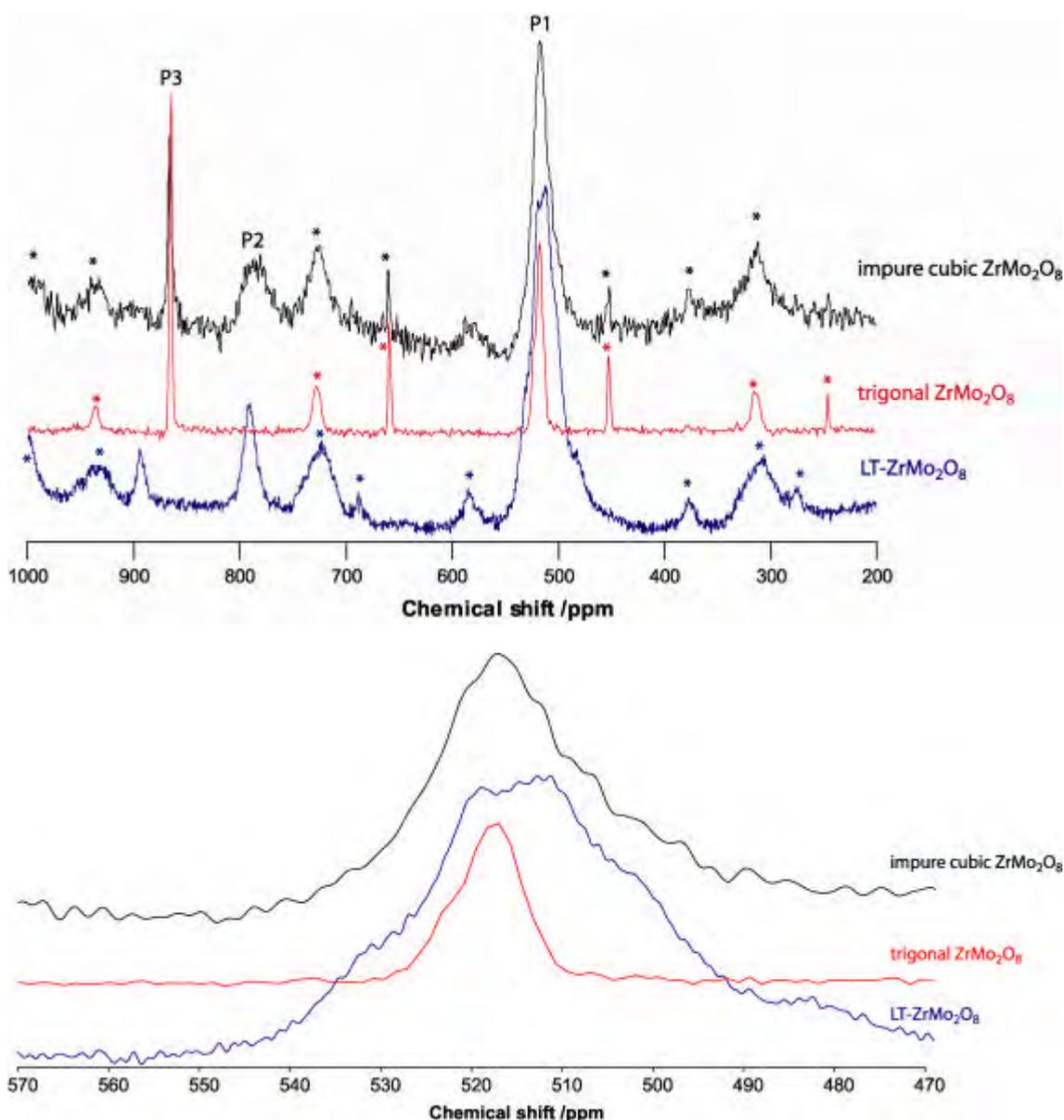
The ^{17}O NMR spectrum of the impure cubic sample was recorded as a function of temperature, as shown in Figure 3-29. The ^{17}O MAS NMR spectrum does not vary significantly over the temperature range from -70 to 220 °C, the operating range of the NMR probe used. It is therefore not possible to obtain any kinetic information from these spectra that may give an insight into the oxygen disordering process that occurs at the phase transition. In fact the lowest temperature at which spectra were obtained is approximately equal to the phase transition temperature observed by Allen and Evans in their diffraction based study.[3] By comparison with the spectra for ZrW$_2$O$_8$, as described in Section 3.1.8, one would expect that around or above the phase transition temperature the observed NMR would consist of one broad peak if there is rapid exchange between all the oxygen sites. It is possible that this is the regime being observed, and it is impossible to observe even a broad peak for cubic ZrMo$_2$O$_8$.
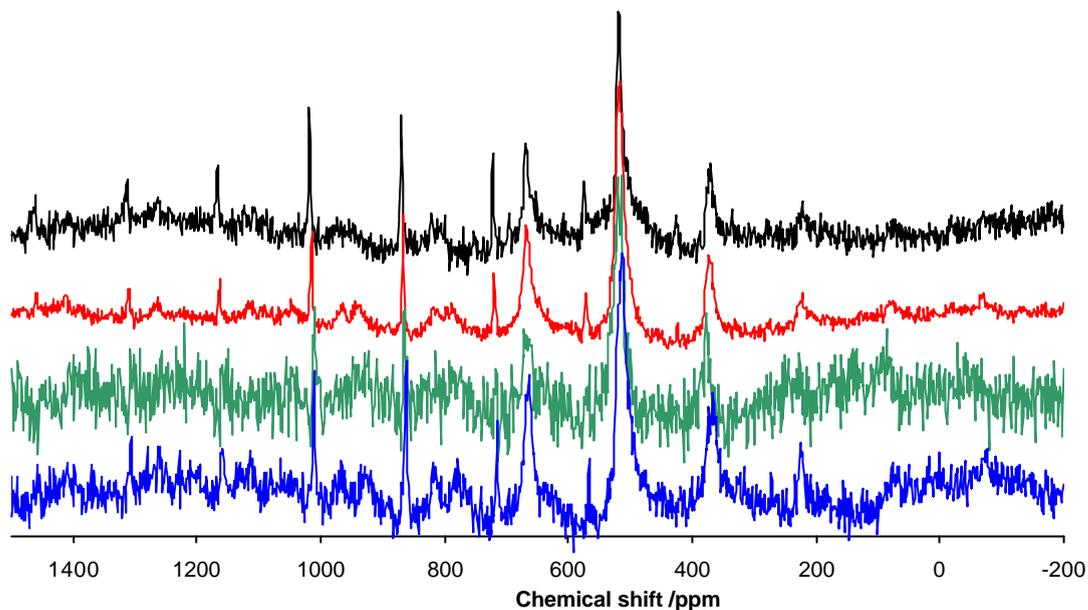
Figure 3-29 Variable temperature [17]**O MAS NMR spectra of mrh143 at ~-70 °C (un-calibrated) (blue), 42 °C (green), 109 °C (red) and 225 °C (black), 14 kHz MAS speed.**

The problem is compounded by the high degree of overlap between peaks for cubic-$ZrMo_2O_8$ and those for the minority phases. If there was one isolated peak seen for the cubic phase, then a study of the variation of T_1 could be carried out, which could help determine the activation energy for oxygen exchange in the high temperature phase, as described for ZrW_2O_8 in Chapter 4. Unfortunately the peak overlap makes this impossible, and it is also not possible to determine with any certainty whether there is any significant change in width of the peaks with increasing temperature.

3.2.8 Comparison of spectra for ZrMo$_2$O$_8$ phases

The spectra of LT-ZrMo$_2$O$_8$ and trigonal-ZrMo$_2$O$_8$ show a very similar trend in peak positions to those for the different oxygen environments in ZrW$_2$O$_8$. The oxygen environments may be classified in three groups, which are represented in the different structures.

Description of oxygen environment	Cubic ZrW$_2$O$_8$		Trigonal-ZrMo$_2$O$_8$		LT-ZrMo$_2$O$_8$	
Strictly one coordinate M-O terminal oxygen	O4	734 ppm	O4	878 ppm	O1	895 ppm
M-O··M, with slight shielding due to weak interaction (d =~2.5 Å) to second M atom.	O3	561 ppm			O4	796 ppm
Zr-O-M bridging oxygens	O1,O2	434 ppm	O1,O2,O3	518 ppm	O2,O3,O5,O6	519 ppm

Table 3-4 Comparison similar oxygen environments and chemical shifts in ^{17}O NMR spectra of ZrM$_2$O$_8$ phases (M = W, Mo).

Table 3-4 lists the structurally similar sites in different structures, and the observed chemical shifts. Although the chemical shifts in the ZrMo$_2$O$_8$ phases are consistently higher than those in ZrW$_2$O$_8$, the trend in chemical shifts within a given structure is very similar, an observation which lends confidence to the assignment of the spectra for each of the phases.

3.3 Conclusions

The ^{183}W spectrum confirms the presence of two tungsten sites in the low temperature phase, although it has unfortunately been impossible to study tungsten site exchange due to insufficient signal to noise in high temperature spectra. ^{183}W NMR remains a difficult technique due to the inherently poor sensitivity of this nucleus. In the case of ZrW$_2$O$_8$, it may be possible to record ^{183}W spectra with improved signal to noise by using a partially reduced sample containing paramagnetic W(V) – this may have shorter T_1 times enabling shorter pulse repetition delays.

The experiments in isotopically enriching ZrW$_2$O$_8$ by hydration and dehydration show that this technique does indeed allow highly effective enrichment. A range of ^{17}O NMR experiments were performed, and an approximate value of the ^{17}O quadrupole coupling C_Q = 0.5 MHz in ZrW$_2$O$_8$ was determined by fitting the well resolved spinning sideband pattern of the O3 site.

^{17}O NMR has proved an extremely powerful technique in complementing XRD to probe the dynamics of oxygen atoms in this structure. The variable temperature NMR spectra show that motion on the NMR timescale involving all the oxygen sites occurs at temperatures above the order-disorder phase transition. 2D EXSY experiments confirm that mutual exchange between all oxygen sites occurs below the phase transition temperature (an unexpected result), on a timescale of 50 ms at 57 °C. This proves that the dominant oxygen exchange process occurring is not the simple S$_N$2 type mechanism as previously suggested. It may therefore be proposed that the dominant mechanism is in fact the rotation of whole intact WO$_4$ tetrahedra. It should be mentioned that any mechanism involving mutual exchange of all oxygen sites would be consistent with the NMR results. The mechanism involving WO$_4$ rotation is entirely consistent with both the diffraction and NMR results. These studies are extended to give quantitative information in Chapter 4.

The experiments to enrich ZrMo$_2$O$_8$ by a different hydration and dehydration technique to that used for ZrW$_2$O$_8$, have allowed the preparation of highly enriched samples of several different ZrMo$_2$O$_8$ phases. ^{17}O NMR spectra have been recorded for the LT and trigonal phases for the first time. There is little variation with temperature in either the spectrum or the values of T_1 values in the trigonal sample. It unfortunately proved impossible to observe any isolated peaks for the (impure) sample of cubic-ZrMo$_2$O$_8$ due to peak overlap. It was noted that the ^{17}O NMR spectra of cubic-ZrW$_2$O$_8$, Lt-ZrMo$_2$O$_8$ and trigonal ZrMo$_2$O$_8$ all show similar trends in the relationships between oxygen environments and chemical shift.

3.4 References

1   J. S. O. Evans, T. A. Mary, and A. W. Sleight, *Physica B*, 1997, **241**, 311-316.
2   S. Allen and J. S. O. Evans, *J. Mater. Chem.*, 2004, **14**, 151-156.
3   S. Allen and J. S. O. Evans, *Phys. Rev. B*, 2003, **68**, art. no. 134101.
4   J. S. O. Evans, T. A. Mary, T. Vogt, M. A. Subramanian, and A. W. Sleight, *Chem. Mater.*, 1996, **8**, 2809-2823.
5   T. A. Mary, J. S. O. Evans, T. Vogt, and A. W. Sleight, *Science*, 1996, **272**, 90-92.
6   A. K. A. Pryde, K. D. Hammonds, M. T. Dove, V. Heine, J. D. Gale, and M. C. Warren, *J. Phys.-Condes. Matter*, 1996, **8**, 10973-10982.
7   Y. Yamamura, N. Nakajima, T. Tsuji, A. Kojima, Y. Kuroiwa, A. Sawada, S. Aoyagi, and H. Kasatani, *Phys. Rev. B.*, 2004, **70**, Art. No. 104107.
8   C. De Meyer, F. Bouree, J. S. O. Evans, K. De Buysser, E. Bruneel, I. Van Driessche, and S. Hoste, *J. Mater. Chem.*, 2004, **14**, 2988-2994.
9   J. S. O. Evans, Z. Hu, J. D. Jorgensen, D. N. Argyriou, S. Short, and A. W. Sleight, *Science*, 1997, **275**, 61-65.
10   N. Nakajima, Y. Yamamura, and T. Tsuji, *J. Thermal Anal. Calorim.*, 2002, **70**, 337-344.
11   Y. Yamamura, N. Nakajima, and T. Tsuji, *Phys. Rev. B*, 2001, **64**, 184109.
12   M. Witschas, H. Eckert, H. Freiheit, A. Putnis, G. Korus, and M. Jansen, *J. Phys. Chem A*, 2001, **105**, 6808-6816.
13   J. F. Stebbins, *Science*, 2002, **297**, 1285-1287.
14   N. Kim and C. P. Grey, *Science*, 2002, **297**, 1317-1320.
15   N. Kim, R. N. Vannier, and C. P. Grey, *Chem. Mater.*, 2005, **17**, 1952-1958.
16   L. L. Y. Chang, M. G. Scroger, and B. Phillips, *J. Am. Ceram. Soc.*, 1967, 211-215.
17   I. J. King, 'Combined Use of Powder Diffraction and Magic-Angle Spinning NMR to Structural Chemistry', Ph.D. Thesis, University of Durham, 2003.

18   S. Allen, 'Thermoresponsive Behaviour of AM$_2$O$_8$ Materials', PhD Thesis, University Of Durham, 2003.

19   N. Duan, U. Kameswari, and A. W. Sleight, *J. Am. Chem. Soc.*, 1999, **121**, 10432-10433.

20   H. Bildsøe, in 'STARS: Spectrum Analysis For Rotating Solids', 1999.

21   A. Bielecki and D. P. Burum, *J. Magn. Reson.*, 1995, **116**, 215-220.

22   J. S. O. Evans, W. I. F. David, and A. W. Sleight, *Acta Crystallogr. B*, 1999, **55**, 333-340.

23   M. G. Tucker, D. A. Keen, M. T. Dove, and J. S. O. Evans, in 'Personal Communication', 2006.

24   K. G. Orrell, 'Encyclopedia of Nuclear Magnetic Resonance', ed. R. K. Harris and D. M. Grant, Wiley, Chichester, 1996.

25   C. Lind, A. P. Wilkinson, C. J. Rawn, and E. A. Payzant, *J. Mater. Chem.*, 2001, **11**, 3354-3359.

26   D. K. Smith and W. Newkirk, *Acta Cryst.*, 1965, **18**, 983-991.

27   B. Y. Bondars, G. Heidemane, J. Grabis, K. Laschke, H. Boysen, J. Schneider, and F. Frey, *J. Mater. Sci.*, 1995, **30**, 1621-1625.

28   M. Auray, M. Quarton, and P. Tarte, *Acta Crystallogr. C*, 1986, **42**, 257-259.

29   S. Allen, N. R. Warmingham, R. K. B. Gover, and J. S. O. Evans, *Chem. Mater.*, 2003, **15**, 3406-3410.

Chapter 4 - Quantitative ^{17}O NMR experiments on ZrW_2O_8

The qualitative ^{17}O NMR studies on ZrW_2O_8 described in Chapter 3 enabled the elucidation of a model for the oxygen exchange in this material. In this Chapter, further quantitative ^{17}O NMR experiments to give kinetic information are described. EXSY experiments and variable temperature measurements of the T_1 relaxation constant are described which provide estimates of oxygen exchange rates and the determination of the activation barrier to oxygen mobility.

4.1 One-Dimensional Exchange Spectroscopy (EXSY)

^{17}O NMR has been used for a number of studies of dynamics in materials,[1-4] but its use for quantitative kinetic studies is less widespread. Whilst a number of studies have made use of solid state NMR experiments to obtain quantitative data about the rates of exchange of various nuclei, these have mainly focussed on either spin ½ nuclei or quadrupolar nuclei with modest quadrupole moments, such as ^2H, ^6Li and ^7Li.[5-7] Experiments using half integer quadrupolar nuclei with relatively large quadrupole moments such as ^{17}O are considerably more challenging for a number of reasons, as explained later in this chapter.[1]

It was decided to make use of the 1D-EXSY experiment for this study. The two-dimensional EXSY experiment described in Chapter 3 was used for qualitative observation of the exchange process, and could in principle also be used to determine the rate of exchange by acquiring a series of 2D spectra as a function of mixing time. This approach, however, would be prohibitively time consuming for detailed quantitative experiments, as multiple 2D experiments (each taking ~57 hours) would be required. Instead, a simpler and less time consuming one dimensional variant of the EXSY technique may be used to probe the kinetics of exchange.

4.1.1 Methodology

In this technique (1D EXSY), a series of one dimensional spectra are recorded, using a pulse program similar to that used in the 2D-EXSY experiment. The difference is that rather than incrementing the evolution time (t_1) with the mixing time ($\boldsymbol{t}_{mix}$) kept constant, it is the mixing time that is arrayed, with a fixed evolution time used to create a non equilibrium state at the start of the mixing time. Spectra with various values of mixing time are thus recorded, and it is possible to plot the intensity of a given signal as a function of mixing time. The change in intensity with increasing mixing time will depend on the rate of exchange, and so can be interpreted to give kinetic information.

There is a variety of variants of the 1D-EXSY experiment, all of which use the basic principle of excitation-evolution-mixing-reading sequence, but with different methods used to achieve excitation beyond the simple 90° pulse.[8] In the simple case of two site exchange in a solution state sample, one can use a selective pulse to invert the magnetisation of one site and then follow the change in intensity with mixing time. In the case of ZrW_2O_8, the situation is

considerably more complicated as selective inversion pulses would be ineffective in the presence of quadrupole couplings, and because there are four sites undergoing mutual exchange (as shown in Chapter 3).

Quantitative experiments using quadrupolar nuclei are inherently complicated, and this study is, to our knowledge, the first published application of the quantitative 1D-EXSY technique to solid-state ^{17}O NMR. The fact that ^{17}O is quadrupolar causes a number of complications. Firstly, the nature of excitation following an NMR pulse is difficult to predict, since the (*2I+1)* transitions are each affected by the orientation-dependent quadrupolar interaction. The distribution of intensity into sidebands also complicates the interpretation of results, and for this reason it was decided to perform quantitative studies on the variation of centre band intensity only. In view of the numerous potential complications, it was decided to use a simple 3 pulse experiment, in which a nominal 90 ° excitation pulse is used. The central transition is independent of the quadrupole interaction to first order and may therefore be treated as "*pseudo* spin ½ nucleus". This eliminates the need to consider the difficult-to-predict distribution of the different NMR coherences on excitation.

In order to extract kinetic data from the experimental results, it is necessary to fit the curve of signal intensity t_{mix}. The signal intensity of a given resonance as a function of t_{mix} will be affected by two main factors – the relaxation of the magnetisation to its equilibrium state and the exchange of nuclei between sites. The range of mixing terms used in an experiment must therefore be chosen carefully in order to capture the full timescale of relaxation (~10 s at 100 °C) as well as that of chemical exchange. The relaxation of quadrupolar nuclei is also difficult to model, since it is multi-exponential. In order to obtain kinetic data, it is essential to have some understanding of the relaxation processes, although exact modelling is not necessarily required.

4.1.2 Rotor Synchronization

Although the pulse program is substantially identical to that used for the 2D EXSY experiments in Chapter 3, it was necessary to make one modification to the pulse program for the quantitative studies. This was to add rotor synchronization to the program, which is required since, if unsynchronized, the signal intensity will be a function of the difference in the MAS rotor position between the start and end of the mixing time. The requirement for synchronization was confirmed by performing a series of 1D-EXSY experiments using the unsynchronized pulse sequence; the results of experiments with short mixing times (where t_{mix} was of the same order as the rotor period) showed a sinusoidal oscillation in the intensity with a period equal to the rotor period.[9, 10]

It is therefore crucial that the rotor is in the same position at the start and end of the mixing period. At short mixing times, it is possible to eliminate this effect by simply setting the mixing

time to multiples of the rotor period. However, in order to capture the full decay of the signal so that it could be quantitatively analysed, the longest values of t_{mix} to be used were of the order of seconds, thousands of times greater than t_{rotor}. In these situations, the simple methodology of setting the mixing time to multiples of t_{rotor} would not work due to deviations in rotor speed (~±5 Hz) and so a more sophisticated technique was required.

A method for active synchronization was achieved by triggering the pulse program using an optical signal from the rotor (as used for spin speed determination) to ensure that the mixing time was always a precise multiple of the rotor period. The output from the optical sensor signal is a square wave, and the increase in voltage, which occurs once per rotor cycle, was used as the trigger. The pulse program for the rotor synchronized EXSY experiment is shown in Figure 4-1. The first pulse is triggered by an optical signal, and the t_1 period is set as normal. After the second pulse, there is a delay of the nominal t_{mix}, followed by a wait period. The third pulse is then triggered by the next optical signature, with an additional delay period t_{del} inserted to ensure that the 2nd and 3rd pulses occur at the same point in the rotor cycle, regardless of t_1.
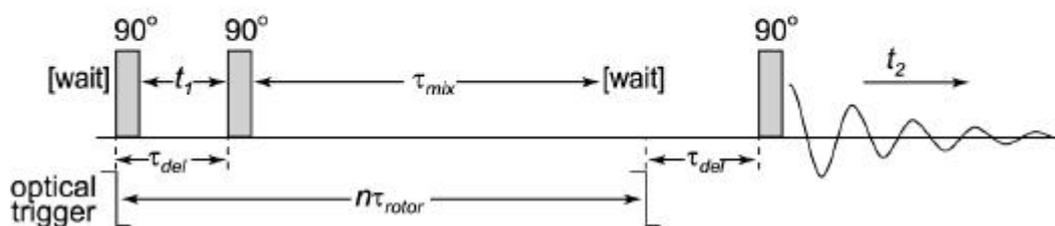

Figure 4-1 Pulse program for rotor synchronized EXSY.

4.1.3 Trial Experiments

Initial experiments with the rotor synchronized 1D-EXSY pulse sequence showed erratic results, in which the recorded intensities and the variation with t_{mix} were not reproducible. Experiments were carried out in order to trace the problem, and it was found that some experiments using short mixing times (with $t_{mix} \sim t_{rotor}$) still showed the sinusoidal oscillation with the same period as t_{rotor}, indicating that the rotor synchronization was not working correctly.

An oscilloscope was used to monitor the rotor signal and NMR pulses simultaneously. This confirmed that although the first pulse was consistently triggered correctly, the third pulse was not always an integer number of rotor cycles after the second. The problem was intermittent and in some cases the rotor synchronization worked exactly as intended. Many test experiments were performed to determine if there was any correlation between the likelihood of synchronization failure and the time parameters used, but no link was found.

Although the problem was not understood, a workaround solution, found by Dean Sindorf and Jim Frye at Varian, was to make a small alteration to the spectrometer operating software. Although the logic behind this modification, or the reason for the problem are not immediately apparent, test experiments using the modified software demonstrated that synchronization worked consistently. Tests were performed with a variety of values of t_{mix} and t_1, and in all cases a smooth decay of signal with increasing mixing time was observed, with reproducible results.

4.1.4 Determination of experimental parameters

Having established that the modified rotor-synchronized pulse program worked correctly, a number of test experiments were carried out, in order to determine suitable settings to use for the quantitative experiments. A MAS spinning speed of 14.5 kHz was used for all 1D-EXSY experiments, since this speed gives no overlap between centreband and sideband peaks for ZrW_2O_8 at the ^{17}O Larmor frequency of 67.7 MHz. A sample temperature of 110 °C was chosen, this being in the region where all oxygen sites are individually resolved, but high enough to give a reasonably short T_1, enabling relatively rapid pulse repetitions and therefore short experimental times. In each experiment, 40 values of the set mixing time were used, ranging between 10 μs and 50 s, the latter value being approximately $5 \times T_1$ (T_1 determined from saturation recovery experiments), in order to allow complete relaxation of the signal. A repetition delay of 50 seconds and a pulse duration of 1.9 μs were used.

Since the exchange process to be studied involves all four oxygen sites in the structure, kinetic data could theoretically be obtained from the signal due to any of the sites. A decision was therefore made to use only the intensity data for the overlapped O1/O2 peak, since this is approximately six times as intense as both the O3 and O4 peaks. This enabled spectra with sufficient signal to noise to give reliable data to be acquired in practically reasonable experimental times.

The choice of values for the other parameters associated with the initial excitation was less obvious. In the simple case of 2 site exchange in a spin ½ system, the transmitter should be set to the midpoint between the frequencies of the two resonances, and the t_1 evolution time set to half of the reciprocal of the frequency difference between them. This leads to a starting point (at zero mixing time) where the peaks for the two sites have the same intensity but opposite phases, and their recovery can easily be followed. In the case of ZrW_2O_8, where four sites are in mutual exchange and the nucleus under study is quadrupolar, the problem is considerably more complex, and it is not straightforward to determine theoretically the optimum values of t_1 and transmitter position. A trial and error approach was therefore used to determine the conditions experimentally.

A series of experiments was performed with a range of starting conditions - various values of t_1 and transmitter frequency as listed in Table 4-1, while the other experimental parameters were as previously described.

Label of data point in Figure 4-3	Transmitter frequency where ^oX is the resonance frequency of site X	t_1 /µs
Unlabelled points	$^oO1/O2$	58
A	$(^oO1/2+^oO4)/2$	100
B	$(^oO1/2+^oO4)/2$	22
C	$^oO4$	22
D	$^oO3$	58
E	$^oO1/O2$	22

Table 4-1 Starting conditions for 1D-EXSY experiments.

In each experiment, the intensity of the O1/O2 centreband peak was determined by integration, and its variation as a function of mixing time plotted. This variation, which is due to a combination of exchange between sites and the relaxation, followed a smooth multi-exponential decay in all cases. Attempts to fit this to either a single exponential decay curve or a double exponential resulted in a poor fit to the data but it was found that the data for each 1D-EXSY experiment (intensity as function of mixing time) could be fitted to the sum of a minimum of three exponential decay curves, as in Equation 4-1.

$$I = A_1 e^{-k_1 t} + A_2 e^{-k_2 t} + A_3 e^{-k_3 t} \qquad [4\text{-}1]$$

where I is the integrated signal intensity, k_1, k_2, k_3, A_1, A_2 and A_3 are fitted parameters. Thus six parameters were obtained from the multi-exponential fitting to Equation 4-1. A sample data set is shown in Figure 4-2. The rate constants obtained from this curve are: k_1 = 550 ± 50 s^{-1}, k_2 = 11 ± 1 s^{-1} and k_3 = 0.17 ± 0.02 s^{-1}.
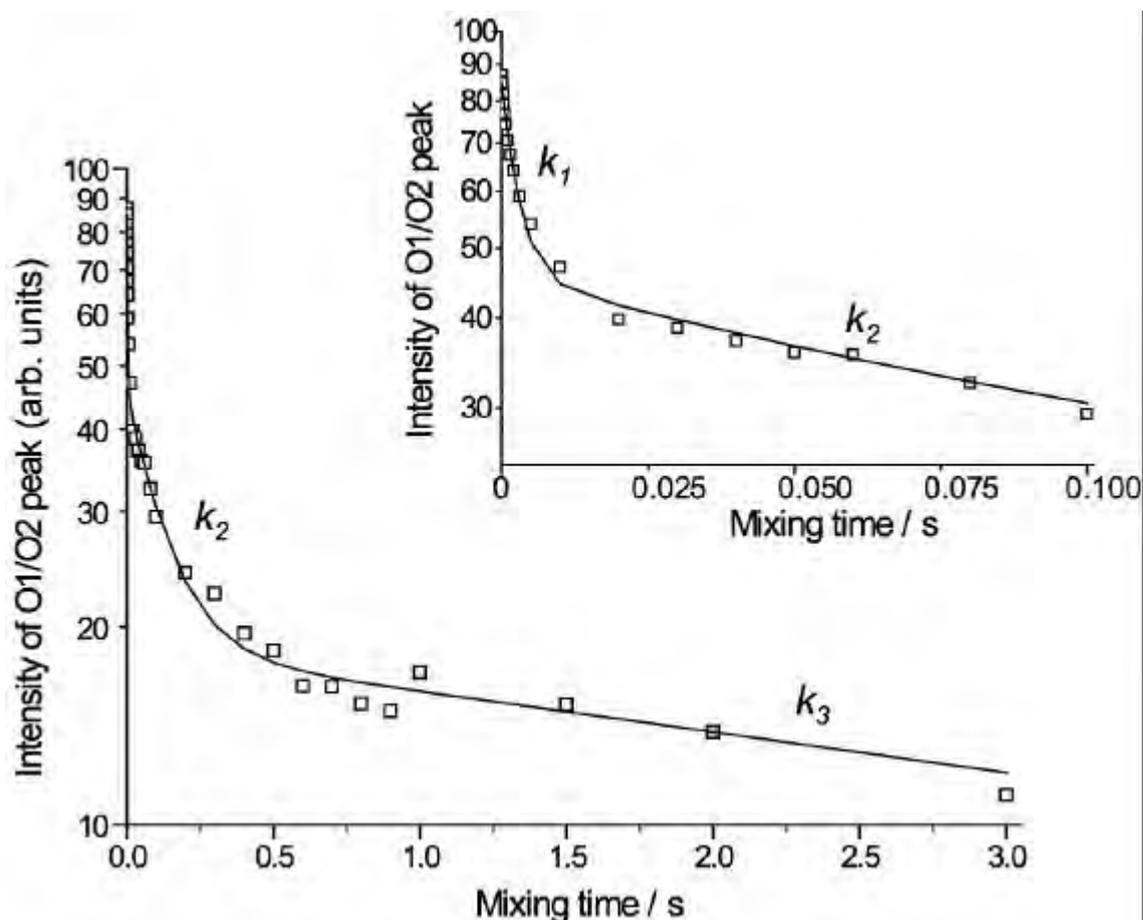
Figure 4-2 Intensity at maximum (437.1 ppm) of the O1/O2 overlapped peaks as function of mixing time obtained by a 1D-EXSY experiment with $t_1 = 58$ µs, transmitter frequency set to 67.771363 MHz. Calibrated temperature 110 ºC, MAS rate 14.5 kHz. Data processed with 900 Hz exponential line broadening. The fitted line is a sum of three exponential decay curves as described in the text. The inset shows an expansion of the data at $t_{mix} = 0.1$ s.

The fitted values of the rate constants k_{1-3} and amplitudes A_{1-3} were seen to vary considerably from experiment to experiment. In order to determine if this was a systematic variation, plots of the fitted parameters were made and inspected for any correlations between the starting conditions and the obtained parameter values. Ideally one would be able to find a clear link between the conditions and the values obtained for the rates, but this proved impossible. Although there was an approximate trend – experiments giving a high rate constant for one process also tended to give higher values for the other rates – there was no clear link to the experimental conditions. Two examples of scatter plots of the determined rate parameters are presented in Figure 4-3, and a complete set of scatter plots is included in the Appendix.
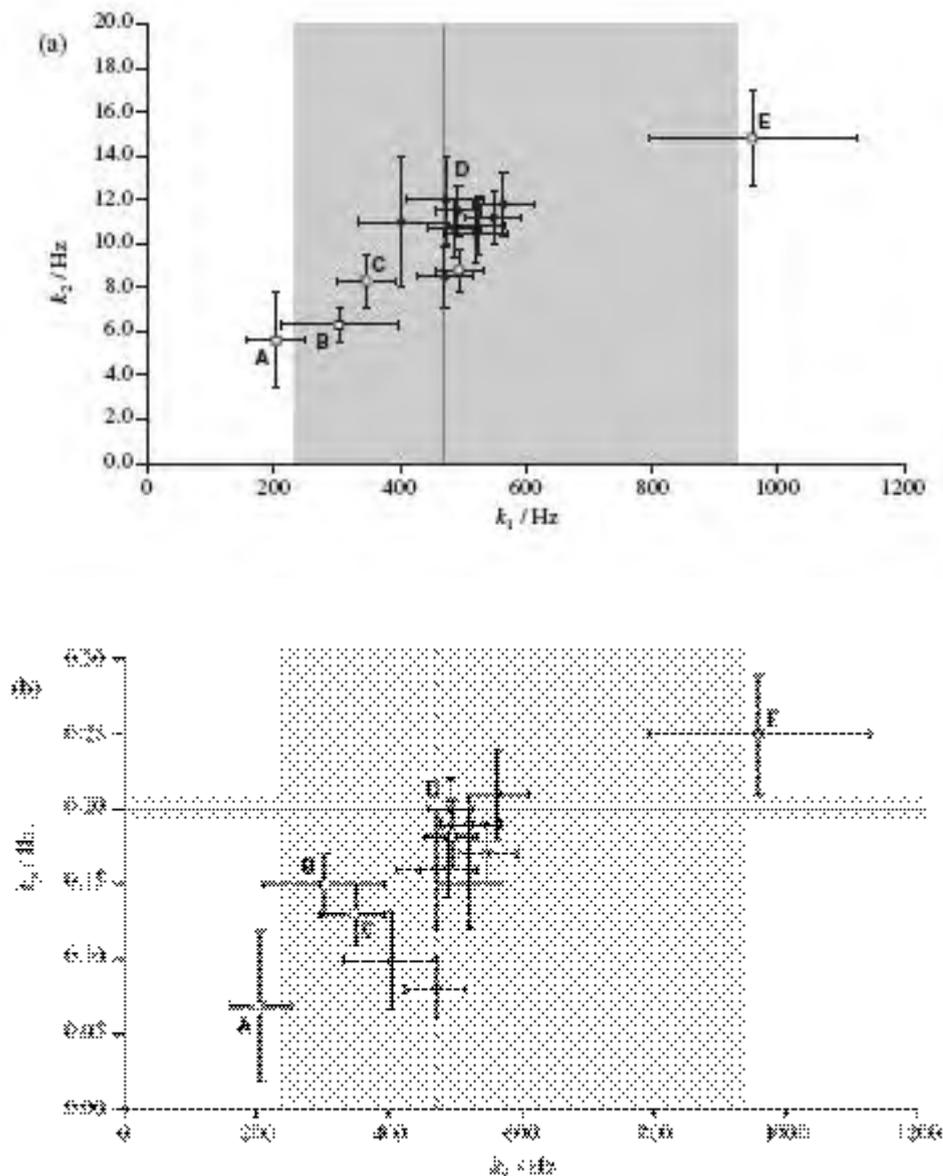
Figure 4-3 Scatter plots of fitted rate parameters for 1D EXSY experiments[11] (a) shows k_2 vs k_1 and (b) shows k_3 vs k_1. All experiments were carried out at 110 ºC, MAS rate 14.5 kHz. Error bars on data points are taken from the fitting of the rate constants. Closed points are for repeated experiments with the same starting conditions (transmitter set to the frequency of the O1/O2 peak and t_1 = 58 µs). Open points are for other experiments with various starting conditions, as defined in Table 4-1. The vertical solid line and shaded area represent the average value and estimated error range for k_1 respectively, while the horizontal line indicates the value of the relaxation rate R_1 (and error range) from a saturation recovery experiment at the same temperature.

The experiments with the transmitter frequency at the frequency of the O1/O2 peak and t_1 = 58 µs gave the greatest signal intensity for the O1/O2 peak, and may therefore be taken to give the most reliable results for the rate constants. A number of experiments with these starting conditions were carried out, to establish the reproducibility of the results. The rate constants obtained from these experiments are shown by the closed points in Figure 4-3. It is seen that

there is still considerable scatter on the rate constants, but the data points are clustered within the error bars of the fitting.

	Mean	Minimum	Maximum
k_1	450	80 ± 7	960 ± 170
k_2	9.5	3.9 ± 0.5	15 ± 2
k_3	0.15	0.05 ± 0.01	0.25 ± 0.04

Table 4-2 Range of values for fitted rate constants (s^{-1}) for 1D-EXSY experiments at 14.5 kHz and 110 ºC. Errors shown for maximum and minimum values are those derived from the fitting.

The fitted values for the three rates are summarised in Table 4-2. Although the variation in the rates is larger than the errors obtained from the individual fits, the rates may be stated, with some confidence, as being within a factor of 2 of their mean values, as indicated by the shaded region in the figures.

4.1.5 Theory for kinetic analysis

Having obtained the results discussed above, attempts were made to develop a theory to explain the observations, with the intention of extracting kinetic information from the fitting of the 1D-EXSY data. The signal recorded by a 1D EXSY experiment such as this is affected by both chemical exchange and the normal T_1 relaxation of the nuclei. In the simplest case (a spin $I = \frac{1}{2}$ nucleus), the change in magnetisation of an NMR signal as a function of mixing time would fit to the sum of two exponential curves: one for the longitudinal (T_1) relaxation and one corresponding to the exchange between nuclei.

In fact, as the results above confirm, the change in signal intensity is notably more complicated in this case. The theoretical basis for the observed behaviour had yet to be developed since, to our knowledge, this is the first attempt to determine quantitative kinetic data from 1D-EXSY of half-integer quadrupolar nuclei in the solid state. It was therefore necessary to construct a theoretical description of both the exchange and the relaxation in order to explain the multi-exponential behaviour.
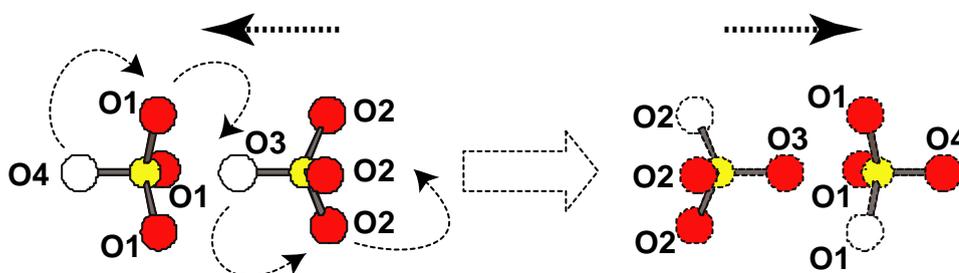

Figure 4-4 The proposed ratcheting model of oxygen exchange in cubic ZrW$_2$O$_8$. The W$_2$O$_8$ groups reverse direction (indicated by the solid black arrows) by a concerted rotation of the intact WO$_4$$^{4-}$ tetrahedra.

A schematic diagram of the exchange process is shown in Figure 4-4. Since the peaks for O1 and O2 are overlapped and impossible to resolve separately reliably, they are treated as one site in the kinetic analysis which follows. The kinetics of site exchange are therefore analysed on the basis of exchange between three environments: O3, O4 and O1/O2. This does not present a problem since it is known (from the studies in Chapter 3) that exchange process involves mutual exchange of all four sites. The rate equation for the change of magnetisation, M, due to chemical exchange is as follows, where M^0 is the magnetisation of each site at the start of the mixing time, as given in 4-2.

$$\left[\frac{d(M_{O1/O2})}{dt} \frac{d(M_{O3})}{dt} \frac{d(M_{O4})}{dt} \right] = \mathbf{K} \begin{bmatrix} M^0_{O1/O2} \\ M^0_{O3} \\ M^0_{O4} \end{bmatrix} \qquad \text{[4-2]}$$

$\mathbf{K}$ is a kinetic matrix with elements K_{ij} giving the rate of magnetisation transfer from site j to site i. Assuming that the exchange occurs due to a ratcheting process, as shown in Figure 4-4, which causes jumps between oxygen sites (O4? O2 and O3? O1) to occur with rate k with equal probability, and given the ratio of sites in the structure of O1/O2 : O3 : O4 = 6 : 1 : 1, the kinetic matrix, $\mathbf{K}$, is obtained, as defined in Equation 4-3.

$$\mathbf{K} = \begin{bmatrix} -2k & k & k \\ k & -k & 0 \\ k & 0 & -k \end{bmatrix} \qquad \text{[4-3]}$$

The function for the magnetisation of O1/O2 derived from this kinetic matrix is as in Equation 4-4.

$$M_{O1/O2}(t) = \mathbf{a}_0 + \mathbf{a}_{-3k} e^{-3kt} \qquad \text{[4-4]}$$

$\mathbf{a}_0$ and $\mathbf{a}_{-3k}$ are coefficients of the eigenvalues of $\mathbf{K}$. Only one rate constant, equal to *-3k*, due to exchange alone would be observed in the 1D-EXSY experiments.

Other models for motion which lead to mutual exchange of all oxygen sites could be proposed, which would also be consistent with the observed NMR spectra. For example, a physically unlikely model in which a single jump causes full random exchange of sites may be considered. In contrast to the ratcheting model, O3 may then be converted directly to O4, with a rate $k/8$. The full exchange matrix would be $\mathbf{K}_{random}$, as in Equation.

$$\mathbf{K}_{random} = \begin{bmatrix} -\dfrac{3k}{2} & \dfrac{3k}{4} & \dfrac{3k}{4} \\ \dfrac{3k}{4} & -\dfrac{7k}{8} & \dfrac{k}{8} \\ \dfrac{3k}{4} & \dfrac{k}{8} & -\dfrac{7k}{8} \end{bmatrix} \qquad \text{[4-5]}$$

This matrix, $\mathbf{K}_{random}$ (Equation 4-5), is very similar to that for the ratcheting model, $\mathbf{K}$ (Equation 4-3) and gives very small differences to the rates which would be observed experimentally. The expression for the O1/O2 magnetisation is essentially identical to that in Equation 4-3, but with the eigenvalue $-9k/4$ rather than $-3k$. It would thus be extremely difficult to distinguish between mechanisms which cause complete oxygen scrambling by ^{17}O NMR, particularly in the presence of multi-exponential T_1 relaxation as discussed below. The simpler, and more physically reasonable, ratcheting model is thus assumed, and the kinetic matrix in Equation 4-3 is used.

The effects of T_1 relaxation on the intensity in the magnetisation transfer experiments must also be considered in some detail. Since ^{17}O is a quadrupolar ($I = ^5/_2$) nucleus the relaxation behaviour is also multi-exponential, with simultaneous relaxation between multiple energy levels. T_1 relaxation in a half integer quadrupolar system may be explained by one of two mechanisms, "quadrupolar" and "magnetic".

In the case of quadrupolar relaxation, it is the effect of motion of a nucleus on the orientation-dependent quadrupole interactions of that nucleus which drives relaxation. Transfers between $\Delta m_I = \pm 1$ and $\Delta m_I = \pm 2$ coherences follow Equations 4-6 and 4-7.

$$W_{m_I \to m_{I-1}} = f_1(I, m_I)W_1 \qquad [4\text{-}6]$$

$$W_{m_I \to m_{I-2}} = f_2(I, m_I)W_2 \qquad [4\text{-}7]$$

where W_1 and W_2 are two distinct rates associated with the $\Delta m_I = \pm 1$ and $\Delta m_I = \pm 2$ transitions respectively and $f_k(I, m_I)$ are numerical factors.

In the case of a magnetic mechanism, it is the variation in local magnetic field caused by fluctuations of surrounding nuclei which drives T_1 relaxation. Relaxation may only occur across NMR allowed transitions, between adjacent ($\Delta m_I = \pm 1$) energy levels, with probability as defined in Equation 4-8. .

$$W_{m_I \to m_{I-1}} = (I + m)(I - m + 1)W \qquad [4\text{-}8]$$

Experiments described in Section 4.2 show that in the case of ZrW$_2$O$_8$ relaxation does occur by a magnetic mechanism, although a precise understanding of relaxation is not necessary for the analysis of data from these magnetisation transfer experiments.

A relaxation matrix, $\mathbf{R}$, for the $I = ^5/_2$ case may be determined by considering the population differences between adjacent energy levels. The elements of this matrix give the rates at which magnetisation is transferred between transitions. The rate of change of $M_i(t)$ for each transition theoretically has one component for each of the five eigenvalues of $\mathbf{R}$ ($2W$, $6W$,

$12W$, $20W$ and $30W$). However, since $M(0)$ is usually symmetrical ($m_i = m_{-i}$), only the odd eigenvalues ($2W$, $12W$ and $30W$) contribute.

It is possible to combine the theoretical description of exchange with that for relaxation, to allow a complete description of the 1D EXSY results. A 15 × 15 matrix, $\mathbf{L}$, which fully describes the combined effect of relaxation and site exchange is obtained by combining the matrices as in Equation 4-9.

$$\mathbf{L} = \mathbf{R} \otimes \mathbf{1_K} + \mathbf{1_R} \otimes \mathbf{K} \qquad [4\text{-}9]$$

The time dependence of the O1/O2 magnetisation under combined effects of exchange and relaxation is determined by the eigenvalue of the matrix $\mathbf{L}$, and has the form of Equation 4-10.

$$\begin{aligned} M_i^{O1/O2} &= \boldsymbol{a}_{2W} e^{-2Wt} + \boldsymbol{a}_{12W} e^{-12Wt} + \boldsymbol{a}_{30W} e^{-30Wt} \\ &+ \boldsymbol{b}_{2W} e^{-(2W+3k)t} + \boldsymbol{b}_{12W} e^{-(12W+3k)t} + \boldsymbol{b}_{30W} e^{-(30W+3k)} \end{aligned} \qquad [4\text{-}10]$$

There are six expected components with rate constants $2W$, $12W$, $30W$, $(2W+3k)$, $(12W+3k)$ and $(30W+3k)$. The coefficients ($\boldsymbol{a}_I$ for pure relaxation and $\boldsymbol{b}_I$ for components combining relaxation and exchange) of the six components depend on the initial magnetisations. Full details of the development of the theory behind the treatment of data is given in a published article, which is included as an Appendix to this thesis.[11]

4.1.6 Application of kinetic theory to data analysis

According to the theory outlined above, the intensity data for the 1D EXSY require six exponentials to fully describe the combination of exchange and relaxation effects. Attempts to fit six exponentials to the data were made, but it proved impossible to independently fit so many exponential components reliably. This is unsurprising given that the time constants for a number of the exponential components are very similar.

The coefficients of each of the six components will depend strongly on the conditions of excitation, and it may be possible to constrain the fitting if information about the initial populations of the different coherences were known. The initial state of the system will be influenced by a large range of factors, including the stimulation of satellite transitions as well as the central $+\frac{1}{2}$? $-\frac{1}{2}$ transition and the transfer of magnetisation between the different coherences over the mixing time. Unfortunately it is not possible to understand precisely the starting conditions of the various experiments in sufficient detail to allow a constrained fitting.

Since it is not possible to determine the coefficients and time constants of all six components, it was decided to limit the fitting to the tri-exponential expression already described. The three rates obtained from the fitting, k_1, k_2 and k_3, may be compared to the rate constants expected by the theoretical analysis, $2W$, $12W$, $30W$, $(2W+3k)$, $(12W+3k)$ and $(30W+3k)$.

The faster process observed (k_1) clearly corresponds to the three $xW + 3k$ components, although it is not possible to separate these components, and hence k_1 can be interpreted as giving only an upper limit of the value of $3k$, rather than an absolute value. It will actually correspond to a sum of the exchange process and components of the relaxation processes. The mean value of k_1 obtained therefore gives a value of k_{exch} of 160 s^{-1} (to 2 s.f.). The values of k_1, as shown in Figure 4-3, show a considerable spread, but most values are included by a range covering a factor of 2 smaller or larger than the average value. It is reasonable to estimate that the actual exchange rate at this temperature (110 ºC), which is determined from k_1, has an analogous error. Hence we may state that k_{exch} is in the range 80 – 310 Hz (to 2 s.f.)

The k_2 component in the fitting will correspond to a combination of the faster relaxation processes ($12W$, $30W$) and the $xW + 3k$ processes involving exchange.

The k_3 component is due to the slowest process, which is dominated by the $2W$ component corresponding to a value of the longitudinal relaxation rate constant, $R_1 = 1/T_1$. The relaxation rate should fit well with the direct measure of T_1 from relaxation experiments (Section 4.2), and indeed the value of $k_3 = R_1 = 0.15$ s^{-1} gives a time constant of 6.7 s, consistent with the T_1 obtained at the same temperature.

The theoretical analysis shows that the processes are considerably more complex than is allowed for in the tri-exponential fitting procedure. It is therefore unsurprising that there is some error in the fitting, and inconsistency between experiments, as it is an approximation to treat k_1, k_2 and k_3 as entirely separate kinetic processes. However, despite these difficulties, it has been possible to use this analysis to obtain an estimate of the exchange rate at this temperature.

4.2 T$_1$ Relaxation Studies

Although there is considerable error in the absolute rate obtained from the 1D-EXSY experiments, these uncertainties do not affect the determination of relative rates, from which the activation energy may be derived. As described in chapter 2, motional processes usually dominate NMR relaxation processes, and so T_1, may be interpreted to give information about dynamics. If the relaxation is dominated by a single motional process, the variation of T_1 as a function of temperature is a simple and robust way to determine activation energy which can be obtained simply by interpretation of the T_1.

In the case of ZrW$_2$O$_8$, the 2D-EXSY experiment has shown that the oxygen atoms are highly mobile and that this mobility is dominated by a rotational process which causes mutual exchange between all oxygen sites, which is understood to follow the ratcheting mechanism shown in Figure 4-4. It may therefore be assumed that this exchange process is the most significant motional process in the structure, and that this will be the dominant process driving the relaxation of magnetisation.

4.2.1 Saturation Recovery Experiments

There are a number of techniques which may be used to measure the spin-lattice relaxation constant, T_1, as described in the introduction (Chapter 2). One of the simplest and most robust methods is the saturation recovery experiment, and this technique was used for the experiments discussed in this chapter.

Estimates of the T_1 at each temperature were first made by carrying out rough saturation recovery experiments, fitting the data to a simple single exponential. The purpose of these rough experiments was to determine appropriate time delays to use in the accurate experiments. Then, at a range of temperatures in the range 40 – 226 °C, more accurate saturation recovery experiments were undertaken. At each temperature, an experiment was carried out using 40 increments of the delay time, with 32 transients per increment. The range of delay times was chosen on the basis of the approximate T_1 values so that the full recovery of signal could be captured in each case.

4.2.2 Fitting of Saturation Recovery Curves

The return to equilibrium of the magnetisation may be measured by taking the intensity of a certain peak at each value of the delay time. In the case of ZrW$_2$O$_8$, it has already been shown that the oxygen sites are in exchange on a time scale much faster than the relaxation time, and so all sites would give the same value of T_1. Since the overlapped O1/O2 peak is considerably more intense than the other peaks, the intensity of this peak was used. A baseline correction was applied to all data and then the integrated intensity of the O1/O2 overlapped peaks was measured as a function of delay time.

In the case of a spin I = ½ nucleus the magnetisation returns to its equilibrium value *via* a single exponential process, and saturation recovery data may be fitted using the Equation 4-11.

$$\mathrm{M}(\boldsymbol{t}) = \mathrm{M}_{eq}\left(1 - \exp\left[\frac{-\boldsymbol{t}}{\mathrm{T}_1}\right]\right) \qquad [4\text{-}11]$$

In the case of quadrupolar nuclei, such as ^{17}O, the relaxation process is complicated by the transfer of magnetisation between different coherences, resulting in a multi-exponential relaxation process.
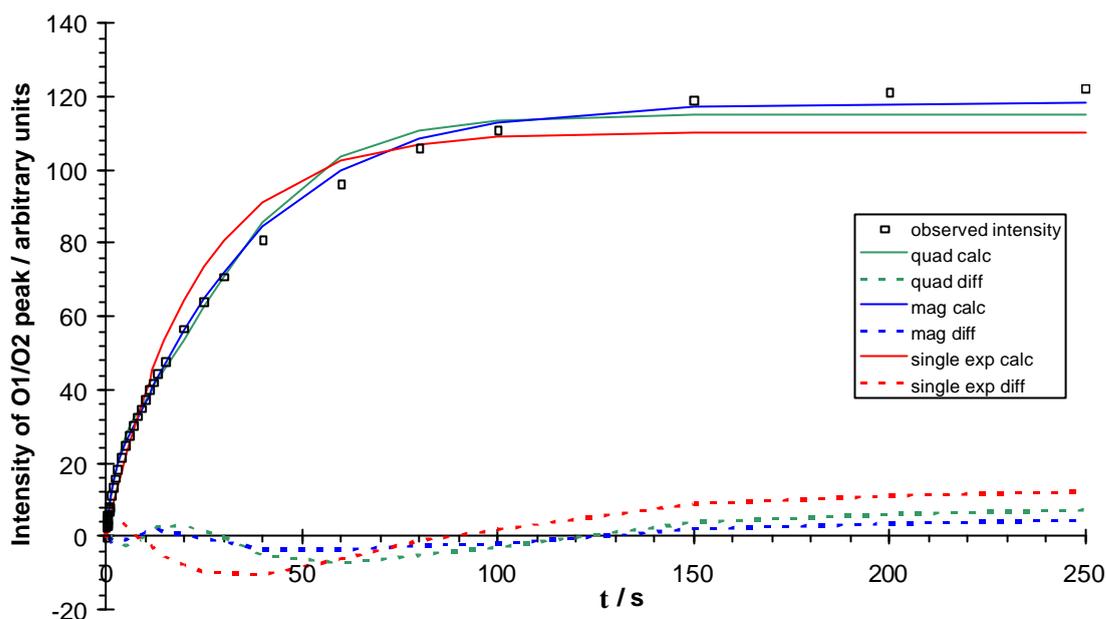
Figure 4-5 Saturation recovery data for ZrW$_2$O$_8$ at 40 °C, fitted using three different models, a quadrupolar relaxation mechanism (green), a magnetic relaxation mechanism (blue), and a single exponential recovery (red).

The saturation recovery data were fitted to three different models, as shown in Figure 4-5: a single exponential recovery, a pure magnetic relaxation model (three rates with fixed ratio 2W : 12W : 30W) and a quadrupolar model (with rates in the ratio $^{4W}/_5$: $^{3W}/_2$: $^{33W}/_{10}$). In fact the quadrupolar model allows for two distinct rates, W_1 and W_2.. The ratio of the two rates was fixed at 1 ($W_1 = W_2$) for the purposes of this fitting so that both multi-exponential fits used the same number of parameters, enabling a fair comparison of the quality of fit.

It is clear that the two multiple exponential methods both fit better than the single exponential, although the residuals show that both still have a systematic error. The two multi-exponential models have the same number of free parameters, and the fits are therefore directly comparable. Whether the quadrupolar or magnetic model is used, the slowest component (equivalent to k_3 in the EXSY analysis) is always dominant, and so is taken to be the characteristic time constant "T_1" for the relaxation. The coefficients of the different rate components depend on the specific nature of excitation. The best fit is given by the magnetic mechanism, across the temperature range studied. As studies of the sample with lower isotopic enrichment also indicated a magnetic mechanism (see section 4.2.3), it was decided to use the magnetic mechanism to fit the saturation recovery data in further quantitative analysis.

For the purposes of kinetic studies, the variable temperature saturation recovery experiments at sample temperatures below 180 °C were therefore fitted to the magnetic mechanism. *i.e.* a sum of three exponentials, with time constants T_1, (T_1 / 6) and (T_1 / 15), as shown in Equation 4-12.

The processes with shorter time constants are due to quadrupolar effects and the dominant process with the longer time constant may be taken as a reliable value of T_1.

$$M(t) = A_{2W}\left(1 - \exp\left[\frac{-t}{T_1}\right]\right) + A_{12W}\left(1 - \exp\left[\frac{-6t}{T_1}\right]\right) + A_{30W}\left(1 - \exp\left[\frac{-15t}{T_1}\right]\right) \quad [4\text{-}12]$$

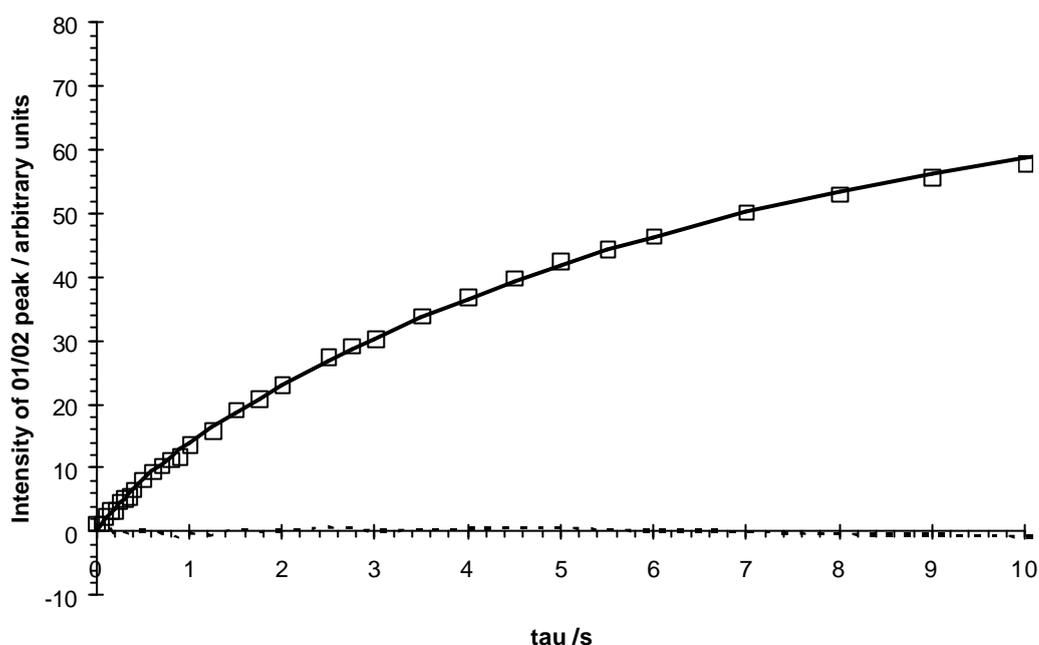A fitted curve is shown in Figure 4-6, illustrating the multi-exponential behaviour.

Figure 4-6 Fitting of sample T_1 relaxation data recorded at 110 ºC, integrated intensity of the overlapped O1/O2 peaks. The fitted curve is the sum of three exponentials with time constants T_1 = 6.3 s ± 0.4 s, (T_1 / 6) and (T_1 / 15). The fitted curve is shown by the solid black line, and the difference by the dashed black line.

At temperatures above the phase transition it was found that the saturation recovery becomes more like a single exponential, as shown in Figure 4-7, and so at temperatures above 180 °C the data were fitted to a single exponential (as in Equation 4-13)

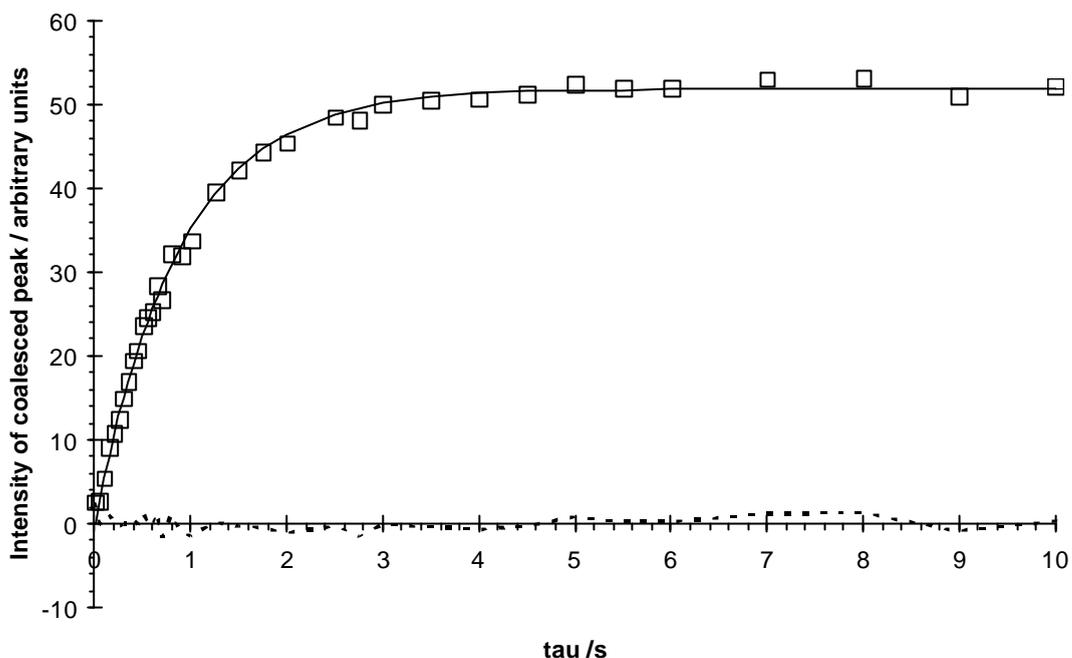$$M(t) = A\left(1 - \exp\left[\frac{-t}{T_1}\right]\right) \quad [4\text{-}13]$$

Figure 4-7 Fitting of sample *T$_1$* relaxation data recorded at 229 ºC, integrated intensity of the coalesced peak. The fitted curve is a single exponential with time constant *T$_1$* = 0.49 s ± 0.02 s. The fitted curve is shown by the solid black line, and the difference by the dashed black line.

In both the multi-exponential and single exponential regimes, the intensity data are well fitted. A plot of T_1 as a function of temperature (Figure 4-8) shows that T_1 decreases steadily with increasing temperature. It is also notable that the error in T_1 decreases significantly with increasing temperature, as shown by the error bars on T_1, reflecting a reduction in the systematic error in fitting as the relaxation tends toward simple exponential behaviour. The temperature variation was used to determine the activation energy for oxygen motion (see Section 4.3).
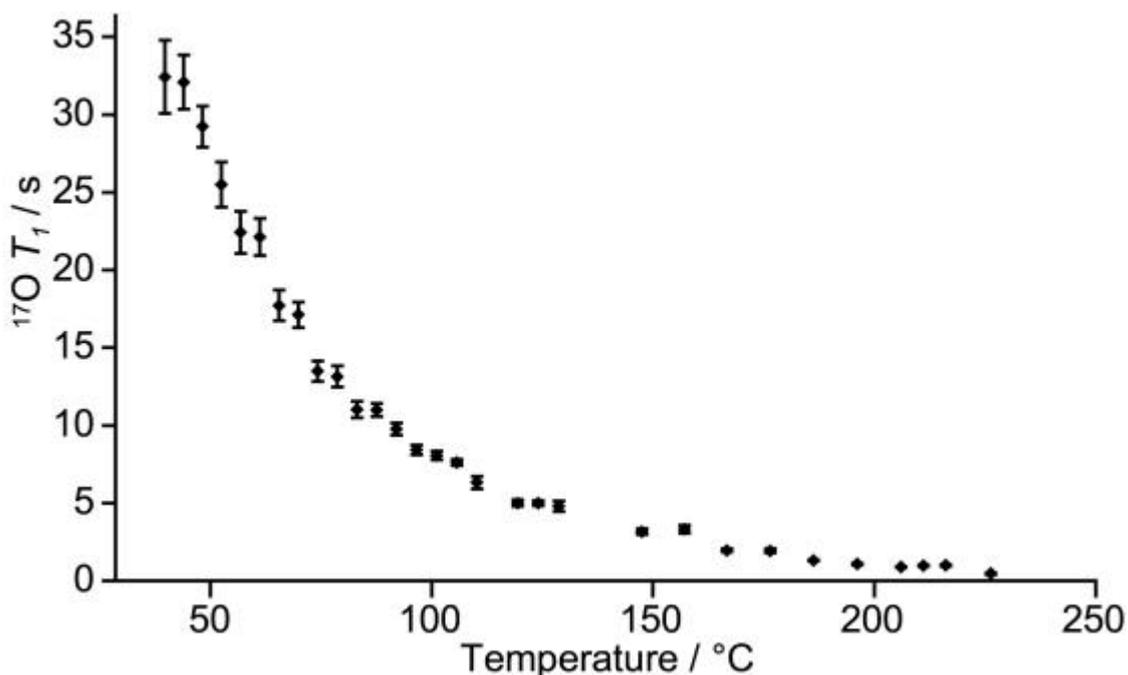
Figure 4-8 Variation of T_1 with temperature. For the temperature range up to 176 °C T_1 values from were obtained by fitting the integral of the O1/O2 peak to a magnetic relaxation model (3 exponentials). For the temperature range from 186 °C to 226 °C the T$_1$ values from were obtained from a single exponential fit of the integral of the coalesced peak. Error bars show the estimated standard deviation (e.s.d.) values determined from the fitting.

4.2.3 Effect of ^{17}O concentration

It is useful to observe how the relaxation behaviour varies with concentration of ^{17}O nuclei in the sample, as this will give additional evidence to help confirm which relaxation mechanism was dominant. If quadrupolar relaxation is dominant, that is the interaction of a nucleus with its own electric field gradient drives relaxation, then concentration of ^{17}O nuclei in the sample should have no effect. If relaxation is driven by the presence of other quadrupolar nuclei in the sample (i.e. magnetic relaxation is dominant), then the values of T_1 should become smaller as the concentration of ^{17}O is increased. Identical T_1 saturation experiments were therefore carried on 2 samples of enriched ZrW$_2$O$_8$ with differing degrees of isotopic enrichment (mrh026 prepared with 41 % ^{17}O water and mrh146 prepared with 28 % ^{17}O water) - see chapter 3 for synthetic details.

A comparison of the T_1 times for the two samples is given in Table 4-3. T_1 is seen to be consistently longer for the less highly enriched sample, suggesting the concentration of ^{17}O nuclei in the sample has a significant effect on the relaxation, and that a 'magnetic' mechanism has a significant contribution to the mechanism of relaxation. The mean ratio of the relaxation times for the two samples, T_1 (mrh146) : T_1 (mrh026) is 2.1.

Sample Temperature / °C	T_1 (mrh146)	T_1 (mrh026)	Ratio T_1 (mrh146) : T_1 (mrh026)
44	94 ± 11	32 ± 2	2.9
70	25 ± 4	17.1 ± 0.8	1.5
83	25 ± 4	11.0 ± 0.5	2.3
101	14 ± 1	8.1 ± 0.3	1.8

Table 4-3 Comparison of T_1 values for the two ZrW_2O_8 samples. Errors stated are those obtained from the fitting.

The variation of T_1 for both samples is shown in Figure 4-9; the data are shown as a plot of $\ln(T_1)$ vs. 1/T for comparison with the Arrhenius plot presented in Figure 4-10.

Figure 4-9 Variation of T_1 with inverse temperature for two samples of ZrW_2O_8 synthesised with 41 % ^{17}O water (mrh026) (square points, open for temperatures above the phase transition temperature, closed below the phase transition) and 28 % (mrh146) (triangular points).

The data derived frrom experiments with the more highly enriched sample were used for all quantitative kinetic studies as this gave higher signal to noise, and also experiments could be completed in less time, due to the shorter T_1 relaxation times enabling shorter pulse repetition delays. It is worth noting that the less highly enriched sample would have made some experiments, such as acquisition of the 2D EXSY spectrum, prohibitively time consuming. *i.e.* high enrichment can influence not only the intrinsic sensitivity due to abundance effects but also sensitivity due to higher repetition rates.

4.3 Temperature dependence of exchange rate

The T_1 data measured by saturation recovery were plotted as a function of temperature (Figure 4-9). As expected from earlier experiments it was found that T_1 decreases significantly over the temperature range studied. The T_1 relaxation rate will be proportional to the rate of the dominant motional process driving the relaxation, and so the exchange rate can be worked out by using a simple constant of proportionality. At 110 °C, the exchange rate, k_{exch} had previously been measured as 160 Hz (2 s.f.) in the 1D-EXSY experiments (Section 4.1), and so the value of the proportionality constant may be calculated. The relationship between T_1 /s and k_{exch} /Hz is as given in Equation 4-14.

$$k_{exch} = \frac{980}{T_1} \qquad\qquad [4\text{-}14]$$

The saturation recovery-derived T_1 values were converted to exchange rate as a function of temperature, as shown in Figure 4-10.
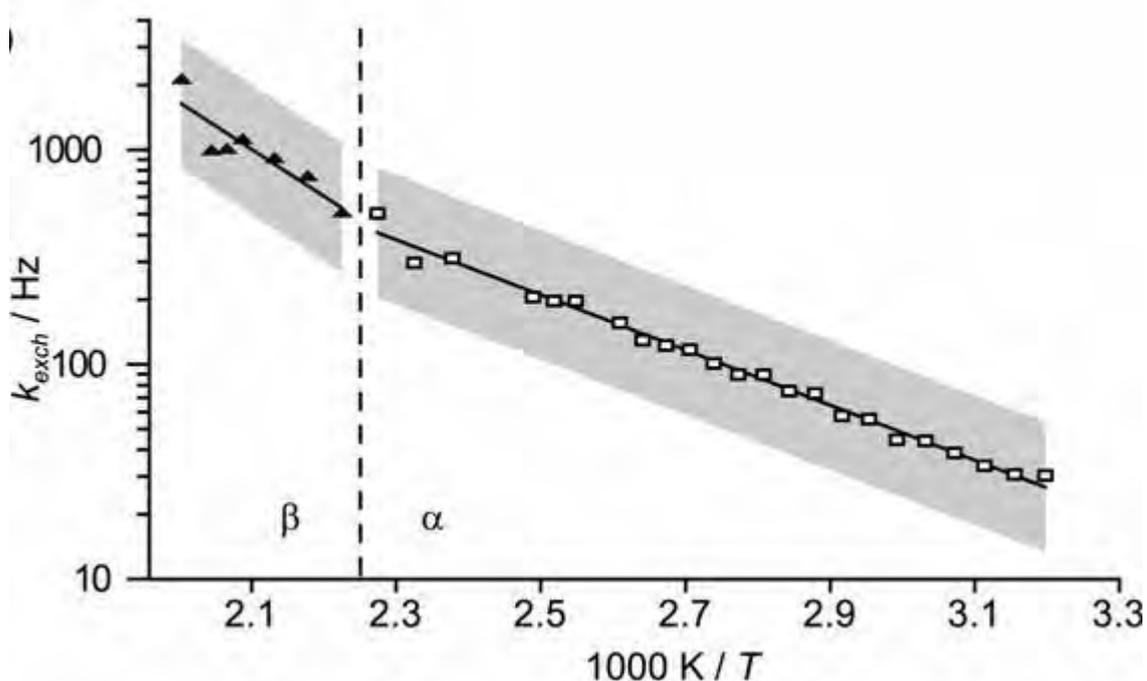

Figure 4-10 Exchange rates calculated from T_1 time constants as function of inverse temperature.

The graph of k_{exch} (plotted on a logarithmic scale) against inverse temperature, shown in Figure 4-9, shows two linear sections, with a distinct change in gradient around the known phase transition temperature of 175 °C. The fact that the two region sections are linear points to a single motional process driving the relaxation, and the dominant motional process is an exchange involving all oxygen sites (as shown by the 2D EXSY experiment in Chapter 3). The two linear sections were fitted separated by linear regression to an Arrhenius expression, giving the values shown in Table 4-4. It should be noted that any uncertainties in the *absolute* rate at

110 °C determined by the EXSY analysis will affect the proportionality constant, but will not affect the activation energy barriers, which are derived from the gradient.

	E_a / kJ·mol^{-1}	$\log_{10}$ (A / s^{-1})
a phase	24.5 ± 0.5	5.5 ± 0.1
β phase	42 ± 9	7 ± 1

Table 4-4 Arrhenius parameters derived from fitting the variation of ^{17}O NMR T_1 in ZrW$_2$O$_8$ (mrh026).

These activation energies in good agreement with results obtained for ZrW$_2$O$_8$ and related materials using different techniques in the literature. At high temperatures, dielectric measurements by Evans *et al.* gave an estimated activation barrier for oxygen exchange[12] of 0.50 eV (48 kJ·mol^{-1}) between ~500 and 800 K for ZrW$_2$O$_8$. Time-dependent powder diffraction studies have provided rate estimates in the low temperature phases of related materials. A series of time-dependent experiments on a quenched sample of the related compound ZrWMoO$_8$ have been carried out by Allen and Evans,[13] these gave an activation energy of 34 ± 5 kJ·mol^{-1} between 205 and 230 K. A possible explanation for the higher activation energy obtained for the *b* phase is that since the cell parameter is smaller, there is more hindrance to rotation of the tetrahedra.

4.4 Discussion

At first sight the NMR results, showing re-orientation of the W$_2$O$_8$ groups at low temperature, would appear to contradict the ordered structure of the low temperature phase indicated by diffraction studies. There are however a number of possible mechanisms which reconcile the information from both methods, two limiting examples of which are illustrated schematically in Figure 4-11.
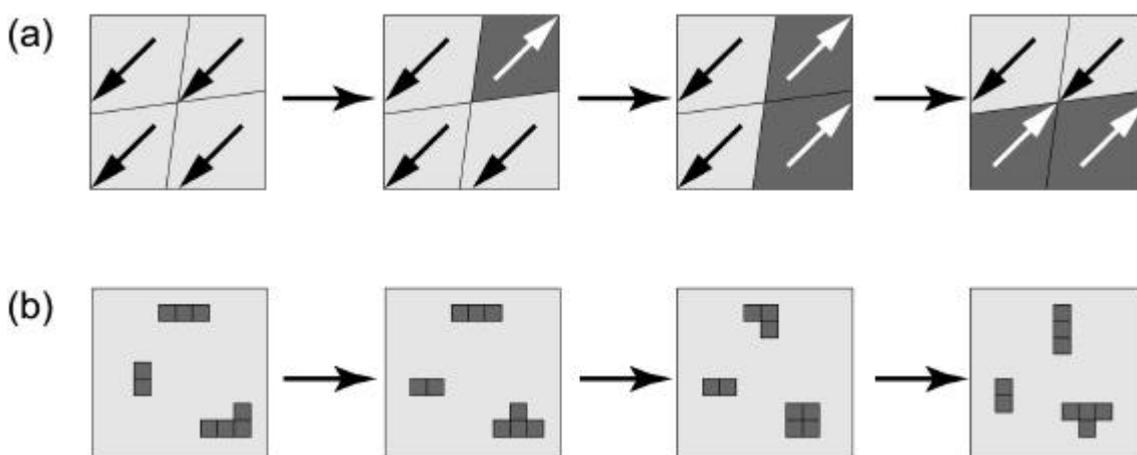

Figure 4-11 Two proposed models of W$_2$O$_8$ re-orientation in ZrW$_2$O$_8$. (a) large domains with a common W$_2$O$_8$ direction indicated by arrows (b) ordered domains (light grey), containing low concentrations of reversed units (dark grey) which fluctuate with time.

One possibility (Figure 4-11 a) is that the structure consists of domains, in which the W$_2$O$_8$ group orientation is fully ordered – if the size of these domains is sufficiently large (>~1000 Å),

diffraction methods would report a fully ordered material. A concerted flipping of the W_2O_8 group orientation throughout the domains could occur, without disordering being observed by diffraction; all configurations in Figure 4-11 a would appear fully ordered by diffraction. As temperature increases towards the phase transition temperature, the size of the ordered domains decreases, so that above the phase transition a fully disordered structure is 'seen' by diffraction.

Another model (Figure 4-11 b) would involve localised flips of W_2O_8 groups within large ordered domains. These fluctuations of small regions of the material (perhaps even individual W_2O_8 groups) could occur many times during the timeframe of a diffraction experiment, but since the predominant structure is ordered, the localised flipped regions would not be observed by diffraction, apart from *via* a gradual change of site occupancies as their concentrations change. This model requires that the rate of reverse jumps, where flipped units realign with the surrounding domain, exceeds the (forward) rate of flipping out of alignment, as would be the case if a jump out of alignment caused increased local strain in the structure. If the rates of forward and reverse jumps were equal, then entropy would drive an equilibrium to a fully disordered structure. As the temperature is increased, the concentrations of the reversed units would be expected to increase, until there are equal numbers of W_2O_8 units with both orientations, giving the time-averaged centrosymmetric *Pa3* structure.

The most significant difference between the two models in terms of kinetics is that the average times between "forward" and "reverse" jumps are identical in the "domain" model, but significantly different in the "fluctuation" model. Unfortunately, it is not possible to distinguish between the two models using the NMR magnetization transfer experiments, as the kinetic exchange matrices would be the same, regardless of the relative rates of forwards and reverse jumps.

Variable temperature diffraction experiments do, however, give evidence for the fluctuation model. The structural investigation by Evans *et al.*[14] shows that there is a gradual decrease in the fractional occupancy of the major W_2O_8 group orientation with increasing temperature (Figure 4-12). The experimentally derived data points, from neutron diffraction, were found to fit well to a three-dimensional Ising model, with essentially no adjustable parameters. An Ising model is a mathematical description of a cooperative order/disorder transition, where the probability of a given element having a particular orientation is dependent on the energy difference caused by that element having a different value to the surrounding nearest neighbour elements. The fact that the occupancy data for the ZrW_2O_8 structure fit to a cooperative ordering model such as the Ising model is consistent with a local fluctuation model, with the reversed units creating local strain.
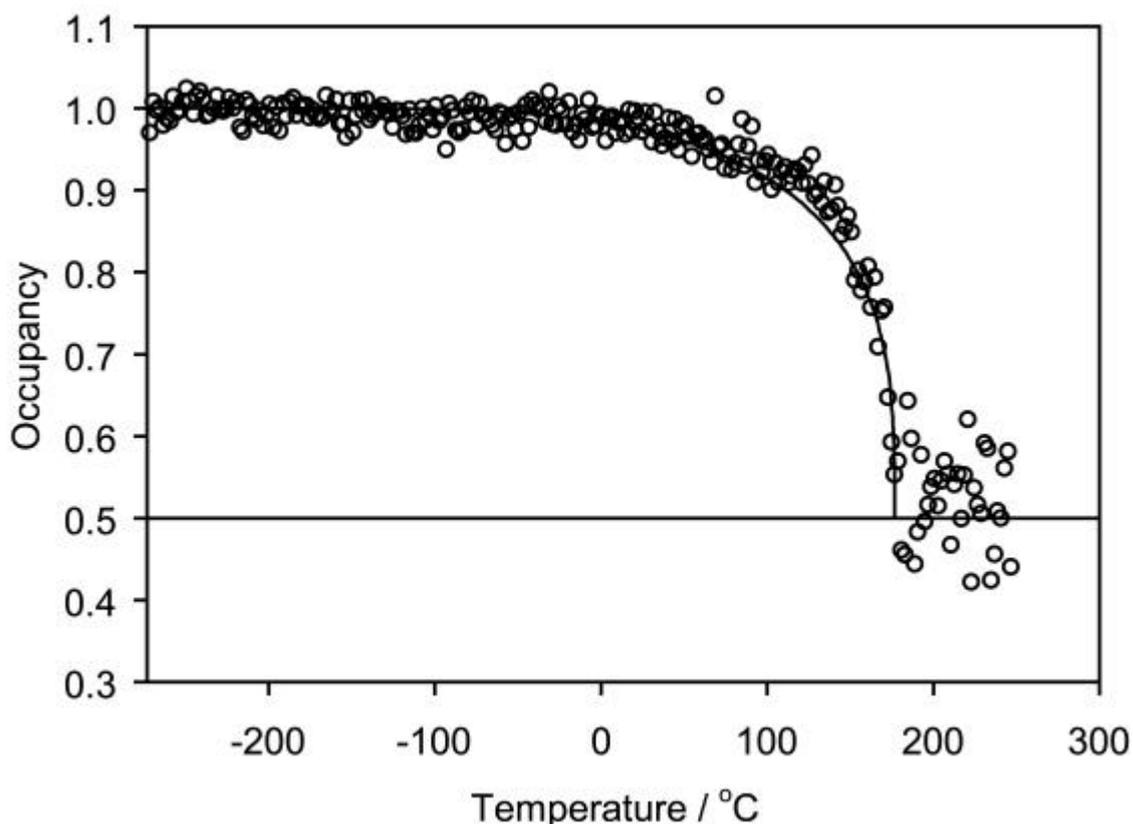
Figure 4-12 Fractional site occupancy of major W$_2$O$_8$ orientation in ZrW$_2$O$_8$ as a function of temperature derived from neutron diffraction data, adapted from Reference 14. The solid line show a fit to a three dimensional Ising model.

Further support for the "fluctuation" model is provided by an examination of the (*h0l*, *h ? 2n*) reflections, which are characteristic of the ordering process. As one approaches the phase transition, these peaks do not show significant broadening relative to other reflections, suggesting a single characteristic length scale for diffraction throughout the material. The "domain" model, in which the size of the ordered domains increases as the phase transition is approaches, would be expected to cause increased broadening of the ordering peaks.

4.5 Conclusions

1D-EXSY experiments have been used to study the rate of oxygen exchange in ZrW$_2$O$_8$. The analysis of the results is complicated by the fact that the combination of exchange and relaxation processes is multi-exponential. A theoretical understanding of the behaviour was developed, which enabled the estimation of an exchange rate from the data. The 1D-EXSY experiments give an approximate value for the rate of exchange between oxygen sites, at one temperature.

It is unfortunately not possible to use the 1D-EXSY results to give a precise value of the exchange rate as a function of temperature. A more appropriate technique to study the temperature dependence of exchange is the measurement of the T_1 relaxation time constant. T_1 saturation relaxation experiments were also carried out. It was found that the relaxation in

ZrW_2O_8 is dominated by a magnetic mechanism, which has important consequences. It has been shown that by increasing the degree of ^{17}O enrichment, T_1 is reduced, thus allowing shorter pulse repetition delays to be used, in addition to the increase in signal to noise obtained by the very fact there is a higher concentration of spin active nuclei. It is worth stating that some of the time-consuming 2D experiments described in Chapter 3 simply would not have been possible with a less highly enriched sample than was used.

Further kinetic information was also obtained from the variable temperature T_1 relaxation studies, which have provided a measure of the activation energy of the exchange process, both above and below the phase transition temperature. It is possible to use the NMR T_1 studies to explore the exchange rate as a function of temperature, provided that the exchange rate at one temperature is known. In this case, the value from 1D-EXSY experiments was used to provide such a reference point, but values from other characterisation techniques could also be used.

The activation energy values found above and below the a / β phase transition were distinctly different, and the results are consistent with activation energy measurements by other techniques. The NMR technique has the additional advantage that it can be used at lower temperatures than dielectric measurements.

4.6 References

1   J. H. Kristensen and I. Farnan, *J. Chem. Phys.*, 2001, **114**, 9608-9624.
2   N. Kim and C. P. Grey, *Science*, 2002, **297**, 1317-1320.
3   N. Kim, R. N. Vannier, and C. P. Grey, *Chem. Mater.*, 2005, **17**, 1952-1958.
4   J. Emery, D. Massiot, P. Lacorre, Y. Laligant, and K. Conder, *Magn. Reson. in Chem.*, 2005, **43**, 366-371.
5   K. Schmidt-Rohr and H. W. Spiess, 'Multidimensional solid state NMR and polymers', Academic Press, 1994.
6   R. Nagel, T. W. Groß, H. Günther, and H. D. Lutz, *J. Sol. State. Chem.*, 2002, **165**, 303-311.
7   Z. Stoeva, R. Gomez, D. H. Gregory, G. B. Hix, and J. J. Titman, *J. Chem. Soc. Dalton*, 2001, 3093-3097.
8   V. Gerardy-Montouillout, C. Malveau, P. Tekely, Z. Olender, and Z. Luz, *J. Magn. Reson. Ser. A*, 1996, **123**, 7-15.
9   A. F. de Jong, A. P. M. Kentgens, and W. S. Veeman, *Chem. Phys. Lett.*, 1984, **109**, 337-342.
10   A. Hagemayer, K. Schmidt-Rohr, and H. W. Spiess, *Adv. Magn. Reson.*, 1989, **13**, 85-130.
11   P. Hodgkinson and M. R. Hampson, *Solid State Nucl. Magn. Reson.*, 2006, **30**, 98-105.
12   J. S. O. Evans, T. A. Mary, T. Vogt, M. A. Subramanian, and A. W. Sleight, *Chem. Mater.*, 1996, **8**, 2809-2823.
13   S. Allen and J. S. O. Evans, *J. Mater. Chem.*, 2004, **14**, 151-156.
14   J. S. O. Evans, W. I. F. David, and A. W. Sleight, *Acta Crystallogr. B*, 1999, **55**, 333-340.

Chapter 5 - Studies of AM$_2$O$_7$ (M = P, V) materials

This chapter describes the characterisation of several AM$_2$O$_7$ phases using both solid state NMR and powder X-ray and neutron diffraction. The AM$_2$O$_7$ family of materials show a number of interesting structural features, with often extremely complex low temperature forms and a variety of temperature dependent phase transitions.

5.1 ZrP$_2$O$_7$ high temperature phase

The room temperature phase of ZrP$_2$O$_7$ has previously been well characterised by ^{31}P NMR, as discussed in Chapter 1.[1, 2] However, the ^{31}P NMR of the high temperature phase has not been recorded, since the phase transition temperature (~290 °C) is above the operating limits of standard NMR probes (typically ~200 °C).
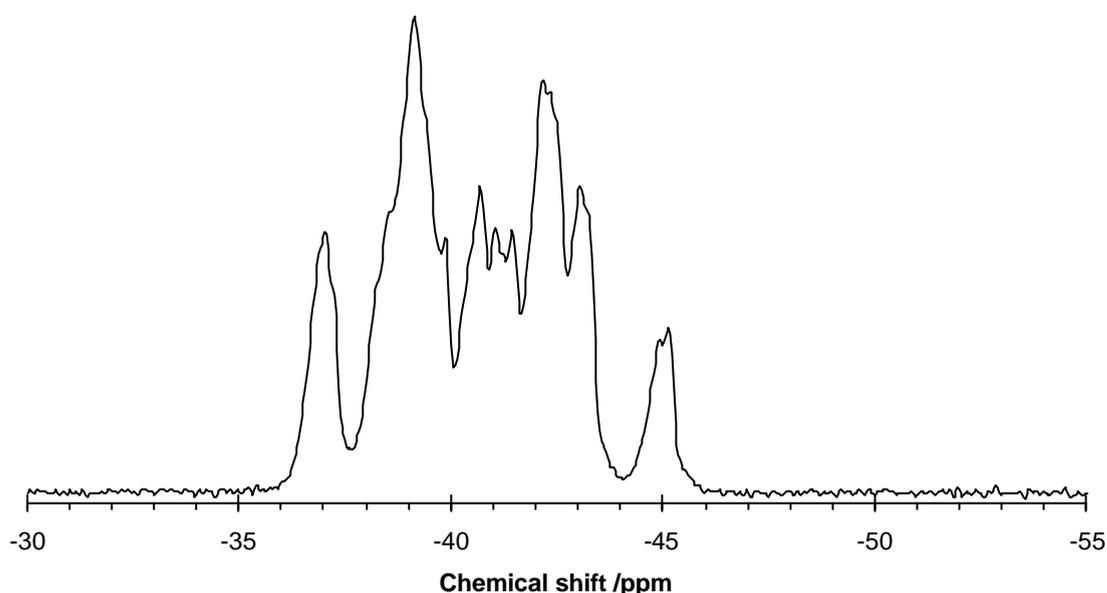
Figure 5-1 Room temperature ^{31}P MAS NMR spectrum of ZrP$_2$O$_7$ (sample JSOE439). [31]P Larmor frequency 202.4 MHz (MAS rate 20 kHz), 8 transients were recorded with a pulse repetition delay of 400 s, pulse duration 4 µs.

A spectrum of a sample of ZrP$_2$O$_7$ (JSOE439) was first recorded using the Varian Infinity Plus 500 spectrometer, to confirm the purity of the sample. This spectrum (Figure 5-1) reproduced that observed by King *et al.*.[1, 2] It is known that the room temperature super-structure of ZrP$_2$O$_7$ belongs to space group *Pbca*, and has 27 inequivalent phosphorus sites, resulting in the highly overlapped ^{31}P NMR spectrum.

The structure of the high temperature phase is known to be considerably less complex. At temperatures above the phase transition at 290 °C X-ray diffraction shows none of the superstructure peaks, and the structure is understood to belong to the simple *Pa3* space group, the most symmetric possible structure for an AP$_2$O$_7$ material. The *Pa3* structure has a highly

symmetric P$_2$O$_7$ group, with an inversion centre on the central bridging (P-O-P) oxygen atom. Although the X-ray diffraction results are fitted well using this simple structure, space group assignment from powder diffraction alone is often difficult, and there is a possibility that the true structure is of lower symmetry. NMR offers the possibility of revealing a lower symmetry.

In order to study the high temperature phase, a specialist high temperature probe was used in conjunction with a Varian UNITY Inova 300 spectrometer with Oxford 7.0 T magnet to acquire spectra of a sample of ZrP$_2$O$_7$ (JSOE439) at set temperatures of up to 350 °C. A room temperature spectrum was first acquired, as shown in Figure 5-2 and Figure 5-3. It was not possible to spin the sample at a faster MAS rate than 2.75 kHz due to practical limitations of the high temperature probe.
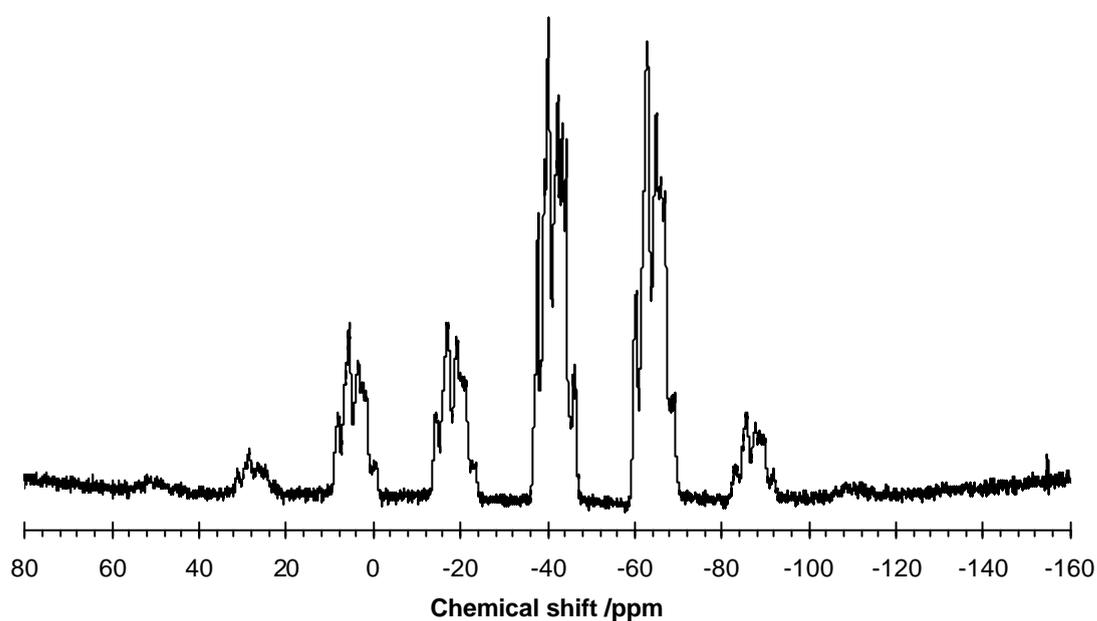

Figure 5-2 Room temperature ^{31}P MAS NMR spectrum of ZrP$_2$O$_7$ (sample JSOE439) Larmor frequency 121.414 MHz (MAS rate 2.75 kHz), 4 transients were recorded with a pulse repetition delay of 300 s, pulse duration 7.5 µs. The full spectrum including the spinning sideband manifold is shown.
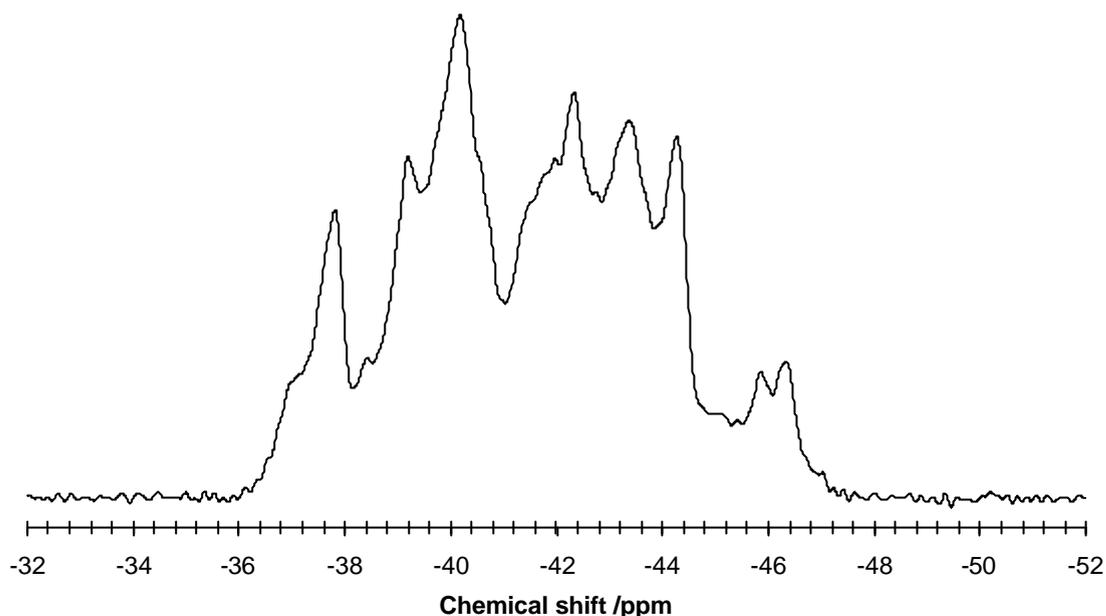
Figure 5-3 Room temperature ^{31}P MAS NMR spectrum of ZrP$_2$O$_7$ (sample JSOE439) Larmor frequency 121.414 MHz (MAS rate 2.75 kHz), 4 transients were recorded with a pulse repetition delay of 300 s, pulse duration 7.5 µs. The figure shows an expansion of centreband region.

The room temperature spectrum is consistent with the previous spectra. There is an increase in peak width, compared with the spectrum of Figure 5-1, due to the lower magnetic field and slower spinning speed, but the general form of the spectrum is similar.

The sample temperature was then increased by introducing a flow of heated nitrogen gas into the probe head, in order to record a high temperature spectrum. The probe was heated to an indicated temperature of 350 °C, the maximum operating temperature of the probe. It should be noted that the temperatures reported here are temperatures at a thermocouple situated in the stream of heated gas entering the probe. A thorough calibration of the sample temperature for this probe would be required in order to state the exact sample temperature. However it was clearly seen that the sample undergoes a significant change in structure at approximately the phase transition temperature (290 °C), and the spectrum observed above this temperature is very different to the room temperature spectrum. It may therefore be surmised that the sample has transformed to the high temperature form at the indicated temperature of 350 °C. The spectrum acquired at an indicated temperature of 350 °C is shown in Figure 5-4 and Figure 5-5.
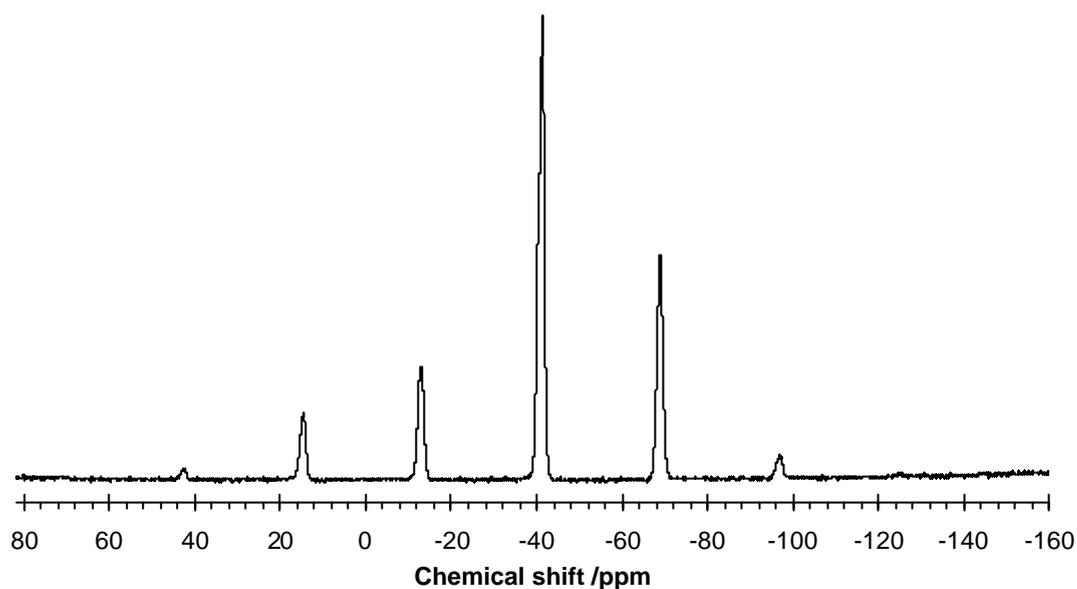
Figure 5-4 ³¹P MAS NMR spectrum of ZrP₂O₇ (JSOE439) at 350 °C, Larmor frequency 121.414 MHz, MAS rate 3.40 kHz, 4 transients were recorded with a pulse repetition delay of 300 s, pulse duration 7.5 µs. Full spectrum showing spinning sideband manifold
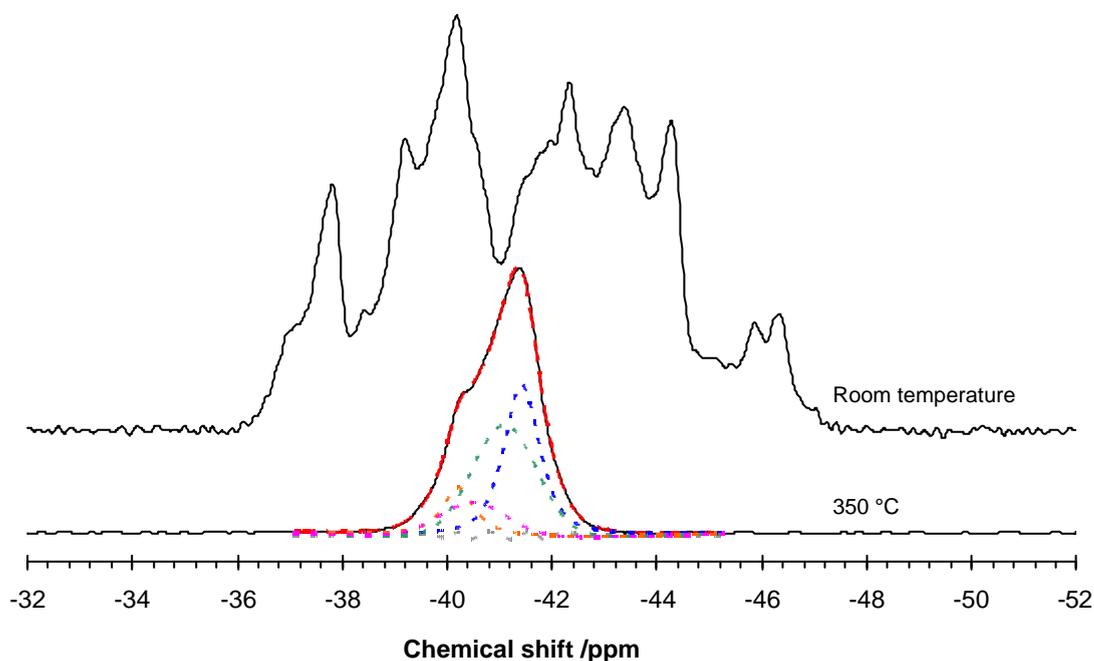

Figure 5-5 ³¹P MAS NMR spectrum of ZrP₂O₇ (JSOE439) at 350 °C and room temperature. Larmor frequency 121.414 MHz, MAS rate 3.40 kHz, 4 transients were recorded with a pulse repetition delay of 300 s, pulse duration 7.5 µs. Expansion of centreband region showing fitting to pseudo-Voigt peaks for high temperature spectrum. The dashed red line shows the overall fitted peak shape, the dotted grey line the difference between observed and fitted spectra, and the green, blue, pink and orange lines the individual fitted peaks.

The spectrum at 350 °C does not show a single symmetrical peak, as would be expected for the

*Pa*3 structure. It (Figure 5-5) consists of an asymmetrically shaped envelope with

FWHM = ~200 Hz. This suggests that there are multiple phosphorus environments in the high temperature phase.

Attempts were made to fit the centreband spectrum to a number of overlapped pseudo Voigt peak shapes, and it was found that a minimum of four peaks were required. The ratio of the integrated intensities of the four fitted peaks was approximately 1:1:3:3. This is compatible with a structure in the *R3* space group, which has four inequivalent phosphorus sites in this ratio. Rhombohedral splitting patterns had been observed in the powder diffraction pattern of the high temperature phase of SnP$_2$O$_7$, suggesting that other high temperature AP$_2$O$_7$ structures may also be rhombohedral. The intensity ratio was then fixed to 1:1:3:3, in order to determine the position and widths of the constituent four peaks. This resulted in the fit shown in Figure 5-5, the fitted peak details are given in Table 5-1.

Peak	Peak position /ppm	FWHM /Hz	Relative Integrated area (fixed)
1	-41.1±0.1	176±9	3
2	-41.4±0.01	100±3	3
3	-40.2±0.02	89±27	1
4	-40.5±0.3	187±20	1

Table 5-1 Parameters for pseudo Voigt functions fitted to high temperature spectrum of ZrP$_2$O$_7$

This fitting illustrates the point that the spectrum may be due to several overlapped peaks, although it is unrealistic to conclude that there are four sites from this evidence alone. There may be more than four overlapped peaks (the *P1* space group would give eight inequivalent phosphorus sites, for example).

It is also important to consider other possible explanations for the broad and unsymmetrical spectrum observed. It is possible for example, that the broad peak is a result of an incorrectly set 'magic angle' adjustment causing incomplete averaging of anisotropic effects such as CSA. However, the magic angle was checked prior to the experiment using the rotational echo train of KBr, and the room temperature ZrP$_2$O$_7$ spectrum shows no unusual broadening. This raises the possibility that there is a change in the geometry of the probe at elevated temperatures resulting in an alteration of the orientation of the MAS spinning axis. This hypothesis is apparently disproved by the fact that no such line broadening effect was seen for HfP$_2$O$_7$ at high temperature (Section 5.2.1).

The simplest explanation for the observed spectrum is that there are multiple peaks which are overlapped. It was therefore thought that a higher magnetic field may allow resolution of individual peaks. The higher field spectrometer at Durham is not compatible with the high temperature probe, and is limited to maximum sample temperatures of ~220 °C. A sample of ZrP$_2$O$_7$ (JSOE439) was sent to Dr Ian Farnan at Cambridge University for high temperature

NMR using a spectrometer operating at higher magnetic field (11.7 T). These experiments were carried out using a custom-modified Varian probe. Farnan recorded two ^{31}P MAS NMR spectra of this sample, shown in Figure 5-6, at room temperature and 359 °C.[3]
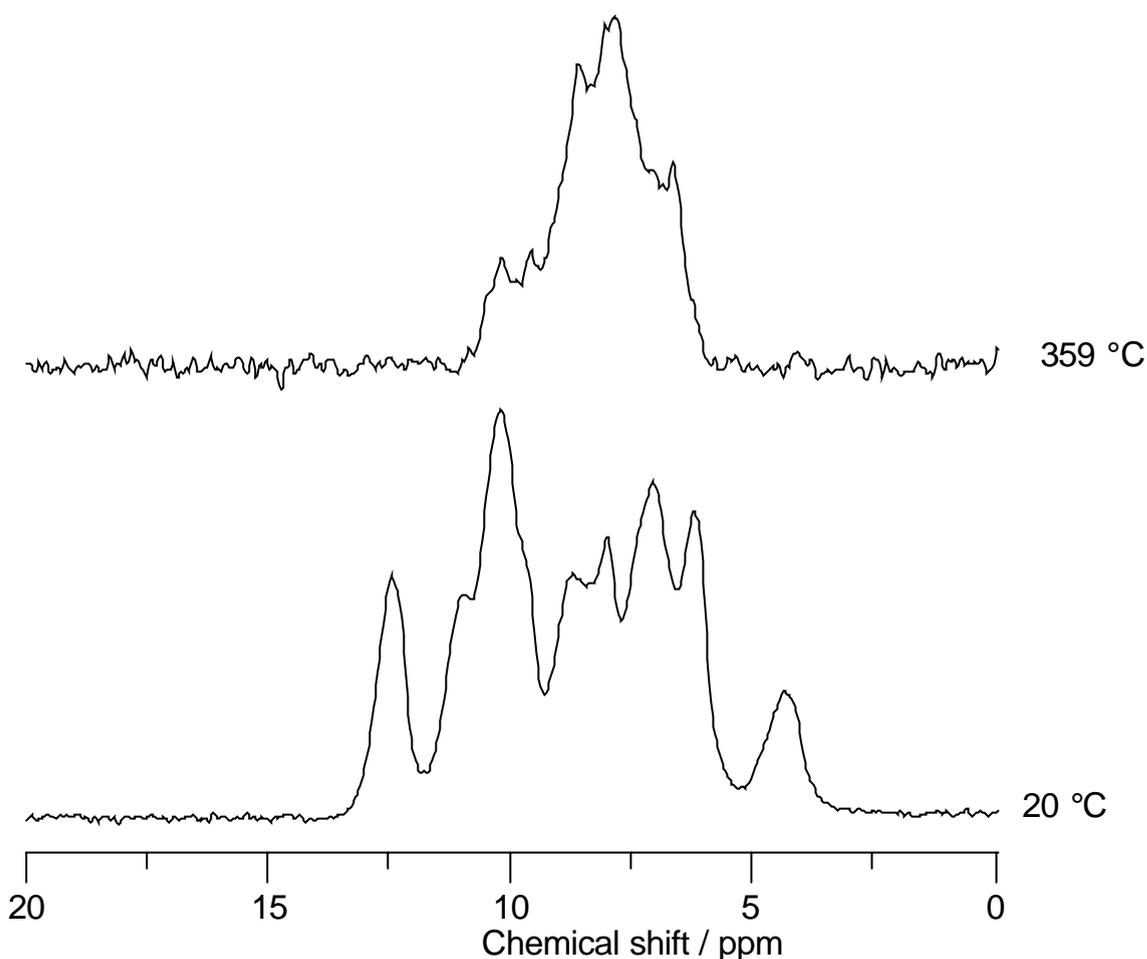

Figure 5-6 ^{31}P MAS NMR spectra of ZrP$_2$O$_7$ spectra (obtained by Dr Ian Farnan). [31]P Larmor frequency 202.4 MHz, MAS speed 5.0 kHz at 20 °C and 359 °C. Note that the chemical shift of these spectra is un-referenced.

Farnan's room temperature spectrum (Figure 5-6, bottom) shows noticeably poorer resolution than that recorded on a standard NMR probe, as shown in Figure 5-1, despite being recorded at the same magnetic field and using a similar single pulse experiment. This suggests that the experimental conditions were not optimised well for the resolution of individual sites, and could be due to a number of factors such as poor shimming, leading to an inhomogeneous magnetic field, or an incorrectly set magic angle adjustment, which would affect the averaging of CSA and other anisotropic interactions.

Farnan's spectrum of the high temperature phase is also shown in Figure 5-6. The shape of the spectrum is similar to the one recorded on the Durham high temperature probe, but the resolution of individual sites is not possible. The width of the spectral envelope is ~5 ppm at high temperature, which is consistent with that observed in Durham (~4 ppm). This is significantly different to the width of the envelope at room temperature (Farnan, ~10 ppm,

Durham, ~11 ppm), and confirms that Farnan's spectra corresponds to the high temperature phase. Unfortunately, Farnan's spectrum at high temperature shows extremely poor signal to noise, and no noticeable improvement in resolution over the spectrum recorded at 121.4 MHz.

In conclusion, the high temperature ^{31}P NMR does not show a single peak, suggesting that the structure is of lower symmetry than the *Pa3*. However, it is not possible to confirm the number of sites from a 1D spectrum alone in this case.

Given the suggestion of lower symmetry, it was decided to re-examine previously collected neutron powder diffraction data. Assignments of space groups from powder diffraction data are often ambiguous. If the true symmetry was indeed lower than the *Pa3* structure used to fit the data, then an improved fit to the data would be obtained by performing a Rietveld refinement with the correct structural model. Attempts were made to carry out comparative refinements in a range of space groups – this technique was used for HfP$_2$O$_7$ as described in Section 5.2.1. This proved unsuccessful since the signal to noise of the data was not sufficient to see any difference in quality of fitting between different space groups.

5.2 HfP$_2$O$_7$

There is very little published work on HfP$_2$O$_7$ but much more work has been carried out on ZrP$_2$O$_7$ (as described in Chapter 1), with which it is understood to be iso-structural. The aim of the work in this section was to fully determine the structure of both high and low temperature phases of HfP$_2$O$_7$ and also to characterise the thermal expansion by variable temperature neutron diffraction.

5.2.1 HfP$_2$O$_7$ high temperature phase

The structure of the high temperature phase of HfP$_2$O$_7$ is understood to be relatively simple, it consists of HfO$_6$ octahedra sharing each of their oxygens with P$_2$O$_7^{4-}$ pyrophosphate groups. The pyrophosphate group itself is made up of two PO$_4$ tetrahedra, with the P-O-P bridging oxygen atom not being bonded to Hf. At high temperature (above ~600 K) the structure is believed to have a simple cubic structure, with a cell parameter of around 8.26 Å. As with all members of the AP$_2$O$_7$ family, the highest possible symmetry for this structure would be the space group *Pa3*, in which there is an inversion centre on the P-O-P bridging oxygen atom and the linear P-O-P bonds lie on a three-fold axis.

NMR spectra were recorded for both the room temperature and high temperature phases of HfP$_2$O$_7$, using the same high temperature probe as for ZrP$_2$O$_7$ (Figure 5-7). The room temperature spectrum shows a number of overlapped peaks, with the same form to the spectra as ZrP$_2$O$_7$, whilst the high temperature spectrum apparently shows only one symmetrical peak (Figure 5-7 and Figure 5-8).
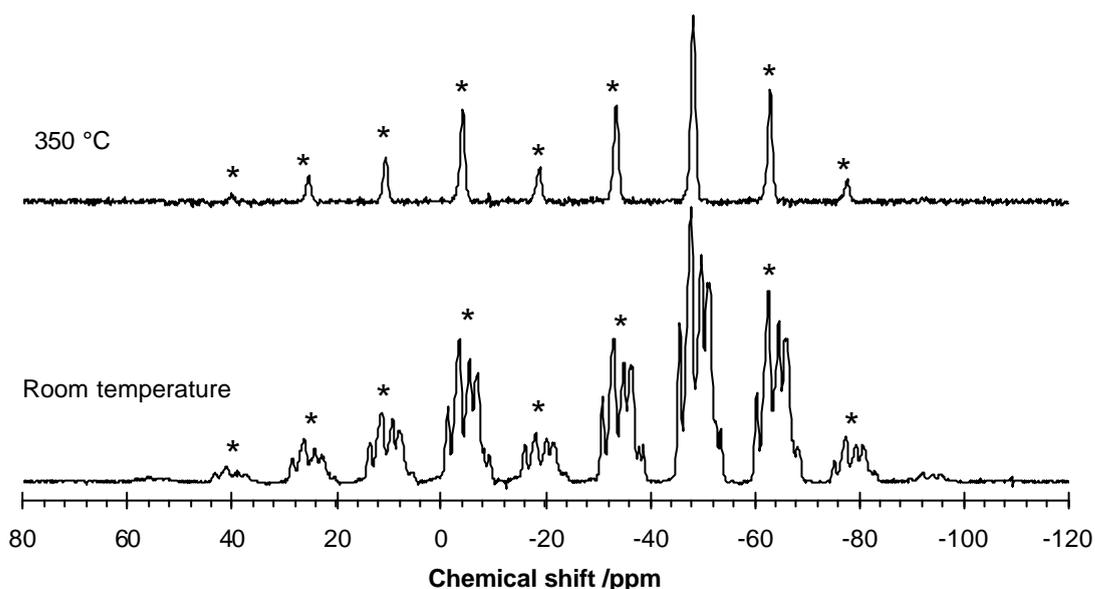
Figure 5-7 ^{31}P MAS NMR spectra of HfP$_2$O$_7$ at room temperature and 350 °C, recorded at a ^{31}P Larmor frequency of 121.414 MHz. Spinning sidebands are marked by asterisks.

The centreband spectrum of high temperature HfP$_2$O$_7$ may be fitted to a single pseudo-Voigt peak shape at 48.23±0.03 ppm with a FWHM of 122±1 Hz. This peak width is somewhat narrower than the width of the spectral envelope in high temperature ZrP$_2$O$_7$ (~200 Hz). Although this suggests only one phosphorus site, it is impossible, using this 1D spectrum alone, to definitively rule out the possibility that there are several sites with overlapping peaks
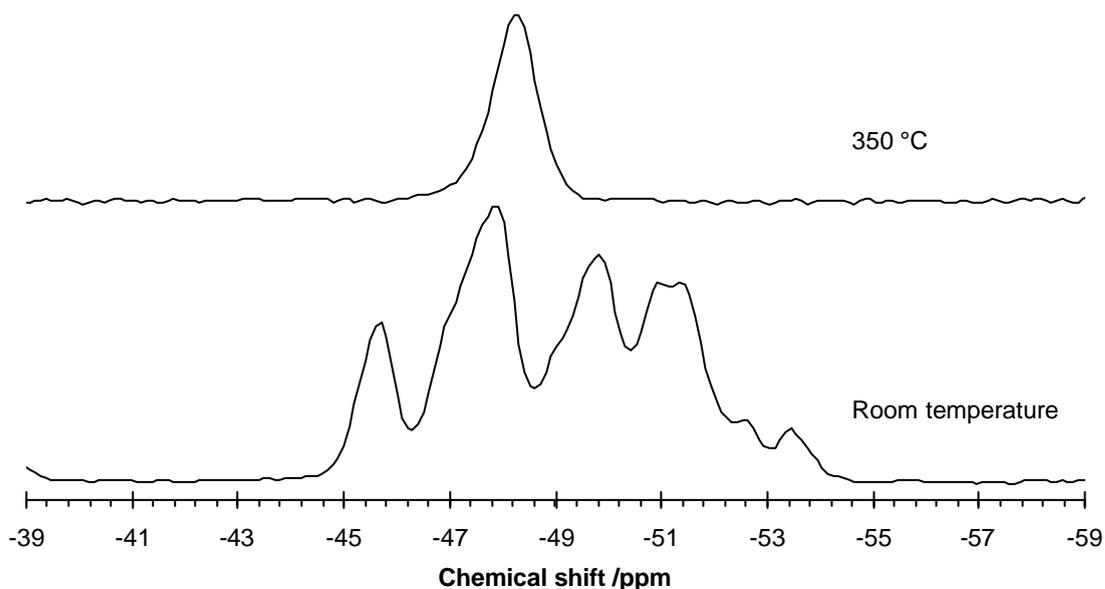

Figure 5-8 ^{31}P MAS NMR spectra of HfP$_2$O$_7$ at room temperature and 350 °C, recorded at a ^{31}P Larmor frequency of 121.414 MHz. An expansion of the centreband region is shown.

The pattern of intensity of spinning sidebands is highly dependent on the chemical shift anisotropy of a site, and so an examination of the observed sideband manifold could reveal the presence of multiple sites. The entire sideband pattern of the ^{31}P MAS NMR spectrum of the high temperature phase was fitted using the STARS simulation package.[4] An analysis of the spinning sideband pattern for high temperature ZrP$_2$O$_7$ was also attempted, but this proved impossible since there are apparently multiple overlapping patterns.
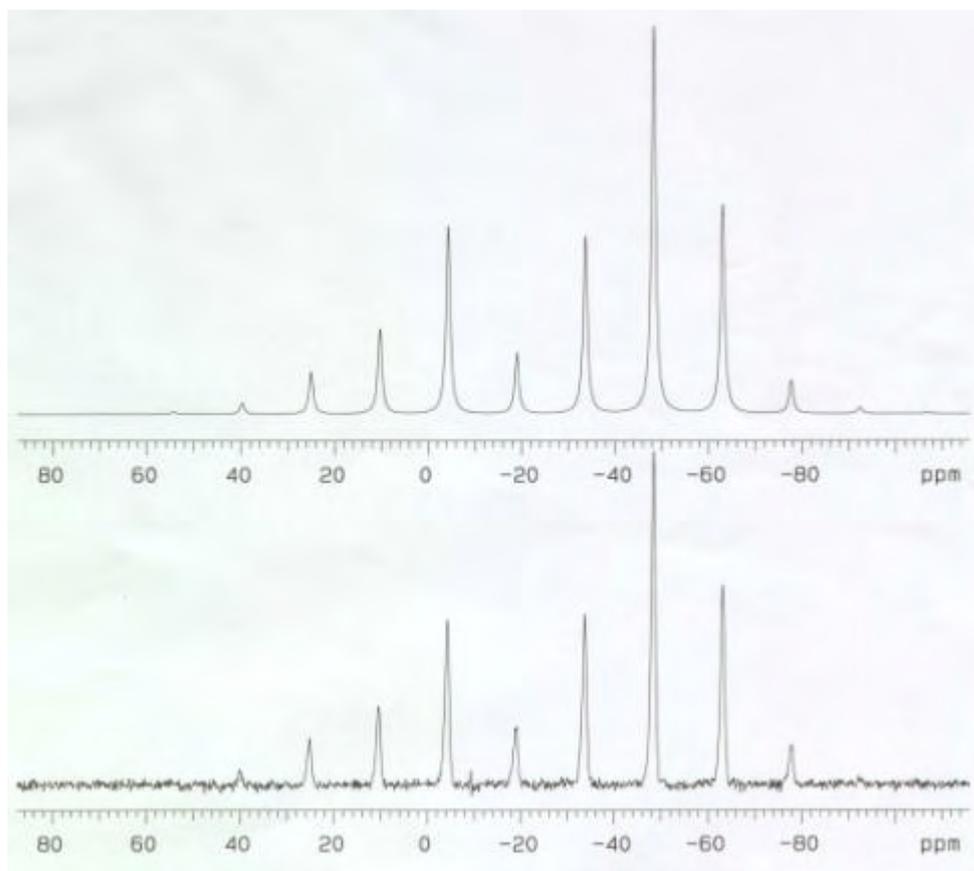

Figure 5-9 ^{31}P NMR spectrum (bottom) of HfP$_2$O$_7$ high temperature phase and calculated fitting (top) to a single site.

It was found that the intensity pattern fits well to a single phosphorus site, the results of this fitting are shown in Figure 5-9. This suggests that if there is more than one phosphorus site, then the chemical shift and CSA are very similar for all sites, producing exactly overlapping peaks. Thus, although it is possible that multiple sites exist, there is no evidence to support this hypothesis and it would seem most likely that the structure contains only one phosphorus environment. As with ZrP$_2$O$_7$, it is possible that higher resolution ^{31}P NMR spectra of the high temperature phase may reveal the presence of multiple peaks which are overlapped in the spectra reported here.

5.2.1.1 Neutron Diffraction and Rietveld Refinement

Although the high temperature NMR results for HfP_2O_7 seem to show a unique phosphorus atom in the asymmetric unit, the results for ZrP_2O_7 (Section 5.1) cast some doubt over the space group symmetry of the high temperature phase, with a suggestion of lower symmetry than the previously accepted cubic *Pa3* space group. The symmetry of high temperature HfP_2O_7, which was thought to be iso-structural with ZrP_2O_7, was also therefore investigated by carrying out Rietveld refinements of neutron diffraction data in a range of possible space groups.

The simplest possible space group for $A_2P_2O_7$ materials is *Pa3*. A range of lower symmetry structures can be formed by removing some of the symmetry constraints imposed by this space group, and forming lower symmetry space groups. Space groups which are related to another in this way are called sub groups, and are generated by removing symmetry elements. If one were to imagine removing all the symmetry elements of a space group, leaving only the translational symmetry of the unit cell, then the resulting structure would belong to the lowest symmetry space group, *P1*. Each space group except *P1* therefore has a number of subgroups, which may be determined by a consideration of the symmetry, these are listed in the *International Tables*.[5] There are 11 sub groups of *Pa*3, as shown in Figure 5-10, the arrows indicating loss of one or more symmetry elements.
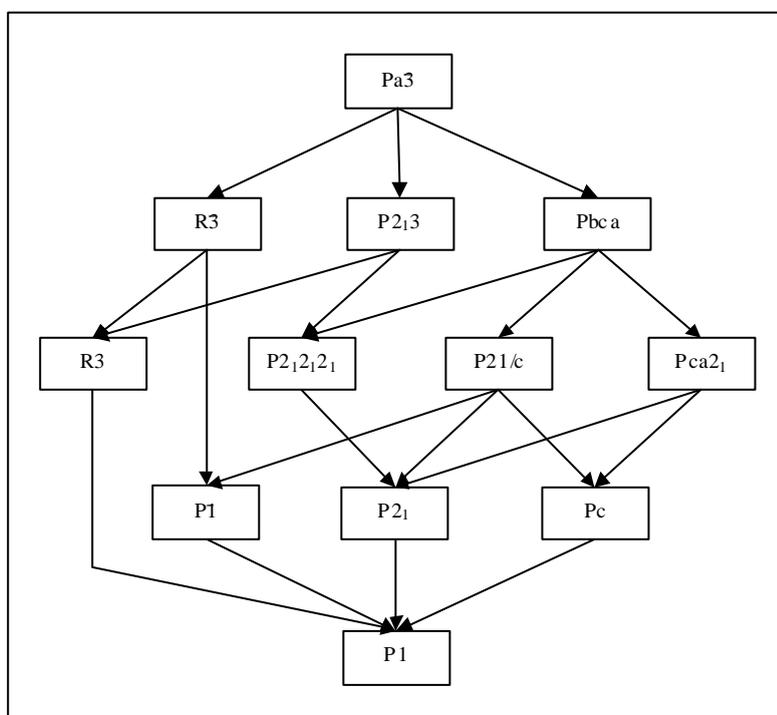

Figure 5-10 Space group / sub-group relationships for *Pa3.*

A structural model may be constructed in each of these space groups, some of which contain different numbers of phosphorus sites. For example, whilst the *Pa3* structure contains only one

inequivalent phosphorus site, the *P1* structural model contains 8 inequivalent phosphorus sites. The numbers and multiplicities of phosphorus sites in the asymmetric unit for each of these space groups was deduced by considering the symmetry of the different sub groups, these are listed in Table 5-2.

Space Group	Number of unique P sites	Ratio of multiplicity of sites (area of NMR peaks)
Pa3	1	-
Pbca	1	-
P2$_1$/c	2	1:1
R3	2	1:3
P1̄	4	1:1:1:1
P2$_1$3	2	1:1
P2$_1$	4	1:1:1:1
P2$_1$2$_1$2$_1$	2	1:1
Pca2$_1$	2	1:1
R3	4	1:1:3:3
Pc	4	1:1:1:1
P1	8	1:1:1:1:1:1:1

Table 5-2 Numbers and multiplicities of phosphorus atoms in asymmetric unit in *Pa3* and its sub groups.

Ideally, the Rietveld fit for the structure should improve with decreasing symmetry until the correct space group is found, as has been shown for Bi$_2$Sn$_2$O$_7$.[6] Using a lower symmetry space group than the correct one should not necessarily improve the quality of fit.

Neutron diffraction data were used for these structural investigations, since the subtle differences in symmetry in these materials are related to positions of oxygen atoms. X-ray diffraction is insensitive to small changes in position of oxygen atoms in the presence of heavy elements. Time-of-flight neutron diffraction data for a sample of HfP$_2$O$_7$ (RKBG276) at 503 ºC were obtained using the GEM instrument at ISIS (Rutherford Appleton Laboratories, UK) (GEM13120, May 2003). Data were collected for a total of 240.2 µAh. The GEM instrument has six detector banks in order to obtain information over a wide range of *d*-spacings. These detector banks are located at 9 °, 19 °, 35 °, 64 °, 91 ° and 154 ° to the incoming neutron beam.

A series of Rietveld refinements was carried out for structural models in a *Pa3* and all its sub-groups, using Topas 3 (local version 43).[7] Data ranges from 4 of the 6 detector banks were selected to include observable Bragg peaks as listed in Table 5-3.

	Filename	Data range used	*d*-spacing
Bank 3 (35 °)	gem13120_35.xye	5000-13000 µs	1.77-4.60 Å
Bank 4 (64 °)	gem13120_64.xye	5000-19000 µs	1.02-3.89 Å
Bank 5 (91 º)	gem13120_91.xye	5000 - 17500 µs	0.74 - 2.62 Å
Bank 6 (154 º)	gem13120_154.xye	5000 - 17100 µs	0.55 - 1.88 Å

Table 5-3 Neutron diffraction data used for refinement of high temperature structure of HfP₂O₇.

Data from all detector banks were fitted simultaneously, using a total of 71 non-structural parameters in each refinement. For each bank 12 background parameters, a scale factor, 2 peak shape parameters (*lor* and *dsp*), and two instrument parameters (*t0* and *difa*) were refined. The parameter '*difc*' is an instrumental parameter which relates to the distance between the neutron source and the detector banks; this was refined for banks 3-5, and for bank 6 fixed at the value obtained by calibration using an external yttrium aluminium garnet (YAG, $Y_3Al_5O_{12}$) standard.

The number of structural parameters for each refinement is given in Table 5-4. Structural refinements can fall into a false minimum, rather than the true global minimum. In order to try to ensure that the refinement found the correct minimum in each case, the technique of simulated annealing was used. In the case of the initial refinements of the *Pa*3 structural model this was done by randomising all the parameters at the end of each cycle of refinement based on the Rietveld e.s.d. on each parameter, with a total of 20,000 iterations being performed.

Test refinements in *Pa*3 were first carried out using both isotropic and anisotropic temperature factors. Treating the atomic displacement with anisotropic displacement parameters (ADP's) gives a significant improvement in the fitted peak intensities, which is shown by the dramatic drop in R factors (overall R_{WP} 6.478 % for isotropic; 2.871 % for anisotropic). The improvement in fit obtained by using ADPs is seen in Figure 5-11.

Since there is such an obvious improvement in quality of fit, anisotropic temperature factors were used for the comparative study of space groups. In order to carry out Rietveld refinements for the sub-groups, the structures in all sub-groups of *Pa*3 were derived from the cell parameters and atomic positions obtained from the anisotropic *Pa*3 refinement. These structures were used as the starting positions for each of the sub-group refinements, with initial ADP values of $u_{11} = u_{22} = u_{33} = 0.1000$, $u_{12} = u_{13} = u_{23} = 0.0200$.
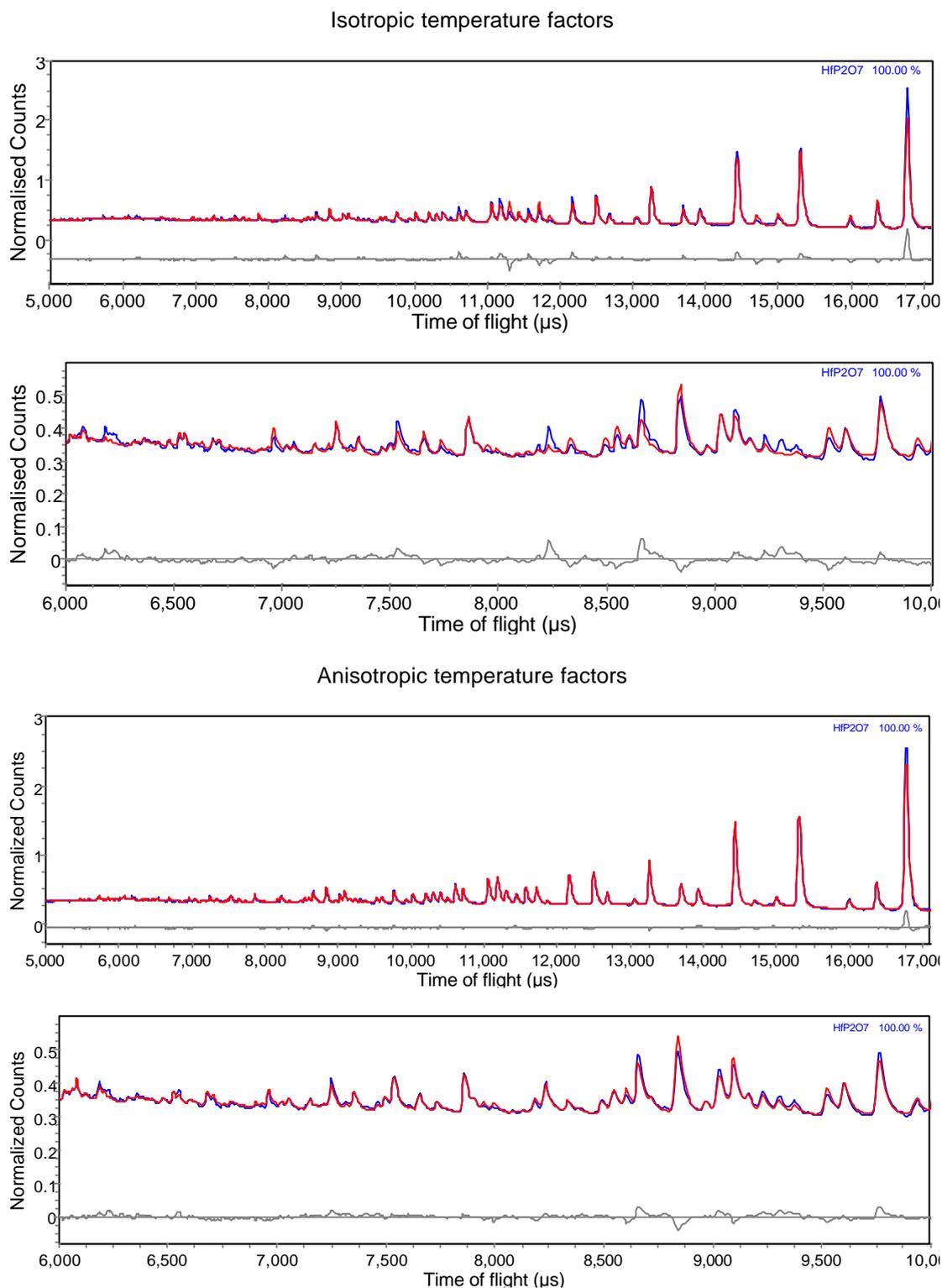
Isotropic temperature factors

Anisotropic temperature factors

Figure 5-11 Comparison of fit for the *Pa3* structure using isotropic (top 2 plots) and anisotropic (lower 2 plots) temperature factors, bank 6 (154 º) data, corresponding *d*-spacing ranges are 0.55 to 1.88 Å and 0.66 to 1.10 Å.

A suitable methodology for the simulated annealing, as previously mentioned, was then devised. It was found that annealing by randomising the parameters according to their errors made refinement unstable for the lower symmetry space groups (with around 200 or more parameters), presumably due to the high error in certain parameters such as the ADPs. A more

'gentle' method of annealing was therefore used, that is to displace each of the atomic coordinates by 0.05 of the cell lengths (equivalent to ~0.4 Å) and returning each of the ADPs to their initial values of $u_{11} = u_{22} = u_{33} = 0.1000$, $u_{12} = u_{13} = u_{23} = 0.0200$ at the end of each cycle of refinement. A 1000-iteration simulated annealing refinement was then carried out for each of the sub-group structures.

The refined *Pa*3 structure with anisotropic temperature factors is shown in Figure 5-12. The thermal ellipsoids are all chemically reasonable. The P and Hf atoms have the smallest thermal ellipsoids, indicating that they undergo the smallest displacements. The oxygen atoms are seen to be more mobile in directions perpendicular to their bonds, as would be expected given the flexibility of these links in the structure. The motion of the P?O?P bridging oxygen atom (O2) perpendicular to the P?O bonds is particularly pronounced.
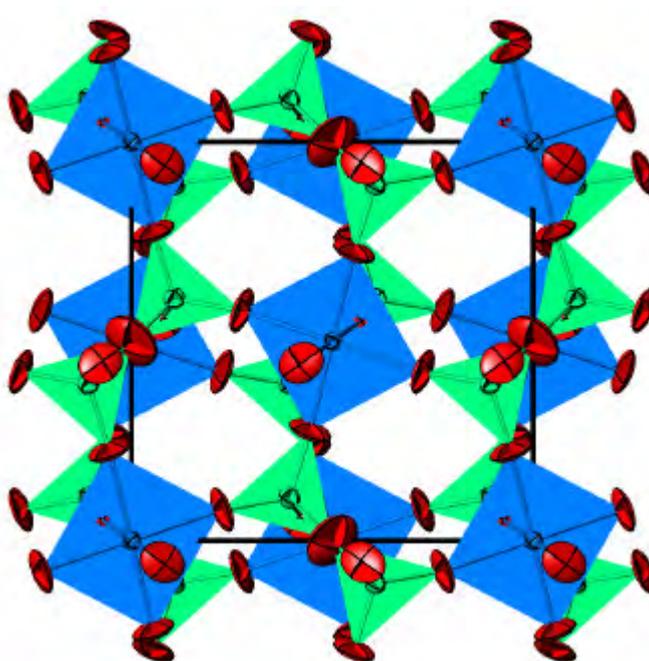

Figure 5-12 Refined structure of high temperature HfP$_2$O$_7$ in *Pa*3, showing atoms as thermal ellipsoids (50% probability) and HfO$_6$ octahedra and PO$_4$ tetrahedra.

It was found that refinements in all space groups gave overall R_{WP} values in the range 2.434 – 2.871 %. A visual inspection shows that all of the Rietveld refinements fit the observed powder patterns very well, with the differences between refinements being very subtle. Plots of the Rietveld fits with the lowest (*P1*) and highest (*Pa3*) values of R_{WP} obtained are shown in Figure 5-16 to Figure 5-19. Some of the subtle differences in the visual quality of the Rietveld fits may be more clearly seen in the close-up views shown by Figure 5-18 and Figure 5-19. A summary of the results of the refinements completed is shown in Table 5-4.

Cell parameters		Pa-3	Pa-3	P2$_1$3	R-3	R3	Pbca	Pca2$_1$	P2$_1$2$_1$2$_1$	P2$_1$/c	Pc	P2$_1$	P-1	P1
Space group number		205	205	198	148	146	61	29	19	14	7	4	2	1
Temperature factor model		Isotropic	ADPs	ADPs	ADPs	ADPs	ADPs	ADPs	ADPs	ADPs	ADPs	ADPs	ADPs	ADPs
Input file		isotropicH HP2O7_pa-3_108.inp	HP2O7_pa-3_80.inp	HP2O7_p2 13_101.inp	HP2O7_r-3_102.inp	HfHP2O7_r3_98.inp	HP2O7_pb ca_104.inp	HP2O7_pca 21_105.inp	HP2O7_p212 121_106.inp	HP2O7_p2 1c_107.inp	HP2O7_pc _100.inp	HP2O7_p2 1_103.inp	HP2O7_p-1_99.inp	HP2O7_p1 _97.inp
Structural parameters refined	Cell parameters	1	1	1	2	2	3	3	3	4	4	4	6	6
	Hf coordinates	0	0	1	0	4	0	3	3	0	6	6	0	12
	Hf temp factors	1	2	2	8	8	6	6	6	12	12	12	24	24
	P coordinates	1	1	2	4	8	3	6	6	6	12	12	12	24
	P temp factors	1	2	4	8	16	6	12	12	12	24	24	24	48
	O coordinates	3	3	7	12	28	9	21	21	18	42	42	36	84
	O temp factors	2	8	14	32	56	24	42	42	48	84	84	96	168
	Total structural parameters	9	17	31	66	122	51	93	93	100	184	184	198	366
Total number parameters refined		80	88	102	137	193	122	164	164	171	255	255	269	437
R-factors	Bank 3 (35 °) R$_{WP}$	5.605	3.978	3.912	3.920	3.887	3.884	3.887	3.885	3.930	3.881	3.887	3.929	3.876
	Bank 3 (35 °) R$_{Bragg}$	2.044	1.076	0.637	0.726	0.447	0.690	0.577	0.600	0.603	0.411	0.468	0.423	0.391
	Bank 4 (64 °) R$_{WP}$	7.086	3.454	3.268	3.197	3.101	3.206	3.214	3.138	3.139	3.061	3.053	3.100	3.025
	Bank 4 (64 °) R$_{Bragg}$	5.228	2.834	2.023	2.013	2.452	2.445	2.309	2.281	1.815	2.298	2.170	1.918	2.287
	Bank 5 (91 °) R$_{WP}$	7.073	2.485	2.284	2.058	1.864	2.033	1.881	1.939	1.969	1.797	1.784	1.913	1.747
	Bank 5 (91 °) R$_{Bragg}$	6.657	1.233	1.107	0.903	0.770	0.937	0.729	0.791	0.909	0.687	0.722	0.712	0.651
	Bank 6 (154 °) R$_{WP}$	4.965	1.955	1.840	1.770	1.672	1.702	1.582	1.639	1.687	1.598	1.609	1.716	1.607
	Bank 6 (154 °) R$_{Bragg}$	7.449	2.169	2.013	1.752	1.549	1.667	1.521	1.611	1.636	1.495	1.563	1.532	1.509
	Overall R$_{WP}$	6.478	2.871	2.718	2.614	2.504	2.591	2.502	2.532	2.557	2.459	2.456	2.533	2.434
	Average R$_{Bragg}$	5.344	1.828	1.445	1.349	1.305	1.435	1.284	1.321	1.241	1.223	1.231	1.146	1.210
Cell parameters	a	8.25701	8.25681	8.25677	8.25715	8.25697	8.25568	8.25673	8.25700	8.25716	8.25564	8.25698	8.25675	8.25691
	b	.	.	.	.	.	8.25593	8.25636	8.25629	8.25605	8.25767	8.25281	8.25684	8.25779
	c	.	.	.	.	.	8.25537	8.25652	8.25640	8.25563	8.25767	8.25705	8.25681	8.25578
	α	.	.	.	89.99065	89.97793	.	.	.	.	.	.	90.08738	89.96123
	ß	.	.	.	.	.	.	.	.	89.95456	90.07764	89.90152	89.96547	90.04776
	?	.	.	.	.	.	.	.	.	.	.	.	90.04651	90.08302

Table 5-4 Parameters refined and summary of results for neutron diffraction data refinement of HfP$_2$O$_7$ high temperature phase, in *Pa3* and all its sub-groups.

It would be expected that simply increasing the number of parameters would always result in a better fit to the observed data. Whilst this is the general trend of the results, as seen in Figure 5-13, there are several exceptions where adding more parameters does not produce an improvement in the fit. This is illustrated most clearly by Figure 5-15, which shows only the variation of the overall R_{WP} value.

It is seen that removing some symmetry elements has more of an effect on the R_{WP} value than others. For example, the loss of a centre of inversion (for example on going from *Pa3* to *P2$_1$3*, *R3* to *R3* and *P1* to *P1*) has a profound effect on the R-factor. The non-centrosymmetric space groups *Pc* and *P2$_1$* both give better overall R_{WP} values than the centrosymmetric *P1*, despite using fewer structural parameters.
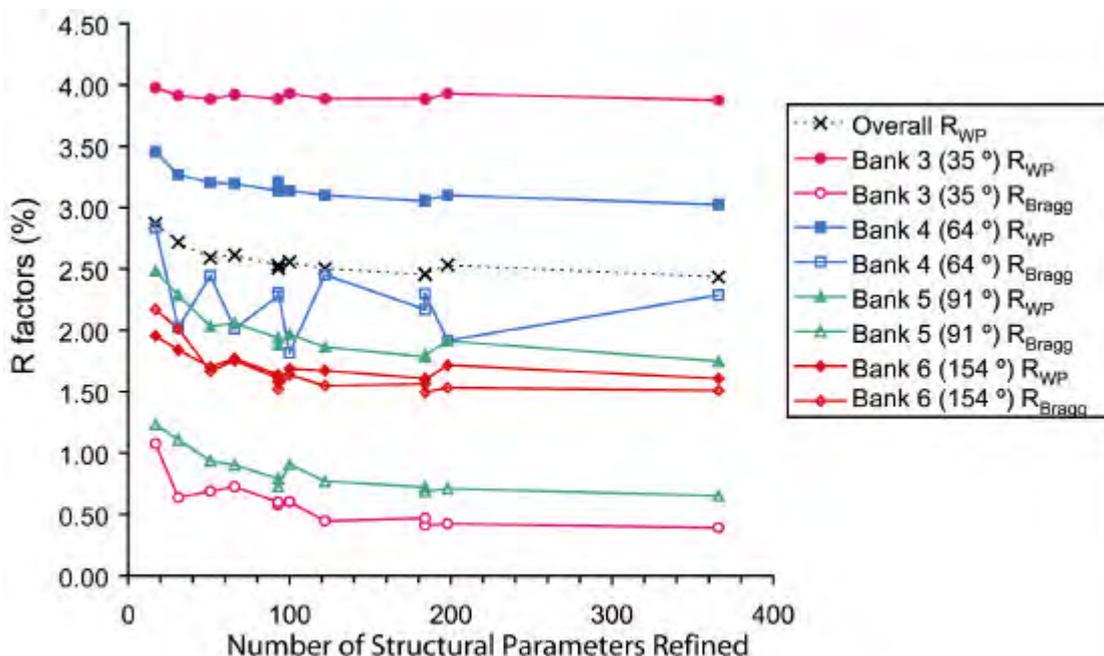
Figure 5-13 Graph of all *R* factors against number of refined structural parameters.

If there were large discrepancies in the variation of the residual indices of the separate banks, then the trend in the overall R_{WP} could not be relied upon to provide useful information about the structural model. As can clearly be seen from Figure 5-13 and Figure 5-14, there is a strong correlation between the residual indices, both R_{WP} and R_{Bragg}, for all detector banks except bank 4. This suggests that the variation of quality of fit is indeed due to the relative accuracies of the structural models. It should, however, be noted that R_{Bragg} values from powder diffraction are biased by the structural model.
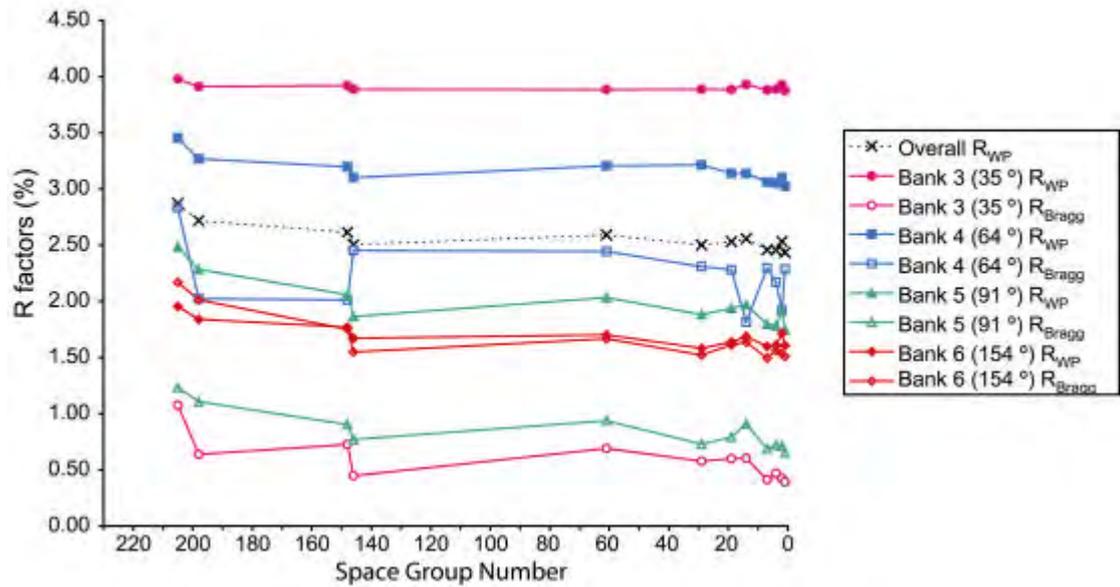
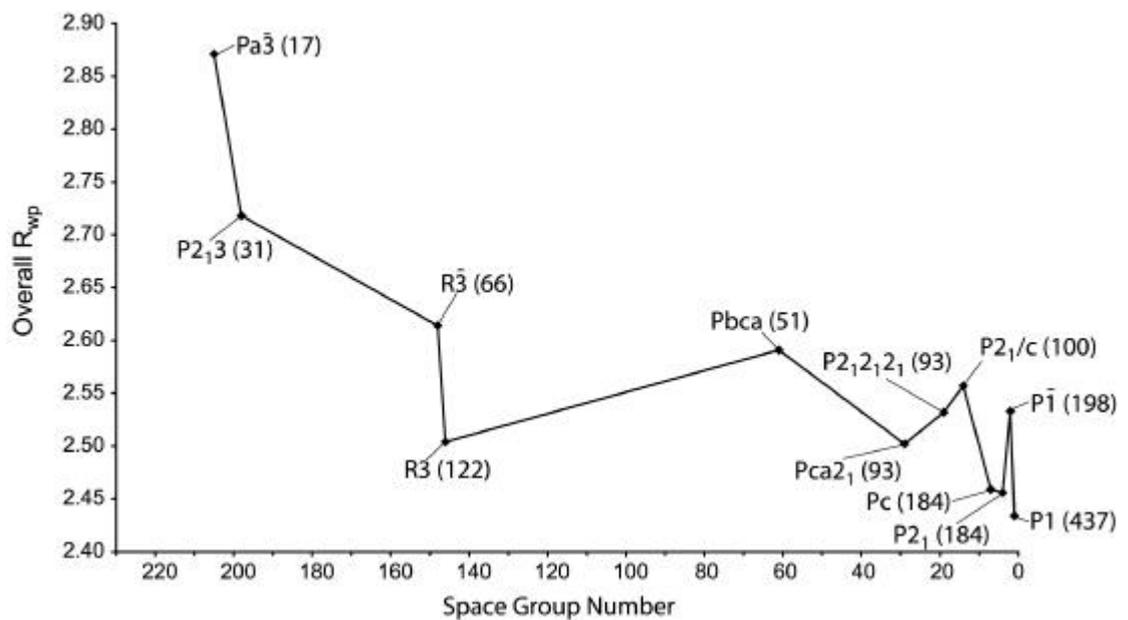**Figure 5-14 Graph of all *R* factors against space group number for Rietveld refinement of neutron diffraction data for high temperature HfP$_2$O$_7$.**
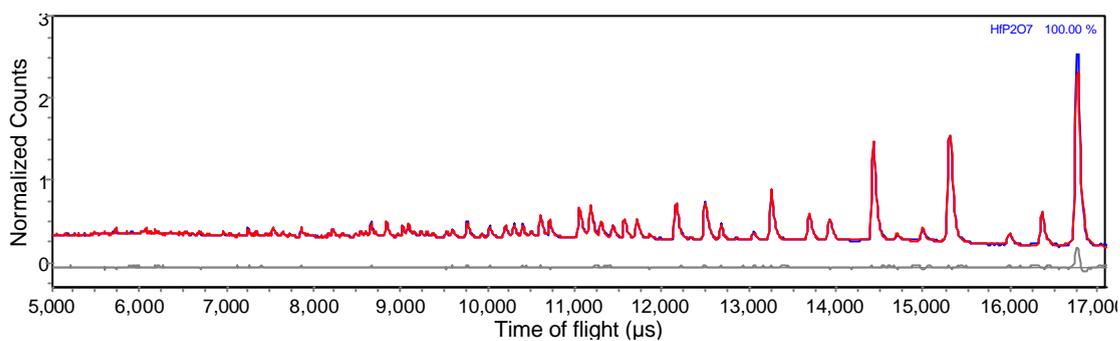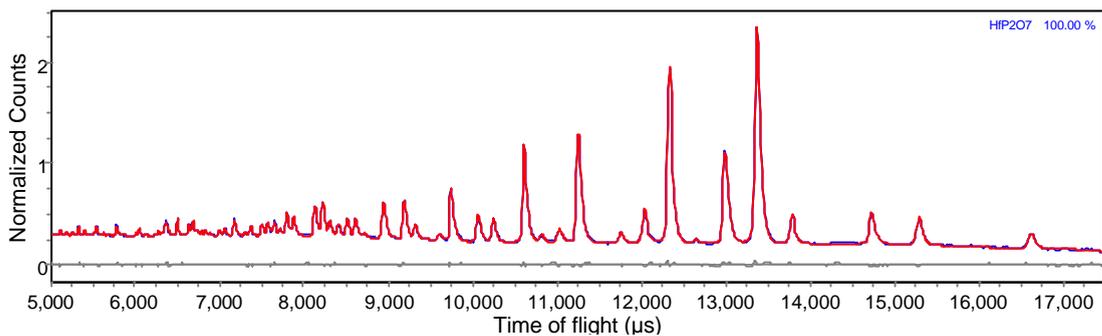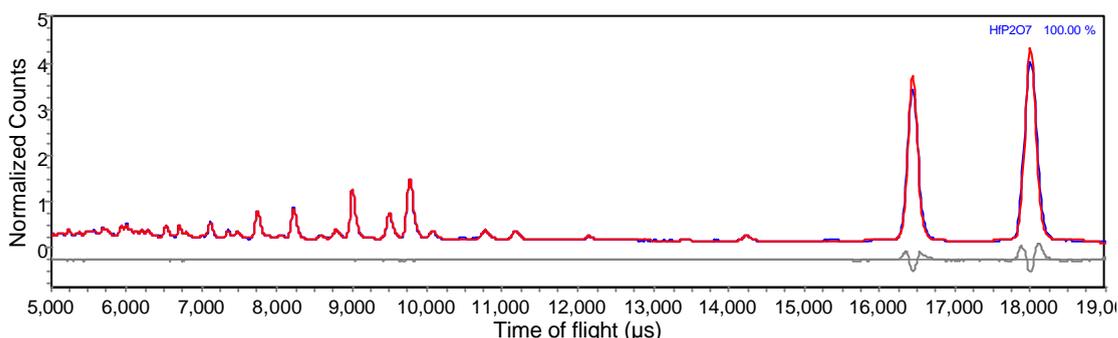

Figure 5-15 Graph of overall *R$_{WP}$* value against space group, each point is labelled with both the space group and the number of structural parameters refined.
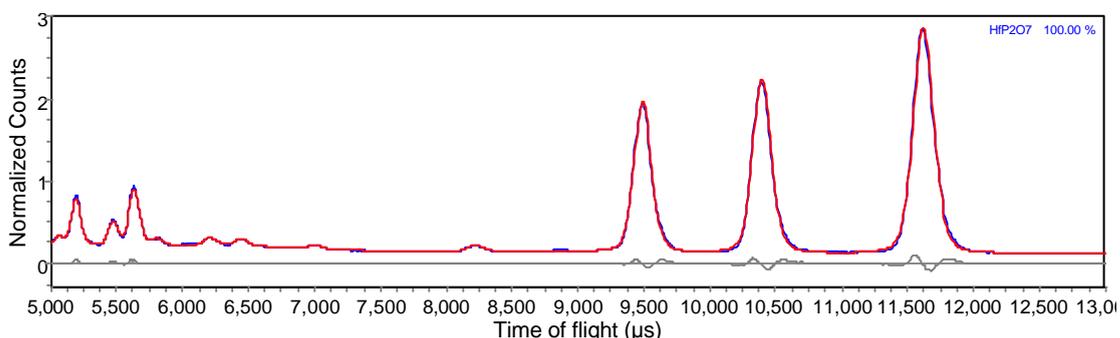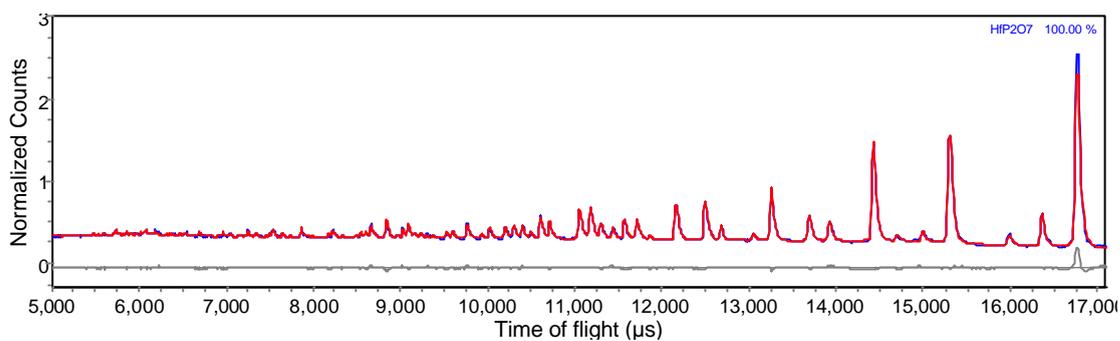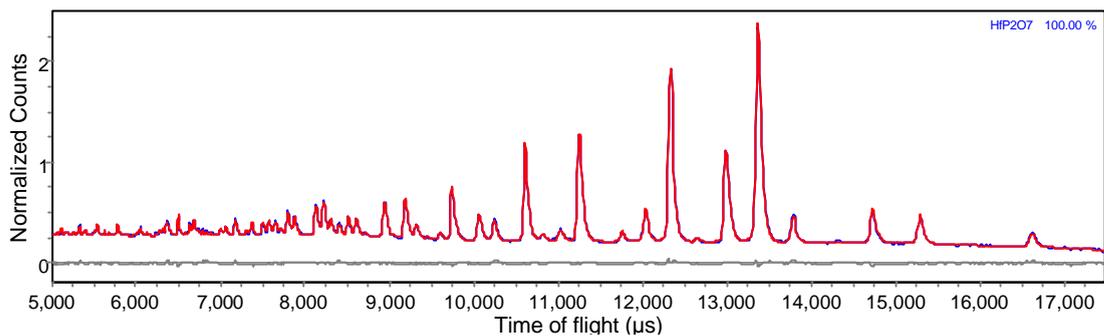
Bank 6 (154 °)

Bank 5 (91 °)
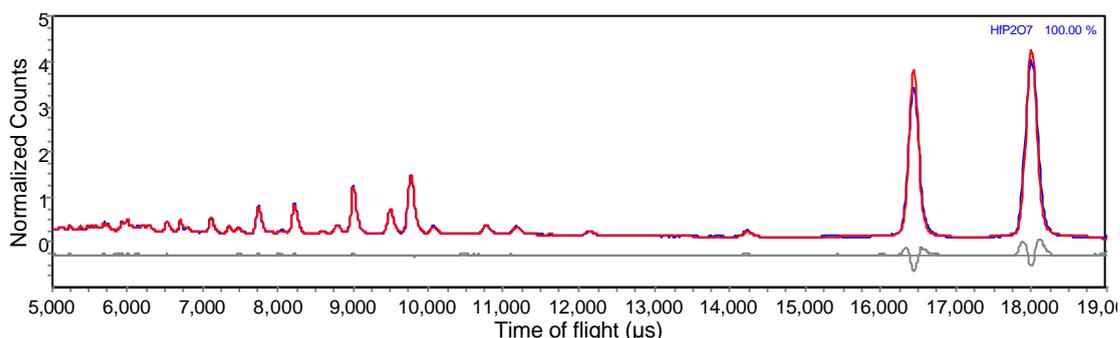
Bank 4 (64 °)

Bank 3 (35 °)

Figure 5-16 Rietveld refinement plots of high temperature HfP$_2$O$_7$ neutron diffraction data for *P1* model. Bank 3 (35 °) 5000–13000 µs, (*d*-spacing 1.77–4.60 Å) bank 4 (64 °) 5000-19000 µs (*d*-spacing 1.02–3.89 Å), bank 5 (91 °) 5000-17500 µs (*d*-spacing 0.74–2.62 Å), bank 6 (154 °) 5000–17100 µs (*d*-spacing 0.55–1.88 Å)
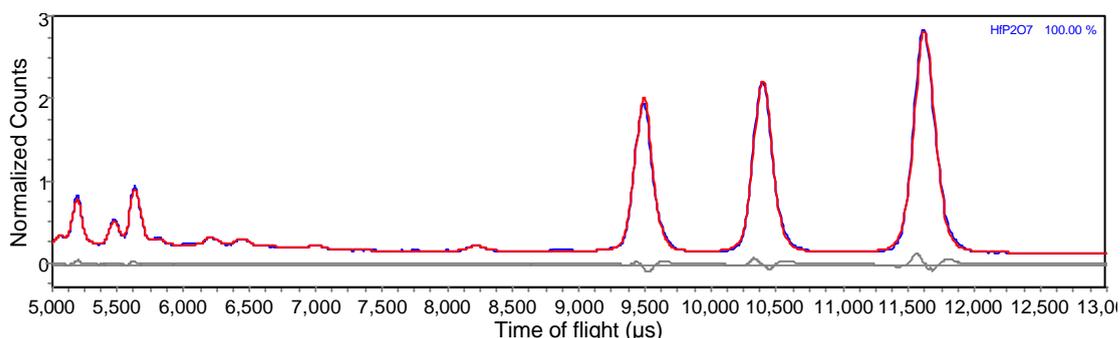
Bank 6 (154 °)

Bank 5 (91 °)

Bank 4 (64 °)

Bank 3 (35 °)

Figure 5-17 Rietveld refinement plots of high temperature HfP$_2$O$_7$ neutron diffraction data for *Pa3* model. Bank 3 (35 º) 5000-13000 µs, (*d*-spacing 1.77–4.60 Å) bank 4 (64 º) 5000–19000 µs (*d*-spacing 1.02–3.89 Å), bank 5 (91 º) 5000–17500 µs (*d*-spacing 0.74–2.62 Å), bank 6 (154 º) 5000–17100 µs (*d*-spacing 0.55?1.88 Å).
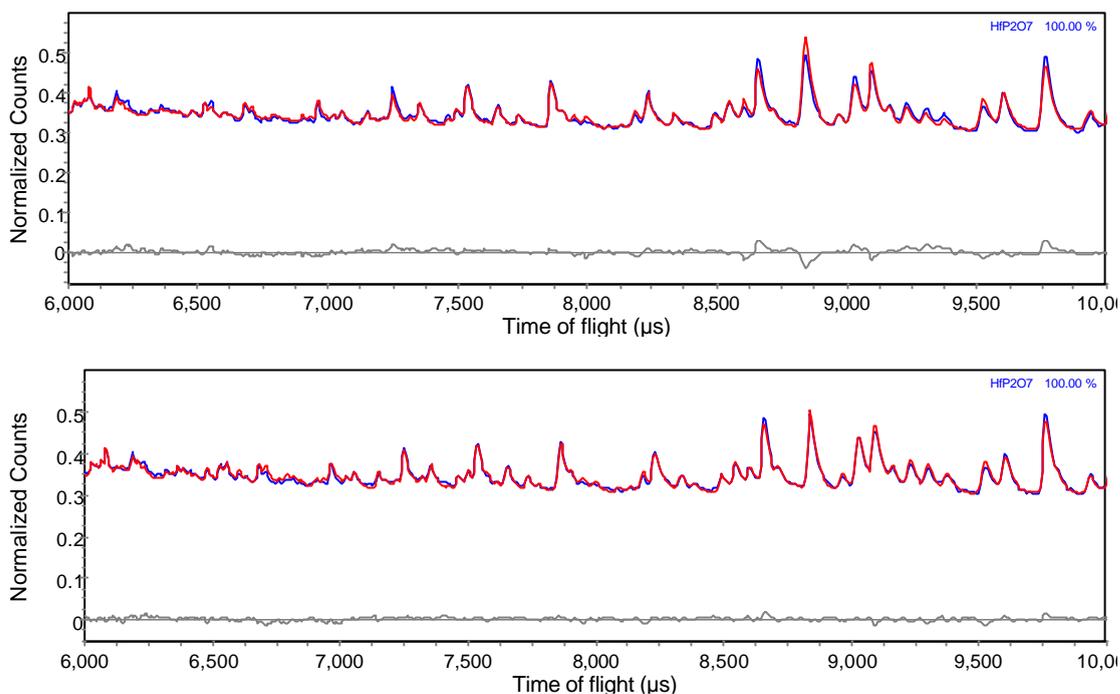
Figure 5-18 Close up comparison of fit for *Pa3* (top) and *P1* (bottom), for bank 6 (154 °) data, (0.66 - 1.10 Å *d*-spacing).

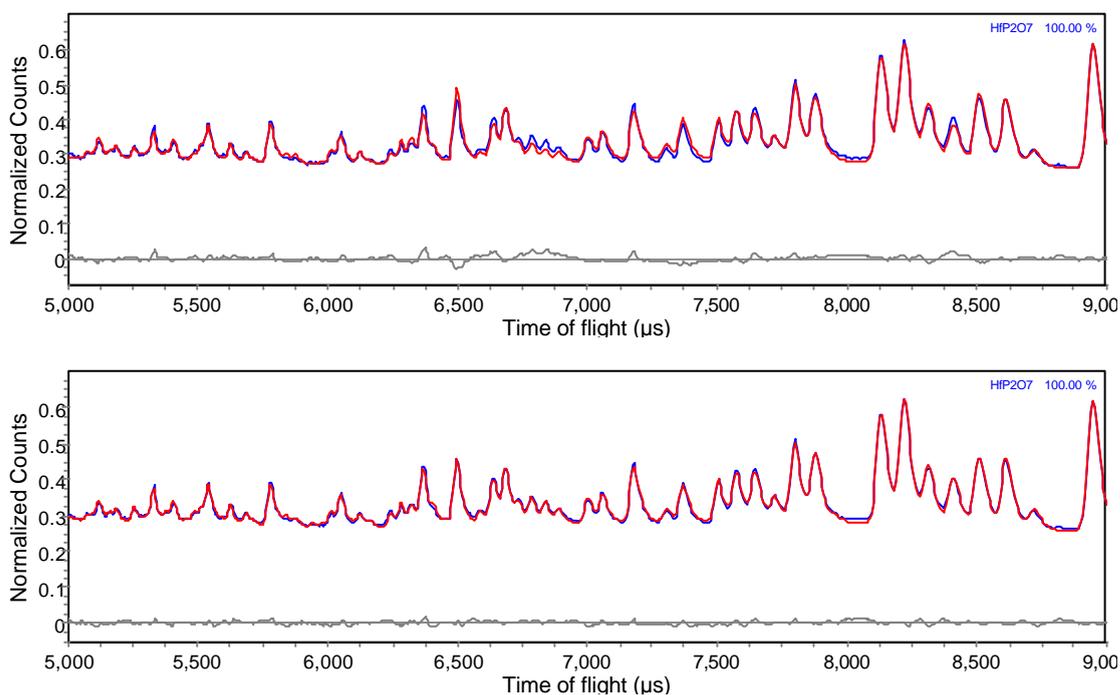**Figure 5-19 Close up comparison of fit for *Pa3* (top) and *P1* (bottom), for bank 5 (91 °) data (0.75 - 1.35 Å *d*-spacing).**

In conclusion, although there is some evidence for a lower symmetry space group, the *Pa3* model fits the data quite well, and it is difficult to state with certainty that the highly symmetric *Pa3* structure is incorrect. The structure observed by diffraction is of course an average structure, and it is possible that individual P$_2$O$_7$ units do not conform to the highly symmetric

structure. It may be possible to distinguish more effectively between the possible space groups using higher resolution neutron powder diffraction data, for example from the HRPD facility at ISIS, and such data should be collected. A number of other possible further experiments are proposed in the Conclusions section of this Chapter (Section 5.7).

5.2.2 HfP$_2$O$_7$ Low Temperature Phase

The structure of HfP$_2$O$_7$ at low temperature is considerably more complicated than the high temperature structure described above. A superstructure is formed, with all three cell parameters being tripled to give a unit cell with approximately 27 times the sub-cell volume. The powder diffraction pattern is dominated by peaks that would be given if the sub cell were the true structure. However, the appearance of supercell reflections at *d*-spacings where the subcell structure would not give any reflections indicates the formation of the larger cell. The connectivity of the structure remains unchanged from the high temperature structure, but small distortions in the structure lead to the lower symmetry larger unit cell. These distortions are presumably due to the competing effects of each of the highly interlinked polyhedra trying to adopt ideal conformations.

The space group of such a complex structure (with 1080 atoms in the unit cell) would be very difficult to determine using powder diffraction alone. Fortunately King had previously investigated the symmetry by a range of ^{31}P NMR experiments which showed HfP$_2$O$_7$ to contain 27 unique phosphorus sites, and thus the superstructure space group is unambiguously determined to be *Pbca*, as is that of ZrP$_2$O$_7$.[1] Given the knowledge of the space group, a structural investigation using the Rietveld method can be undertaken to determine the full room temperature structure from powder diffraction.

Time of flight neutron diffraction data for a sample of HfP$_2$O$_7$ (RKBG276) at 23 °C were obtained using the GEM instrument at ISIS (Rutherford Appleton Laboratories, UK) (GEM13116, May 2003). Data were collected for a total of 240.2 μAH. Room temperature X-ray diffraction data (d8_02186) in the 2*θ* range 10 – 120 ° were collected for the same sample on the Bruker d8 diffractometer in a total scan time of 5 hours.

The relative complexity of the powder pattern for the superstructure is illustrated by Figure 5-20, which shows Rietveld refinements of neutron diffraction data at 23 °C and 503 °C. In the data range shown in the figure (12000 - 17100 μs), there are 82 reflections for the high temperature sub cell structure, whereas for the low temperature superstructure there are 2223. Although the low temperature powder pattern is much more complex, the additional peaks are fitted well by use of the supercell structure in the refinement.
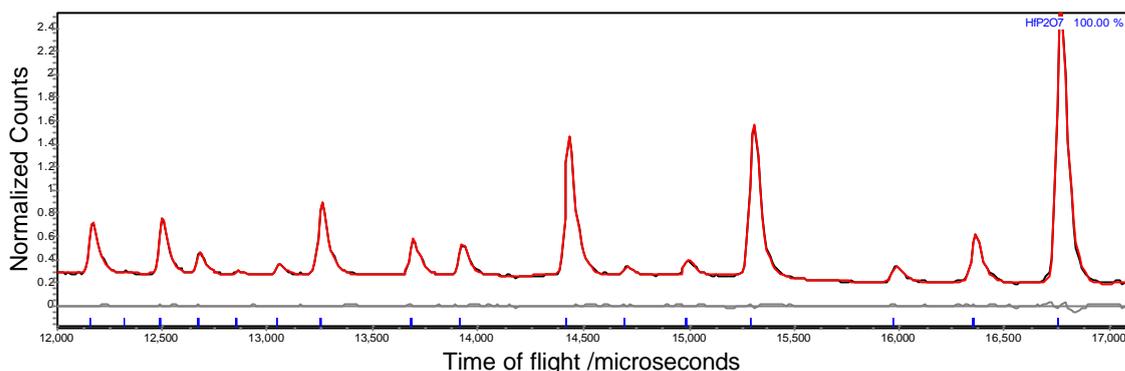
(a)
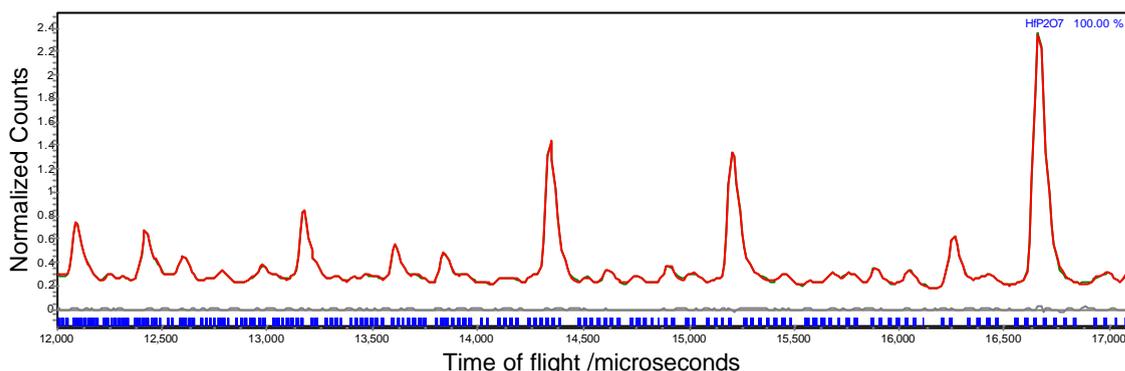
(b)

Figure 5-20 Comparison of Rietveld refinement of 154 ° bank neutron diffraction data for HfP$_2$O$_7$. (a) 503 °C data (GEM13120), fitted to *Pbca* HfP$_2$O$_7$ sub cell structure (b) 23 °C data (GEM13116) fitted to *Pbca* superstructure. In both cases the observed data are shown in blue, the calculated pattern in red and the difference in grey. The blue tick marks show the position of Bragg reflections.

Rietveld refinement was carried out by simultaneous refinement of the neutron and X-ray diffraction data, since the two techniques give different and complementary information about the structure. Data recorded by the 91 ° and the 'backscattering' 168 ° detector banks in the neutron diffraction experiment were selected since these give data with the highest signal to noise. The ranges of data used for the refinements are stated in Table 5-5.

	Filename	Data range used	d-spacing
X-Ray (1.541 Å)	d8_02186.raw	10 - 120 ° 2?	4.44 - 0.89 Å
Bank 5 (91 º)	gem13116_91.xye	5000 - 17500 µs	0.74 - 2.62 Å
Bank 6 (154 º)	gem13116_154.xye	5000 - 17100 µs	0.55 - 1.88 Å

Table 5-5 Data used for refinement of room temperature structure of HfP$_2$O$_7$.

The Topas Academic software[8] was used for all these refinements, using the three data ranges simultaneously. The initial starting structure used for this full structural refinement was that determined by Stinton for the room temperature phase of ZrP$_2$O$_7$,[9] which has been shown by NMR to have the same space group as the HfP$_2$O$_7$ superstructure[1]. Restraints were used to ensure the conformation of the PO$_4$ tetrahedra and HfO$_6$ octahedra remained chemically

reasonable throughout the refinement. An unrestrained refinement of such a complex structure (with 409 refined structural parameters) would be likely to result in an unreasonable structure which nonetheless gave an improved fit to the experimental data. Restraints based on the geometry of polyhedra are commonly used to avoid such an outcome, although care must be taken to ensure the correct weighting of restraints.

In this case restraints were implemented by imposing penalty functions according to the deviation of the Hf-O and P-O distances and O-P-O and O-Hf-O angles from ideal values. Bridging P-O-P oxygen sites were given labels starting in 'S' rather than 'O' so that they could be easily distinguished. The ideal geometry of the P$_2$O$_7^{4-}$ units was determined from the average values of the 84 PO$_4$ units in Mo$_2$P$_4$O$_{15}$, the largest framework oxide structure solved to date, and the single compound with most pyrophosphate groups.[10] These values were 1.5000 Å for P-O$_{Hf}$ bonds where oxygen is bonded to Hf, 1.5775 Å for P-O$_{bridging}$ bonds involving the bridging P-O-P bond and 1.5300 Å for the P-O$_{bridging}$ bonds in the P$_2$O$_7^{4-}$ unit in which the P-O-P bond angle is constrained by symmetry to be 180 ° (P133-S52-P133). The intra-tetrahedral O-P-O bond angles were given ideal values of 109.47 °. The Hf-O bonds were restrained with an ideal value of 2.0695 Å, with internal octahedral O-Hf-O angles of 90 ° and 180 °. The weighting of individual restraints was determined on the basis of test refinements.

The comparative weighting of X-ray and neutron data was adjusted so that the overall R_{WP} approximately equalled the average of the R_{WP} for separate refinements of the X-Ray and backscattering neutron data.

In order to obtain correct cell parameter data from time of flight neutron data, the value of the instrument parameter '*difc*', which is related to the distance between the neutron source and each detector bank must be correctly calibrated. This was carried out by fitting only the bank 6 data to the simple *Pa3* sub cell structure with the cell parameter fixed to 8.2141 Å, the value determined by Tait in room temperature X-Ray diffraction experiments calibrated with a silicon internal standard.[11] A refined value of *difc* = 9063.9537(2) was obtained, which was fixed for all subsequent refinements. Since fixing this parameter ensures the refined cell parameters are correct, the '*difc*' value for the bank 5 data, and a sample height correction for the X-ray data were allowed to refine freely.

A total of 467 parameters was refined: 58 instrumental / histogram terms and 409 structural parameters. 17 parameters were refined for each of the two neutron data ranges: 12 background parameters (coefficients of a Chebychev polynomial), a scale factor, 2 peak shape parameters (lor and dsp), and two instrument parameters (t$_0$, and difa). The *difc* instrument parameter was refined for the 91 ° data but fixed for the 154 ° data, as described above. For the X-Ray data, 21 parameters were refined: 12 background parameters (coefficients of a Chebychev polynomial), a scale factor, 6 peak shape parameters to describe a Thompson-Cox-Hastings pseudo-Voigt (TCHZ) function[12], a sample height correction, an axial divergence

parameter. An additional absorption correction term (*fixb*) was refined for both the X-ray and 91 ° neutron data in order to ensure temperature factor information consistent with that obtained by refinement using the more reliable backscattering neutron data only.

The structural parameters refined were: 3 cell parameters, a total of 402 coordinates (for 13 Hf, 27 P and 94 O atoms), and four B_{eq} isotropic displacement parameters (for Hf, P, non-bridging oxygen and bridging oxygen). All but two atomic sites are on general positions (Wyckoff site *8c*), for which all 3 coordinates were refined, whilst the coordinates of Hf1 (*4b* site) at 0,0,0 and S52 (*4a* site), 0,0,0.5 are fixed by symmetry.

A simulated annealing process was used to ensure that the refinement found the correct minimum rather than a false minimum. 1000 iterations of least squares refinement were carried out, and after each convergence of the refinement, each of the refined fractional atomic coordinates were shifted by a random displacement of up to 0.01 (~0.25 Å) from Stinton's ZrP$_2$O$_7$ coordinates, the atomic displacement parameters were returned to the values previously refined and the cell parameters were set to be metrically cubic (with cell parameter of the mean of the previously refined *a*, *b* and *c* parameters).

A summary of the results obtained from the final refinement is given in Table 5-6. The value of c^2 is small due to the effect of a large contribution by the background in the neutron diffraction patterns, and the values of R_{Bragg} are a more reliable indication of the quality of fit. Rietveld plots are shown in Figure 5-21.

a / Å	24.637(1)	**B(Hf)**	0.57(3)
b / Å	24.6145(6)	**B(P)**	0.73(4)
c / Å	24.636(1)	**B(O$_{non-bridging}$)**	1.26(4)
Vol / Å^3	14940(1)	**B(O$_{bridging}$)**	1.5(1)
Space Group	*Pbca*	**Structural parameters**	409
Number of reflections (154 °/91 °/X-Ray)	45774/18170/11105	**Total refined parameters**	467
Overall R_{WP}	4.788		
R_{WP} (154 °/91 °/X-Ray)	2.080/1.845/11.529	**R_{Bragg}(154 °/91 °/X-Ray)**	0.929/0.893/3.996

Table 5-6 Summary of results from Rietveld refinement of HfP$_2$O$_7$ structure.

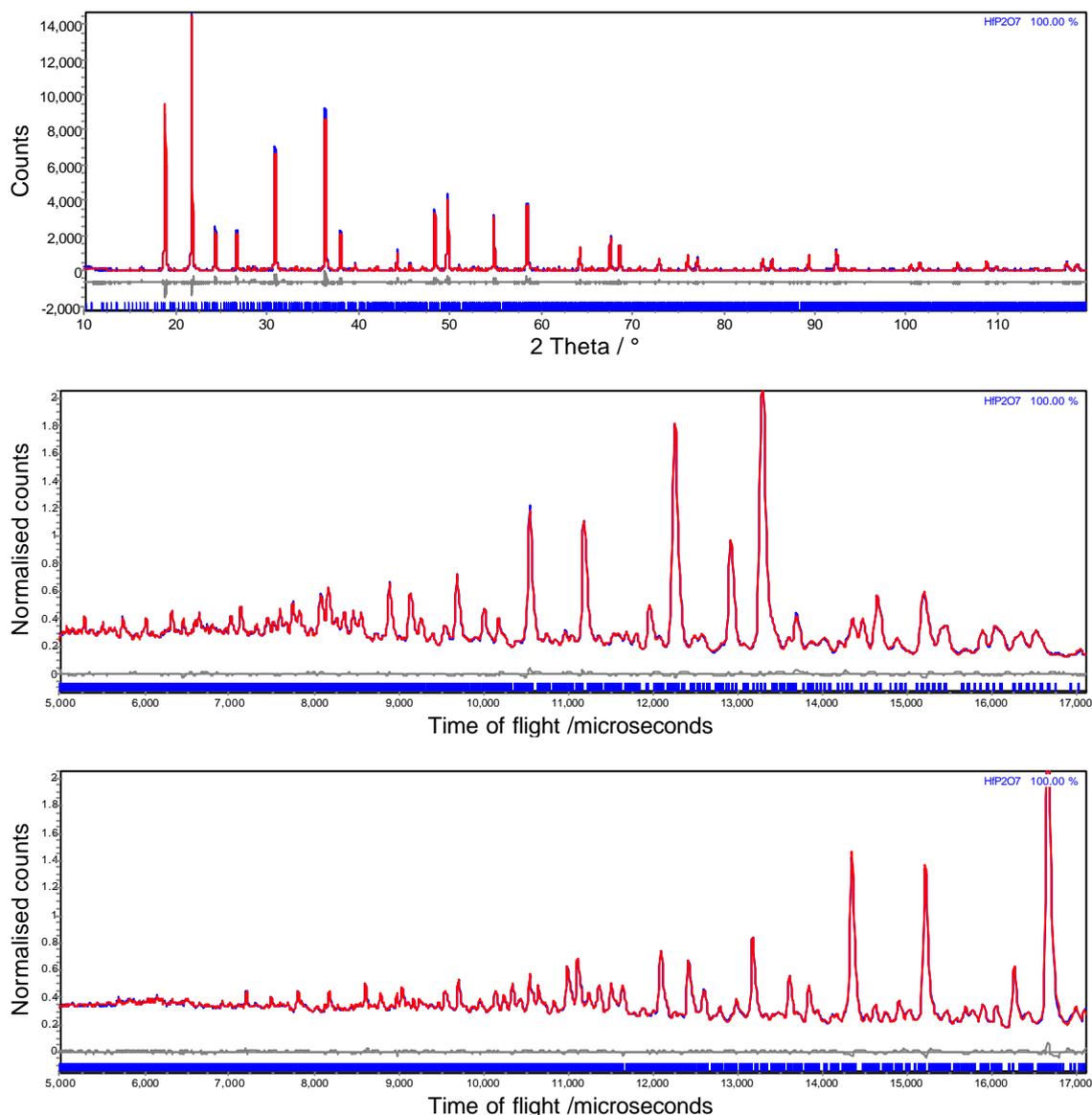**Figure 5-21 Rietveld refinement plots of HfP$_2$O$_7$: X-ray (*top*, d8_02186, *d* = 4.44 - 0.89 Å), and 91 ° (*middle*, *d* = 0.74 − 2.62 Å) and 154 ° (*bottom*, *d* = 0.55 − 1.88°Å) bank neutron (gem13116) diffraction data.**

The structure of ZrP$_2$O$_7$ has been determined by similar methods by Stinton.[9] The refined HfP$_2$O$_7$ structure was compared to Stinton's ZrP$_2$O$_7$ by determining the distance between equivalent atoms when the two sets of coordinates were superimposed using the ZrP$_2$O$_7$ cell parameters (*a* = 24.7437(4) Å, *b* = 24.7258(3) Å, *c* = 24.7507(4) Å). A histogram of the distances between equivalent sites for which the coordinates were refined is shown in Figure 5-22. The mean displacement is 0.0693 Å (standard deviation 0.037 Å)., so the structure of HfP$_2$O$_7$ has thus been shown to be extremely similar to that of ZrP$_2$O$_7$.
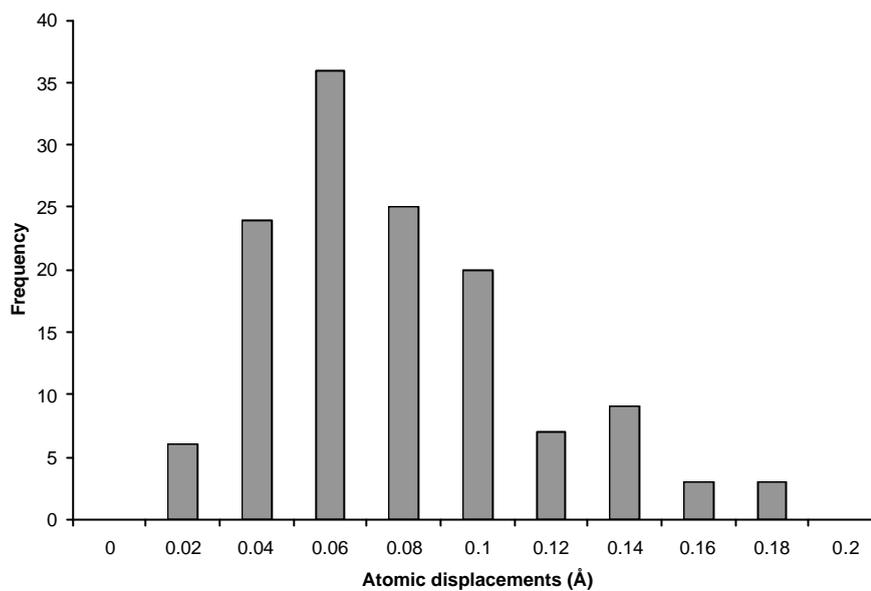
Figure 5-22 Histogram of distances between equivalent sites in HfP$_2$O$_7$ refinement and Stinton's ZrP$_2$O$_7$.

The final refined structure of the HfP$_2$O$_7$ superstructure is shown in Figure 5-23.
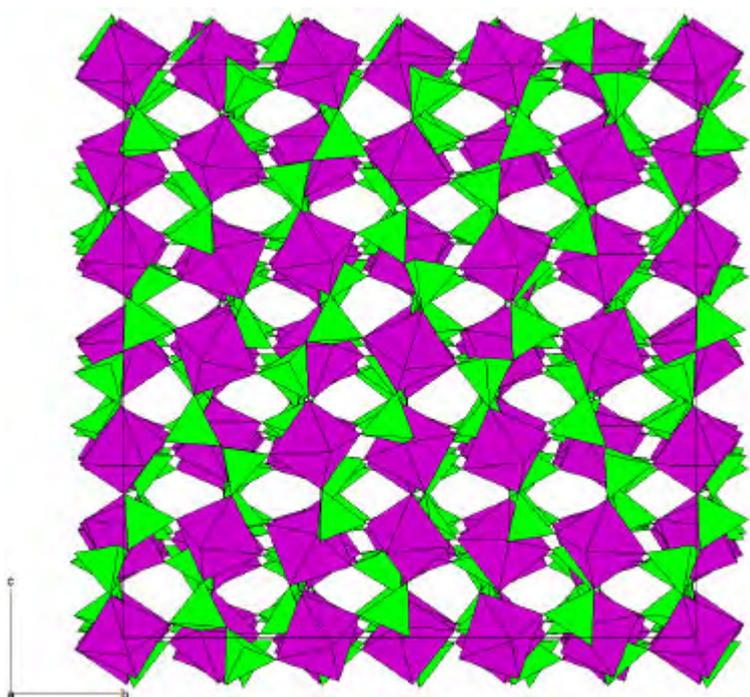

Figure 5-23 The unit cell of the refined HfP$_2$O$_7$ structure with HfO$_6$ octahedra shown in purple and PO$_4$ tetrahedra shown in green.

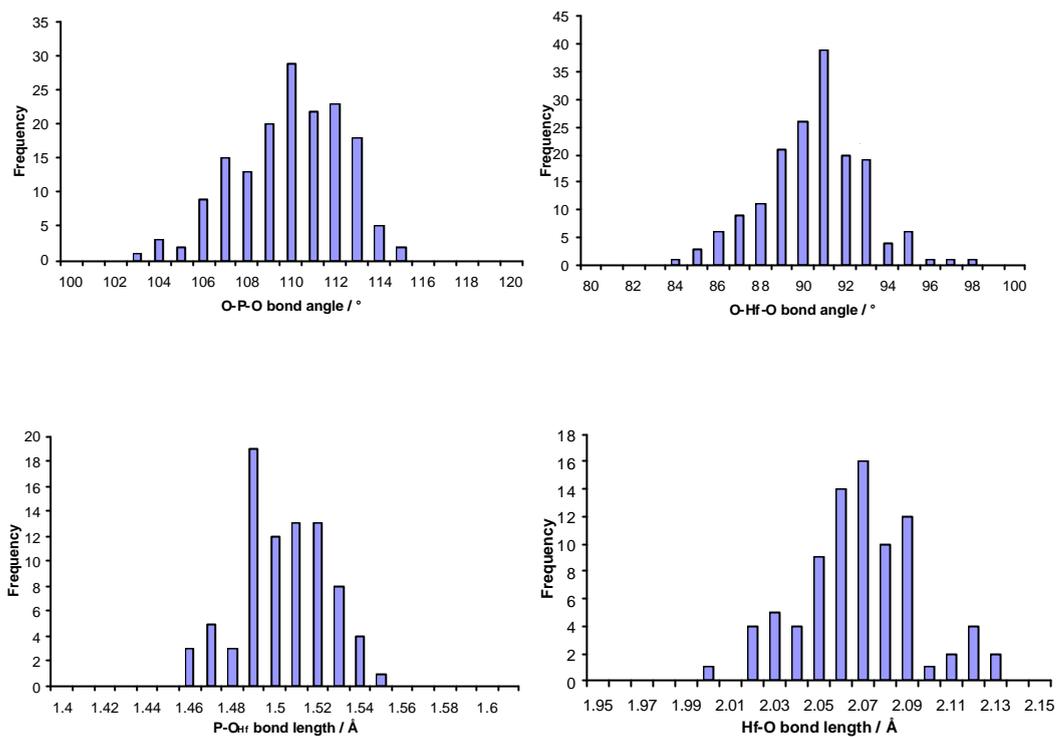Histograms of bond lengths and angles in the refined structure are given in Figure 5-24.

Figure 5-24 Histograms of bond lengths and angles in the final refined structure of HfP$_2$O$_7$

The input file used for the final refinement, which includes full atomic coordinates, bond angles and lengths, and Rietveld intensity profiles for each bank are given in the Appendix CDR.

5.2.3 Variable Temperature Neutron Diffraction Study

Having determined the structure at high and low temperature, variable temperature data were then examined. Neutron diffraction data were recorded as the temperature was decreased from 493 °C to 143 °C. A beam current of 25.2-25.6 μAh was collected at each of 23 temperatures. The data (see Figure 5-25) show the emergence of the superstructure-only peaks as the temperature is decreased.
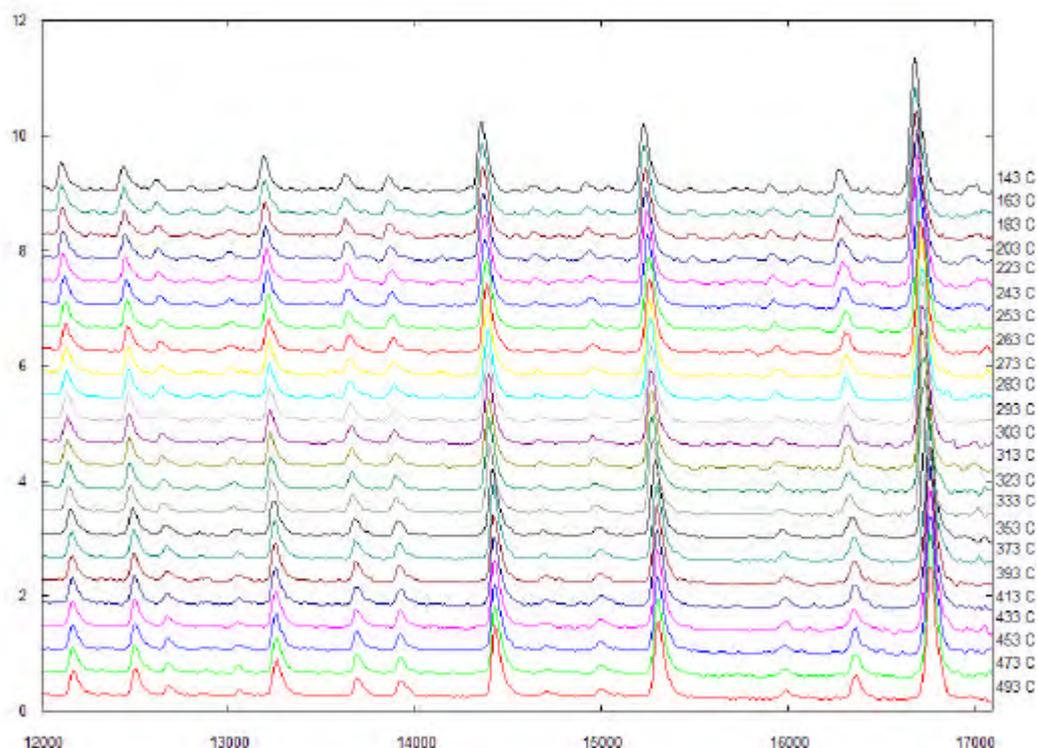

Figure 5-25 Variable temperature neutron diffraction data of HfP$_2$O$_7$. at temperatures in the range 143-493 °C. Data from the backscattering detector (GEM13121-13143).

HfP$_2$O$_7$ undergoes two phase transitions in this temperature range: from the subcell to the superstructure *via* an incommensurate intermediate. [11] It has not been possible to determine the structure of the incommensurate phase. However, the variable temperature data may be fitted to the high temperature *Pbca* subcell structure as an approximation in order to determine the variation of cell volume with temperature. Although the superstructure peaks will not be fitted, the cell parameters obtained are accurate, as these are derived from the *positions* of the largest peaks.

Rietveld refinement was carried out on each of the scans in the VT experiment using data from the backscattering detector, in the range 12000-17100 μs. 16 parameters were refined: 6 background terms, 2 peak shape terms, 3 cell parameters, 4 isotropic temperature factors and a histogram scale factor. The atomic coordinates were fixed at those refined for the *Pbca* high temperature structure. In order to ensure correct calibration of the cell parameters, the *difc*

value was fixed at that obtained by refining room temperature data against a subcell structure with the cell parameter fixed to that obtained by Tait.[11]

The unit cell volume as a function of temperature is shown in Figure 5-26, which also includes a comparison to values obtained by X-ray diffraction by Tait.[11]
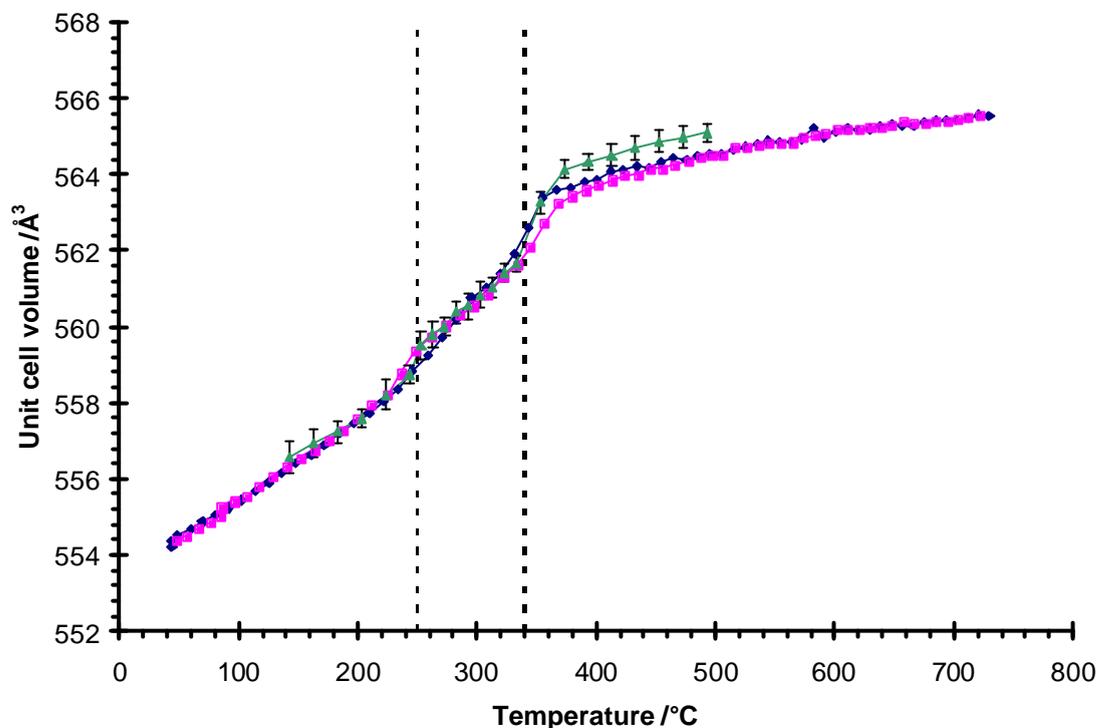

Figure 5-26 Unit cell volume of HfP$_2$O$_7$ derived from Rietveld refinement of variable temperature neutron diffraction (green). Error bars shown are e.s.d. values from the refinement. The volumes obtained by Tait by X-ray diffraction on heating (blue) and cooling (pink) are shown for comparison. Vertical dotted black lines indicate the phase transition temperatures at 250 and 340 °C.

Tait used a *Pa3* model to fit the data from X-ray diffraction. The phase transitions are seen by changes in gradient in the plot of unit cell volume. The as yet uncharacterised incommensurate phase exists between ~250 and 340 °C.

5.3 ZrV$_2$O$_7$

Some [51]V NMR results for ZrV$_2$O$_7$ had previously been reported by Korthuis *et al.*[13], who showed that the room temperature spectrum consisted of a number of overlapped peaks, which could not be separately resolved. Subsequent results by King showed that the ambient temperature [51]V spectrum appeared to contain more than 11 overlapped peaks, suggesting that either the symmetry was lower than *Pa3*, and there were more than 11 vanadium sites, or that peak shoulders or splitting effects were seen due to quadrupolar effects.[1]

Similar results have been observed for the high temperature phase of ZrV$_2$O$_7$. One of the more interesting results obtained by Korthuis *et al.*,[13] was a [51]V NMR spectrum of the high temperature phase which showed two peaks, separated by 507 ppm. This was said to be a single site splitting as a result of quadrupolar coupling producing a spectrum characteristic of an axially symmetric quadrupole powder pattern. However, no evidence was presented for this unusual spectrum being due to quadrupole coupling rather than more than one independent vanadium site, and Korthuis *et al.* had only recorded spectra at one magnetic field strength.

In order to investigate these unusual results, variable temperature spectra were recorded on two spectrometers, operating at different frequencies, as it was hoped this would enable quadrupolar effects to be distinguished from multiple sites. A pure, highly crystalline sample of ZrV$_2$O$_7$, synthesised by Dr John Evans by a previously published method,[14] was used. This sample (JSOE389) was packed in a 7.0 mm diameter MAS rotor. Experiments were first carried out using the InfinityPlus 500 (with a [51]V Larmor frequency of 131.3 MHz). Experiments were also carried out on the Varian Innova 300 (operating at a [51]V Larmor frequency of 78.9 MHz).

The spectra recorded at 131.3 MHz at three temperatures are shown in Figure 5-27 to Figure 5-29. At room temperature (Figure 5-27), there are apparently 13 peaks, although they are heavily overlapped. This result essentially confirms the result of King, who recorded a spectrum at lower magnetic field strength. The peak at ~830 ppm was seen as a shoulder in King's spectrum, but appears here to be a definite peak.
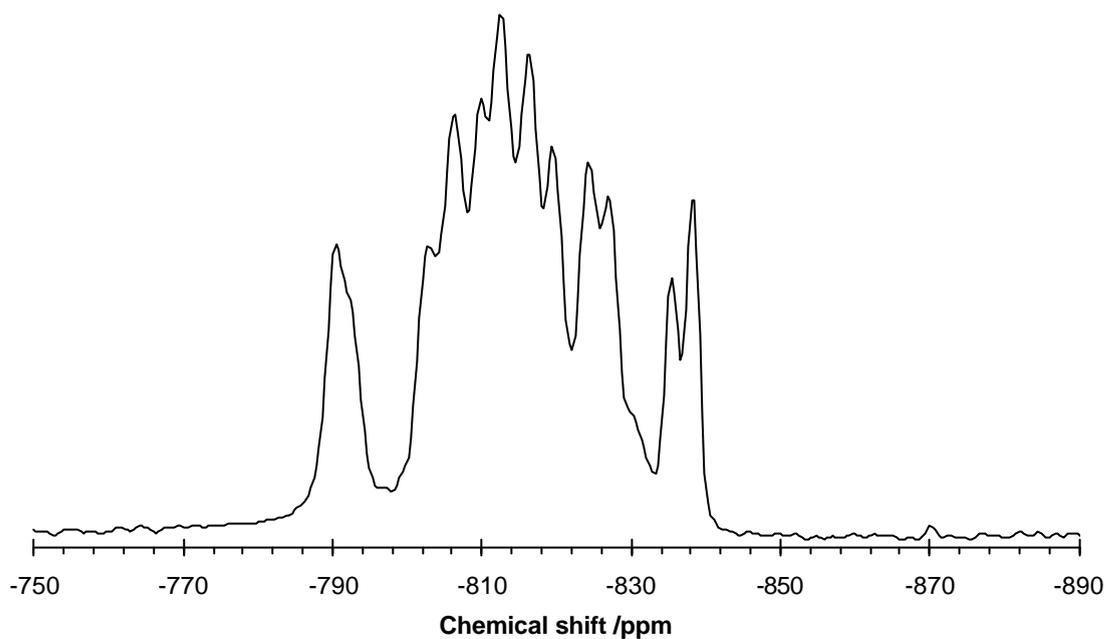
Figure 5-27 ^{51}V NMR spectra of ZrV$_2$O$_7$ at room temperature acquired at 131.35 MHz, excitation pulse width 1 µs, repetition delay 25 s., MAS speed 16.2 kHz.

The observation of more than 11 peaks can be explained either by there being more than 11 inequivalent vanadium sites (*i.e.* the superstructure has lower symmetry than *Pa3*) or peak splitting due to quadrupolar effects. If the former were the case, then there would have to be at least 22 overlapped peaks, since this is the number of inequivalent vanadium sites in a *P2$_1$3* 3×3×3 superstructure, the most symmetric subgroup of *Pa3*. Further work, including 2 dimensional ^{51}V experiments such as MQMAS NMR would be required to confirm if this is the case.
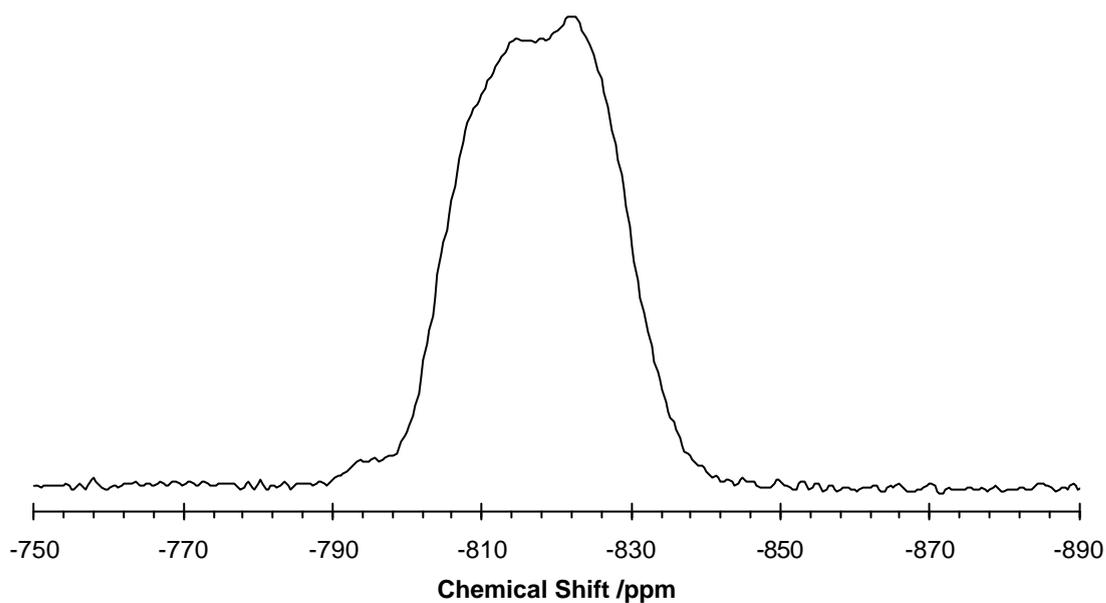
Figure 5-28 ^{51}V NMR spectra of ZrV$_2$O$_7$ at 90 °C, acquired at 131.35 MHz, MAS speed 16.2 kHz.

The spectrum at 80 °C (Figure 5-28) shows a broad envelope with no well defined individual peaks, a result which is compatible with the incommensurate nature of the intermediate phase. The high temperature spectrum (120 °C, Figure 5-29) is significantly different from the 80 °C spectrum, confirming that the sample has undergone a second phase transition. The 120 °C spectrum appears to show two highly overlapped peaks, separated by 400 Hz, and thus, in terms of the qualitative appearance of the spectrum, this reproduces the result of Korthuis *et al.*.[13]
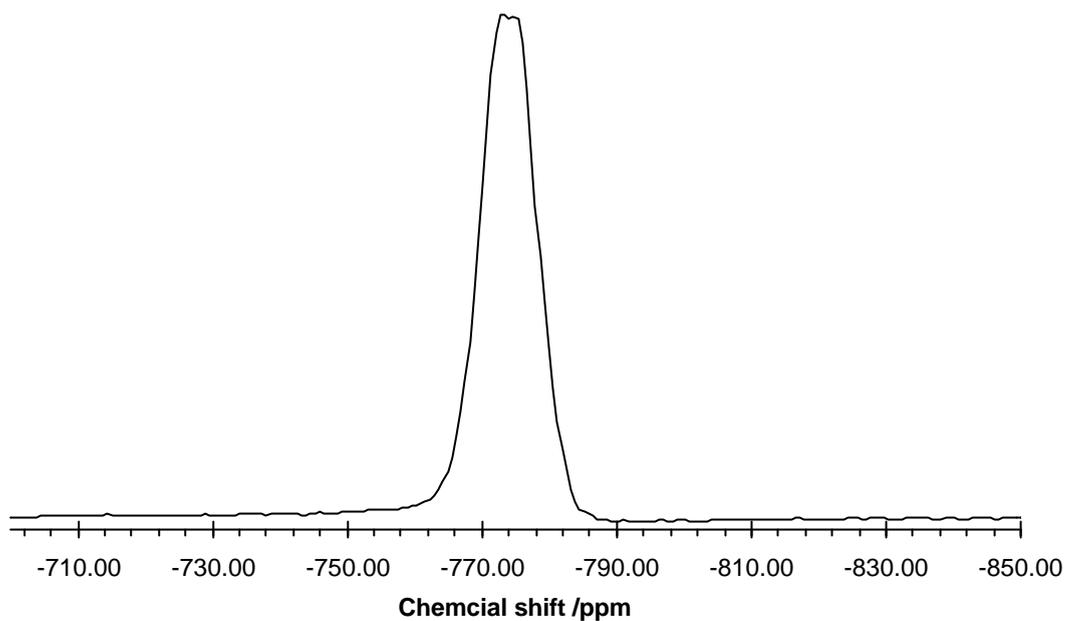
Figure 5-29 ⁵¹V NMR spectra of ZrV₂O₇ at 200 °C acquired at 131.333 MHz, MAS speed 20 kHz.

In order to gain a further insight into this observation, a spectrum at 78.9 MHz was recorded, as shown in Figure 5-30. It was expected that comparison of the spectra recorded at different magnetic fields would either show the same peak separation in chemical shift units (indicating the presence of two sites), or that the separation (in frequency units) would be scaled by the ratio of the magnetic fields (indicating that the unusual lineshape is due to quadrupolar effects).

Figure 5-30 ⁵¹V MAS NMR Spectrum of ZrV₂O₇ at room temperature. ⁵¹V Larmor frequency of 78.9 MHz.

In fact, the high temperature spectra obtained at both magnetic field strengths show approximately the same peak separation, in frequency units. This is an unusual result, and in fact apparently disp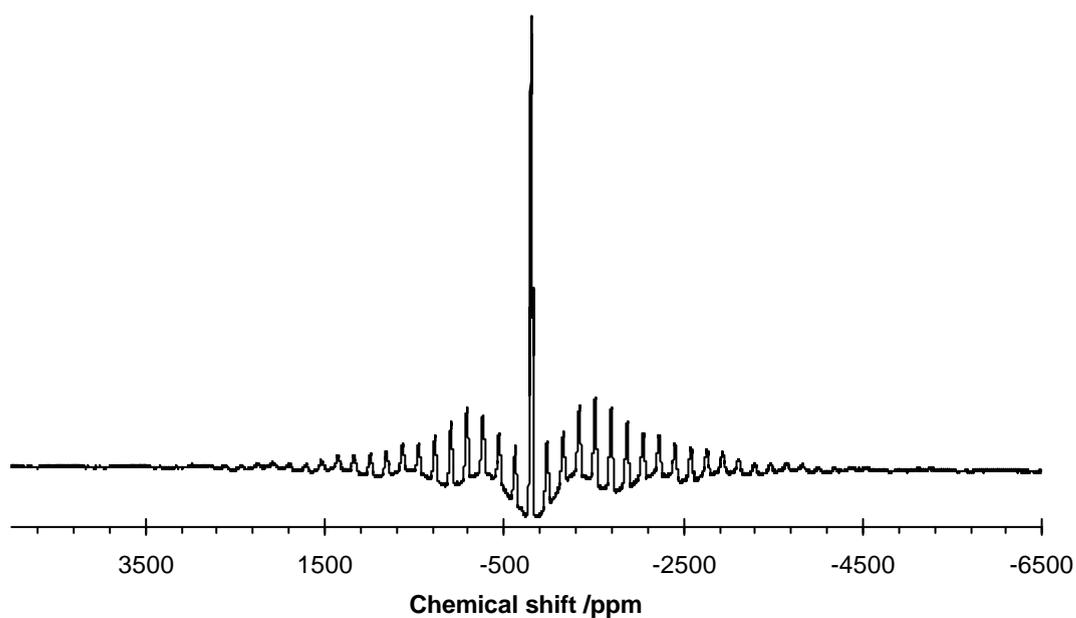roves the two most obvious potential explanations of the appearance of the spectrum. If two sites were present then the peak separation would be expected to remain constant in chemical shift units (ppm), and the separation in frequency units would scale with magnetic field. If the unusual peak shape were due to a quadrupolar coupling effect, then the separation (in frequency units) would be expected to scale with the magnetic field. The results are thus inconclusive. It is possible that these effects may be due to the transfer of second order quadrupole effects *via* dipolar or *J* coupling, as has been observed in other several studies.[15, 16] Further investigations into these results are required in order to determine the cause.

5.4 HfV₂O₇

The results from ^{51}V NMR of ZrV_2O_7 are inconclusive, and it was hoped that NMR of the supposedly iso-structural HfV_2O_7 would provide additional useful information. HfV_2O_7 was prepared by solid state methods and then variable temperature ^{51}V MAS NMR experiments were carried out.

5.4.1 Synthesis of HfV₂O₇

A sample of HfV_2O_7 (mrh035) was prepared by heating together $HfOCl_2 \cdot 8H_2O$ and NH_4VO_3. On heating these materials decompose to form HfO_2 and V_2O_5 respectively. The yield of HfO_2 and V_2O_5 was determined previously by separately heating and accurately weighing samples of the precursor materials. It was found that $HfOCl_2 \cdot 8H_2O$ gave 49.7 % HfO_2 and NH_4VO_3 gave 76.9 % by mass V_2O_5. 2.6998 g $HfOCl_2 \cdot 8H_2O$ (Alfa Aesar, 98+ %) and 1.5083 g NH_4VO_3 (Alfa Aesar, 99.93 %) were therefore mixed and thoroughly ground with a pestle and mortar giving a red-brown mixture which was transferred to a platinum crucible and heated in a furnace to 650 °C at a rate of 0.5 °K·min⁻¹ and maintained at this temperature for 8 hours. The initial product (mrh030, a dull yellow-brown powder), shown by powder diffraction to be made up of ~ 40 % HfV_2O_7, ~ 20 % HfO_2 and ~ 40 % V_2O_5, was re-ground and returned to the furnace, for a second heating, this time to 700 °C at a rate of 0.5 ° K·min⁻¹ and maintained at this temperature for 1 hour. The product from this second heating (mrh031) was shown to be composed of ~ 77 % HfV_2O_7, ~ 7 % HfO_2 and ~ 16 % V_2O_5. After another 2 cycles of grinding and heating the composition was ~ 90 % HfV_2O_7, ~ 5 % HfO_2 and ~ 5 % V_2O_5, and the purity of HfV_2O_7 was not measurably increased by a fifth cycle of heating. The Rietveld refinement plot of the final sample (mrh035) is shown in Figure 5-31.
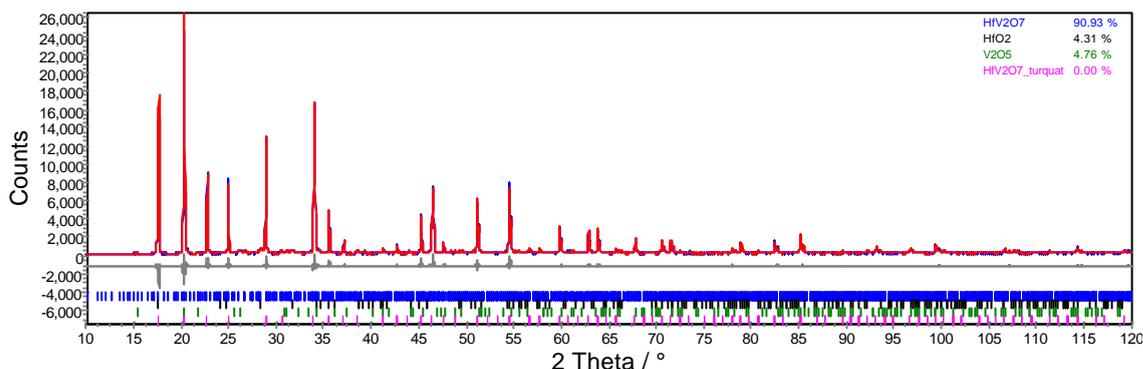
Figure 5-31 Rietveld refinement of powder diffractogram (d5_05253) of HfV$_2$O$_7$ (mrh035). Tick marks show positions of Bragg peaks for HfV$_2$O$_7$ assuming superstructure (blue), HfO$_2$ (black), V$_2$O$_5$ (green), and the simple HfV$_2$O$_7$ structure (pink).

The only published structure of HfV$_2$O$_7$ is that by Torquay *et al.*, who fitted the room temperature structure to a simple sub cell with *Pa3* symmetry, and there is still some doubt over the true complete structure, due to electron diffraction results.[17] However the powder pattern of HfV$_2$O$_7$ (mrh035) fits well to the ZrV$_2$O$_7$ room temperature *Pa3* superstructure determined by Evans *et al* [18] with Hf atoms on the Zr sites, since the HfV$_2$O$_7$ superstructure is similar. The purity of samples was checked by Rietveld refinement, refining a total of 38 parameters: 12 background parameters, an axial divergence correction, a sample height correction; 11 parameters for the *Pa3* HfV$_2$O$_7$ structure (1 cell parameter, 3 BEQ temperature factors, 6 (TCHZ) peak shape parameters and a histogram scale parameter); 7 parameters for the *P2$_1$/c* HfO$_2$ structure[19] (4 cell parameter, 1 B_{EQ} temperature factors, crystallite size and a histogram scale parameter); 6 parameters for the *Pmmn* V$_2$O$_5$ structure[20] (3 cell parameter, 1 B_{EQ} temperature factors, crystallite size and a histogram scale parameter).

5.4.2 ^{51}V NMR of HfV$_2$O$_7$

^{51}V NMR spectra were obtained for the sample of HfV$_2$O$_7$ (mrh035). All experiments were performed at 131.3 MHz. A sample of HfV$_2$O$_7$ (mrh035) was packed into a thick-walled 3.2 mm rotor. Spectra were recorded at a range of temperatures and spinning speeds. The spectra were referenced to a 0.16 M aqueous solution of NaVO$_3$ (d_{iso} = -574.38 ppm). Given the known impurity, it was expected that a ^{51}V NMR peak for the V$_2$O$_5$ impurity would be observed. The chemical shift of the ^{51}V peak for V$_2$O$_5$ is known to be -610 ppm from published results.[21]

HfV$_2$O$_7$ has been shown by diffraction to undergo two phase transitions at 67 and 96 °C[17]. The spectra from room temperature to 90 °C were very similar to the results for ZrV$_2$O$_7$, clearly showing the phase transition to the incommensurate intermediate phase. The room temperature spectrum (Figure 5-32) and intermediate phase spectrum (Figure 5-33) are both very similar to that for ZrV$_2$O$_7$.
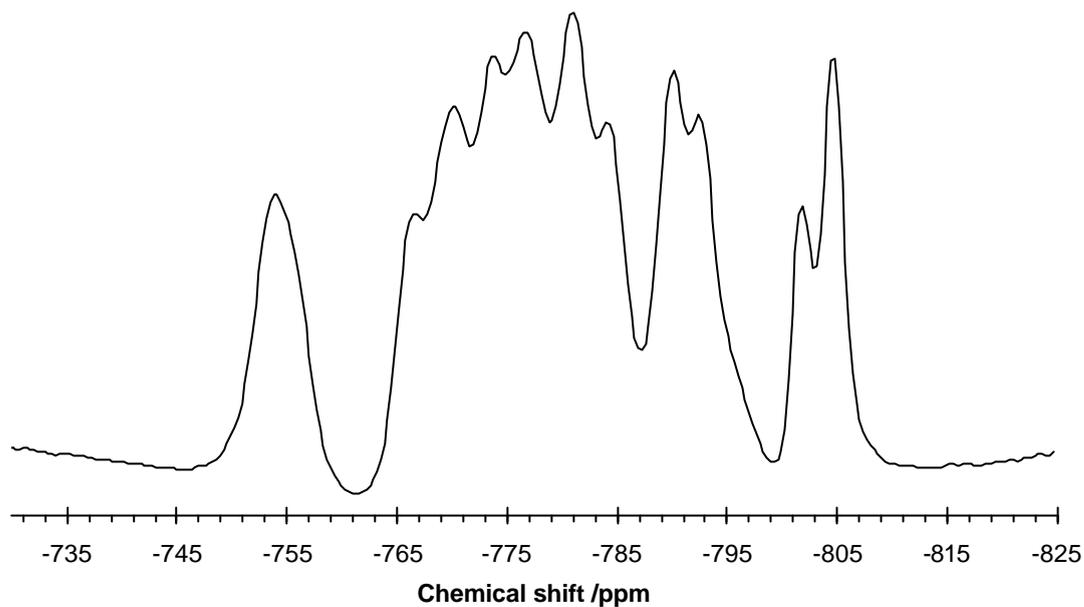
Figure 5-32 Centreband region of ^{51}V MAS NMR spectrum of HfV$_2$O$_7$ at room temperature, MAS speed 14 kHz. Excitation pulse width 0.5 µs, pulse delay 30 s, 256 transients.
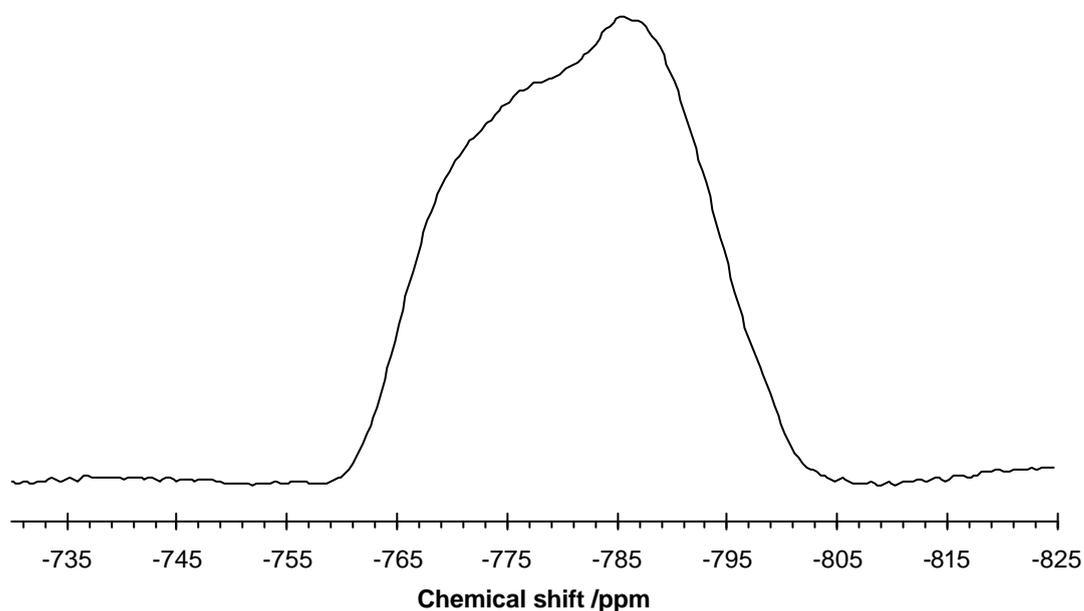
Figure 5-33 Centreband region of ^{51}V MAS NMR spectrum of HfV$_2$O$_7$ at 90 °C, MAS speed 14 kHz. Excitation pulse width 0.5 µs, pulse delay 30 s, 256 transients.

^{51}V NMR spectra of the high temperature phase were then recorded. A spectrum at a 200 °C is shown in Figure 5-34. Close inspection of the high temperature spectra shows the V$_2$O$_5$ peak at -610 ppm, which is concealed by peak overlap in the low temperature spectrum. The spectrum at 200 °C is substantially similar to that of ZrV$_2$O$_7$.
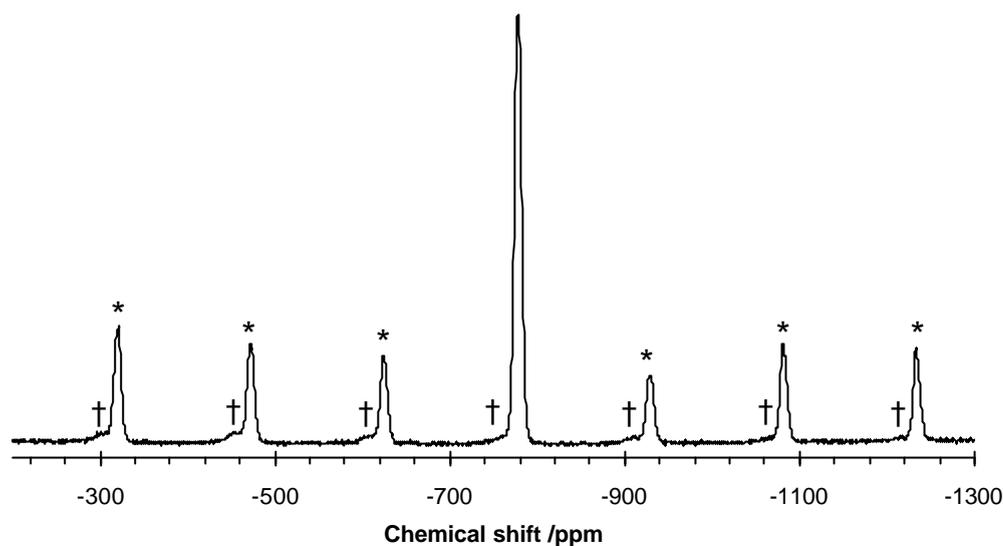
(a)
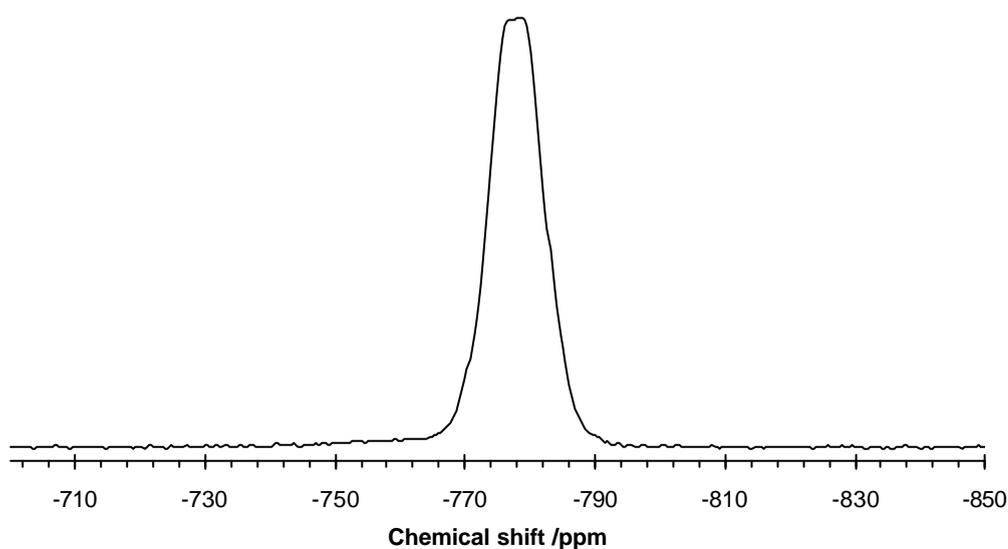
(b)

Figure 5-34 [51]V MAS NMR spectrum of HfV$_2$O$_7$ at 200 °C, MAS speed 20 kHz. Excitation pulse width 0.5 µs, pulse delay 10 s, 64 transients. (a) Spectrum showing sidebands,*, and V$_2$O$_5$ impurity peaks, †. (b) centreband peak only.

A series of spectra were recorded at different MAS spinning rates, and it was found that the variation of spinning speed (Figure 5-35) produces no significant change in the peak shape, although the peak width was decreased by faster spinning as is usual.
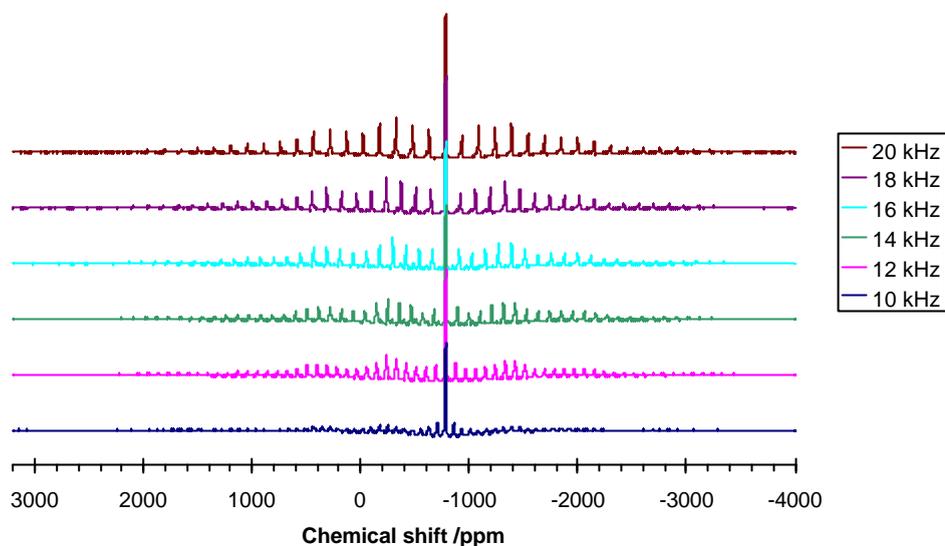
(a)
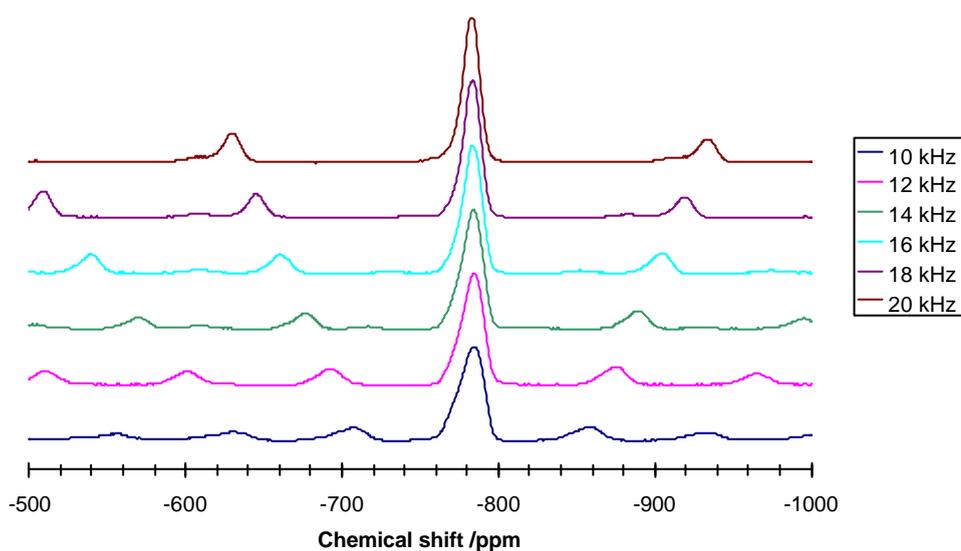
(b)

Figure 5-35 ^{51}V MAS NMR spectra of HfP$_2$O$_7$ at 120 °C recorded at different MAS speeds. (a) shows the complete spinning sideband manifold, (b) shows only the centre band region. 0.5 µs excitation pulse width, 30 s pulse delay, 64 transients.

The ^{51}V NMR results for HfV$_2$O$_7$ confirm the findings of the experiments on ZrV$_2$O$_7$. It was hoped that there would be some difference in the spectrum that may help to explain the unusual result in the high temperature spectra. It is thus not clear whether this is an unusual NMR phenomenon, or a breaking of the symmetry of the crystallographic space group. Although these results represent an intriguing discovery, they have not been investigated further within this project as a decision was made to concentrate on other areas. Further experiments, such as ^{51}V MQMAS experiments may provide more information.

5.5 SnP$_2$O$_7$

The ^{31}P NMR of the room temperature phase of SnP$_2$O$_7$ had been studied extensively by Fayon *et al.*, who used a variety of experiments to determine that the asymmetric unit contains at least 49 unique P$_2$O$_7$ groups. [22] NMR results have not been published for either the high temperature (>560 °C) phase or the incommensurate intermediate phase. [23]

The ^{31}P MAS NMR spectra of samples synthesised (by Dr Richard Gover) at three different temperatures were recorded. X-ray diffraction of these samples had previously suggested that sintering at 1200 °C is necessary to produce highly crystalline samples, and that those samples heated to lower temperatures had subtle differences in the superstructure reflections.[23] The ^{31}P MAS NMR spectra (Figure 5-36) apparently show a trend for a more ordered structure, with a large number of overlapped peaks at higher synthesis temperatures, with the sample synthesized at 600 °C appearing to show a continuous range of phosphorus environments. This result is in agreement with previous X-Ray diffraction data.
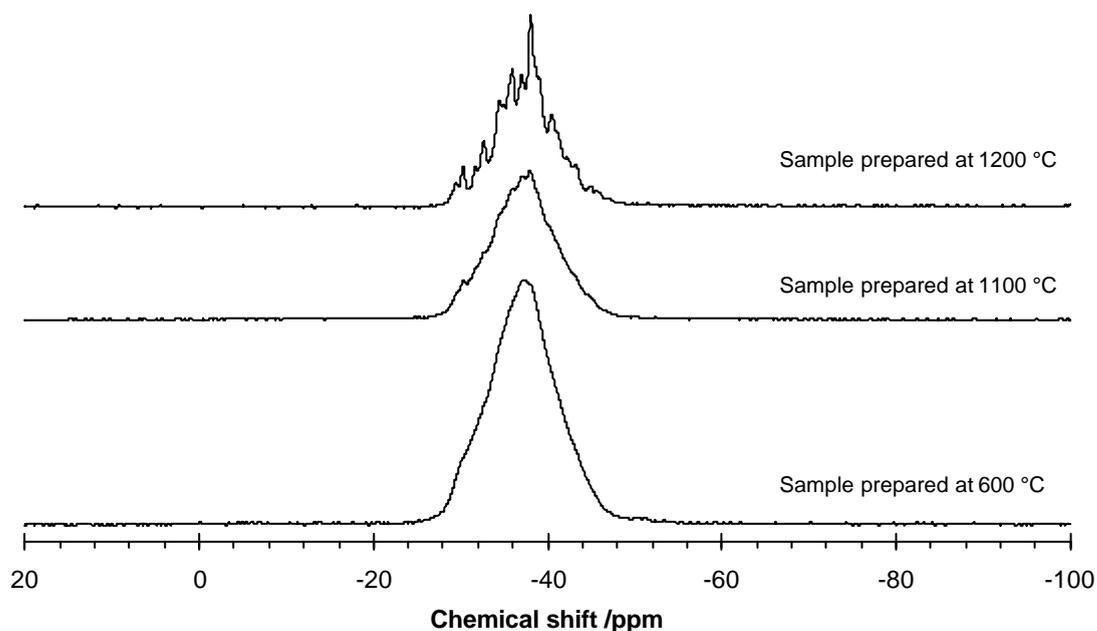
Figure 5-36 ^{31}P MAS NMR spectra of SnP$_2$O$_7$ synthesised at 600 °C (rkbg1) 1100 °C (rkbg11) and 1200 °C (rkgb29). MAS speed 18 kHz, room temperature. 32 transients were acquired for each spectrum, with a pulse excitation width of 3.4 µs, and a pulse repetition delay of 70 s, [31]P Larmor frequency 202.30 MHz. The centre-band region only is shown in each case.

^{31}P MAS NMR Spectra of the SnP$_2$O$_7$ sample synthesised at 1200 °C (rkbg29 - 120 mesh sieve) were also recorded using the high temperature probe on the Innova 300 spectrometer. A room temperature spectrum was first recorded, with a MAS speed of 2.8 kHz, the maximum that could be achieved using this probe. The room temperature spectrum, as shown in Figure 5-37,

shows a number of highly overlapped peaks, very similar to that observed by Fayon *et al.*.[22] This is also comparable to that recorded on the Infinity Plus 500 (Figure 5-36), with slightly lower resolution of the overlapped peaks, as is expected due to the lower magnetic field strength.

Figure 5-37 ^{31}P NMR spectra of SnP$_2$O$_7$ (rkgb29) at room temperature and 350 °C, 32 transients were recorded, with a pulse delay of 200 seconds MAS speed 2.3 kHz, ^{31}P Larmor frequency 121.414 MHz.

The 1D ^{31}P MAS spectrum at 350 °C was also recorded, and is shown in Figure 5-37. At this high temperature it proved impossible to set the spinning speed faster than 1.7 kHz. Unfortunately there is then some overlap between the centreband and sideband peaks in the 350 °C spectrum as can be seen in a close-up of the centreband region (Figure 5-38). Nevertheless, it is clear that there is little change in the spectrum between room temperature and 350 °C. The spectrum shows a single broad envelope, which has a FWHM of 6 ppm. The observed chemical shift range was -47 to -63 ppm very similar to that observed for the room temperature phase.

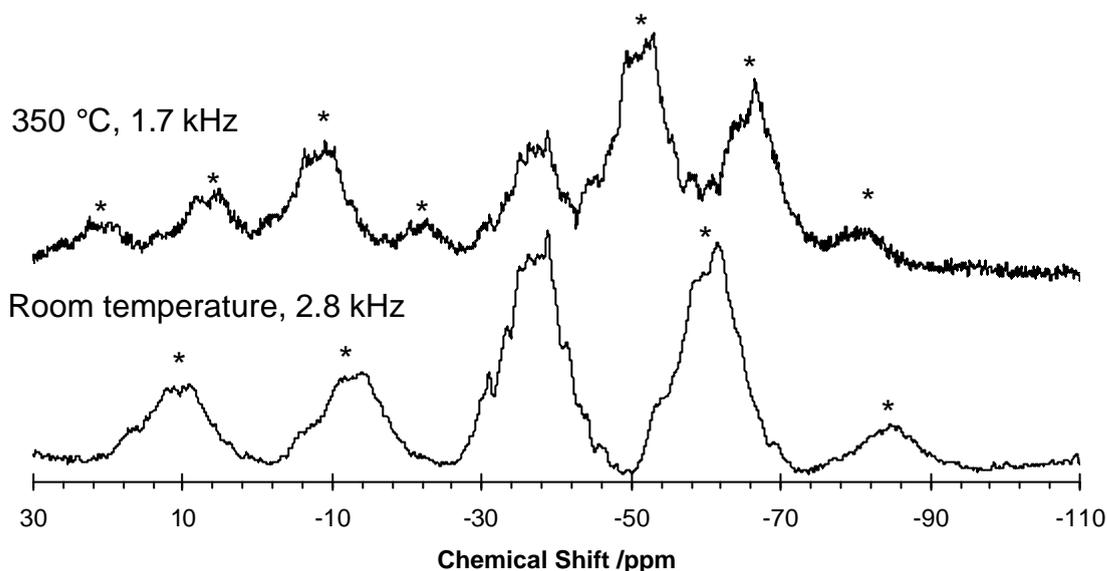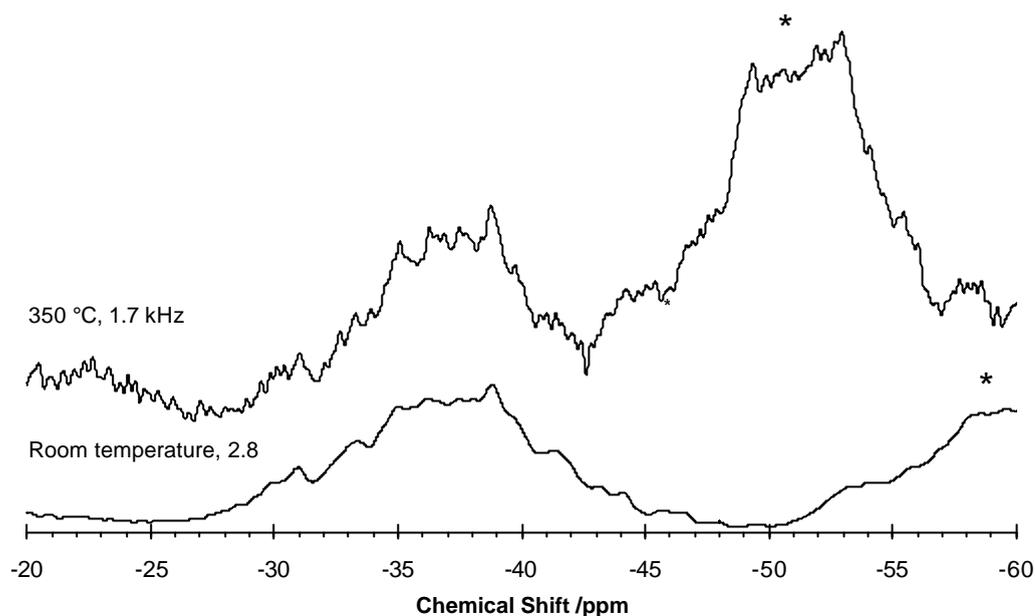**Figure 5-38** **^{31}P NMR spectra of SnP$_2$O$_7$ (rkgb29) at room temperature and 350 °C, 32 transients were recorded, with a pulse delay of 200 seconds MAS speed 2.3 kHz, ^{31}P Larmor frequency 121.414 MHz. This figure shows a close up of the centreband region.**

The 350 °C spectrum is above the ~290 °C phase transition and therefore represents the intermediate phase, the structure of which is not currently well understood. It is possible that the intermediate phase has an incommensurate structures as in ZrP$_2$O$_7$ and ZrV$_2$O$_7$.[24, 25] Alternatively, the intermediate phase may be commensurately ordered, with a change in symmetry at the phase transitions giving a superstructure with a different space group. The observed ^{31}P NMR spectrum is consistent with both possibilities. An incommensurate phase would show a continuum of chemical shifts, and a highly complex commensurate structure would show a large number of inequivalent phosphorus sites. Since there is a large degree of peak overlap, it is not possible to distinguish between these possibilities from the recorded spectra.

A 2D NMR experiment, such as INADEQUATE, could provide further information about the structure. If the structure is not incommensurate, it may be possible to resolve individual sites, and even determine the connectivity. An incommensurate structure would reveal a continuum of chemical shifts, and no peaks would be resolvable. However, with the available equipment, it was not practically possible to maintain the high temperature for a sufficiently long time to record a 2D spectrum of this kind. Unfortunately 350 °C is the maximum operating temperature of the temperature of the NMR probe used in this study, and it has not been possible to obtain spectra for the high temperature (>560 °C) phase.

5.6 MoP$_2$O$_7$

An attempt was made to record a ^{31}P NMR spectrum of MoP$_2$O$_7$ but unfortunately this was largely unsuccessful. The spectrum shown in Figure 5-39 was acquired - a signal with spinning sidebands can clearly be seen but no structure in the spectrum can be identified.
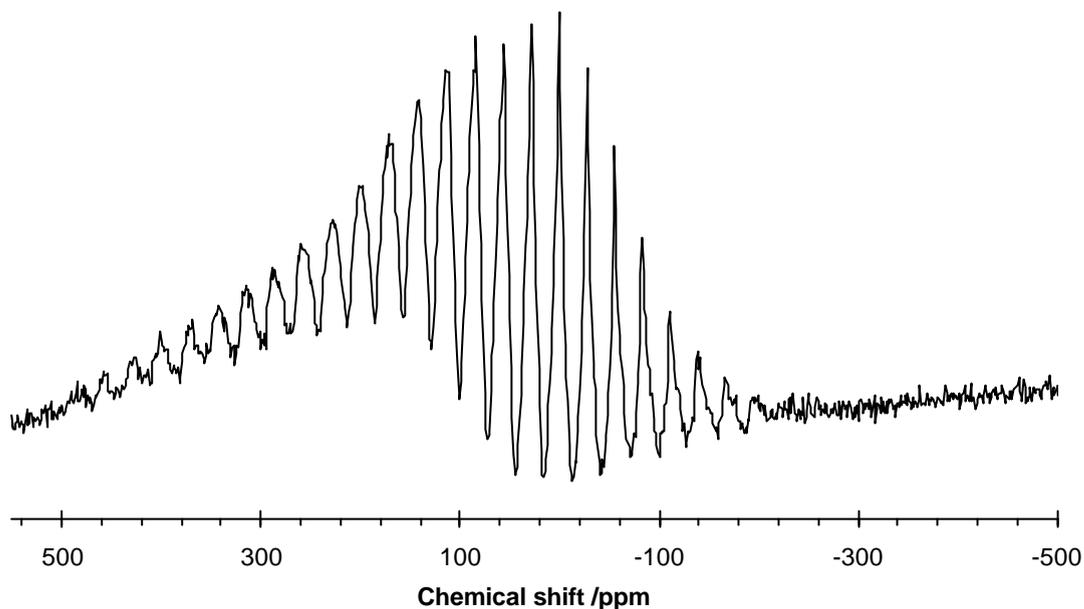
Figure 5-39 Room temperature ^{31}P MAS NMR spectrum of MoP$_2$O$_7$. 1,000,000 acquisitions with a pulse delay of 0.1s, pulse width 4 µs, [31]P Larmor frequency 212.17 kHz. MAS speed of 5.55 kHz

Mo(IV) is paramagnetic, which represents a severe problem for standard NMR techniques, since the spin-lattice relaxation times are extremely short. This causes relaxation of the nuclear spins on a timescale too rapid to be observed by NMR. [95]Mo NMR was also attempted with a sample of MoP$_2$O$_7$, but unfortunately no signal at all was detected, again presumably due to the paramagnetism of the compound.

5.7 Conclusions

The high temperature structures of HfP$_2$O$_7$ and ZrP$_2$O$_7$, which were previously thought to be iso-structural, were investigated. The ^{31}P NMR of the high temperature phases of ZrP$_2$O$_7$ and HfP$_2$O$_7$ cast some doubt on the space group of these phases, which had previously been assumed to be *Pa*3. The NMR results appear to indicate that high temperature HfP$_2$O$_7$ has only one unique phosphorus atom in the asymmetric unit. This result is in agreement with the previously accepted *Pa*3, high temperature structure of HfP$_2$O$_7$. However, the ^{31}P NMR spectrum of the high temperature phase of ZrP$_2$O$_7$ appears to show a number of overlapped peaks, suggesting a lower symmetry.

Rietveld refinement of neutron diffraction data was used to further investigate the symmetry of these materials. The signal to noise of existing neutron diffraction data for ZrP$_2$O$_7$ was insufficient to distinguish structural subtleties in the high temperature phase. However, in the case of HfP$_2$O$_7$ neutron diffraction data were sufficiently intense to enable a study of the effect of space group on the quality of Rietveld fit. Although lower symmetry space groups gave an improved fit to the neutron diffraction data, the improvement was not judged to be significant. It is therefore not possible to make a definitive conclusion about the symmetry of high temperature HfP$_2$O$_7$, and at this stage there is no evidence for symmetry lower than *Pa*3.

A number of further experiments can be proposed which would give further insight into the true structure of HfP$_2$O$_7$ and ZrP$_2$O$_7$. Higher quality neutron powder diffraction data for ZrP$_2$O$_7$ could potentially reveal a lower symmetry structure, using the same method as performed for HfP$_2$O$_7$ in this chapter. Single crystal diffraction studies would also be highly informative, since space group determination is likely to be more definite than from powder diffraction data. It had not previously been possible to obtain a single crystal of these compounds of sufficient size for diffraction experiments. However, since the completion of experimental work on this thesis, a single micro crystal Synchrotron X-ray diffraction study of the room temperature phase of ZrP$_2$O$_7$ has been published.[26] At the time of writing, variable temperature single crystal studies have not been performed, but these would be extremely useful in confirming the symmetry.

There are also a number of NMR experiments which would allow a more certain conclusion about the number of inequivalent phosphorus sites. High resolution one dimensional ^{31}P NMR spectra recorded on a higher magnetic field strength instrument could help resolve individual sites, if the observed spectra are indeed due to peak overlap. Two dimensional NMR experiments such as the ^{31}P INADEQUATE as used for room temperature ZrP$_2$O$_7$, would also be likely to show separated peaks, as well as showing the *J*-coupling pattern between sites, if multiple sites are present. Two dimensional experiments were not attempted as part of this work, since the high temperature NMR probe is not suitable for the extended experiment durations which would be required. Although ^{31}P NMR may offer a valuable insight into the symmetry, many of the necessary experiments are dependent on the development of appropriate equipment.

It is also possible that ^{17}O NMR of the high temperature phases of HfP$_2$O$_7$ and ZrP$_2$O$_7$ would be informative. The *Pa*3 structural model contains just two oxygen sites (a bridging oxygen which links the PO$_4$ tetrahedra in the P$_2$O$_7$ group, and the terminal oxygen atoms are shared between ZrO$_6$ octahedra and the PO$_4$ tetraheda). Observation of more than two oxygen sites would therefore prove that the structure had lower symmetry. It should be stated that there are a number of difficulties in performing such experiments, not least the production of a [17]O-enriched sample of ZrP$_2$O$_7$ of sufficient purity and enrichment level. A second potential problem is that in order to obtain a well resolved [17]O spectrum (such as those for ZrW$_2$O$_8$, as presented

in Chapter 3), the quadrupolar coupling must not be too large. It is thus not known whether ^{17}O NMR of the high temperature phase of ZrP$_2$O$_7$ would be successful.

The structure of room temperature HfP$_2$O$_7$ was determined by simultaneous Rietveld refinement of X-ray and neutron diffraction data. This showed very close correlation to that determined for the ZrP$_2$O$_7$ structure, by powder and single crystal diffraction.[26-28] The variation with cell parameter also determined from neutron diffraction data gave results which are in close agreement with those of Tait, who used XRD data only.[11] Further high resolution neutron diffraction data are required in order to determine the exact nature of the incommensurate phase.

^{51}V NMR of HfV$_2$O$_7$ and ZrV$_2$O$_7$ showed unusual effects which could not be fully explained. The observation of the ^{51}V NMR spectra at different field strengths demonstrates that a quadrupolar line shape is not responsible for the appearance of two peaks in the high temperature phase of these materials. However, it also shows that the two peaks are not due to two separate V sites in the asymmetric unit. Further investigation by ^{51}V NMR is required to determine whether the result is due to a true structural effect.

The ^{31}P spectra of samples of SnP$_2$O$_7$ prepared at various temperatures apparently confirm the observation from powder X-ray diffraction that the disorder in the structures is related to the synthesis temperature. The high temperature NMR experiments showed no noticeable change in the ^{31}P NMR spectrum of SnP$_2$O$_7$ between room temperature and intermediate phases.

A further investigation of the high temperature NMR of SnP$_2$O$_7$ would be of interest, particularly if it were possible to acquire a ^{31}P MAS NMR spectrum of the high temperature phase at >560 °C. This would require specialist equipment, and would not be straightforward experimentally. However, the high temperature phase of SnP$_2$O$_7$ is highly unusual, in that superstructure peaks are seen in the X-ray diffraction pattern even at high temperature and subcell peaks show a rhombohedral splitting pattern. ^{31}P NMR may provide information about the structure of this phase to compliment the observations from diffraction. 2D ^{31}P spectra (such as INADEQUATE) of the intermediate and high temperature phases may reveal the number of inequivalent P$_2$O$_7$ groups and connectivity of the phosphorus sites.

5.8 References

1   I. J. King, 'Combined Use of Powder Diffraction and Magic-Angle Spinning NMR to Structural Chemistry', Ph.D. Thesis, University of Durham, 2003.
2   I. J. King, F. Fayon, D. Massiot, R. K. Harris, and J. S. O. Evans, *Chem. Commun.*, 2001, 1766-1767.
3   I. Farnan, in 'Personal communication', 2003.
4   H. Bildsøe, in 'STARS: Spectrum Analysis For Rotating Solids', 1999.
5   'International Tables for Crystallography', International Union of Crytallography, 1983.
6   I. R. Evans, J. A. K. Howard, and J. S. O. Evans, *J. Mater. Chem.*, 2003, **13**, 2098-2103.

7   A. A. Coelho, *General Profile and Structure Analysis Software for Powder Diffraction Data*, 2000, **TOPAS v2.0**, Bruker AXS, Karlsruhe

8   A. Coelho, in 'Topas Academic', Karlsruhe, 2004.

9   G. Stinton and J. S. O. Evans, *unpublished results*, 2005.

10   S. E. Lister, I. R. Evans, J. A. K. Howard, A. Coelho, and J. S. O. Evans, *Chem. Commun.*, 2004, **22**, 2540-2541.

11   M. Tait, 'The Structure and Properties of AM$_2$O$_7$ Materials', Undergraduate Project, University Of Durham, 2003.

12   R. A. Young, in 'The Rietveld Method', ed. R. A. Young, Oxford, 1993.

13   V. Korthuis, N. Khosrovani, A. W. Sleight, N. Roberts, R. Dupree, and W. W. Warren, *Chem. Mater.*, 1995, **7**, 412-417.

14   N. Khosrovani, A. W. Sleight, and T. Vogt, *J. Solid State Chem.*, 1997, **132**, 355-360.

15   J. McManus, R. Kemp-Harper, and S. Wimperis, *Chem. Phys. Lett.*, 1999, **311**, 292-298.

16   W. Sungsool and L. Frydman, *J. Chem. Phys.*, 2000, **112**, 3248-3261.

17   C. Turquat, C. Muller, E. Nigrelli, C. Leroux, J. L. Soubeyroux, and G. Nihoul, *Eur. Phys. J.-Appl. Phys.*, 2000, **10**, 15-27.

18   J. S. O. Evans, J. C. Hanson, and A. W. Sleight, *Acta. Cryst.*, 1998, **B54**, 705-713.

19   R. E. Hann, P. R. Suitch, and J. L. Pentecost, *J. Am. Chem. Soc.*, 1985, **68**, 285-286.

20   R. Enjalbert and J. Galy, *Acta Crystallogr. C*, 1986, **39**, 1467-1469.

21   S. D. Gornostansky and G. V. Stager, *J. Chem. Phys.*, 1967, **46**, 4959-4962.

22   F. Fayon, I. J. King, R. K. Harris, R. K. B. Gover, J. S. O. Evans, and D. Massiot, *Chem. Mater.*, 2003, **15**, 2234-2239.

23   R. K. B. Gover, N. D. Withers, S. Allen, R. L. Withers, and J. S. O. Evans, *J. Solid State Chem.*, 2002, **166**, 42-48.

24   R. L. Withers, J. S. O. Evans, J. Hanson, and A. W. Sleight, *J. Solid State Chem.*, 1998, **137**, 161-167.

25   R. L. Withers, Y. Tabira, J. S. O. Evans, I. J. King, and A. W. Sleight, *J. Solid State Chem.*, 2001, **157**, 186-192.

26   H. Birkedal, A. M. Krogh Andersen, A. Arakcheevaa, G. Chapuis, P. Norbyd, and P. Pattisona, *Inorg. Chem.*, 2006, **45**, 4346-4351.

27   G. Stinton and J. S. O. Evans, 'PhD thesis (unpublished at time of writing)', University of Durham, 2006.

28   G. W. Stinton, M. R. Hampson, and J. S. O. Evans, *Inorg. Chem.*, 2006, **45**, 4352-4358.

Chapter 6 - Theoretical and computational studies of $A_2P_2O_7$ structures

6.1 Aims

The aims of the exploratory work described in this chapter were to carry out calculations of ^{31}P NMR parameters in a range of pyrophosphate-containing compounds. Ultimately it would be desirable to gain an insight into the relationship between structure (in particular the conformation of the pyrophosphate, $P_2O_7{}^{4-}$, group) and the NMR parameters, which are determined by the electronic distribution at the nucleus. The work described in this chapter is intended to examine the potential of such studies. This work is limited to $A_2P_2O_7$ materials, as described in the introduction, since these have considerably simpler structures than the AP_2O_7 materials described in Chapter 5.

The initial aim was to carry out a survey of the published structures of $A_2P_2O_7$ compounds, in order to find appropriate model compounds and particularly to observe the variation in P_2O_7 group conformation in real compounds, prior to theoretical studies. This work was carried out with the assistance of Sarah Kelly, a final year undergraduate project student.[1]

The theoretical studies involved calculations of NMR parameters using the density functional theory (DFT) program CASTEP.[2, 3] The NMR parameters of a number of known structures were calculated in order to test the calculation methodology and to assess the reliability of the technique in comparison to experimentally obtained spectra.

A series of structural models were then devised, using distance least squares refinement to produce theoretical structures. These structures were devised to give a range of P_2O_7 conformations, and were subject to chemical constraints to ensure they adopted reasonable geometries. The NMR parameters of these model structures were then calculated using CASTEP. The aim of this section of work was to establish a method by which correlations between structure and NMR parameters could be observed, without the limitation of having to use actual structures.

6.2 Introduction

Chemical shift calculations on complex structures such as the room temperature superstructures of the AP_2O_7 compounds discussed in Chapter 1 and Chapter 5 would be highly desirable. Such calculations are unfortunately impractically time consuming, since the calculation time is strongly dependent on the number of atoms in the unit cell. The unit cell of a structure such as TiP_2O_7 contains 1080 atoms. The $A_2P_2O_7$ compounds represent a much simpler class of inorganic materials with pyrophosphate (P_2O_7) groups; for example, the unit cell of ß-$Mg_2P_2O_7$ contains 22 atoms. It is therefore appropriate to use the $A_2P_2O_7$ class of compounds as a model for developing understanding of the relationship between structure and NMR parameters in pyrophosphate materials. In the long term it is hoped that this will lead to

methods which assist in the prediction and assignment of NMR spectra and structure solution of the more complex materials.

A review of the known structural types of $A_2P_2O_7$ materials is presented here. $A_2P_2O_7$ compounds are generally classified according to the conformation of the P_2O_7 groups as either thortveitite (with staggered P_2O_7 groups) or dichromate (eclipsed).[4] $A_2P_2O_7$ compounds containing A^{2+} ions with radii smaller than 0.97 Å tend to have P_2O_7 units in the staggered conformation (A = Mg, Mn, Fe, Co, Cu, Ni, Zn).[4]

A database of published crystal structures of $A_2P_2O_7$ materials was prepared. This section of work was carried out with Sarah Kelly, an undergraduate student, as part of her final year project. The method and a summary of results are presented in the Appendix; full details of the database are given in Sarah Kelly's project report.[1]

6.2.1 Thortveitite type structures

Thortveitite itself is a naturally occurring mineral with formula: $Sc_2Si_2O_7$, its structure was originally solved in 1930 by Zachariasen in space group *C2/m*, and confirmed by Cruickshank *et al.* in 1962. [5, 6] It consists of two-dimensional layers made up of edge sharing distorted ScO_6 octahedra, as seen in Figure 6-1, with the layers linked by Si_2O_7 units, made of corner-sharing SiO_4 tetrahedra, analogous to P_2O_7 units. The Sc and Si atoms are on 4h and 4i sites respectively. There are 3 crystallographically distinct oxygen sites, O1 (Wyckoff site *2a*), the central two-coordinate O in the linear Si-O-Si bridge, and O2 (*4i*) and O3 (*8j*), which are both 3-coordinate, shared between two ScO_6 octahedra and one SiO_4 tetrahedra. ScO_6 octahedra share edges to give a hexagonal structural motif of Sc atoms which is shown in Figure 6-1(b), whilst Figure 6-1 (a) shows the layers side on.
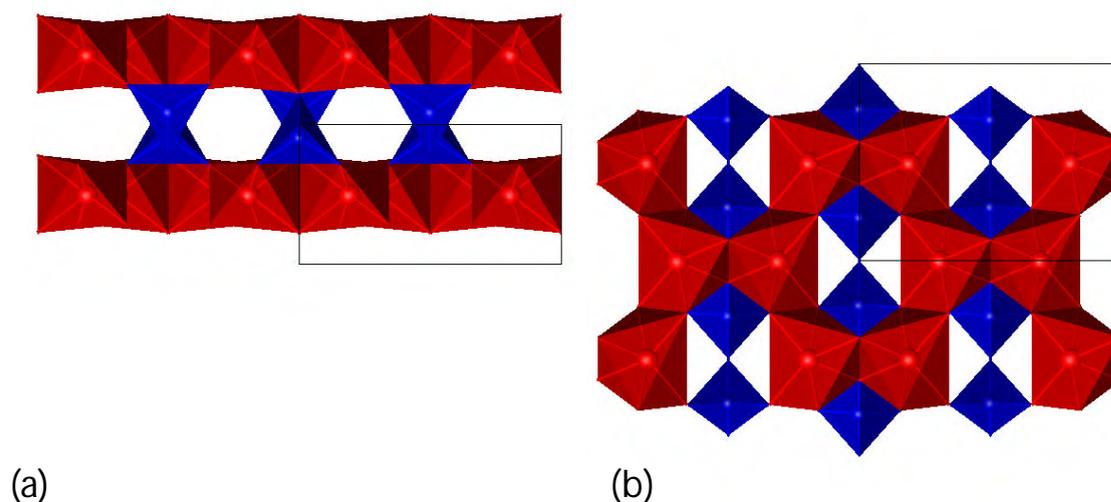
(a)   (b)

Figure 6-1 Structure of thortveitite, Sc₂Si₂O₇ (a) view down *a* axis , with *b* axis horizontal (b) view down *c* axis , with a axis vertical.

6.2.1.1 High temperature thortveitite A₂P₂O₇ phases

The high temperature forms of several $A_2P_2O_7$ materials are reported to be iso-structural with thortveitite. These include $\beta\text{-}Mg_2P_2O_7$[7, 8], $\beta\text{-}Mn_2P_2O_7$[9], $\beta\text{-}Cu_2P_2O_7$[10], $\beta\text{-}Ni_2P_2O_7$[11], $\beta\text{-}Co_2P_2O_7$[12] and $\beta\text{-}Zn_2P_2O_7$[13]. It should be noted that the structure of $\beta\text{-}Co_2P_2O_7$[12] was solved in space group *A2/m*, simply a non-standard setting of *C2/m*. At low temperature these materials tend to form less symmetric phases, as described below, and the formation of the ß phases involves a rearrangement of the metal atoms, most obviously evidenced by the formation of the regular hexagonal motif of edge sharing octahedra.

$Fe_2P_2O_7$ and $Mn_2P_2O_7$ have both only been observed in forms with the thortveitite structure. [9, 14, 15] The structure of $Fe_2P_2O_7$ was first determined in space group *P1* by Stefandis and Nord[14], but this was disputed by Hoggins *et al.*, who used statistical tests to argue for a centrosymmetric structure.[16] Hoggins *et al.*[15] solved the structure in the centrosymmetric triclinic space group *C1̄*, and suggested that this may also be the correct space group for $\beta\text{-}Mg_2P_2O_7$. Stefandis and Nord refined the structure[9] of $\beta\text{-}Mn_2P_2O_7$ in several space groups (*C2/m*, *C2* and *Cm*) and found that *C2/m* with a disordered bridging O atom gave the best fit to the data.

6.2.1.2 Low temperature thortveitite phases

A number of the $A_2P_2O_7$ thortveitite type compounds adopt less symmetrical structures at low temperatures (typically below 400 °C). The term 'thortveitite' is also often applied to these low temperature forms, which exhibit structural distortions from the ideal thortveitite structure, but still contain staggered $P_2O_7^{4-}$ groups. The transitions between high temperature and low

temperatures forms are usually subtle displacive phase transitions, resulting in a less symmetrical arrangement of metal atoms at low temperature.

The structure[17, 18] of *a*-$Co_2P_2O_7$ (shown in Figure 6-2) and the iso-structural[19] *a*-$Ni_2P_2O_7$ is similar to the *ß* phases, but with a disruption of the hexagonal pattern of metal atoms.[12] In the *ß* phases all metal atoms are six coordinate (octahedral) and all are bridged by oxygen atoms in a hexagonal motif. In the *a* phases, there is no bridging O atom between one pair of intra-layer metal atoms, and thus the material contains un-bridged five-coordinate (square pyramidal) metal atoms.
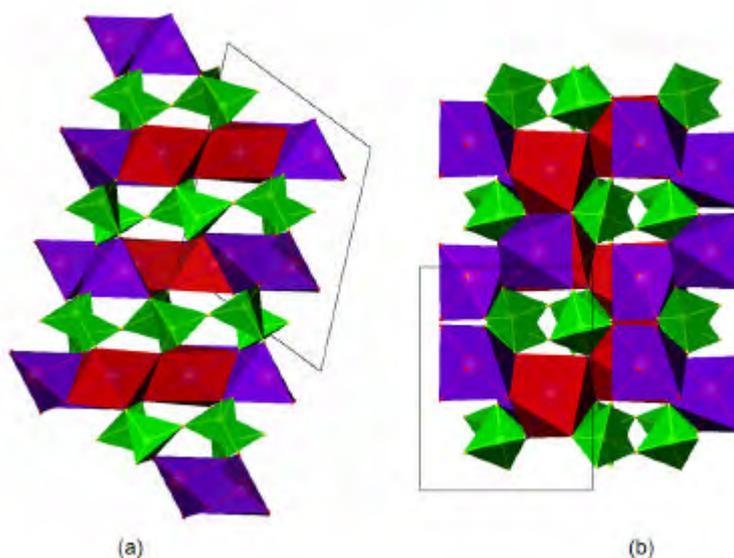
Figure 6-2 Structure[17, 18] of *a*-$Co_2P_2O_7$ viewed down (a) *b* axis, (b) *c* axis. CoO₅ square pyramids are shown in blue and CoO₆ octahedra in red.

There are also other structural forms of both $Co_2P_2O_7$ and $Ni_2P_2O_7$, known as *?* and *s* phases respectively.[20, 21] *?*-$Co_2P_2O_7$ was prepared by hydrothermal methods.[20] The structure (Figure 6-3) is very similar to *ß*-$Co_2P_2O_7$ but with a zigzag conformation of the layers. All the metal atoms are six coordinate, and the six-membered rings within the metal layers are intact as in the *ß* thortveitite phase. These structures show a different distortion of the regular hexagonal metal array – although they contain an unbroken hexagon of octahedral metal atoms, these are highly irregular, with two distinct metal-metal distances.[21]

(a)

(b)
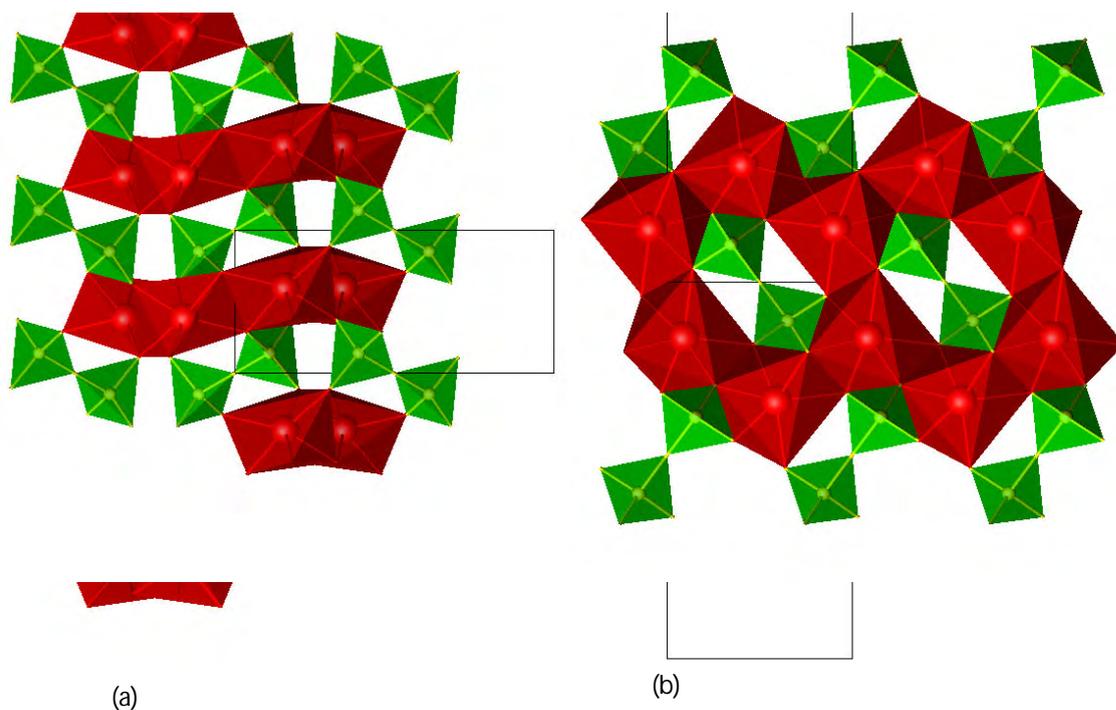
Figure 6-3 Structure of *?*-$Co_2P_2O_7$ [20] viewed down (a) *a* axis, (b) *c* axis.

The *a*-$Mg_2P_2O_7$ structure is similar to that of *a*-$Co_2P_2O_7$. The Mg ions are all in a mixture of 6 coordinate and 5 coordinate environments. The octahedra are paired together by a shared edge, and the pairs of octahedra are then linked by edge sharing to the distorted square pyramidal MgO_5 units. This leads to a structure with a break in the metal hexagonal array, as seen in Figure 6-4(a).

(a)

(b)
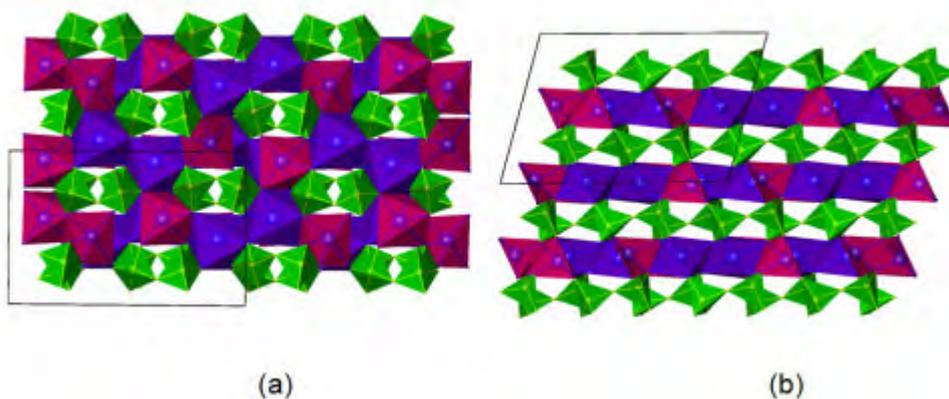
Figure 6-4 Structure[7] of *a*-$Mg_2P_2O_7$ viewed down (a) *c* axis, (b) *b* axis showing 5-coordinate (pink) and 6-coordinate (blue) Mg sites.

The structure[22, 23] of *a*-$Cu_2P_2O_7$ (*C2/c*) is slightly different. The hexagonal motif is broken in two places, and the single metal site is five-coordinate, with square pyramidal geometry, which is common for Cu(II). The structure is shown in Figure 6-5.

(a)

(b)

Figure 6-5 Structure of *a*-Cu$_2$P$_2$O$_7$ [22] viewed down (a) *a* axis, (b) *c* axis.

The *a* phase[24, 25] of Zn$_2$P$_2$O$_7$ is different to any other A$_2$P$_2$O$_7$ phase. This structure, which contains both five- and six-coordinate metal atoms, is a similar layered structure to other a phases but with a slightly different arrangement of metal atoms. It may be considered as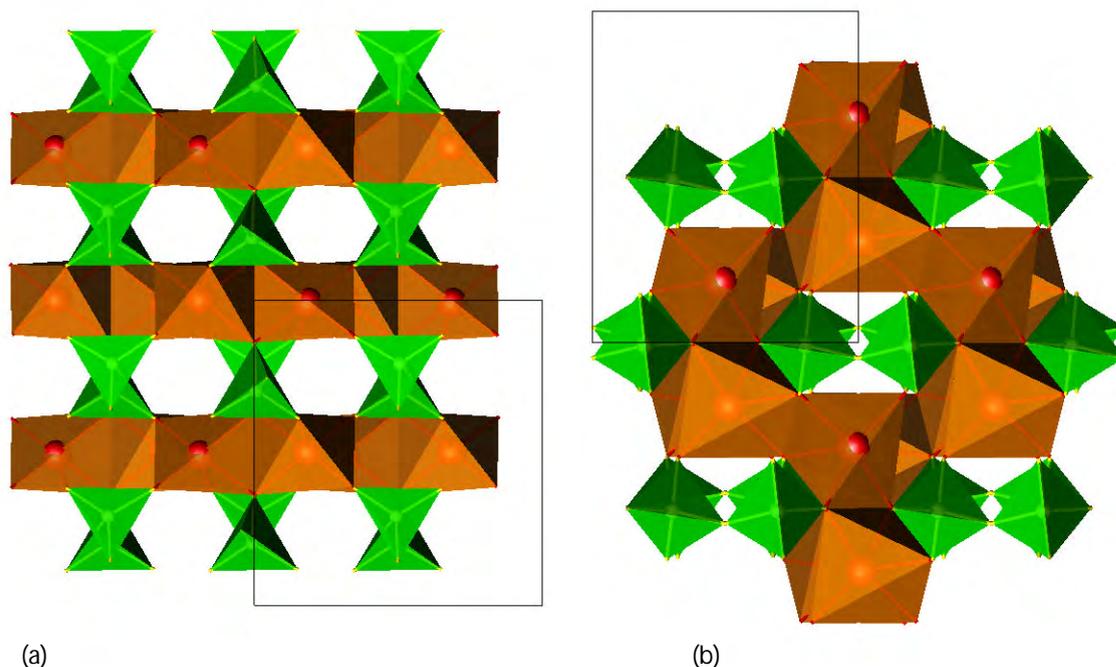 consisting of 2 layers like those found in *a*-Mg$_2$P$_2$O$_7$ (with the hexagonal motif broken in one place) followed by one layer like those in *a*-Cu$_2$P$_2$O$_7$ (with the hexagonal motif broken in two places).[25]

In addition to the usual *a* and *ß* thortveitite phases, three more Zn$_2$P$_2$O$_7$ polymorphs have been observed in the decomposition of zinc phenylphosphonate hydrate[26] . One of these is amorphous, another, labelled *d*-Zn$_2$P$_2$O$_7$, is poorly crystalline, and the third has been labelled as ?-Zn$_2$P$_2$O$_7$. Bataile *et al.* were able to solve the structure of ?-Zn$_2$P$_2$O$_7$ from powder X-Ray diffraction.[26] *?*-Zn$_2$P$_2$O$_7$ is a metastable phase, which converts to the *ß* phase at high temperatures. The structure, shown in Figure 6-6, consists of corrugated chains of edge-sharing ZnO$_5$ trigonal bipyramids along the [*001*] direction, which are linked by P$_2$O$_7$ groups in the other directions. The relationship to the *ß* (thortveitite phase) can most clearly be seen in Figure 6-6 (a), where the arrangement of the metal atoms in the chains closely resembles the 'broken hexagonal' motif of the metal layers in a-thortveitite phases such as *a*-Cu$_2$P$_2$O$_7$ [23] The chains are twisted considerably, and do not link up to form a complete two dimensional layer, but instead form zigzag chains, as seen in Figure 6-6(c). Unusually, the P$_2$O$_7$ groups are in the eclipsed formation, despite the fact that the *a* and *ß* phases have staggered P$_2$O$_7$ groups.

(a)

(b)

(c)
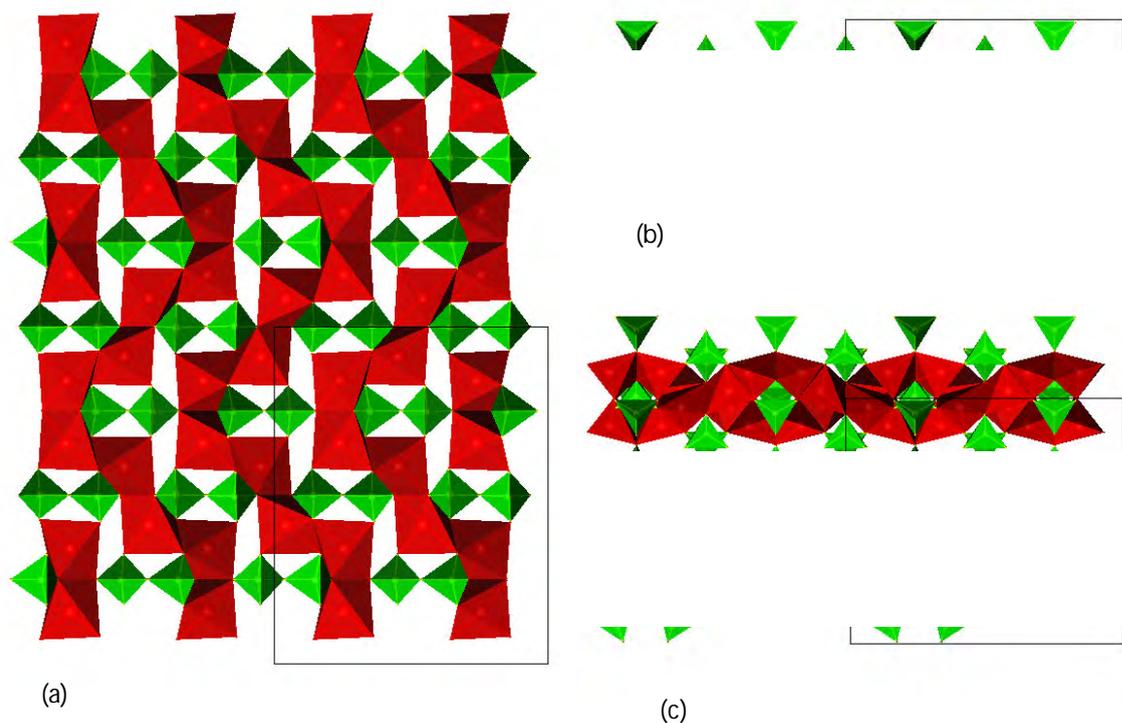
Figure 6-6 Structure[26] of $?$-$Zn_2P_2O_7$ views down (a) *a* axis, (b) *b* axis and (c) *c* axis.

The densities of the $Zn_2P_2O_7$ phases[13, 25, 26], calculated from the crystal structures, are as follows: *a* - 4.212 g·cm^{-3}, *ß* - 4.275 g·cm^{-3} *?* - 3.720 g·cm^{-3}. It is clear that the *a* and *ß* phases have very similar densities, whilst the gamma phase, with eclipsed P_2O_7 units, is considerably less dense. The reported density for the amorphous *d* phase is 3.688 g·cm^{-3} [26], suggesting that this form also has eclipsed P_2O_7 units.

6.2.1.3 Summary of thortveitite structures

The geometry and symmetry of the thortveitite type A$_2$P$_2$O$_7$ structures is summarised in Table 6-1.

Metal	Ionic Radius /pm	Structure type and space group	Metal coordination number
Mg	86.0	*a* phase type 2 – hexagon broken in two places *B2$_1$/c* [7]	6
		ß phase *C2/m* [7, 8]	6
Mn	97.0	*ß* phase, *C2/m* [9]	6
Fe	92.0	*ß* phase *C1̄* [15]	6
Co	88.5	*a* phase type 1 - Broken hexagon *B2$_1$/c* [17, 18]	5,6
		ß phase *A2/m* [12]	6
		? phase P2$_1$/a. [20]	6
Ni	83.0	*a* phase type 1 - Broken hexagon *P2$_1$/c* [19]	5,6
		s phase *P2$_1$/a* [21]	6
		ß phase, *C2/m* [11]	6
Cu	87	*a* phase type 2 – hexagon broken in two places *C2/c* [23]	5
		ß phase *C2/m* [10]	6
Zn	88.0	*a* phase type 3 *A12/a* [24]	5,6
		ß phase *C2/m* [13]	6

Table 6-1 Summary of known structures of thortveitite-type A$_2$P$_2$O$_7$ compounds.

6.2.2 Dichromate structures - eclipsed phosphate groups

A$_2$P$_2$O$_7$ compounds containing A^{2+} ions with radii greater than 0.97 Å tend to have P$_2$O$_7$ units in the staggered conformation (A = Ca, Sr, Ba, Pb).[4] These structures are generally known as "dichromate" structures, since the conformation of the P$_2$O$_7$ group is similar to that of the Cr$_2$O$_7$ group in Na$_2$Cr$_2$O$_7$.[27] The range of structure types observed is more diverse, reflecting the greater diversity of A site cations. It should be noted that the nomenclature of dichromate phases is entirely different from that of the thortveitite phases previously mentioned. Several of these so-called "dichromate-type" A$_2$P$_2$O$_7$ structures have phase transition temperatures of above 973 K.[28]
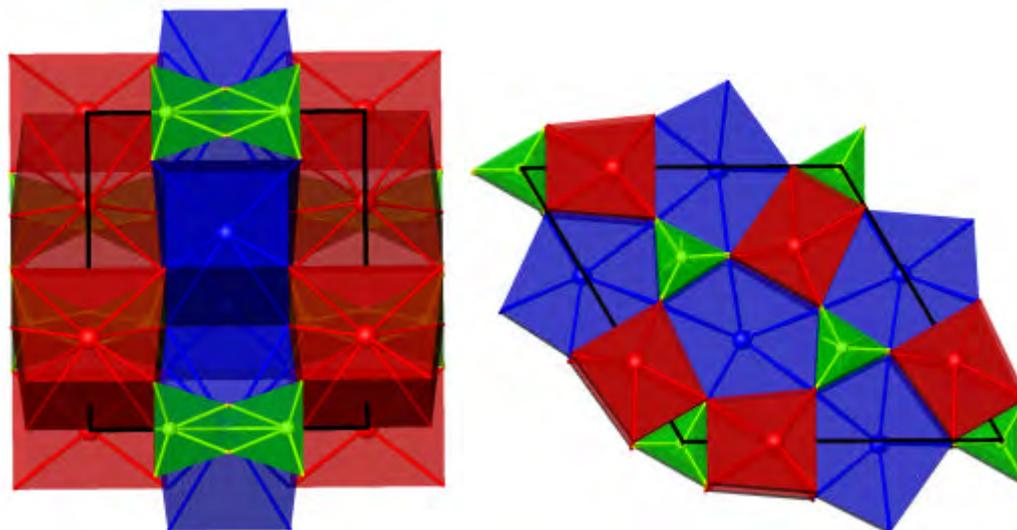
Figure 6-7 Structure of $Ba_2P_2O_7$: (a) view down *a* axis (b) view down *c* axis. BaO_8 polyhedra are shown in red, with BaO_{10} polyhedra in blue.

The structure of *s*-$Ba_2P_2O_7$ (shown in Figure 6-7) is found to be different to any other known form of alkaline earth diphosphate.[28] It belongs to the *P$\bar{6}$2m* space group, and is a highly interlinked three dimensional network. The Ba atoms are in 10 coordinate and 8 coordinate configurations, and the BaO_8 and BaO_{10} polyhedra are linked by shared edges, with vertices shared by the PO_4 tetrahedra. The staggered P_2O_7 groups are clearly shown by the view down the *c* axis. The bridging P-O-P oxygen atoms are disordered about the 3-fold axis.

The iso-structural forms of $Hg_2P_2O_7$ and $Cd_2P_2O_7$ both have space group *P$\bar{1}$*. This structure contains a 3D network of corner sharing CdO_6, CdO_5, and P_2O_7 units.

6.3 Preparation of samples

Two compounds, $Ba_2P_2O_7$ and $Cd_2P_2O_7$ were synthesised by solid state methods, and their ^{31}P MAS NMR spectra recorded. The aim was to obtain experimental data which could subsequently be compared to calculated NMR parameters.

6.3.1 $Ba_2P_2O_7$ Synthesis

A sample of $Ba_2P_2O_7$ was prepared by solid-state reaction of $BaCO_3$ and $(NH_4)_2HPO_4$, using a 10 % molar excess of $(NH_4)_2HPO_4$. The two solids were ground and mixed in an agate pestle and mortar, and then transferred to an alumina crucible, which was then placed in a furnace at 1120 °C for 90 minutes. The crucible was removed and quenched to room temperature. X-ray diffraction of this sample (SHK01) showed the presence of $BaCO_3$. A second attempt at producing pure $Ba_2P_2O_7$ was carried out, using an identical method to that described above, but with a 25 % molar excess of $(NH_4)_2HPO_4$. The product of this second synthesis (SHK06) was shown to be pure $Ba_2P_2O_7$ by powder X-ray diffraction.

6.3.2 $Cd_2P_2O_7$ Synthesis

A sample of $Cd_2P_2O_7$ was prepared by heating a mixture of cadmium carbonate, $CdCO_3$, and diammonium hydrogen phosphate, $(NH_4)_2HPO_4$, in stoichiometric quantities. The mixture was intimately mixed and ground in an agate pestle and mortar, and pressed into a pellet. The pellet was heated in a platinum crucible to 1120 °C at a rate of 10 K·min^{-1} and held at this temperature for 90 minutes. The sample was then quenched to room temperature and ground to a white powder (SHK08). Powder X-ray diffraction confirmed that the product was pure $Cd_2P_2O_7$.

6.4 NMR experiments

^{31}P MAS NMR spectra were recorded for *a*-$Zn_2P_2O_7$, $Ba_2P_2O_7$ and $Cd_2P_2O_7$. The intention was to observe the range of ^{31}P NMR chemical shifts, and to enable future comparison of calculated chemical shifts with the experimental values. The synthesis of $Ba_2P_2O_7$ and $Cd_2P_2O_7$ is as described above, while the sample of $Zn_2P_2O_7$ was prepared by Ian King[29]. Since the relative chemical shifts are of interest, it was particularly important to ensure that all spectra were recorded with consistent referencing. All ^{31}P NMR spectra were recorded using the same spectrometer, the Varian Infinity Plus 500, and referenced to the single peak of brushite ($CaHPO_4·2H_2O$) at 1.2 ppm.

The ^{31}P NMR spectrum of $Ba_2P_2O_7$ (shown in Figure 6-8) shows two intense peaks at -8.1 and -11.1 ppm and a small less intense peak, presumably due to an impurity, at -9.7 ppm. This result is in agreement with the crystal structure which has two inequivalent phosphorus sites.
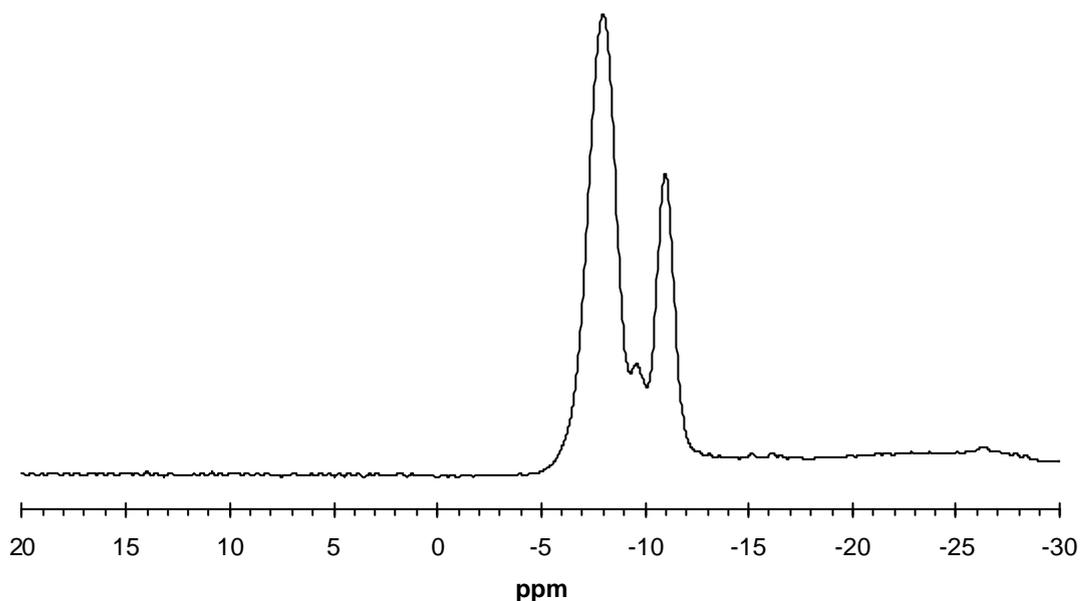
Figure 6-8 ^{31}P MAS NMR spectrum of Ba$_2$P$_2$O$_7$.

The ^{31}P NMR spectrum for Cd$_2$P$_2$O$_7$ (Figure 6-9) shows two clearly resolved peaks of approximately equal intensity at -4.8 and -2.9 ppm. The observation of two peaks is consistent with the known crystal structure.
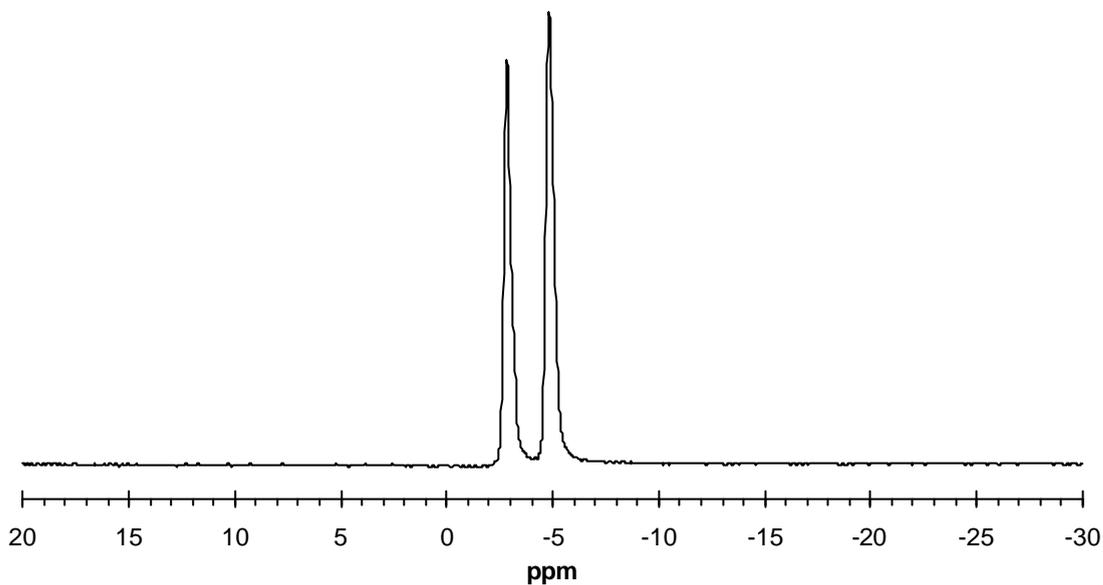
Figure 6-9 ^{31}P MAS NMR spectrum of Cd$_2$P$_2$O$_7$.

The NMR spectrum of *a*-Zn$_2$P$_2$O$_7$ (Figure 6-10) shows three intense, well resolved separate peaks, corresponding to the three crystallographically inequivalent sites.[25] A much less intense peak observed at around -27 ppm is presumably due to a minor impurity.
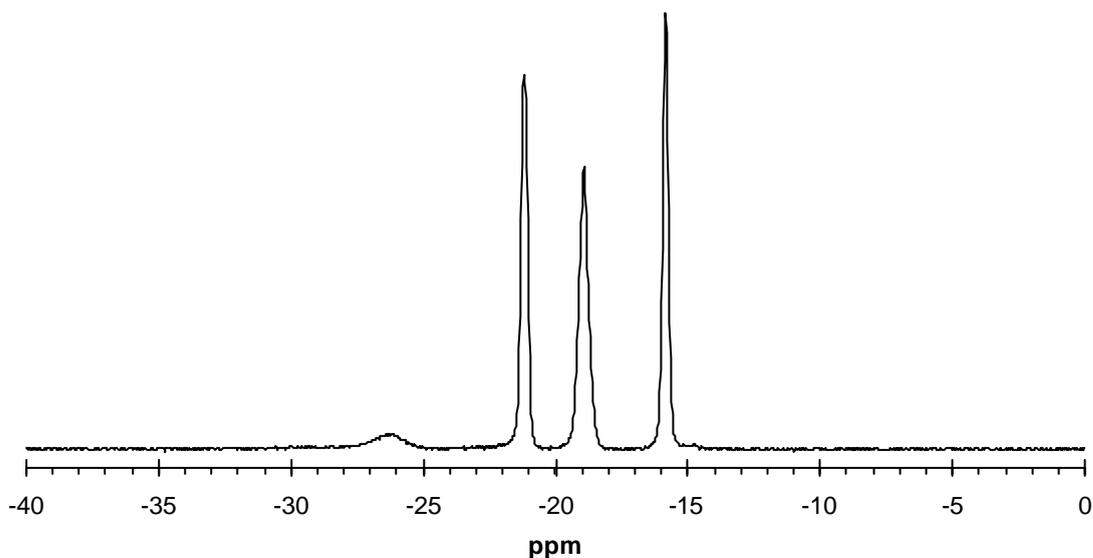
Figure 6-10 ^{31}P MAS NMR spectrum of *a*-Zn$_2$P$_2$O$_7$.

6.5 CASTEP Calculations

A series of calculations of NMR parameters were performed, using published crystal structures. These calculations were carried out using the CASTEP program,[2, 3] which calculates the electron density distribution (and hence electronic energy) of an arrangement of atoms. This technique is particularly well suited to extended solids due to its use of a plane wave basis set for the valence electrons rather than the localised atomic-like orbitals used for quantum chemical calculations on isolated molecules. Hence the three dimensional translational repetition of the crystallographic unit cell of the material may be used as the basis for the structure, without the construction of artificial "clusters" to approximate an extended structure.

The periodic translational symmetry of the structure is defined by a unit cell of atomic coordinates as an input to the program. CASTEP was used to calculate NMR parameters for *a*-Mg$_2$P$_2$O$_7$, *ß*-Mg$_2$P$_2$O$_7$ and Zn$_2$P$_2$O$_7$. These structures were selected to exclude any compounds in which disorder was reported by XRD, since this cannot be modelled in the periodic structural model used by CASTEP.

A series of test calculations were first carried out in order to assess the effect of changing parameters in the calculations on the results obtained. The CASTEP program was used with default settings for most parameters. Two parameters which were adjusted were the cut off energy, and the *k*-point spacing. The cut off energy defines at what point a calculation is judged to have converged, a low cut off energy giving a more accurate calculation, at the expense of more computational time. The *k*-point spacing determines the number of points in the reciprocal space used by the plane wave basis, with a small value corresponding to a greater number of sampled points, and hence a more accurate calculation. It was found, by carrying out trial calculations, that using a cut-off energy of 400 eV and a *k*-point spacing of 0.05 Å^{-1} allowed calculations to be carried out within 11 hours using 12 parallel processor nodes, with results consistent with more accurate, but much slower, calculations.

CASTEP reports a number of NMR parameters for each NMR-active nucleus, including quadrupolar coupling, shielding and shielding anisotropy. This study was limited to an analysis of the ^{31}P chemical shifts, although the calculations yielded results for all nuclei in the structure. The shielding values are the absolute shielding relative to an unshielded nucleus, a parameter which is impossible to obtain directly from experiment. However, these unreferenced values may still be used to assess the accuracy of the calculations, since chemical shift *differences* between different A$_2$P$_2$O$_7$ compounds, will be directly comparable with experimental results. In an attempt to provide referenced values, the NMR parameters for brushite, (CaHPO$_4$·2H$_2$O, a standard often used for referencing experimental ^{31}P spectra) were also calculated, and a ^{31}P isotropic shielding of 276.78 ppm was obtained. The true chemical shift of brushite is well known to be 1.2 ppm, and thus the calculated spectra could be referenced relative to this point.
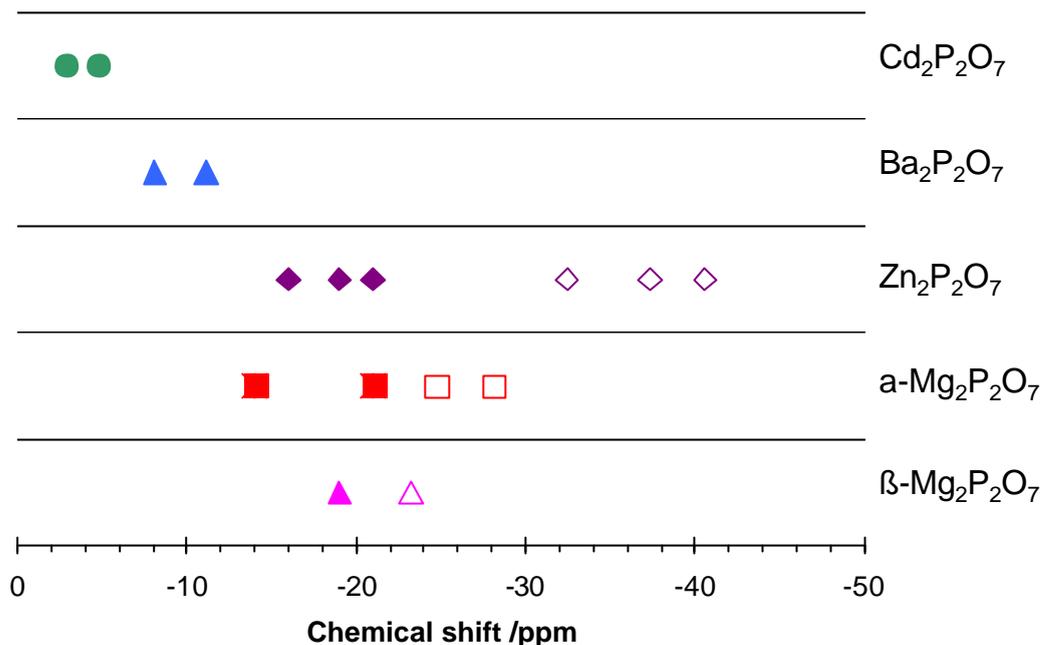
Figure 6-11 A comparison of calculated) and experimentally observed chemical shifts in $A_2P_2O_7$ compounds. Calculated shifts are shown by open shapes, and experimental values by filled shapes. All chemical shifts are referenced to brushite.

A comparison of the CASTEP derived shifts and experimental values (as shown in Figure 6-11) illustrates that there are significant discrepancies. This would seem to rule out any attempt at using the calculations of absolute chemical shift to predict spectra. The difference between experimental and calculated shifts is not consistent between different compounds. However, there is much better agreement between calculations and experiment if one looks at the chemical shift differences between sites in a given compound. This is a promising result, since this could allow assignment of spectra. Having established this result, these studies were not pursued further due to time limitations and the desire to develop a methodology for the study of theoretical structures.

6.6 Theoretical studies of $A_2P_2O_7$ compounds

In order to use the density functional theory (DFT) calculations described above to help understand the relationship between NMR parameters and structure, it is helpful to use theoretical structures. A series of model structures may be devised, with structural features fixed in each case, and the NMR parameters calculated. This approach allows structural parameters, such as bond angles, to be varied individually, and thus allows direct correlations between the varied parameters and the calculated NMR results. A study of this sort is not possible using only known structures, where there are limited numbers of phases, with multiple, often complex, differences between them.

A hypothetical structural model was therefore required, and it was decided to use a structure based on that of MgP_2O_7, since this structure is representative of the larger thortveitite group of $A_2P_2O_7$ structures. Having determined the starting point for the structure, it could then be adapted by small incremental steps to give a range of theoretical models.

The distance least squares (DLS) method is a least squares minimisation technique which is data-independent, and allows a structural model to be fitted to a series of chemical restraints. The first stage was to define the *ß*-$Mg_2P_2O_7$ structure, as determined by Lukaszewicz[30] in terms of rigid bodies, which could subsequently be manipulated. A theoretical structure was described using two crystallographically inequivalent magnesium atoms (with positions defined conventionally by coordinates relative to the three crystal axes) and a P_2O_7 unit defined as consisting of two rigid tetrahedra with regular (109.47 °) bond angles. The P_2O_7 unit was defined by a total of 10 parameters:

- 2 bond lengths (P-$O_{bridging}$ bonds to oxygens which bridge the two P atoms of the P_2O_7 unit, and P-$O_{terminal}$ bonds to oxygens which are bonded to Mg);

- 1 bond angle (P-O-P angle at the centre of the P_2O_7 group)

- 1 torsion angle (the torsion angle between oxygens on the two P atoms, as viewed down the P-$O_{bridging}$-P axis)

- 3 coordinates defining the position of the central $O_{bridging}$ atom of the P_2O_7 structure in the unit cell

- 3 angles defining the orientation of the whole P_2O_7 group in relation to the crystal axes.

This approach means that the complete P_2O_7 group may be defined with considerably fewer parameters than would be required to describe the individual atomic positions (for example defining the position of each of the 9 atoms conventionally would require 27 coordinates), and is particularly useful for adapting simplified structural models.

The structural model above was first refined against the known crystal structure for *ß*-$Mg_2P_2O_7$ by minimising the distances between equivalent atomic sites in the two models. The structure used[30] was originally published in the non-standard space group setting *B2₁/c* but was converted to the standard *P2₁/c* space group, giving a transformed unit cell with dimensions: a = 6.946 Å, b = 8.29 Å, c = 9.053 Å, *ß* = 113.79 °. The unit cell parameters were fixed at these values. A data-independent DLS penalties-only refinement was used to fit the 10 parameters for the P_2O_7 group structure, as listed above, and the coordinates of the Mg atoms (which were allowed to refine freely).

The structural model derived by this method was used to derive the subsequent theoretical structures. These were formed by fixing internal parameters of the P_2O_7 unit and then carrying out a refinement in which all other structural parameters were refined. In order to ensure the models formed were chemically plausible, bond valence sum and bond distance restraints were used.

The bond valence sum[31, 32] of a structure may be used to give an estimate of its stability, by a consideration of the electrostatic interactions between atoms. The bond valence for each atom V_i is defined as in Equation 6-1.

$$V_i = \sum_j v_{ij}$$
[6-1]

where v_{ij} is the bond valence between atom i and a bonded atom j. These bond valences are calculated from the bond distances, d_{ij}, and bond valence parameters, R_{ij}, for a given atom-atom pair, as in Equation 6-2.

$$v_{ij} = \exp\left(\frac{R_{ij} - d_{ij}}{b}\right)$$
[6-2]

where b is a universal constant with value 0.37 Å. The structures were refined to minimise the value of a penalty function, P, as in Equation 6-3.

$$P = \sum \left(V_i - V_{\exp}\right)^2$$
[6-3]

where V_i is the bond valence for each atom i, and $V_{\exp}$ is the expected bond valence for each atom. This penalty function is related to the global instability index, g, which is defined as in Equation 6-4.

$$g = \sqrt{\frac{P}{N}}$$
[6-4]

where N is the number of atoms in the asymmetric unit. The value of g may be taken as a measure of the stability of the model structures.

In order to ensure chemically reasonable geometry around the magnesium and oxygen sites, some additional restraints on the bond valences were used. The P-O$_{terminal}$ and P-O$_{bridging}$ bond lengths were fixed at 1.5000 Å and 1.5944 Å respectively. The bond valence contribution from the P-O$_{terminal}$ bonds (with fixed length 1.5000 Å) is 1.3246, and the Mg-O bond must therefore contribute 0.6754 in order to give each of the 'terminal' oxygens a total bond valence of 2. Restraints were therefore implemented such that a penalty function was applied if there was any deviation from this value of the Mg-O bond valence. A further restraint was applied to

ensure the Mg-O bond lengths remained chemically reasonable: a penalty function was applied if the bond length deviated from the range 1.85-2.25 Å.

A series of structural models (listed in Table 6-2) was formed by this method. The O-P-O-P-O torsion angle of the P_2O_7 group was fixed at 60° (*i.e.* perfectly staggered) and the P-O$_{bridging}$-P bond angle varied for these initial experiments. The bond valence sums for each atom were calculated, and are also listed in Table 6-2.

Model ref.	P-O-P bond angle /°	Bond valences								
		Mg1	Mg2	O1	O2	O3	O4	O5	O6	O7
mg2p2o7_03_050_060	130	1.993	1.955	2.052	1.973	1.997	1.993	1.978	1.993	1.961
mg2p2o7_03_045_060	135	1.991	1.960	2.052	1.967	2.002	1.999	1.974	1.985	1.972
mg2p2o7_03_040_060	140	2.007	1.947	2.052	1.965	1.995	1.983	1.988	2.004	1.967
mg2p2o7_03_037_060	143	1.991	1.953	2.052	1.977	1.996	1.987	1.977	1.987	1.969
mg2p2o7_03_032_060	148	1.995	1.962	2.052	1.965	2.006	1.992	1.994	1.984	1.964
mg2p2o7_03_030_060	150	1.991	1.956	2.052	1.965	2.003	1.987	1.989	1.998	1.951

Table 6-2 Bond valences of the model structures for Mg₂P₂O₇. Torsion angles were fixed at 60 ° for all models.

The global instability index (g) values (listed in Table 6-3) for the model structures are all in the range 0.0256-0.0255; these are reasonably consistent, indicating that the model structures are plausible.

Model ref.	P-O-P bond angle /°	Global instability index, g	*Profile residual index, R_{WP}*
mg2p2o7_03_050_060	130	0.0264	0.0060
mg2p2o7_03_045_060	135	0.0256	0.0050
mg2p2o7_03_040_060	140	0.0276	0.0060
mg2p2o7_03_037_060	143	0.0260	0.0050
mg2p2o7_03_032_060	148	0.0255	0.0050
mg2p2o7_03_030_060	150	0.0281	0.0020

Table 6-3 Global instability indices for the model structures for Mg₂P₂O₇. Torsion angles were fixed at 60 ° for all models.

The NMR parameter calculations for each of the structural models were performed using the same methodology as described in Section 6.5. The results were then compared to experimental spectra of *a*- and *ß*-Mg₂P₂O₇. Mg₂P₂O₇ tends to be produced as a mixture of phases, and the experimental spectrum[29] of a mixture of *a*-Mg₂P₂O₇ and *ß*-Mg₂P₂O₇ shows three peaks, as would be expected from the crystal structures of the two phases (see Figure 6-12).
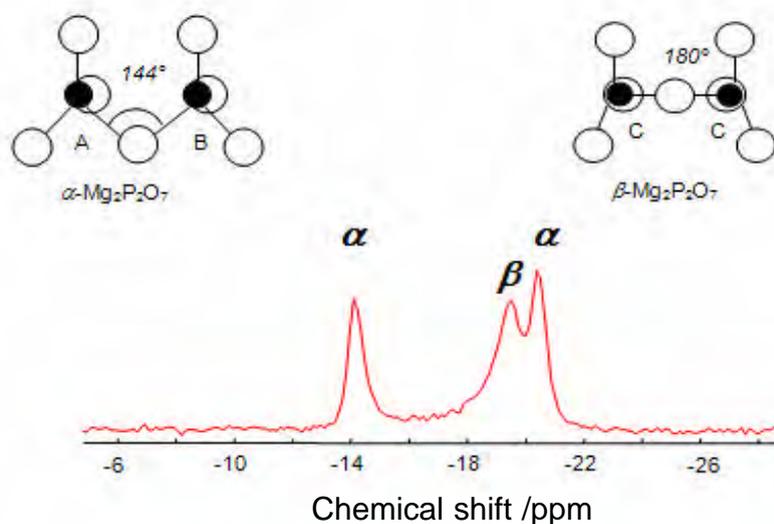
Figure 6-12 Experimental ³¹P MAS NMR spectrum of a mixture of the *a* and *ß* phases of Mg₂P₂O₇ recorded by King.[29] MAS spinning speed 10 kHz. King confirmed the assignment of the spectrum using 2D POST –C7 NMR experiments.

The observed chemical shifts for *a*- and *ß*- Mg₂P₂O₇ were first compared to those calculated using the known crystal structures (those shown in Figure 6-11). The calculated chemical shifts were initially referenced by comparison with the calculated shielding for brushite, as previously described. The results are listed in Table 6-4. It was found that there is a significant discrepancy between the calculated and observed chemical shifts, suggesting an error in the referencing.

Referencing	Observed chemical shift /ppm	Calculated absolute shielding/ppm	Calculated chemical shift /ppm	Calculated chemical shift /ppm.
	Brushite at 1.2 ppm	Theoretical unshielded nucleus	Brushite at 1.2 ppm	Referencing adjusted
a-Mg₂P₂O₇ peak 1	-14	301.5	-24.7	-17.4
a-Mg₂P₂O₇ peak 2	-21	304.9	-28.1	-20.7
ß-Mg₂P₂O₇	-19	300.0	-23.2	-15.9

Table 6-4 Comparison of calculated and experimental chemical shifts for a- and ß-Mg₂P₂O₇. Adjusted chemical shifts for all peaks were shifted by a constant to minimise difference between experimental and calculated peaks.

Although the source of this error is not known, it appears to be systematic; the comparisons between individual peak positions in the Mg₂P₂O₇ phases remain valid regardless of the referencing. Thus, for the sake of comparisons, the referencing of the calculated chemical shift was adjusted to give the best match to experimental data. The calculated chemical shifts were altered by addition of a constant in order to provide the smallest difference between calculated and observed peaks.

The calculated chemical shifts for the theoretically derived structural models were then compared to the results for the known structures. The positions of the peaks are shown in Figure 6-13.
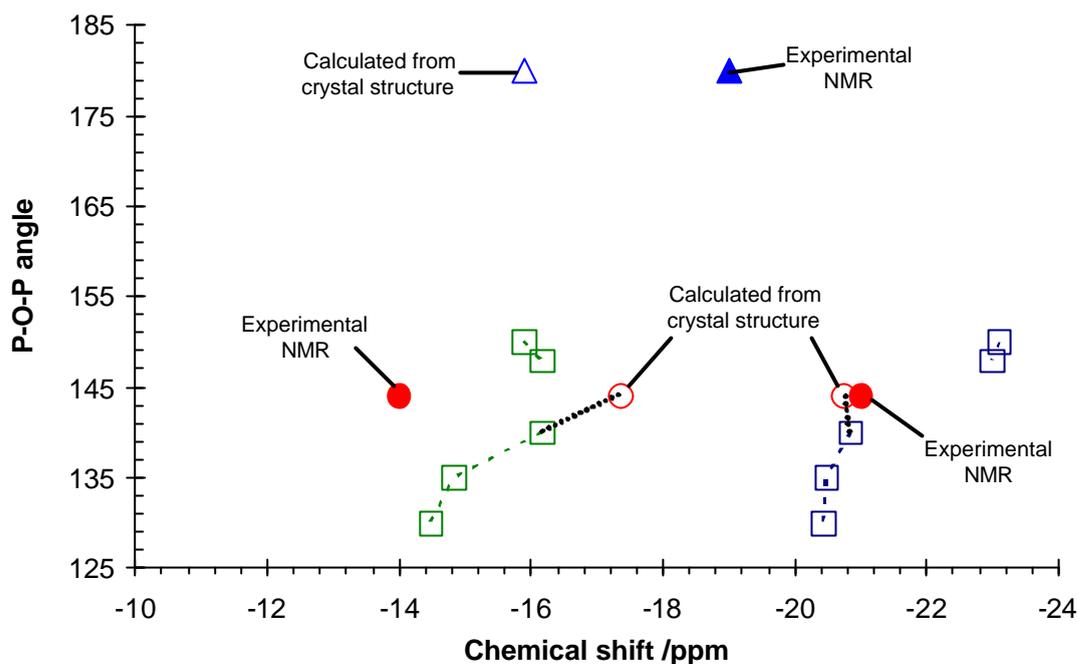
Figure 6-13 Calculated ³¹P NMR chemical shifts with P-O-P angle for a structural model based on *a*-Mg₂P₂O₇. The peak positions of the two sites for the theoretical structure are shown by the dark blue and green open squares. For comparison, peak positions for the actual *a*- (red circles) and *ß*- (blue triangle) Mg₂P₂O₇ structures are also shown (filled shapes correspond to experimentally observed ³¹P NMR peaks and open shapes to calculated shifts based on the structures determined by diffraction). Experimental chemical shifts, are referenced to brushite at 1.2 ppm; calculated chemical shifts are shifted by a constant to minimise the difference between experimental and calculated shifts for *a*- and *ß*-Mg₂P₂O₇. Lines are added as guides to the eye showing apparent smooth variation.

An alternative way to compare the data is to examine the difference in chemical shift between the two sites, as shown in Figure 6-14. The chemical shift difference for the theoretical structural models is comparable to that obtained for the *a*-Mg₂P₂O₇.

Figure 6-14 The variation of the difference between calculated chemical shifts of the two **^{31}P sites in theoretical structures based on *a*-Mg$_2$P$_2$O$_7$ (blue squares). The values for the actual *a*-Mg$_2$P$_2$O$_7$ are shown by r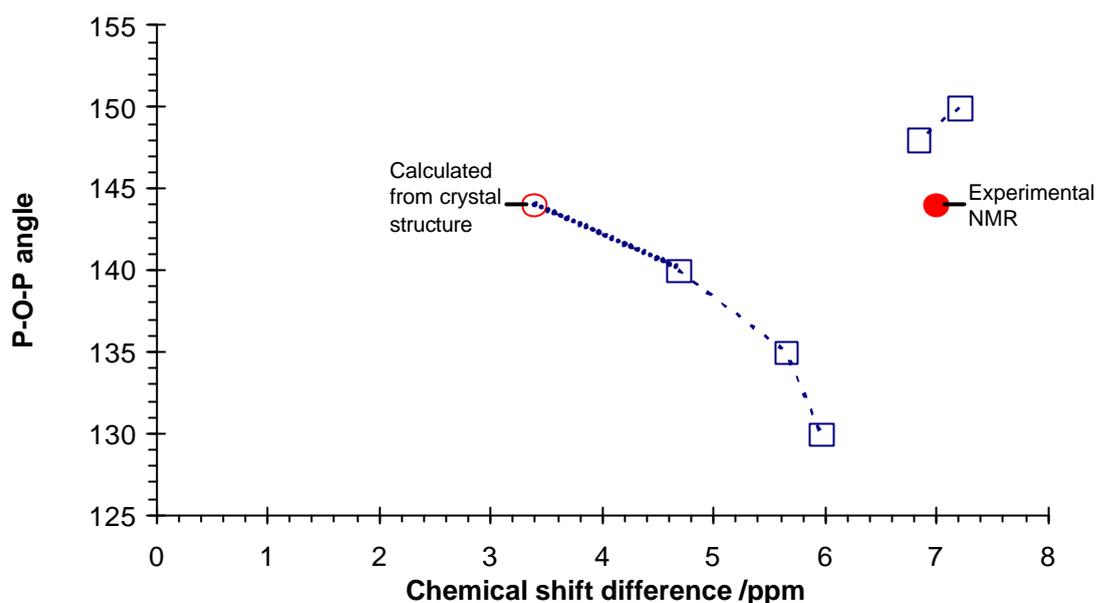ed circles (filled – experimental spectra, open – calculated shifts). Lines are added as guides to the eye showing apparent smooth variation.**

The calculated NMR data, in terms of both chemical shift of the individual peaks (Figure 6-13) and the difference between them (Figure 6-14), show a discontinuous change in structure between 140 and 148 ° P-O-P angle. At either side of this "transition" however, the calculated chemical shifts apparently vary systematically, with the value for the true structure, as derived from the crystal structure lying on the same smooth line as the theoretical structures.

The calculated shifts suggest that there is a structural difference between the structures derived with bond angles either side of a distinct transition. This is an interesting result since the theoretical structures were previously thought to be similar, showing no differences apart from the gradual change in the P-O-P angle. In the light of the calculated NMR data, the structures were re-examined. It was found that there was indeed a subtle but clear shift in the position of certain atoms. The definite difference in structures is most clearly seen by an examination of the calculated powder diffraction patterns for the theoretical models, as shown in Figure 6-15.
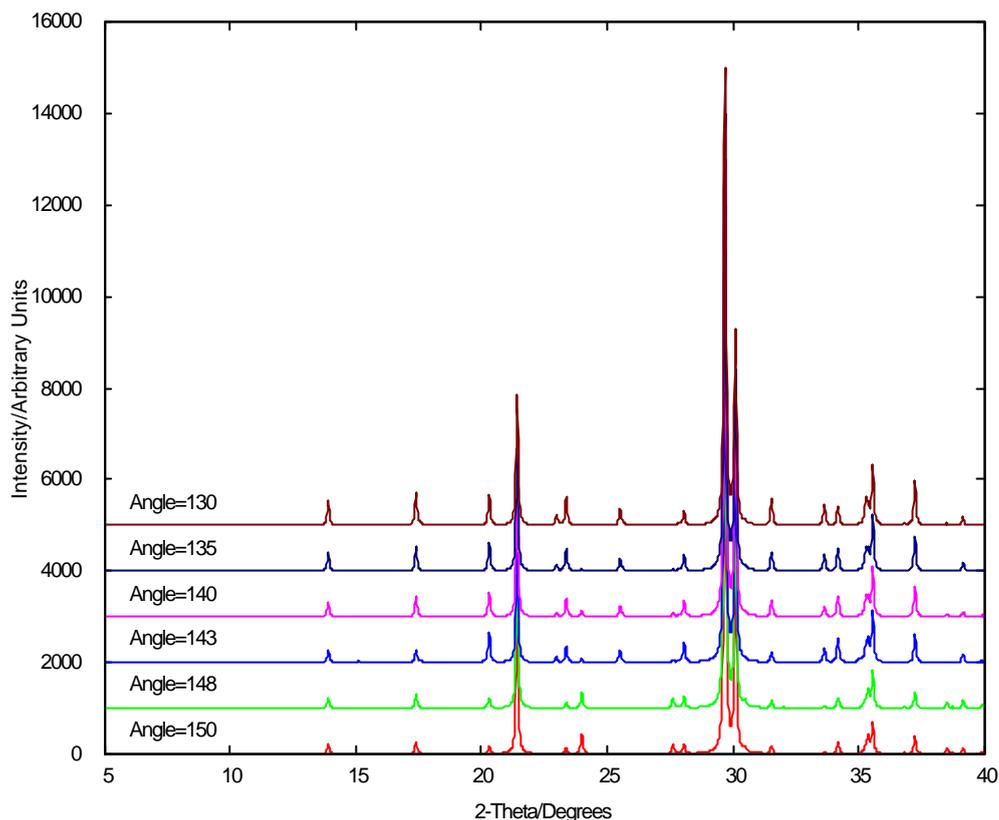
Figure 6-15 Calculated powder diffraction patterns for the theoretical Mg₂P₂O₇ structures (as listed in Table 6-2) with various P-O-P bond angles.

The most obvious discontinuous change in the powder patterns (Figure 6-15) is the dramatic change in intensity of the *120* and *121* peaks at around 25.5 ° 2?. This clearly shows that there is a transition between distinctly different structures, which was not detected until the calculated chemical shifts were examined. This suggests that NMR chemical shift calculations may be able to probe relatively subtle structural changes, and illustrates the potential for NMR to detect phase transitions.

6.7 Conclusions

The survey of the literature and crystallographic database shows that the A₂P₂O₇ group of compounds is indeed a useful series of materials for the study of ^{31}P chemical shifts. Overall, there is a wide range of structures with different metal ions and P₂O₇ group geometries, and thus the effect of a variation of a number of structural parameters on chemical shift could be studied in future.

The CASTEP chemical shift calculations show that although absolute chemical shifts are not reliably determined, chemical shift differences within a given structure are calculated more accurately, with errors typically less than 5 ppm. Further work is required before this approach may be used to assist in the assignment of spectra.

A series of preliminary experiments have been carried out in order to determine a method for future theoretical studies. The DLS method was used to define model structures. This method allows the formation of structures which are chemically reasonable on the basis of bond valence considerations. Although the models used for these calculations were relatively simple, with the PO_4 tetrahedra bond angles constrained, the method could be used to produce structures with less constrained symmetry. This would allow a detailed investigation of the relationship between structural symmetry and the actual atomic positions which determine NMR chemical shifts. One of the most interesting conclusions from these early studies is that relatively subtle differences in structures can be detected by the NMR calculations, as illustrated by the chemical shift calculations for a series of theoretical model structures.

It is important to note that one of the fundamental limitations of this approach is that disordered structures can not be modelled. The P_2O_7 groups of many materials exhibit some degree of disorder, as seen by crystallographic methods. Such disorder, either dynamic (for example movement of the central P-O-P bridging oxygen atom) or static, is neglected since the structure is assumed to conform to the periodic structure. Nevertheless, the approach outlined in this Chapter is interesting, and has the potential to give an improved understanding of the relationship between structure and NMR parameters.

6.8 References

1   S. Kelly, 'Preliminary Studies of the Relationship Between ^{31}P NMR Shifts and Structure in Negative Thermal Expansion Materials', University of Durham, 2005.
2   M. D. Segall, P. J. D. Lindan, M. J. Probert, C. J. Pickard, P. J. Hasnip, S. J. Clark, and M. C. Payne *J. Phys.: Cond. Matt.*, 2002, **14**, 2717-2473.
3   C. J. Pickard and F. Mauri, *Phys. Rev. B.*, 2001, **63**, Article no. 245101.
4   A. Boukhari, *J. Alloys Comp.*, 1992, **188**, 14-20.
5   W. H. Zachariasen, *Z. Kristallgr.*, 1930, **73**, 1.
6   D. W. J. Cruickshank, H. Lynton, and G. A. Barclay, *Acta Cryst.*, 1962, **15**, 491-498.
7   C. Calvo, *Acta Cryst.*, 1967, **23**, 289-295.
8   C. Calvo, *C. J Chemistry*, 1965, **43**, 1139-1146.
9   T. Stefanidis and A. G. Nord, *Acta Crystallogr.,Sect.C.*, 1984, **40**, 1995-1999.
10   B. E. Robertson and C. Calvo, *Can. J. Chem.*, 1968, **46**, 605-612.
11   A. Pietraszko and K. Lukaszewicz, *B. Acad Pol Sci-Chim*, 1968, **16**, 183-187.
12   A. A. ElBelghitti and A. Boukhari, *Acta Cryst., C.*, 1994, **50**, 482-484.
13   C. Calvo, *Canadian. J Chemistry*, 1965, **43**, 1147-1153.
14   T. Stefandis and A. G. Nord, *Z. Kristallogr.*, 1982, **159**, 255-264.
15   J. T. Hoggins, J. S. Swinnea, and H. Steinfink, *J. Sol. State. Chem.*, 1983, **47**, 278-283.
16   W. H. Baur and E. Tillmanns, *Acta Cryst., B.*, 1986, **42**, 95-111.
17   N. Krishnamachari and C. Calvo, *Acta Cryst., B.*, 1972, **28**, 2883-2885.
18   J. B. Forsyth, C. Wilkinson, S. Paster, and B. M. Wanklyn, *J. Phys. Condens. Matter*, 1989, **1**, 169-178.
19   K. Lukaszewicz, *Bull. Acad. Pol. Sci. SerSci.Chim.*, 1967, **15**, 47-51.
20   D. Kobasshi, S. Kohara, J. Yamakawa, and A. Kawahara, *Acta Cryst.,C.*, 1997, **53**, 1523-1525.
21   B. Masse, A. Guitel, and A. Durif, *Mat. Res. Bull.*, 1979, **14**, 337-341.
22   H. Effenberger, *Acta Cryst., C.*, 1989, **46**, 691-692.
23   B. E. Robertson and C. Calvo, *Acta Cryst.*, 1967, **22**, 665-672.

24   B. E. Robertson and C. Calvo, *J. Sol. State. Chem.*, 1970, **1**, 120-133.
25   O. V. Karimova, O. V. Yakubovich, and V. S. Urusov, *Vestnik Moskovskogo Universiteta, Geologiya*, 1997, **52**, 32-40.
26   T. Bataile, P. Bénard-Roccherullé, and D. Louër, *J. Sol. State. Chem.*, 1998, **140**, 62-70.
27   N. C. Panagiotopoulos and I. D. Brown, *Acta Cryst.*, 1972, **B28**, 1352-1357.
28   A. A. ElBelghitti, A. Elmarzouki, A. Boukhari, and E. M. Holt, *Acta Cryst., C.*, 1995, **51**, 1478-1480.
29   I. J. King, 'Combined Use of Powder Diffraction and Magic-Angle Spinning NMR to Structural Chemistry', Ph.D. Thesis, University of Durham, 2003.
30   K. Lukaszewicz, *Bulletin de l'Academie Polonaise des Sciences, Serie des Sciences Chimiques*, 1967, **15**, 53-57.
31   N. E. Brese and M. O'Keeffe, *Acta. Cryst. B*, 1991, **47**, 192-197.
32   I. D. Brown and D. Altermatt, *Acta. Cryst. B*, 1985, **41**, 244-247.

Appendices

6.9 Correlation plots for fitted parameters from 1D-EXSY experiments

The 1D-EXSY data (intensity, *I* vs. mixing time, *t*) in Chapter 4 were fitted to an equation of the form , $I = A_1 e^{-k_1 t} + A_2 e^{-k_2 t} + A_3 e^{-k_3 t}$. As discussed previously, this gave a range of values for fitted parameters. It was not possible to determine any correlation between the starting conditions and the values obtained for A_1, A_2, A_3, k_1, k_2 and k_3. Scatter plots were used to search for any correlations which may have aided understanding of the NMR. These plots are presented here as they may assist future work in this area.

All experiments were carried out at 110 ºC, MAS rate 14.5 kHz. Error bars on data points are taken from the fitting of the rate constants. Closed points are for repeated experiments with the same starting conditions (transmitter set to the frequency of the O1/O2 peak and t_1 = 58 μs). Open points are for other experiments with various starting conditions, as stated in Chapter 3.
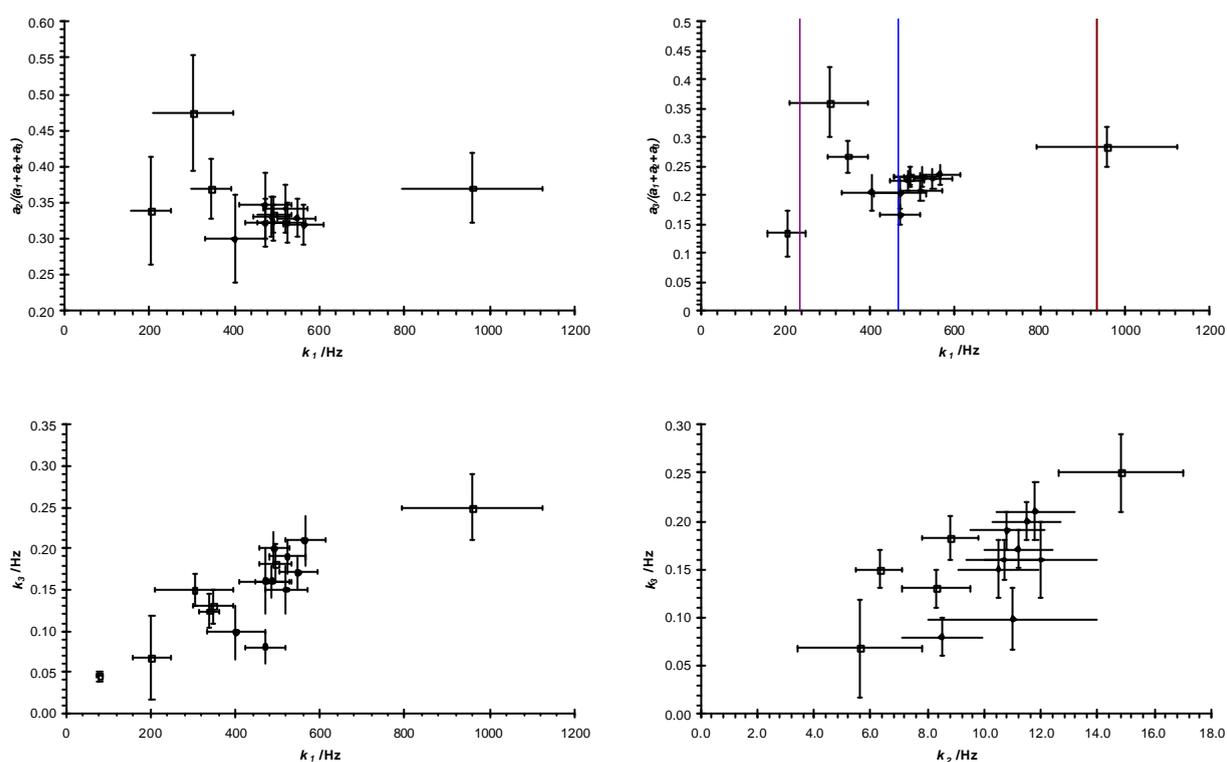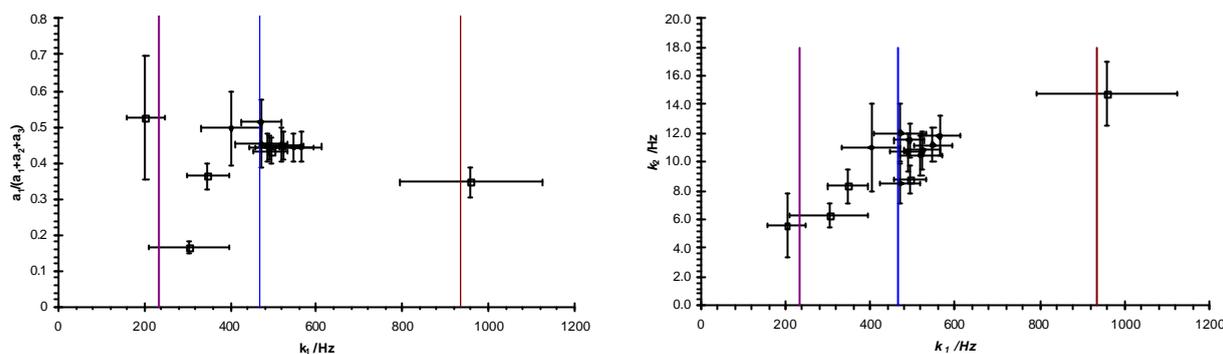
6.10 Database studies of $A_2P_2O_7$ compounds

As part of the preliminary theoretical work described in Chapter 6, a database of published crystal structures of $A_2P_2O_7$ materials was complied. This work was carried out with Sarah Kelly, as part of her final year undergraduate research project, and is detailed in her project report (Department of Chemistry, university of Durham, 2005). The methodology and a summary of results are outlined in this Appendix.

The intention was to observe the variation of configuration of P_2O_7 groups in real systems, so that suitable structures could be generated for theoretical studies. The structure files were selected from the ICSD [1] and a local database made using the CCDC PreQuest software. [2] The database was then searched using ConQuest [3] and geometric data about the conformation of P_2O_7 groups obtained.

The ICSD was searched for all compounds with the formula $A_2B_2X_7$ containing phosphorus and oxygen. There were multiple published structures for a number of phases, in these cases the most up-to-date and accurate structure was used. Several difficulties were encountered in producing this database. A number of structures had been published in unconventional space group settings, and were not imported correctly by PreQuest. In these cases, the structures were converted to standard settings using Cryscon [4]. For example, the structure of $Mg_2P_2O_7$ had been published in $B2_1/c$, and was converted to the primitive cell $P2_1/c$.

It was found that in some cases there were problems with the formation of a 3D structure from the imported CIF. This caused some problems when using the database to extract structural parameters such as bond angles. The problem is rooted in the fact that PreQuest is designed for the display of organic molecules, and the default settings are not suited to extended inorganic structures. The solution to the problem was to select "POLYM, option 11" to "expand to formula unit around metals", and then selecting the "GENERATE-FORMULA" option. Confirmation that the 3D structure now had the correct connectivity was shown by the message "chemical & crystallographic connectivities perfectly matched".

Histograms of the P-O bond lengths, P-O-P bond angles and O-P-O-P-O torsion angles are presented in the following figure.

Parameter	Max	Min	Mean
P-O bond length	1.500 Å	1.668 Å	1.591 Å
P-O-P bond angle	122.8 °	180.0 °	147.8 °
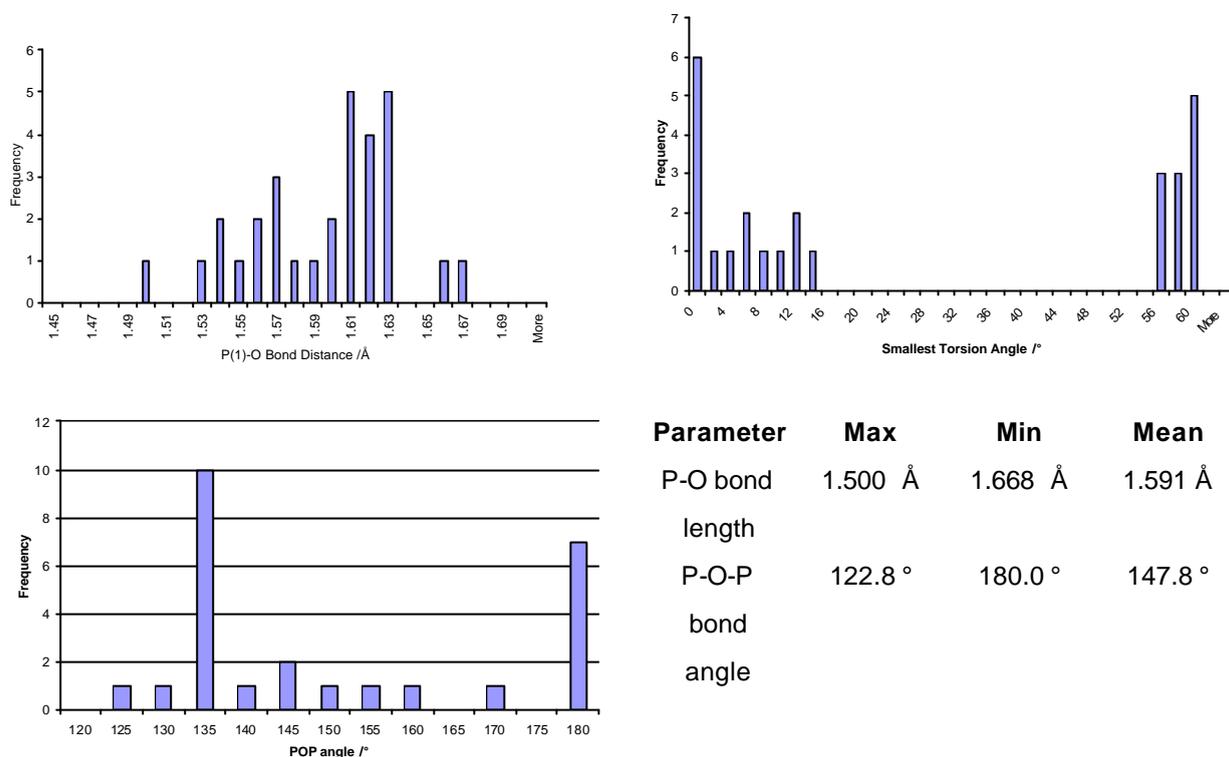
Further details are given in Sarah Kelly's project report.[5]

1   ICSD, *Inorganic Crystal Structure Database*, EPSRC Chemical Database Service, www.cds.dl.ac.uk.
2   PreQuest, *Cambridge Crystallographic Data Centre*, **CCDC**, www.ccdc.cam.ac.uk.
3   ConQuest, *Cambridge Crystallographic Data Centre*, **CCDC**, www.ccdc.cam.ac.uk.
4   CrysCon, *Shape Software*, General crystallographic conversion utility.
5   S. Kelly, 'Preliminary Studies of the Relationship Between ^{31}P NMR Shifts and Structure in Negative Thermal Expansion Materials', University of Durham, 2005.

6.11 List of publications

The following publications were prepared in relation to work presented in this thesis.

- The nature of oxygen exchange in ZrW_2O_8 revealed by two-dimensional solid-state ^{17}O NMR, M.R. Hampson, P. Hodgkinson, J.S.O. Evans, R.K. Harris, I.J. King, S, Allen, F. Fayon, *Chemical Communications*. 2004, 392-393

- Structure and phase transitions of trigonal $ZrMo_2O_8$ and $HfMo_2O_8$, S. Allen, R.J. Ward, M.R. Hampson, R.K.B, Gover and J.S.O. Evans, *Acta Crystallographica*, 2004, **B60**, 32-40

- Synthesis and NMR studies of [17]O enriched AM_2O_8 phases, M.R. Hampson, S. Allen, I.J. King, C.J. Crossland, P. Hodgkinson, R.K. Harris, F. Fayon and J.S.O. Evans, *Solid State Sciences*, 2005, **7**, 819-826

- Characterization of oxygen dynamics in ZrW_2O_8, M.R. Hampson. J.S.O. Evans and P. Hodgkinson, *Journal of the American Chemical Society*, 2005, **127**, 15175-15181

- Quantitative analysis of [17]O exchange and T_1 relaxation data: application to zirconium tungstate, P. Hodgkinson and M.R. Hampson, *Solid State Nuclear Magnetic Resonance*, 2006, **30**, *2*, 98-105

NB: The above paper is reproduced on the following pages, since it provides essential background theory relevant to Chapter 4.

- The 136 atom structure of ZrP_2O_7 and HfP_2O_7 from powder diffraction data, G.W. Stinton, M.R. Hampson, J.S.O. Evans, *Inorganic Chemistry*, 2006, **45**, *11*, 4352-4358

Quantitative analysis of ^{17}O exchange and T_1 relaxation data: Application to zirconium tungstate

Paul Hodgkinson*, Matthew R. Hampson

Department of Chemistry, University of Durham, South Road, Durham DH1 3LE, UK

Abstract

The theoretical basis behind a recent quantitative analysis of ^{17}O exchange in ZrW_2O_8 [M.R. Hampson, J.S.O. Evans, P. Hodgkinson, J. Am. Chem. Soc. 127 (2005) 15175–15181] is set out. Despite the complexities of combining the multi-exponential relaxation of half-integer quadrupolar nuclei with chemical exchange, it is shown how magnetisation transfer experiments can be analysed to obtain estimates of absolute exchange rates. The multi-exponential relaxation is best modelled using a magnetic mechanism, i.e. the rapid T_1 relaxation observed, particularly at high temperatures, can be directly related to the relatively high degree of ^{17}O labelling employed. The combination of the 1D EXSY results with T_1 values as a function of temperature provides exchange rates and activation barriers over a wide temperature range (40–226 °C).
© 2006 Elsevier Inc. All rights reserved.

Keywords: Solid-state; NMR; Exchange; Relaxation; O-17; Quadrupole

1. Introduction

Understanding the motion of oxygen within inorganic framework materials is of major scientific and technological interest [1,2]. While NMR is well placed to study motional processes in solids, the NMR of quadrupolar nuclei such as ^{17}O ($I = \frac{5}{2}$) is often complicated by the presence of strong quadrupolar interactions, making ^{17}O NMR a far from obvious tool for detailed studies of dynamics in solids. Although ^{17}O NMR is widely used for the study of materials [3], including for dynamic studies [4–7], we are not aware of *quantitative* studies of slow dynamics using ^{17}O. Spin-$\frac{1}{2}$ NMR is, of course, much more amenable to quantitative analysis, but suitable nuclei may not be available. In the case of zirconium tungstate, ZrW_2O_8, for example, it is extremely difficult to obtain an NMR signal from ^{183}W, due to its low receptivity and extremely long relaxation times, making detailed quantitative studies impractical [8]. In this paper, we show that ^{17}O magnetisation transfer and T_1 relaxation experiments can be analysed quantitatively to provide estimates of exchange rates and barriers to motion in framework solids.

We have previously demonstrated the application of ^{17}O NMR to the characterisation of oxygen mobility in ZrW_2O_8, including the use of ^{17}O EXSY to distinguish between possible motional models [9]. The oxygen dynamics could be qualitatively described in terms of ratcheting motion of the W_2O_8 units of the structure, leading to a random scrambling of the distinct oxygen sites, O1–4, Fig. 1. This work has been recently extended to *quantitative* studies of the oxygen exchange, and the results synthesised with information from X-ray diffraction to construct a comprehensive picture of the oxygen motion [8]. In this article, we describe the analytical framework behind this study of exchange using a half-integer nuclear spin, and discuss the relevance of this treatment to other studies of dynamics in solids.

2. Analysis

Previous studies of exchange processes in solids have generally involved spin-$\frac{1}{2}$ nuclei, such as ^{1}H and ^{13}C [10,11]

---

*Corresponding author. Fax: +44 191 384 4737.
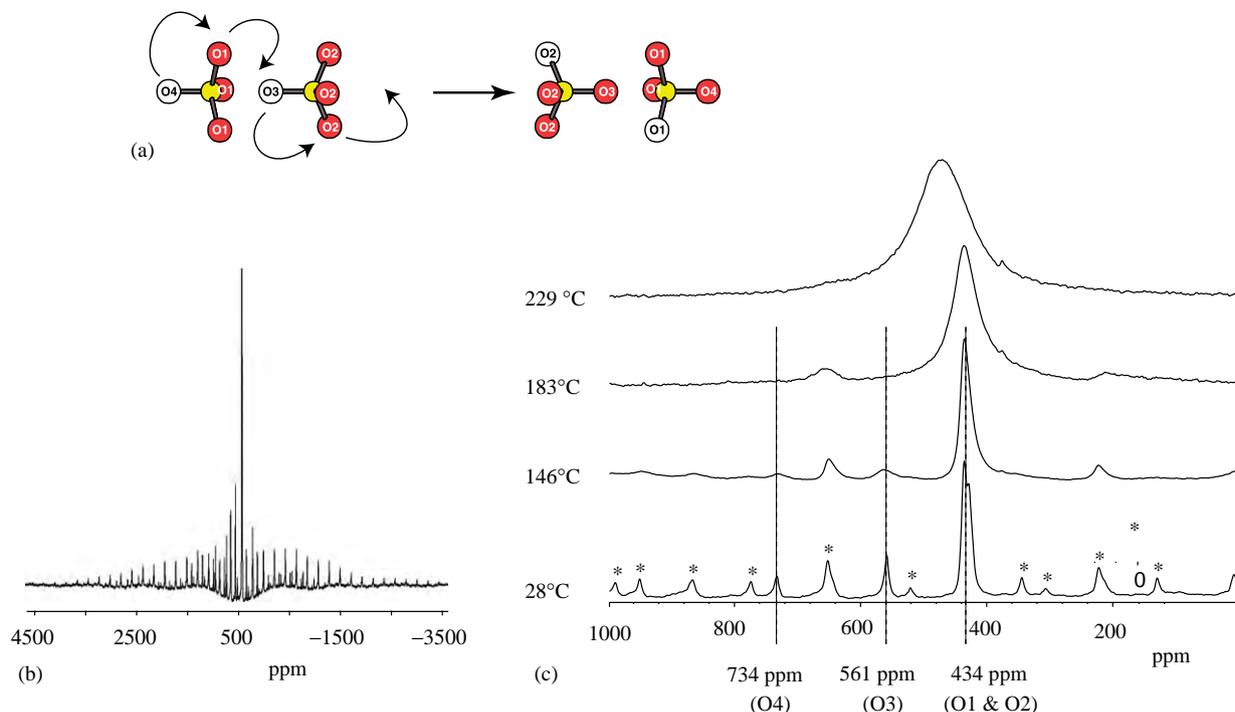E-mail address: paul.hodgkinson@durham.ac.uk (P. Hodgkinson).

Fig. 1. (a) Schematic illustration of the "ratcheting" motion of the W_2O_8 units which is considered to be responsible for the oxygen dynamics in ZrW_2O_8. (b) ^{17}O NMR spectrum at 57 °C showing full spinning sideband manifold. (c) Centre-band regions of ^{17}O spectra at representative temperatures.

or quadrupolar nuclei with relatively modest quadrupole moments, such as ^2H [12], ^6Li [13] and ^7Li [14,15]. The effect of the quadrupole coupling on the NMR frequency to first order is analogous to that of the chemical shift anisotropy, but with the two NMR-allowed transitions of spin-1 nuclei resulting in symmetrical spectra. As a result, studies of exchange processes using ^2H and ^{13}C spectra are closely related, and involve determining the effect of re-orientational motions on the sideband patterns or static lineshapes associated with the relevant anisotropy.

In contrast, the central transition ($m_I = -\frac{1}{2} \leftrightarrow m_I = \frac{1}{2}$) of half-integer spins is unaffected to first order by the quadrupole interaction. The centre band of an ^{17}O MAS spectrum is thus not significantly affected by re-orientational processes, since the exchange does not change the NMR frequency. However, in cases such as zirconium tungstate, where the isotropic shift is changed by the dynamic process, we expect the effect of exchange of the centre-band frequencies to be closely analogous to that of spin-$\frac{1}{2}$ nuclei, i.e. slow exchange rates will cause line-broadening, while exchange rates that are comparable to the shift differences will result in "coalescence" of the spectrum. Such effects are clearly observed in the ^{17}O spectra, cf. Fig. 1. The different oxygen sites are resolved at low temperature (although the O1 and O2 sites are strongly overlapped), but broaden and coalesce as the temperature, and rate of exchange, increases.

The satellite transitions (i.e. NMR-allowed transitions other than the central transition) are directly affected by

the quadrupole interaction, and so will show additional sensitivity to motional processes, since re-orientations will generally change the quadrupole coupling. In particular, we would expect the satellite transitions to broaden strongly if the exchange rate, k, is of the same order as the quadrupole coupling, $\omega_Q/2\pi$ [16]. Slow exchange processes can be studied using the satellite transitions in the same way that dynamics are probed in ^2H and ^{13}C NMR [14,15]. However, it would be very difficult to analyse the extremely large spinning sideband manifolds associated with the much larger quadrupole couplings of nuclei such as ^{17}O. Since the exchange in zirconium tungstate involves resolved sites, it is more practical to study the exchange using the strong centre bands, and the effects of exchange on the satellite transitions are not considered further.

The slow exchange regime is the easiest to treat analytically and is well adapted to accurate quantitation [17], while fitting the intermediate regime is not straightforward even for spin-$\frac{1}{2}$ systems, due to the strong correlations between the different parameters. Moreover, complete modelling of the NMR bandshape would require a complete knowledge of the NMR parameters (including those of the quadrupole interaction) for each site.

Since the chemical shift difference between the O1 and O2 sites is too small to be reliably resolved, we consider the exchange of magnetisation between three sites, O1/2, O3 and O4. As can be seen in Fig. 1(a), the effect of the motion is to exchange O4 $\leftrightarrow$ O2 and O3 $\leftrightarrow$ O1. The corresponding

kinetic exchange matrix is then

$$
\mathbf{K} = \begin{array}{c} \\ O1/2 \\ O3 \\ O4 \end{array} \begin{array}{ccc} O1/2 & O3 & O4 \\ \begin{pmatrix} -2k & k & k \\ k & -k & 0 \\ k & 0 & -k \end{pmatrix} \end{array}, \tag{1}
$$

where the element K_{ij} gives the rate of magnetisation transfer *from* site j *to* site i, and k is the jump frequency. The diagonal elements are the rates of loss of magnetisation from the different sites, i.e. $K_{jj} = -\sum_{i \neq j} K_{ij}$.

If we consider the site exchange in isolation, the time dependence of the site magnetisations, expressed as the vector $\mathbf{M} = (M_{1/2}, M_3, M_4)$, is simply

$$
\mathbf{M}(t) = e^{\mathbf{K}t} \mathbf{M}(0). \tag{2}
$$

The eigenvalues of $\mathbf{K}$ are 0, $-k$ and $-3k$, and the site magnetisation for O1/2 site is a function of the form

$$
M^{O1/2}(t) = \alpha_0 + \alpha_{-3k} e^{-3kt}, \tag{3}
$$

where the coefficient of eigenvalue λ, α_λ, is determined by the eigenvectors of $\mathbf{K}$ and the initial magnetisation vector $\mathbf{M}(0)$. Note that, unlike the O3 and O4 sites, the time dependence of the O1/2 magnetisation does not contain a component from the k eigenvalue.

In principle, other models could be proposed that lead to full exchange of the sites and so would also be consistent with the observed NMR spectra. We can consider, for example, a somewhat physically unlikely model in which a single jump process causes a fully random exchange of the sites in the W_2O_8 unit, i.e. that each site has an equal probability of finishing in any of the eight sites. The rate at which, say, an O4 site converts into an O3 site is then $k/8$ (this direct exchange is not possible in the more realistic model). The exchange matrix is then

$$
\mathbf{K} = \begin{pmatrix} -3k/2 & 3k/4 & 3k/4 \\ 3k/4 & -7k/8 & k/8 \\ 3k/4 & k/8 & -7k/8 \end{pmatrix}. \tag{4}
$$

The matrices of Eqs. (1) and (4) are very similar, and such small differences would be extremely difficult to distinguish experimentally. For example, the two models give essentially identical time dependencies for the exchange of O1/2 magnetisation, Eq. (3) (the $-3k$ eigenvalue is simply replaced by an eigenvalue of $-9k/4$). Given the complexities introduced by multi-exponential T_1 relaxation discussed below, it would be difficult to use ^{17}O NMR to distinguish between mechanisms that have such similar overall effects (complete site scrambling in this case).

It is also important to note that magnetisation transfer experiments are only sensitive to the total rates of transfer. If, for example, there is an exchange of oxygen atoms *between* W_2O_8 pairs which also leads to a ratcheting-type exchange, then the total exchange matrix, $\mathbf{K} = \mathbf{K}_{\text{intra}} + \mathbf{K}_{\text{inter}}$ has the same form as the intra-pair exchange matrix $\mathbf{K}_{\text{intra}}$. The magnetisation transfer experiment will only be

able to determine the total rate $k = k_{\text{intra}} + k_{\text{inter}}$. In contrast, relaxation rates are sensitive to the exchange rates themselves and it might be able to observe distinct intra- and inter-pair exchange via relaxation time studies, provided that the motions have sufficiently different time-scales to be distinguished, but still fall within the time-scale of the relevant relaxation process.

It may be possible to neglect T_1 relaxation if it is sufficiently slow in comparison with the chemical exchange. In general, however, it is necessary to include the T_1 relaxation in analysing magnetisation transfer experiments. The T_1 relaxation of the coherences of quadrupolar half-integer nuclei is generally multi-exponential, since relaxation occurs simultaneously between pairs of states linked by $\Delta m_I = \pm 1$ (and also $\Delta m_I = \pm 2$, depending on the relaxation mechanism). Although exact fitting of the T_1 relaxation is not critical to obtaining exchange rates, T_1 measurements are also used here to follow the temperature dependence of the exchange rate, and so it is important to be able to model the T_1 relaxation in these systems.

Two distinct mechanisms are proposed for T_1 relaxation of half-integer quadrupolar nuclei in solid samples [18]. In most circumstances, the relaxation is driven by the modulation of the orientation-dependent quadrupole interaction as a result of the motion. This "quadrupolar" mechanism links states related by $\Delta m_I = \pm 1$ and $\Delta m_I = \pm 2$ with the rates of transfer between coherences given by

$$
W_{m_I \to m_I - 1} = f_1(I, m_I) W_1, \quad W_{m_I \to m_I - 2} = f_2(I, m_I) W_2, \tag{5}
$$

where the $f_k(I, m_I)$ are numerical factors and W_n are transition rates associated with $\Delta m_I = \pm n$.

Alternatively, the relaxation may be dominated by a "magnetic" mechanism, that is, T_1 relaxation is driven by fluctuations of the local magnetic field at the Larmor frequency. In this case, relaxation only occurs across NMR-allowed transitions, with the transition probability [18]

$$
W_{m \to m-1} = (I + m)(I - m + 1) W. \tag{6}
$$

The problem can be usefully recast in terms of population *differences* between adjacent states, N_i, i.e. across the NMR-allowed transitions. We can then determine the relaxation matrix, $\mathbf{R}$, which gives the rate at which magnetisation is transferred between one NMR-allowed transition and another as a result of T_1 relaxation. If we consider the simpler magnetic mechanism, $\mathbf{R}$ has non-zero elements along just the zero and ± 1 diagonals, e.g. for $I = \frac{5}{2}$:

$$
\mathbf{R} = \begin{array}{c} \\ M_{-2} \\ M_{-1} \\ M_0 \\ M_1 \\ M_2 \end{array} \begin{array}{ccccc} M_{-2} & M_{-1} & M_0 & M_1 & M_2 \\ \begin{pmatrix} -10W & 8W & & & \\ 5W & -16W & 9W & & \\ & 8W & -18W & 8W & \\ & & 9W & -16W & 5W \\ & & & 8W & -10W \end{pmatrix} \end{array}, \tag{7}
$$

where M_0 is the population difference across the central transition, M_1 is the difference across the +1 satellite transition, etc. The evolution of the vector of population differences, $\mathbf{M} = (M_{-2}, M_{-1}, M_0, M_1, M_2)$, is simply

$$\mathbf{M}(t) = \mathrm{e}^{\mathbf{R}t}\mathbf{M}(0). \tag{8}$$

In general, each $M_i(t)$ will have up to five components corresponding to the eigenvalues of $\mathbf{R}$, $2W$, $6W$, $12W$, $20W$, $30W$ (or $p(p+1)W$ where $p = 1\ldots 2I$). Under most conditions, however, $\mathbf{M}(0)$ will be "symmetrical" in the sense that $M_i = M_{-i}$, and only the odd eigenvalues ($2W$, $12W$ and $30W$) will contribute [18]. The analysis of the relaxation via the quadrupolar mechanism follows similar

same for all sites to avoid unnecessary complication. Since the exchange rate is generally considerably faster than the T_1 relaxation, it will not be possible to observe distinct relaxation rates for different sites in any case. The Liouvillian for the combined exchange-relaxation problem is then

$$\mathbf{L} = \mathbf{R} \otimes \mathbf{1}_\mathrm{K} + \mathbf{1}_\mathrm{R} \otimes \mathbf{K}, \tag{10}$$

where $\mathbf{1}_\mathrm{K}$ and $\mathbf{1}_\mathrm{R}$ are identity matrices spanning the exchange and relaxation Liouville spaces, respectively, and $\otimes$ represents the Kronecker (or direct) product. This gives the 15×15 matrix below (in which the rows and columns for the ± 2 satellite transitions and zero elements are omitted for clarity)

$$\mathbf{L} = \begin{array}{c} \\ M_{-1}^{\mathrm{O1/2}} \\ M_{0}^{\mathrm{O1/2}} \\ M_{1}^{\mathrm{O1/2}} \\ M_{-1}^{\mathrm{O3}} \\ M_{0}^{\mathrm{O3}} \\ M_{1}^{\mathrm{O3}} \\ M_{-1}^{\mathrm{O4}} \\ M_{0}^{\mathrm{O4}} \\ M_{1}^{\mathrm{O4}} \end{array}
\begin{pmatrix}
-16W - 2k & 9W & & k & & & k & & \\
8W & -18W - 2k & 8W & & k & & & k & \\
& 9W & -16W - 2k & & & k & & & k \\
k & & & -16W - k & 9W & & & & \\
& k & & 8W & -18W - k & 8W & & & \\
& & k & & 9W & -16W - k & & & \\
k & & & & & & -16W - k & 9W & \\
& k & & & & & 8W & -18W - k & 8W \\
& & k & & & & & 9W & -16W - k
\end{pmatrix}. \tag{11}$$

lines, except that the three eigenvalues of interest are functions of the two fundamental rates, W_1 and W_2, and the form of the magnetisation recovery curve depends on the ratio W_1/W_2.

The initial distribution of magnetisation between the coherences, $\mathbf{M}(0)$, depends strongly on the size of the quadrupole interaction with respect to the RF used for excitation. If the quadrupole coupling is large, then soft RF pulses may selectively excite the central transition. In this case, the decay of the central transition magnetisation is given by

$$M_0(t)/M_0(0) = \tfrac{9}{35}\mathrm{e}^{-2Wt} + \tfrac{4}{15}\mathrm{e}^{-12Wt} + \tfrac{10}{21}\mathrm{e}^{-30Wt}. \tag{9}$$

On the other hand, if a hard RF pulse excites satellite and central transitions equally, then $M_0(t)/M_0(0) = \exp(-2Wt)$.

The case of ZrW$_2$O$_8$ falls, unfortunately, into an intermediate regime in which both satellite and central transitions are excited, but the excitation is far from uniform. This introduces considerably uncertainty into the initial excitation profile, $\mathbf{M}(0)$. Moreover, the effective quadrupole coupling is clearly modified by the motional exchange, so $\mathbf{M}(0)$ is expected to vary as a function of temperature.

The distinct Liouville spaces describing the site exchange and relaxation can be combined in a "composite Liouville" space [19]. We assume that the relaxation parameters are the

Note how the exchange terms (involving k) link corresponding coherences on different sites, i.e. we are making the common assumption that the jumps are "sudden" and do not themselves result in any re-distribution of magnetisation between the coherences on an individual nucleus.

Because the two components of $\mathbf{L}$ of Eq. (10) commute, the eigenvalues and eigenvectors of $\mathbf{L}$ are simply related to those of the parent matrices. As discussed above, the relevant eigenvalues for the evolution of the O1/2 signal are 0 and $-3k$ for $\mathbf{K}$, and $2W$, $12W$ and $30W$ for $\mathbf{R}$. As a result, the time dependence of the O1/2 magnetisation under exchange will be of the form

$$\begin{aligned}
M_i^{\mathrm{O1/2}} = & \; \alpha_{2W}\mathrm{e}^{-2Wt} + \alpha_{12W}\mathrm{e}^{-12Wt} + \alpha_{30W}\mathrm{e}^{-30Wt} \\
& + \beta_{2W}\mathrm{e}^{-(2W+3k)t} + \beta_{12W}\mathrm{e}^{-(12W+3k)t} \\
& + \beta_{30W}\mathrm{e}^{-(3k+30W)t},
\end{aligned} \tag{12}$$

where the coefficients for the pure relaxation components, α_λ, and exchange plus relaxation, β_λ, depend on the eigenvectors of $\mathbf{L}$ and the initial magnetisations. The evolution of the O3 and O4 signals is more complex still since it also contains analogous components from the $-k$ eigenvalue of $\mathbf{R}$.

Clearly attempts to fit magnetisation exchange data to the six-exponential function of Eq. (12) will be extremely problematic. In particular, the eigenvalues at $-3k - 2W$,

$-3k - 12W$ and $-3k - 30W$ are very similar (since $3k \gg 2W$). Since the fitting of similar exponentials is notoriously unstable, we will not attempt to fit the relaxation-modified exchange processes (i.e. β eigenvalues) separately.

The analysis above uses a magnetic model for the T_1 relaxation. The principles are, however, equally applicable to other relaxation models, although the final fitting functions will tend to be even more complex. Moreover, since k is generally much faster than T_1 relaxation in practical cases, accurate fitting of the relaxation behaviour is not critical to extracting estimates of the exchange rate. As we show below, the difficulties of the combined exchange and relaxation analysis mean that the systematic error on the final k values is already considerable.

3. Experiments and analysis

The preparation of the ^{17}O-labelled ZrW_2O_8 samples has been described elsewhere [20]. NMR experiments were carried out using a Varian InfinityPlus 500 spectrometer (frequency of 67.8 MHz for ^{17}O). The samples were packed in 4 mm zirconia rotors, and spun at a rate of 14.5 kHz, actively maintained to within 5 Hz by an automated MAS controller. Temperatures were calibrated using the chemical shift of the ^{207}Pb NMR signal of $Pb(NO_3)_2$ [21].

1D EXSY experiments were used to study the transfer of magnetisation due to chemical exchange, since full 2D EXSY experiment as a function of the mixing time would be unfeasibly long. The initial non-equilibrium state was simply created by an appropriate choice of t_1 and transmitter frequency. Unlike two site exchange where the initial magnetisation vectors would normally be chosen to be 180° out of phase at the start of the mixing time, there is not a natural choice of initial starting condition in this case. Hence, a number of different starting conditions (t_1 values and transmitter offsets) were used. Active synchronisation from an optical signal from the rotor was used to trigger the pulses to ensure that the mixing time was always a multiple of rotation period, i.e. the pulses at the start and end of τ_{mix} occurred at precisely the same point in the rotor cycle [22,23]. As, however, we were only interested in the exchange of centre-band intensity, it was not necessary to acquire an additional "time reversed" data set in order to obtain pure-phase sideband patterns [23]. The saturation recovery experiment was used to determine the T_1 relaxation behaviour over the temperature range 40–226 °C. The pulse program used for the rotor-synchronised EXSY, together with details of the spectrometer software modification required for successful synchronisation, is available on request.

EXSY experiments were carried out at a calibrated sample temperature of 110 °C, using an excitation pulse width of 1.9 μs. Forty values of the mixing/recovery time, in the range of 10 μs–50 s, were used in order to capture the different rate processes. The peak intensities as a function of τ_{mix} were obtained from the peak heights of approxi-
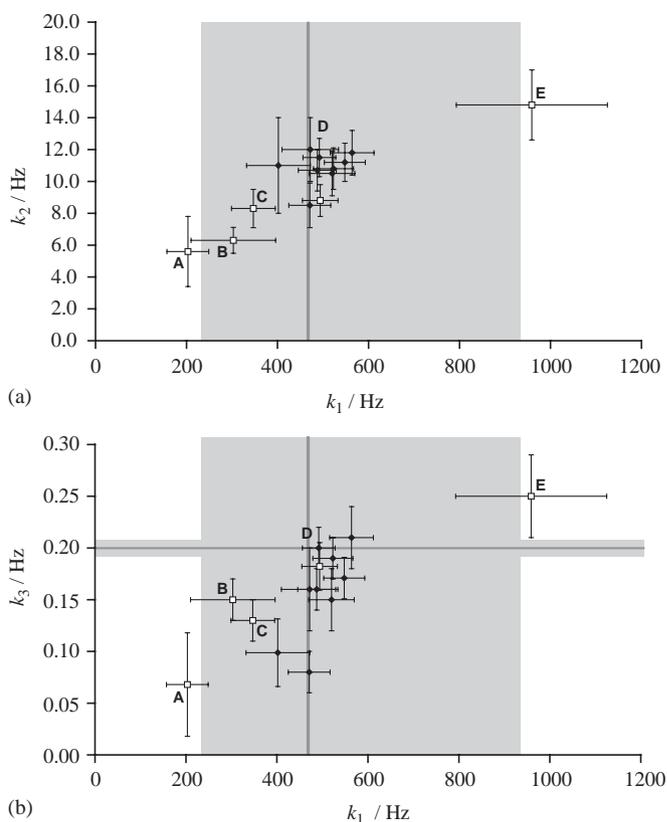

Fig. 2. Scatter plots of fitted rate parameters at 110 °C for different initial starting conditions (white squares): (a) k_1 vs. k_2 and (b) k_1 vs. k_3. Points marked with black diamonds used a common set of starting conditions (D). The vertical solid line and shaded area represent the average value and estimated error range for k_1, respectively (see text for details), while the horizontal line indicates the value of R_1 (and error range) from a saturation recovery experiment at the same temperature. The different starting conditions were: A: $v_{trans} = (v_{O1/2} + v_{O4})/2$, $\tau_{mix} = 100$ μs, B: $v_{trans} = (v_{O1/2} + v_{O4})/2$, $\tau_{mix} = 22$ μs, C: $v_{trans} = v_{O4}$, $\tau_{mix} = 22$ μs, D: $v_{trans} = v_{O3}$, $\tau_{mix} = 58$ μs, E: $v_{trans} = v_{O1/2}$, $\tau_{mix} = 22$ μs, where v_X is the resonance frequency of site X.

mately matched-filtered spectra (900 Hz of Lorenztian line-broadening). Ideally the resulting curves from each of the centre bands would be fitted simultaneously. However, only the data from the overlapped O1/O2 signals (∼430 ppm) had sufficient intensity for reliable quantitative analysis. These decays were analysed by fitting to three time constants (i.e. six variable parameters), the fastest of which (k_1) could be associated with the site exchange, while the slowest (k_3) process corresponded to the dominant component of the T_1 relaxation.

As anticipated earlier, the fitting of such complex exchange plus relaxation behaviour is problematic, and the fitted values are subject in consequence to significant systematic distortions. This can be seen in Fig. 2(a), which plots the resulting k_1 and k_2 from a number of experiments at the same temperature, varying only in the initial starting conditions of the EXSY experiment. The results from repeat experiments using identical initial conditions (black diamonds) are clustered within the error bars on the fitting.

However, varying the starting conditions has a significant effect on the fitted parameters, which demonstrates that systematic errors are more significant than the estimated random error bars would imply. Plots of other parameter pairs, e.g. k_1 vs. k_3 in Fig. 2(b), also show correlations. Although it is tempting to exclude points such as E which might appear to be outliers from the plots, they are not consistently outliers and so cannot be dismissed as erroneous. In the end, we have to accept that even Eq. (12) involves assumptions about the nature of the relaxation (e.g. that the mechanism is essentially magnetic), and so a fit to a tri-exponential is a gross simplification. In particular, the k_2 process is not well defined and can probably regarded as a combination of processes that lie between k_1 (mostly exchange) and k_3 (underlying T_1 relaxation rate). Fitting this as a single process will introduce systematic errors on the value of k_1 (which is of most interest), and the degree of distortion will be dependent on the starting conditions. Despite these uncertainties, we can make a conservative estimate of the underlying exchange rate and the "error bar" on this value. These are indicated by the vertical solid lines and shaded areas of Fig. 2. A more direct measurement of k_3 from saturation recovery experiments (horizontal line) is in good agreement with this estimate; the intersection of the horizontal and vertical lines lies close to the trend line for the correlation between k_1 and k_3, Fig. 2(b).

In principle, the number of fitted variables and the uncertainty could be reduced by predicting the relative amplitudes of the different components via the excitation efficiency of the different coherences. However, a complete model of the process including excitation efficiencies and finite pulse effects (i.e. evolution under the quadrupole interactions during the RF pulses) would be extremely complex and would require detailed information about the quadrupole interactions and how these are modulated by the motion. Coupled with the intrinsically low sensitivity of
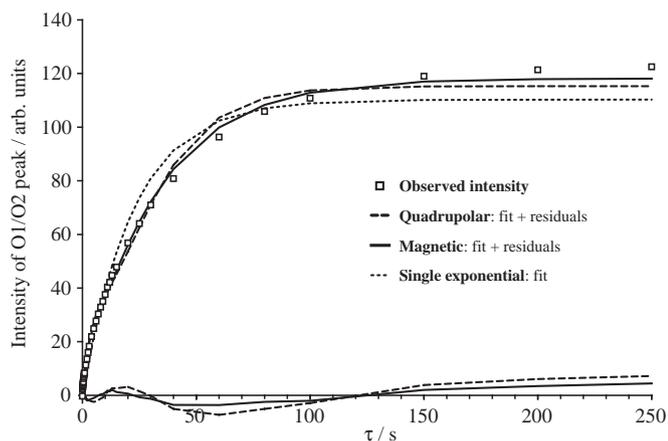
the experiments, it is doubtful the uncertainties could be reduced sufficiently to justify the considerable effort involved. Despite the relatively large uncertainties, however, we are able to obtain a quantitative measurement of the slow oxygen exchange. Moreover, as shown below, the determination of activation barriers via T_1 relaxation is essentially unaffected by the uncertainties in the absolute rate constants.

The T_1 relaxation was quantified from the integrated intensity of the O1/O2 peak of the saturation recovery data sets. As shown in Fig. 3 for data acquired at 40 °C, the relaxation is clearly multi-exponential in character. The figure shows fits to tri-exponential recoveries based on either a pure magnetic mechanism (ratio of $2W:12W:30W$ between the three rates) and a pure quadrupolar mechanism (ratio of $4W/5:3W/2:33W/10$ between the rates on the assumption that $W = W_1 = W_2$[18]). The W_1/W_2 ratio was kept fixed since a differing number of free parameters would largely invalidate the comparison of the two models. Although the systematic trends in the residuals indicate that neither tri-exponential fit is perfect, the fit using the magnetic mechanism is noticeably better, and this trend was observed consistently across the temperature range. (More convincing evidence that the magnetic mechanism dominates the relaxation is presented below.) As the temperature increases, the multi-exponential character of the relaxation becomes less pronounced.

Therefore the curves for temperatures below 180 °C were fitted to a tri-exponential with the relative values of the rate constants fixed to $1:6:15$. This reduces the number of fitting parameters, in comparison to the EXSY results, to a single rate value and three amplitude coefficients. The different oxygen sites are not resolved above 180 °C and the integral of the broad coalesced peak fitted well to a single exponential decay. The slowest component of the relaxation is always dominant and can be unambiguously identified with the k_3 rate of the EXSY analysis. This can be seen in Fig. 2(b) where the R_1 value obtained from the
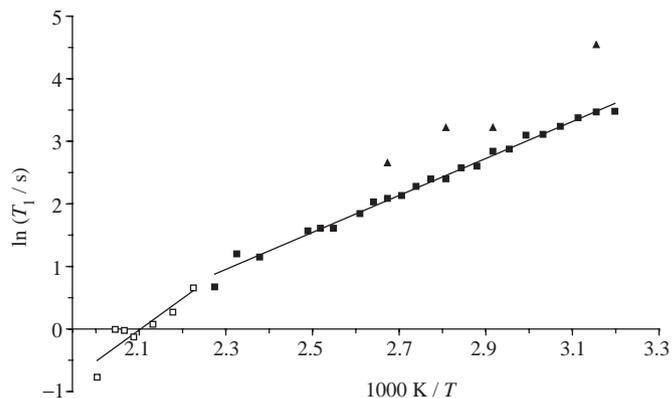

Fig. 3. Illustration of fitting the T_1 saturation recovery results with different relaxation models using data acquired at 40 °C. The fit to a single exponential (dashed line) is poor. Solid and dash-dot lines show fittings to a pure magnetic mechanism and a pure quadrupolar mechanism (with $W_1 = W_2$), respectively.

Fig. 4. Temperature dependence of $^{17}OT_1$ values for two samples: (squares) principle sample synthesised with 40% ^{17}O H_2O and (triangles) sample synthesised with 28% $^{17}OH_2O$. Open and solid symbols distinguish data points acquired below and above the phase transition at 175 °C, respectively.

saturation recovery agrees well with the average value of k_3 estimated from EXSY experiments under the same conditions.

The proposition that the T_1 relaxation is a strong function of the motional exchange is confirmed by Fig. 4 which shows a monotonic decrease in T_1 as the temperature is increased. The linearity of the plot of $\ln T_1$ vs. inverse temperature confirms that a single motional process is responsible for the relaxation.

If a single correlation time is dominant and the motion is quasi-isotropic then the relaxation rate ($R_1 = 1/T_1$) is proportional to the spectral density of the motion at the ^{17}O Larmor frequency:

$$R_1 \propto \frac{\tau_{exch}}{1 + 4\pi^2 \tau_{exch}^2 \nu_{NMR}}, \tag{13}$$

where τ_{exch} is a correlation time (inversely proportional to k_{exch}). Although using such a random-field relaxation model is typically a gross assumption for solid-state dynamics, it should be quite appropriate for this case given the simplicity of the relaxation behaviour and the similarity of the random ratcheting re-orientation of the WO_4 units with random isotropic re-orientation.

If $k_{exch} \ll \nu_{NMR}$, then R_1 will increase with increasing temperature (and k_{exch}), as observed, hence $R_1 \propto k_{exch}$. The constant of proportionality can then be determined from the estimate of k_{exch} at 110 °C derived from the EXSY experiments, allowing the T_1 values to be converted to exchange rates. The significance of these results in terms of materials chemistry are discussed elsewhere [8], but we can clearly see that robust values of the activation barrier either side of the α/β phase transition are obtained. The difficulties in quantifying the EXSY data only affect the absolute values of the rate constants, but do not affect the activation barriers which are sensitive to the *relative* values of the exchange rate. The accuracy of the activation barriers is determined by the fitting of the saturation recovery data, which is considerably more robust, as indicated by the quality of the fitting in Figs. 3 and 4.

Fig. 4 includes additional data points for a sample deliberately prepared with a lower ^{17}O concentration by using 28% rather than 40% ^{17}O enriched H_2O. The T_1 values for this sample were found to be consistently longer, by an average factor of 2.1. Unfortunately estimating the level of enrichment of the synthesised material is very difficult, and we have not been able to verify whether the relaxation rates are directly proportional to ^{17}O concentration. Nevertheless, this dependence of the relaxation rate on the concentration of the magnetic nuclei is convincing evidence that the magnetic mechanism dominates the T_1 relaxation, since the rate of relaxation due to coupling (via dipolar interactions) to neighbouring moving spins will increase monotonically with the concentration of magnetically-active spins. In contrast, quadrupolar relaxation, which involves only the nucleus' own quadrupole coupling, will be independent of ^{17}O concentration. Hence, as well as

increasing the signal intensity, the use of highly enriched samples also allows pulse repetition rates to be proportionately increased. Indeed, it is doubtful that such a detailed study would have been possible using the less fully enriched sample.

4. Discussion and conclusions

NMR is a powerful tool for the study and characterisation of dynamics in the solid state. Most previous applications of NMR to dynamic processes in solids have involved spin-$\frac{1}{2}$ nuclei (such as ^{13}C) or nuclei with relatively modest quadrupole couplings (most notably ^2H). In many applications, however, we would like to study the dynamics of half-integer spin nuclei, especially ^{17}O, with larger quadrupole couplings. We have shown that solid-state ^{17}O NMR can provide quantitative information about oxygen dynamics, even in this relatively awkward "intermediate" case in which the quadrupole couplings are neither particularly large nor particularly small in comparison with the nuclear Larmor frequency.

We have considered how magnetisation transfer experiments for half-integer spin nuclei can be described in terms of the chemical exchange and T_1 relaxation. In general, the T_1 relaxation behaviour may be complex, as it will be multi-exponential and may result from a combination of two distinct mechanisms: the magnetic mechanism (relaxation driven in this case by the motion of *other* ^{17}O nuclei) or the quadrupolar mechanism (relaxation driven by the local modulation of the quadrupole coupling by the motion of the observed spin). A detailed analysis of the relaxation would be possible if the quadrupole parameters of each of the sites were fully characterised [24], and, in principle, it may be possible to distinguish between the different mechanisms by varying the starting conditions of the magnetisation recovery experiments [25]. Even then, the difficulty of separating multi-exponential processes makes it difficult to cleanly distinguish the two mechanisms [26].

In this particular case, the concentration dependence of the ^{17}O relaxation shows that the magnetic mechanism is dominant, and satisfactory fits of the experimental relaxation data can be obtained with a minimal number of fitting parameters. Moreover, the characterisation of the nature of the T_1 relaxation is secondary to the goal of extracting rates for the site exchange, and it is sufficient to be able to approximately model the relaxation behaviour to be able to separate the T_1 relaxation and exchange components from the EXSY magnetisation transfer curves, and to obtain "central transition" T_1 values from the saturation recovery curves. In the process, however, we have demonstrated that the magnetic mechanism provides a consistently better fit to relaxation data.

The observation that T_1 values in these materials can be strongly reduced by high-efficiency labelling is very significant, as it has permitted information about the oxygen behaviour to be obtained within reasonable experimental times. The modification of T_1 relaxation

rates of quadrupolar nuclei by the presence of magnetic spins has recently also been observed in ^{31}P NMR studies (Prof. Hellmut Eckert, University of Münster, unpublished results). It is encouraging that the presence of the very dynamics under study increases the viability of the experiments; T_1 values in corresponding materials in which there is little motion are often extremely long. The combination of effective synthetic strategies and ^{17}O solid-state NMR experiments has proved extremely effective for the study of oxygen dynamics in these materials. We are currently conducting parallel studies on other members of AM_2O_8 family of materials, but the same approaches should be applicable to a wide variety of other materials containing half-integer spin nuclei.

References

[1] J.-C. Boivin, Int. J. Inorg. Mater. 3 (2001) 1261–1266.

[2] J. Routbort, S. Rothman, J. Appl. Phys. 76 (1994) 5615–5628.

[3] K.J.D. Mackenzie, M.E. Smith, Multinuclear Solid-state NMR of Inorganic Materials, Pergamon, Oxford, 2002.

[4] J.H. Kristensen, I. Farnan, J. Chem. Phys. 114 (2001) 9608–9624.

[5] N. Kim, C.P. Grey, Science 297 (2002) 1317–1320.

[6] N. Kim, R.-N. Vannier, C.P. Grey, Chem. Mater. 17 (2005) 1952–1958.

[7] J. Emery, D. Massiot, P. Lacorre, Y. Laligant, K. Conder, Magn. Reson. Chem. 43 (2005) 366–371.

[8] M.R. Hampson, J.S.O. Evans, P. Hodgkinson, J. Am. Chem. Soc. 127 (2005) 15175–15181.

[9] M.R. Hampson, P. Hodgkinson, J.S.O. Evans, R.K. Harris, I.J. King, S. Allen, F. Fayon, Chem. Commun. (2004) 392–393.

[10] N.M. Szeverenyi, A. Bax, G.E. Maciel, J. Am. Chem. Soc. 105 (1983) 2579–2582.

[11] Z. Luz, P. Tekely, D. Reichert, Prog. Nucl. Magn. Reson. Spectrosc. 41 (2002) 83–113.

[12] K. Schmidt-Rohr, H.W. Spiess, Multidimensional Solid-State NMR and Polymers, Academic Press, New York, 1994.

[13] R. Nagel, T. Groß, H. Günther, H. Lutz, J. Solid State Chem. 165 (2002) 303–311.

[14] R. Messer, H. Birli, K. Differt, J. Phys. C 14 (1981) 2731–2746.

[15] Z. Stoeva, R. Gomez, D.H. Gregory, G.B. Hixb, J.J. Titman, Dalton Trans. (2004) 3093–3097.

[16] S.E. Ashbrook, S. Antonijevic, A.J. Berry, S. Wimperis, Chem. Phys. Lett. 364 (2002) 634–642.

[17] A.D. Bain, Prog. Nucl. Magn. Reson. Spectrosc. 43 (2003) 63–103.

[18] E.R. Andrew, D.P. Tunstall, Proc. Phys. Soc. 78 (1961) 1–11.

[19] R.R. Ernst, G. Bodenhausen, A. Wokaun, Principles of Nuclear Magnetic Resonance in One and Two Dimensions, Clarendon Press, Oxford, 1987 Section 2.4.3.

[20] M.R. Hampson, S. Allen, I.J. King, C.J. Crossland, P. Hodgkinson, R.K. Harris, F. Fayon, J.S.O. Evans, Solid State Sci. 7 (2005) 819–826.

[21] A. Bielecki, D.P. Burum, J. Magn. Reson. 116 (1995) 215–220.

[22] A. de Jong, A. Kentgens, W. Veeman, Chem. Phys. Lett. 109 (1984) 337–342.

[23] A. Hagemayer, K. Schmidt-Rohr, H.W. Spiess, Adv. Magn. Reson. 13 (1989) 85–130.

[24] J. Seliger, R. Blinc, J. Phys. Condens. Matter 5 (1993) 9401–9410.

[25] T. Rega, J. Phys. Condens. Matter 3 (1991) 1871–1876.

[26] A. Suter, M. Mali, J. Roos, D. Brinkmann, J. Phys. Condens. Matter 10 (1998) 5977–5994.

6.12 Electronic Appendix

A CD-R of files is included, as listed in the following table.

Chapter	Files
1	• Endnote database of references
2	• Log of X-ray diffractometer scans
3	• X-ray diffraction data and Rietveld input files for: ZrW_2O_8, $ZrW_2O_8.xH_2O$, trigonal-$ZrMo_2O_8$, cubic $ZrMo_2O_8$, LT-$ZrMo_2O_8$ and $ZrMo_2O_7(OH)_2.2(H_2O)$
4	• Spreadsheet of 1D EXSY results for ZrW_2O_8
5	• Rietveld input files for HfP_2O_7 (high temperature and low temperature)
	• Rietveld input file for HfV_2O_7
6	• Input files for DLS refinements
	• CIF and Atoms input files for theoretical $Mg_2P_2O_7$ structures